Enhanced Patient-Specific Brain Biomechanical Modeling: Structure and Disease

By

Saramati Narasimhan

Dissertation
Submitted to the Faculty of the
Graduate School at Vanderbilt University
in partial fulfillment of the requirements
for the degree of

DOCTOR OF PHILOSOPHY
in
Biomedical Engineering

June 30, 2019

Nashville, TN

Approved:
Michael I. Miga, Ph.D.
Brett C. Byram, Ph.D.
Benoit Dawant, Ph.D.
Reid C. Thompson, M.D.
Jared A. Weis, Ph.D.

DEDICATION

This dissertation is dedicated to my fellow patients. Your unconditional support during my darkest times gave me the strength to continue treatments and fight for the next day. Thank you for being my courage, my motivation, and my continual inspiration. This dissertation belongs to all of us.

I would also like to dedicate this dissertation to the most important people in my life, Swati Narasimhan and Hernán González. Swati, you are the best sister the world has ever seen. Thank you for always literally and metaphorically being at my side. I cannot wait to see how you will change the world for the better. Hernán, this would not be possible without you. Thank you for hogging the lab equipment October 5th, 2012. Here is to a lifetime of love and science to come.

ACKNOWLEDGEMENTS

I would like to thank the members of the Biomedical Modeling Laboratory, past and present, for their assistance in my research. Rebekah Griensenaur, Yifei Wu, Jarrod Collins, Hernán González, Sarah Goodale, Ma Luo, Jon Heiselman, Winona Richey, Derek Doss, and Logan Clements have helped through their discussions, debugging, and data collection.

My committee members - Dr. Michael I. Miga, Dr. Brett C. Byram, Dr. Benoit Dawant, Dr. Reid C. Thompson, and Dr. Jared A. Weis – have been instrumental in my scientific growth as well as development as an independent scientist. I would like to sincerely thank Dr. Jared A. Weis for his instrumental help in the development of my technical skills and knowledge. His continued support during my Ph.D. played a vital role in my research. I sincerely appreciate all of the time Dr. Reid C. Thompson invested in educating me about neurosurgery and neuroanatomy. His time and effort led to the formulation of my research and my understanding of the physics I aimed to capture. I would also like to thank Dr. Michael I. Miga for being my thesis advisor. Without Dr. Miga, this thesis would not have been possible.

I would like to acknowledge all of my funding sources. This work was supported in part by the National Institute of Health - National Institute of Neurological Disorders and Stroke R01NS049251 and R21NS087796. It is also supported in part by the NIH Training Grant T32 EB021937, the National Institutes of Health-National Cancer Institute K25CA204599 and P30CA012197. It was also supported by the VISE Seed Grant Program.

Finally, I would like to thank all of the patients who consented to be a part of my studies. This research would have been impossible without their willingness to participate.

TABLE OF CONTENTS

Page

CHAPTER

VI Quantifying Influence of Tumor Growth 78

VII Future Directions and Conclusions 103

LIST OF TABLES

Table VI. 1: This contains a summary of the shift correction of the measured points in the two simulations in the four types of atlas corrections performed. Magnitude is abbreviated with mag.. 93
Table VI. 2: This contains a summary of the brain shift categories used to reconstruct the two simulation measured displacements based on atlas type. 94
Table VI. 3: This contains a summary of the shift correction of the measured points in all six patients in the four types of atlas corrections performed. Magnitude is abbreviated with mag.. 96

LIST OF FIGURES

Figure **Page**

CHAPTER I

I. Specific Aims

In a study of the global disease burden of cancer in 2018, an estimated 296,851 new cases of brain and nervous system cancer were diagnosed with 241,037 of these cases resulting in death [1]. Approximately one third of diagnosed brain and other nervous system tumors are malignant [2], [3]. The US population greater than 65 years of age is anticipated to double by 2030, and the amount of individuals diagnosed with cancer is expected to increase correspondingly; consequently the demand for effective cancer treatment will increase proportionately [3]. This reflects an increase not only in primary brain tumors, but also in metastatic brain cancer. Glioblastomas are the most common form of malignant primary brain tumors [2], [3]. In a study performed by M.D. Anderson Cancer Center on patients with glioblastoma multiforme, they found that it was necessary to resect a minimum of 89% of the tumor volume in order to improve the patients' survival after index surgery [4]. Additionally, they found that resection of a minimum of 98% of the tumor volume is associated with a significant survival advantage [4]. Generally, this thesis retrospectively investigates if the integration of computational modeling approaches can increase surgical fidelity through enhancing localization of cancerous tissue while simultaneously preserving healthy brain.

There has been extensive research into biomechanical modeling of the brain with the goal of improving various aspects of neurosurgery. These have not been translated into clinical workflow. Currently there has not been consensus on what model is appropriate to use to simulate brain tissue [5]. There have been investigations into elastic, poroelastic, viscoelastic, and hyper-elastic representations of brain tissue. Given the poroelastic model's ability to account for both the solid and liquid components of brain tissue, it is the intuitive choice. Additionally, despite preliminary work into anatomical specificity, there is also no consensus on what features within the brain are required to accurately capture its behavior. Biomechanical models have the potential to improve a variety of neurosurgical procedures.

Beyond common anatomical features, patient brains can also contain tumor(s). Modeling of the diseased tissue differs from modeling of healthy brain tissue. There is a rich history of mathematical modeling of the biomechanical effects of brain tumor growth [6], [7], [8]. Rather than investigating intracranial tumors in isolation, this thesis explores treating an intracranial tumor as a brain structure itself. One patient population that may benefit from studying biomechanical tumor growth effects are those who have undergone stereotactic radiosurgery (SRS). An adverse effect of SRS is radiation-induced necrosis, which occurs in up to 20% of patients [9]. Since radiation-induced necrosis and tumor recurrence often appear similarly on imaging, these patients are often monitored with serial scans and are diagnosed with brain biopsies [9].

Studying this patient population can aid in refining a model of tumor growth to assess intracranial lesion influence. By calibrating a tumor growth model in those who have undergone SRS, the model could be used to differentiate radiation-induced necrosis from recurrence, which is currently an important, but unmet clinical need in surgical planning [9], [10].

The developed enhanced structure and disease modeling can be tested in multiple applications. One such application is image-guided neurosurgery for tumor resection. Current image-guidance systems are static and do not account for brain shift during tumor resection. The research into biomechanical models to correct for brain shift has shown promise to actively update intra-operative guidance [11], [12], [13], [14], [15]. Existing shift correction procedures, however, do not account for the mechanics of brain shift resulting from tumor cavity collapse due to tumor resection. We will refer to this type of shift as 'debulking.' Surgical practice certainly reflects the complex mechanical behavior with tumor resection as the release of tissue tension in resection can result in tissue collapse. Characterizing both the normal brain anatomy and the impact of diseased tissue on surgical localization could improve image-guidance. As evident from studies of tumor volume resection [4], further improvements in image-guidance using a model-based method can have a significant impact on patient outcomes by improving resection accuracy. **This research hypothesizes that enhancing anatomical brain models with the addition of effects from space-occupying lesions will improve the predictive fidelity of biomechanical models of the brain for use in neurosurgical and interventional applications.**

Specific Aim 1: Enhance modeling of a normal brain by incorporating realistic anatomical constraints and reconstructing material properties. Previous modeling studies have attempted to enhance deformation models of the brain by accounting for the dural septa and interstitial pressure dynamics [14], [16]. This aim hypothesizes that enhanced modeling of the brain will enable *in vivo* interstitial pressure gradients and compartmentalization to be captured. To account for these, boundary conditions and anatomically based mesh specifications will be tested along with novel tissue material properties reflective of tissue compressibility. Using an *in vivo* study of interstitial pressure in a porcine brain subject to surgical loads, the material properties of grey and white matter will be reconstructed. It is expected that accounting for the main structures of the brain and its material properties will enhance the modeling of interstitial pressure compartmentalization, pressure gradients, and intra-operative brain deformation.

Specific Aim 2: Enhance brain modeling by developing tumor growth behaviors for the purpose of determining biomechanical effects. Previous studies have used mechanically coupled reaction-diffusion models to model intracranial tumors [17], [10]. In this aim, the underlying hypothesis is that a biomechanically coupled tumor growth model can be used to noninvasively determine the etiology of enhancing intracranial lesions. Using serial imaging in patients with intracranial metastases who have previously undergone SRS, the biophysical tumor growth model will be fit and compared to recurrent tumors and cases of radiation-induced necrosis. To determine the accuracy of the model classification, the predicted diagnoses will be compared to the known clinical diagnoses. At the conclusion of this aim, a means of modeling intracranial tumor growth and approximating the effect of space-occupying lesions will have been developed. This aim can develop a noninvasive, patient specific surgical classification tool using standard-of-care clinical imaging for radiosurgery.

Specific Aim 3: Evaluate the influence of quantifying tumor growth for application in image-guided neurosurgery by predicting intra-operative brain shifts from tumor debulking. Incorporating enhanced anatomical modeling (**Aim 1**) and estimations of displacement and pressure due to the patient's tumor (**Aim 2**), the effects of tumor debulking during resection will be approximated with a novel model based atlas. This aim hypothesizes that accounting for the mechanics of tumor debulking will improve intra-operative brain shift predictions. This aim involves using pre-operative data (Magnetic Resonance (MR)) and collected intra-operative data (laser range scan, intra-operative MR (iMR), or Ultrasound) collected during tumor resection. The intraoperative brain shift predictions accounting for tumor debulking will be assessed. The deformation prediction improvement will be assessed relative to the three intra-operative modalities. At the completion of this aim, improvements due to the incorporation of the effects from space-occupying lesions will be assessed. Development in this aim can indicate the significance of accounting for tumor debulking in image-guided neurosurgery and improve brain shift predictions.

CHAPTER II

II Background and Significance

II.1 Clinical Significance

II.1.1 Disease Burden

Intracranial tumors, including primary and metastatic cancers, affect all portions of the population and can cause significant morbidity and mortality. Metastatic intracranial tumors can arise from various primary cancers. One study suggested up to 40% of patients with certain cancers may develop intracranial metastases [18]. Some of the most common metastatic intracranial tumors include lung, renal, and breast cancer [19]. Primary brain tumors also have multiple types including glioblastomas, pituitary tumors, meningiomas, and oligodendrogliomas [20]. In a report of brain and other nervous system primary tumors, between 2011 and 2015, there were approximately 121,277 primary brain and other nervous system tumors diagnosed in the United States of America [21]. In a separate statistical report, the average annual age-adjusted rate of incidence for primary brain and central nervous system tumors was 21.97 per every 100,000 people [2]. For malignant brain and central nervous system tumors, the approximate five and ten year survival rates were approximately 35.0% and 29.3% respectively [21].

Not only do intracranial tumors carry a poor prognosis, but they also affect a significant portion of the population. The median diagnosis age of patients with primary and central nervous system tumors was 60 years of age in a survey of patients between 2011 and 2015 [21]. These tumors represented the 8th most common type of cancer in adults over 40 years of age [21]. Intracranial tumors not only affect the elderly, but in reality have a bimodal distribution, affecting the young and the aged. Between 2011 and 2015, brain and central nervous system tumors were the most common cancers in people between the age of 0 and 14 [21]. This bimodal distribution has been observed for some time now. Over the survey of patients between 2004 and 2007, nonmalignant tumors represented approximately two-thirds and one-thirds of adult and childhood brain tumors respectively [3]. Given the prevalence and significant morbidity of these tumors multiple modalities of treatments have been developed including chemotherapy, radiotherapy, and surgical resection [22], [20]. Unfortunately, despite a plethora of research toward improving these treatments there remain certain challenges limiting the efficacy of each of these. Within the scope of this thesis, issues concerning the implementation of radiotherapy and surgical resection will be addressed.

II.1.2 Diagnosis

II.1.2.1 Detection of Tumor/ Clinical Presentation

Accurate diagnosis of brain tumors is central to developing an effective treatment plan, however, diagnosis is complicated by the fact that clinical presentation of intracranial tumors is extremely varied [23, 24]. Symptoms of intracranial tumors can include focal neurologic deficits, confusion, memory loss, and changes in personality; however, headaches and seizures are the most common symptoms of brain tumors [23]. Intracranial tumors cause diverse clinical symptoms through multiple mechanisms such as brain invasion, compression of nearby regions, and/or increased intracranial pressure. Furthermore, the signs and symptoms produced by a tumor also depends on the location of tumor and the function of the brain regions affected. Given the nonspecific presentation of intracranial tumors, clinical signs and symptoms may provide little guidance for treatment. Therefore, patients with suspected either primary or metastatic brain tumor typically undergo neuroimaging.

II.1.2.2 Initial Imaging

Central nervous system imaging plays a vital role in both diagnosis and treatment planning for intracranial tumors. Except in cases of emergency, magnetic resonance imaging (MRI) with contrast is the best study for brain tumors [25]. Different tumors may have certain appearances on MRI that may aid in diagnosis. For example, common radiographic features of metastatic lesions include presence of multiple intracranial tumors and location of tumor at gray-white junction [26]. High-grade gliomas typically appear hypointense on T1 weighted MRI and enhance with contrast. Additionally, GBM typically display rim enhancement with a central clearing due to necrosis. Features that may be indicative of infiltrative tumors include T2 hyperintense signals in the cortex and adjacent white matter [25]. These radiographic features may suggest the etiology of intracranial lesions, however, appearance on MRI alone is not diagnostic of any particular tumor.

Newer imaging techniques, such as magnetic resonance spectroscopy (MRS) and diffusion weighted imaging, have attempted to improve upon specificity of diagnosis achievable by neuroimaging. For example, MRS has shown some promise in improving diagnosis of intracranial tumors by analyzing presence of metabolites which may assist in distinguishing a tumor from necrosis or benign lesions [24]. However, high quality studies of MRS are still needed to determine the utility of this technique [27]. Diffusion weighted provides information that may help differentiate between pyogenic abscesses and necrotic intracranial tumors that may appear similar on imaging [25]. Despite the promise of new imaging techniques and the information garnered from classical imaging, neuroimaging currently provides insufficient detail to arrive at a final diagnosis. The gold standard for diagnosis of a brain tumor remains invasive intracranial tissue sampling, by stereotactic biopsy or open surgery, for histopathologic and molecular studies [24]. However, this thesis proposes that in certain instances clinical imaging for diagnosis and surgical intervention may be augmented through biomechanical modeling.

II.1.3 Treatment

II.1.3.1 General Treatment Strategy

Complete treatment of patients with intracranial tumors is often an interdisciplinary process including medical oncologists, radiologists, neurosurgeons and other providers [24]. General medical therapy for this patient population includes treatment of seizures, peritumoral edema, venous thromboembolism, fatigue, and neurocognitive difficulties. Standard tumor specific therapy for patients with intracranial tumors currently involves a combination of a primary therapy, for example surgical resection or radiosurgery, and adjuvant therapies, such as chemotherapy. Adjuvant therapies are defined as those given after primary treatment to lower risk of tumor recurrence and are often an integral part of the treatment plan. A complete discussion of adjuvant therapies for intracranial tumors is beyond the scope of this work. However, adjuvant therapies play a crucial part in modern treatment paradigms therefore we will highlight some examples of adjuvant therapies here. For example, high-grade gliomas are best managed through a combination of treatment modalities including surgical resection, adjuvant postoperative radiotherapy, and adjuvant chemotherapy. Likewise, in one study, patients with a solitary intracranial metastasis treated by surgical resection alone may have up to 50-60% risk of local recurrence over a period of 6-12 months [28],[29],[30]. In fact, there are level 1 recommendations that surgical resection followed by adjuvant whole brain radiation therapy represent improved local tumor control compared to surgical resection alone [31]. Adjuvant therapies have been shown to be efficacious in radiotherapy as well. A review on the role of SRS in patients with brain metastases provided level 1 evidence that a combination of single-dose SRS with whole brain radiation therapy led to significantly longer patient survival as compared to whole brain radiation therapy alone [32]. As evidenced by these examples, adjuvant therapy often augments the efficacy of primary treatments, such as radiotherapy or surgical resection and are central to treatment of intracranial tumors.

II.1.3.2 Radiation Therapy

Radiotherapy can be used to treat both primary and metastatic disease, and may be used alone or in combination with chemotherapy and surgery [33]; while there are a variety of radiotherapy options for intracranial tumors, this work specifically concerns stereotactic radiosurgery (SRS). The goal of SRS is to destroy tumor cells while limiting harm to adjacent healthy brain. SRS is a noninvasive radiation therapy that delivers precisely focused beams of radiation to treat tumors by distorting or destroying DNA of tumor cells. SRS helps establish local control of intracranial metastases, but is complicated by radiation-induced necrosis. Radiation-induced necrosis occurs typically three months or later after SRS treatment and is an adverse reaction of the brain tissue to the radiation treatment [9, 34]. Following SRS, up to 20% of patients exhibit radiation-induced necrosis [9, 35], which often appears as an enhancing lesion in MR T_1-weighted contrast-enhanced imaging with accompanying T_2-weighted and Fluid-Attenuated Inversion Recovery (FLAIR) abnormalities [9, 36, 37]. For patients with intracranial metastases that are treated solely by SRS, local recurrent disease may arise in some patients [38]. The not insignificant incidence of local recurrence complicates diagnosis of radiation-induced necrosis. To monitor for recurrence after SRS patients undergo serial imaging however, this may lead to the detection of new lesions of unknown significance at the site of treatment.

Diagnosis of the lesion etiology presents enormous clinical challenges since recurrence and radiation-induced necrosis often appear radiographically similar. Treatments for radiation-induced necrosis include observation and corticosteroids, with symptoms sometimes resolving without further treatment [39]. Unfortunately, these treatments could delay treatment of recurrence, or even worse, accelerate tumor progression. As in primary brain tumor diagnosis, biopsy is the current gold standard for diagnosis but introduces considerable risk. There have been studies into alternative noninvasive methods of reaching a diagnosis such as using perfusion imaging [9, 40-43], positron emission tomography [44], and magnetic resonance spectroscopy [9, 45-47], but these have only had limited success. Patients that undergo SRS for intracranial lesions would benefit greatly from a noninvasive method to determine the nature of these enhancing lesions.

II.1.3.3 Surgical Intervention

The other treatment of intracranial tumors evaluated within the scope of this thesis is surgical resection. The most common type of malignant primary tumor is glioblastoma, which is particularly infiltrative and aggressive [21], [48]. In patients with primary brain tumor amenable to surgical resection, maximal safe surgical resection is the primary approach to diagnosis and management. In an investigation of patients with glioblastomas, 416 individuals, who had undergone tumor resection were studied to identify predictors of survival outcomes [4]. The median survival time in patients, who received a resection of 98% or more of the tumor volume, was 13 months. This is in contrast to the median survival time of 8.8 months in other patients, who had less tumor volume resected [4].

The resection of tumors is also related to tumor recurrence; 80% of recurrent glioblastomas occur within a 2 cm margin of the original resection [49]. The significance of accurate tumor resection is also seen in lower grade intracranial tumors. For instance, in low-grade gliomas, extent of resection serves as a predictor of overall patient survival [50]. From these investigations, and numerous others, it is evident that the optimal resection of intracranial tumors, regardless of etiology, is vital to successful treatment and this work suggests that resection of tumor could be enhanced by improving accuracy of intraoperative localization of diseased brain tissue.

Image-Guided Neurosurgical Systems (IGNS) are common intraoperative assistive devices that help surgeons localize the diseased tissue [51], [52], [53]. Briefly, in IGNS the patient's preoperative imaging is registered into the physical, intraoperative space providing surgeons knowledge of where they are within the brain. A shortcoming of this technology, however, is that it treats the preoperative image as static. This is not reflective of intraoperative changes during neurosurgery due to brain shift [51], [52], [53]. There are a variety of causes of brain shift, including hyperosmotic drugs, gravity, removal of the tumor, loss of cerebrospinal fluid, edema, and the craniotomy [51], [52], [14], [13]. Improving the fidelity of IGNS by updating the preoperative imaging to reflect the intraoperative configuration of the brain could improve patient outcomes. This work proposes one approach to improving the fidelity of IGNS would be to employ biomechanical models incorporating anatomical features of the brain to predict intraoperative brain shift.

II.2 Relevant Brain Anatomy

The brain is a complex organ with a variety of physical structures which increases the difficulty for surgeons and those developing assistive tools for use in neurosurgical procedures and planning. Historically, the Monro-Kellie doctrine has attempted to describe the complexity of brain biomechanics by stating that the cranial cavity is a fixed volume that is the sum of the volumes of brain tissue, intracranial blood, and cerebrospinal fluid (CSF) [54]. It naturally follows that with an increase in one of the three components, there must be a decrease in one of or both of the other components [54]. Treating the brain as only a solid tissue (often the case in brain models) negates the inherently biphasic nature of the brain within the cranial environment.

The anatomical geometric configuration of the brain is distinct from other organs. The brain is encapsulated by the dura, which is a fibrous membrane [55]. The dura extends into folds of the brain forming the dural septa, which consist of the falx cerebri and the tentorium cerebelli. As a part of its function, the dural septa reduces brain displacements during motion [55] and divides regions of the brain. The falx cerebri partially separates the cerebral hemispheres, and the tentorium cerebelli separates the occipital lobe and the cerebellum [55]. The pattern on the surface of the brain consists of sulci and gyri. The sulci are the groves in the brain, and the gyri are the plateaus formed by the boundary ridges of sulci pairs [55]. In addition to these structures, there are also the four connected ventricular cavities present within the brain to consider. These cavities, which are filled with CSF, are connected to the central canal within the spinal cord and the space around the brain [55]. Beyond these physical structures contained within it, the brain parenchyma is a heterogeneous material, consisting of grey and white matters. Grey matter consists predominantly of cell bodies, and white matter is mainly nerve fibers [55].

Intracranial clinical measurements and observations reflect the influence of these anatomical features. An example of this is intracranial pressure. Intracranial pressure is the pressure measured within the cranial vault [56]. Experimental evidence suggests that intracranial pressure can vary spatially within the brain, which is possibly the result of the brain's anatomy. This was previously suggested in a porcine study in which an extradural temporal mass lesion was simulated with an epidural balloon [57]. Similar experiments with an expanding frontal mass also reported analogous findings [58]. These findings also indicate the influence of a space-occupying lesions in the cranial cavity.

A more dramatic demonstration of intracranial compartmentalization and its significance is brain herniation which can be fatal [59], [60]. Herniation is the displacement of swollen parenchyma [61]. There are four forms of herniation: cingulate herniation, uncal or tentorial herniation, tonsillar or cerebellar herniation, and herniation through the craniotomy [61]. A cause of herniation is cerebral edema that results in elevated intracranial pressure [59]. This edema can be the result of an intracranial tumor [59].

When considering how to appropriately model both a normal and brain with a space-occupying lesion (tumor), we believe that enhancing the computational description of these anatomical features can lead to the more accurate representation of effects such as pressure compartmentalization and brain shift.

II.3 Computational Modeling

II.3.1 Soft Tissue Modeling and Structure

There is a rich history of using computational models of the brain in clinical settings, such as neurosurgery [62], [11], [63], [64]. Despite the ample research done on biomechanical modeling of the brain, there is still not a general consensus on what mechanical description of the organ should be used [52], [5], [65], [66]. Model types, are discussed below, include viscoelastic [67], [68], poroelastic [69], [70], elastic [71], [72], and hyper-elastic [73], [66] biomechanical models. Evidence for all of these representations of the brain in clinical settings such as IGNS has been provided, but they have yet to achieve fidelity which can be translated to improvements in patient outcomes. The various mechanical descriptions capture different characteristics of the brain tissue.

II.3.1.1 Elastic Mechanical Description

The elastic description of the brain prescribes that the stress state depends on strain alone [5]. This mechanical description is sometimes used since there is evidence for soft tissue deformations being accurately represented with linear elasticity, given that it is undergoing small strains [74]. An example of a clinical application of the elastic model is registration. A study utilizing the elastic model tracked brain deformations, with the goal of updating preoperative images was performed [72].

This study accomplished this by acquiring intraoperative magnetic resonance (MR) images during intracranial surgery [72]. Then key features (ventricles, cortical surface, and tumor) were segmented from the intraoperative MR images, and the boundary surfaces of these key features in the model were deformed to the new target boundaries sequentially. During this investigation, both the resection of the tumor and the CSF volume loss from the ventricles were accounted for [72]. The conclusion of that investigation was that the inclusion of the ventricular surface deformation was necessary to obtain accurate results. This application of an elastic model reflects a patient-specific application of a biomechanical model of the brain towards registration, while accounting for structural features deemed significant by the investigators. Despite the use of the elastic model, which neglects the fluid components within the cranium, the conclusions of this study indicate the importance of incorporating anatomical features in order to improve the fidelity of intracranial modeling results. The importance of anatomical features has also been observed in other biomechanical descriptions.

II.3.1.2 Poroelastic Mechanical Description

The poroelastic description of the brain depends on multiple phases. More specifically, it describes brain tissue as consisting of a fluid component and an elastic solid [5]. Poroelastic models are used typically to model quasi-static and long term processes, since they are able to capture interstitial fluid movement [5]. Due to its agreement with the Monro-Kellie Doctrine, through its ability to capture both solid and liquid components, we use a poroelastic description of the brain in the scope of this thesis. Potential applications of poroelastic models include modeling tissue retraction [69], hydrocephalus [75], and image-guided neurosurgery (IGNS) [53]. During neurosurgery, the brain shifts due to a variety of intraprocedural factors such as swelling, hyperosmotic drugs and changes in cerebrospinal fluid levels [64]. As a result, the preoperative imaging used for guidance is no longer aligned with the patient's brain. An accurate prediction of intraoperative brain deformation could enhance IGNS by actively compensating for brain shift throughout the surgical procedure and reestablishing alignment fidelity with the patient's preoperative imaging [76], [13].

One investigation into the use of the poroelastic model for this application involved the generation of an atlas of possible deformations associated with gravity and mannitol's influence during tumor resection [14].

The novelty of this study stemmed from its inclusion of the dural septa in the finite element mesh and quantifying its influence. The average shift correction without the inclusion of the dural septa was 68±17%, while the inclusion of this features resulted in an average shift correction of 75±12% [14]. Even though this finding was not statistically significant, it does speak towards the importance of anatomical specificity in modeling. It is worth noting that this investigation did not account for brain shift from all possible causes. This was observed in the discrepancy in their predicted deformation solutions relative to the measured deformations. These discrepancies were related to the influences around the resection cavity [14]. Tumor cavity collapse has been observed in multiple other investigations [15], [77]. Based on these conclusions and those of other groups, we included the dural septa as a part of our enhanced anatomical description of the brain. Furthermore, as a part of this thesis, we sought to address how to capture the influence of the tumor itself on the surrounding normal brain tissue. This was done for diagnostics and for IGNS correction.

II.3.1.3 Viscoelastic Mechanical Description

Another type of mechanical description of the brain is the viscoelastic model. It prescribes that the stress state depends on the strain history and the strain [5]. These mechanical descriptions can be functions of stress rates, strain rates, and higher order derivatives. One investigation using a viscoelastic description compared the results of a finite element representation of a viscoelastic model to analytic solutions [68]. They developed a linear, finite element representation to capture conditions representative of neurosurgical procedures. In the study, the viscoelastic models used were used to capture the stress-strain rate dependence [68].

Another group used a viscoelastic mechanical description in order capture the behavior of a bovine brain undergoing uniaxial compression [78]. They used fresh, cylindrical brain tissue samples undergoing step-and-hold tests between two plates which quantified the compressive forces being applied during the dynamic experiment. For their study, the tissue samples were exposed to engineering compressive strains between 5 and 25% [78]. They were able to validate their model viscoelastic model for up to strains levels of 35%. Generally, viscoelastic models can be used to describe short term process, including impact [5].

II.3.1.4 Hyper-Elastic Mechanical Description

Finally, hyper-elastic descriptions of the brain prescribes that the material can undergo large strains and recover elastically [73]. It ability to undergo large strains and recover results in its use to describe soft tissues. One group used a hyper-elastic description of the brain tissue in order to characterize the response of brain tissue that is undergoing large deformations. As an additional source of anatomical complexity in their model, they captured the anisotropic behavior resulting from the presence of axonal bundles throughout the tissue [73]. For their experiments, they used this mechanical description in order to model white matter tissue that had anisotropic characteristics undergoing shear and axial loading. While preliminary in nature, due to limited experimental data, this investigation looked into applying a hyper-elastic model to a microscale representation of brain tissue [73].

The hyper-elastic description has also been used in the context of computing brain deformations during image-guided surgery [66]. This biomechanical description was used assuming the strain rates during surgical procedures are negligible, and as a consequence the strain rate history is not significant [66]. They used this description in order to model craniotomy induced shift during neurosurgery. While this study concluded that the level of complexity present in hyper-elastic was not necessary to capture craniotomy induced shift, this investigation demonstrates this mechanical description in the context of neurosurgical applications [66].

II.3.1.5 Anatomical Features in Mechanical Descriptions

While all of the mechanical descriptions capture different behaviors of the brain and other soft tissues, it is evident that the types of anatomical features included in the descriptions influenced the results, regardless of mechanical description. The importance of incorporating the influence anatomical features within the brain is illustrated in the modeling of intracranial drug delivery. One specific application that has been investigated is convection-enhanced delivery (CED), which is a treatment mechanism where macromolecular therapeutic agents are delivered to the brain tissue through direct infusion [79]. In an investigation a computational transport model was developed in order to predict tracer distributions and infusion flow fields based on diffusion tensor imaging MR with the intent of improving targeted delivery [79]. They performed simulations to elucidate the influence of cerebrospinal fluid and hippocampal fissures on the targeted delivery of the tracer. Their model also enabled the diffusion and hydraulic conductivity properties to be different between the cerebrospinal fluid, grey matter, and white matter which allowed for isotropy and anisotropy to be captured accordingly [79]. The results of their simulations captured the apparent influence of CSF spaces and fissures [79]. The evidence from this investigation indicates the need to account for the evacuation of intra-sulci/intra-fissure fluid into subarachnoid spaces. This concept is explored in Chapter IV.

The investigations described are only a small sample of the breadth of literature involving using biomechanics to represent the brain in a variety of surgical and interventional applications. There are countless others, not presented here, which reflect the various opinions on what appropriate biomechanical modeling of the brain entails. From a physiological perspective, we hypothesize that the poroelastic description of the brain is the most appropriate due to its ability to account for both the solid and fluid components within the cranial cavity. This is congruent with the Monro-Kellie Doctrine. Additionally, from the literature it is evident that enhanced anatomical modeling influences the results of computational models, regardless of the parenchyma's mechanical definition. In this thesis, we propose that to address limitations of prior biomechanical brain models, identifying the boundary conditions and mesh specifications representative of anatomical features of the brain is necessary to appropriately capture the brain's behavior.

II.3.2 Tumor Growth Modeling and Structure

The computational models above account for normal brain geometry, however, they do not specifically model diseased intracranial tissue. The clinical application for this thesis involves interventional applications and surgery for patients who suffer from both primary and metastatic brain cancer. The intention behind this dissertation was to use brain cancer models in conjunction with enhanced anatomical modeling of a normal brain. By incorporating both the brain parenchyma and diseased tissue, this research aims to influence surgery and treatment planning in this patient population. There has been development of models of glioma growth and behavior, and in this dissertation we build upon these for primary and metastatic tumor modeling [80], [6]. Gliomas are a group of primary brain tumors that account for close to half of all primary brain tumors [80]. They are both diffusive and proliferative in nature [80], [6]. Below we will explore historical uses of tumor growth modeling of gliomas, including predicting growth dynamics for diagnoses, response to chemotherapy, and surgical resection [80], [6]. Building upon this existing precedent for modeling tumor growth, this dissertation applies a mechanically coupled reaction-diffusion tumor model of tumor growth for surgical planning and IGNS respectively.

There has been extensive work into modeling intracranial tumors. One group modeled untreated glioma growth in three dimensions (3D) in a spherical coordinate system and assumed symmetric spherical growth [81]. The growth of gliomas was modeled by setting the rate of change in tumor cell density to be equal to the sum of the tumor cell diffusion and the tumor cell growth [81]. They described the diffusion of tumor cells as D, and the proliferation of tumor cells as ρ [81]. The equation representation of glioma growth here was $\frac{\partial c}{\partial t} = \nabla \cdot (D \nabla c) + \rho c$, where c is tumor cell density [80]. According to this description, the relationship between the diffusion and proliferation of the cells captures the nature of gliomas specifically.

This equation can also be understood relative to possible cellular distributions within the tumor [81]. A highly diffuse intermediate-grade glioma would have a low proliferation (ρ) and a high diffusion (D). On the other hand, a high-grade glioma would have a high proliferation (ρ) and a high rate of diffusion (D) [80]. In a simulation study, one group explored the behavior of various intermediate-grade gliomas. From this work, they suggested that a highly diffuse intermediate-grade glioma may have a worse survival rate versus patients with high grade gliomas [80], [81]. It is important to note that in this investigation, they neglected anatomical features associated with the brain [81]. This is in contrast with numerous other studies which have suggested the importance of incorporating features of the brain to varying extents.

An example of incorporating brain anatomy was a study modeling the growth of gliomas. The anatomy was introduced by modifying the reaction-diffusion model in a way that the diffusion rates in white and grey matter are different, reflecting the heterogeneity of the parenchyma [82]. The equation representation of this model of tumor growth is $\frac{\partial c}{\partial t} = \nabla \cdot (D(x)\nabla c) + \rho c$ where the diffusion coefficient can spatially vary [82]. This enabled the investigators to account for the heterogeneity in diffusion properties of brain tissue. This type of specificity may be necessary to appropriately model intracranial disease phenomena in a patient-specific manner.

Another study, which incorporated the anatomy of the brain, was one which utilized magnetic resonance diffusion tensor imaging (MR DTI) [83]. In this investigation, the researchers were simulating the growth of low-grade gliomas with $\frac{\partial c}{\partial t} = \nabla \cdot (D(x)\nabla c) + \rho c$ [83]. Using MR DTI, they were able to account for both heterogeneity and anisotropy of the parenchyma [83]. This model, coupled with the imaging data, enabled them to model the anisotropic growth of the gliomas by relating the cell diffusion tensor to the water diffusion tensor obtained from the DTI image [83]. The unique aspect of their model, as compared to other reaction-diffusion models of glioma growth, was how they treated the spatially varying diffusion coefficient. More specifically, in this representation $D(x)$ is a tensor [83]. They compared model simulations to two patients diagnosed with WHO grade II gliomas [83]. They concluded the best solutions were obtained when the cell diffusion tensor was more anisotropic than the water diffusion tensor. They also found that anisotropic diffusion was necessary to fit the lesion shapes from the MRI scans [83]. Also, the location of tumor's growth initialization resulted in various behaviors with respect to the final shape [83]. It is worth noting the concept of tumor initialization impacting growth patterns was observed and utilized in the generation of atlases of tumor cavity collapse in Chapter VI. Similarly to the healthy brain models, it is evident that certain levels of anatomical specificity is necessary in order to model tumor growth.

There have also been models generated to account for treatments that patients may receive. In these models of growth and treatment, rather than describing the rate of change of tumor cells as the sum of diffusion and proliferation, the rate of change of the tumor cell is equal to the summation of the diffusion and proliferation of the tumor cells with a subtraction term representative of the loss of cells due to treatment [80]. An illustration of accounting for the effect of chemotherapy on the spatio-temporal growth of a glioma is defined by $\frac{\partial c}{\partial t} = \nabla \cdot (D\nabla c) + \rho c - G(t)c$ [84]. In this equation, $G(t) = k$ or $G(t) = 0$ when chemotherapy is being administered or is not being administered respectively [84]. They estimated model parameters using optimization techniques, fitting the modeled tumors to computerized tomography (CT) scans of the tumor [84]. Additionally, two distinct cell populations were defined. The cell populations diffused at the same rate, but were able to grow at distinct growth rates [84]. The inclusion of multiple populations enabled heterogeneity within the tumor and also enabled varied responses to chemotherapy within the tumor [84]. The inclusion of treatment effects into models of tumor growth is highly significant for clinical translation and effectively capturing both the tumor and its influences.

Not only have there been models of chemotherapy, but there have also been modeling efforts towards surgical resection [85], [86]. One group modeled the rate of change of glioma cell density in two cell populations as the result of the diffusion, increase due to growth, change due to mutation, and losses due to treatment [85]. They simulated resection by designating the cell density within the excision diameters (3, 4, 5 cm) to be zero at the first time step [85]. While the density within the resection diameter was set to zero, the cell density outside of the resection diameter was permitted to be non-zero. This permitted residual tumor to recur. The results of their investigation indicated that resection alone would not be sufficient to cure a patient with a glioma [85]. They also compared the results of their model to clinical data and found a strong agreement between their model predicted survival rates and the survival of real patients. Their work speaks to the complexity in treating gliomas and more generally the predicative abilities of tumor growth models for clinical applications.

A separate group performed an investigation to predict *in vivo* glioma growth using a reaction-diffusion model [87]. The equation used to describe the glioma growth in this investigation was $\frac{dN(\bar{x},t)}{dt} = \nabla \cdot \left(D(\bar{x})\nabla N(\bar{x},t)\right) + k(\bar{x})N(\bar{x},t)\left(1-\frac{N(\bar{x},t)}{\theta}\right)$ [87]. $N(\bar{x},t)$ is the number of tumor cells at a given location and point in time, $k(\bar{x})$ is the tumor cell proliferation at a location, $D(\bar{x})$ is tumor cell diffusion coefficient at a location, and θ is the cell carrying capacity [87]. Using initial MRI scans, parameters (D for grey and white matter, and k*)* for the equation were estimated. These estimated parameters were then used to predict the tumor's growth [87]. This *in silico* study generated accurate results that predicted future tumor growth [87]. Within the scope of the same study, they also performed *in vivo* experiments where they inoculated female Wistar rats with C6 glioma cells [87]. The *in vivo* data was more prone to error, and they concluded that the equation used was not sufficient to capture the full nature of C6 glioma [87]. This group attempted to account for this missing behavior in a follow up study.

They mechanically coupled their reaction-diffusion model [17]. A separate study indicated that the growth of tumor spheroids was inhibited if the matrix they were grown in was stiffened [88]. With this rational, in addition to the reaction-diffusion equation ($\frac{dN(\bar{x},t)}{dt} = \nabla \cdot \left(D(\bar{x})\nabla N(\bar{x},t)\right) + k(\bar{x})N(\bar{x},t)\left(1-\frac{N(\bar{x},t)}{\theta}\right)$), they modeled the mechanical coupling with $D(\bar{x},t) = D_0 e^{-\lambda_1 \sigma_{VM}(\bar{x},t)}$ and $\nabla \cdot G\nabla\vec{u} + \nabla\frac{G}{1-2v}(\nabla\cdot\vec{u}) - \lambda_2\nabla N(\bar{x},t) = 0$ [17]. D_0 symbolizes the tumor cell diffusion when no stress is present,

$\sigma_{VM}(\bar{x}, t)$ is the von Mises stress, and $\vec{u}$ is the tissue displacement [17]. λ_1 is an empirically derived coupling constant, λ_2 is a second coupling constant, G is shear modulus, and v is the Poisson's ratio [17]. They also accounted for cellular heterogeneity within the tumor by allowing the carrying capacity to vary on a voxel to voxel level [17]. They estimated the model parameters from the first three imaging points and used these parameters to predict the growth [17]. They concluded that mechanical coupling and cellular heterogeneity provided more accurate predictions of *in vivo* C6 glioma growth in their rat subjects [17]. This mechanically coupled reaction-diffusion model was implemented in thesis in Chapter V to represent metastatic disease.

There have been many other investigations directed towards computational tumor modeling. These include modeling cellular and metabolic processes to optimize chemotherapy administration [89], and angiogenesis associated with tumors [90]. The development of these models, both in the context of understanding the growth and in treatment, provide a rich history of tumor growth modeling. In the studies presented, there are common features including spatial and temporal dependence. There are also varying degrees of anatomical specificity ranging from homogenous treatment to accounting for the mechanical influence of the surrounding tissue. Similar to healthy brain models, there are no defined rules on the extent to which anatomical specificity should be captured in tumor models. Accounting for realistic anatomical constraints and the effects from space-occupying lesions (primary and metastatic tumors) can improve the fidelity of biomechanical models of the brain.

II.4 Clinical Impact

The work within the scope of this thesis has the potential to improve outcomes for patients with primary and metastatic intracranial tumors. Computational models have shown great promise for applications in clinical areas, such as neurosurgery and non-invasive diagnostics. The complexity of the brain itself increases the difficulty of generating translatable models capable of capturing the net behavior of the brain parenchyma. This is especially true when a disease state, such as a tumor, further increases the level of detail necessary to approximate its behavior. This research hypothesizes that enhancing anatomical brain models with the addition of effects from space-occupying lesions (tumors) will improve the predictive fidelity of biomechanical models of the brain for use in neurosurgical and interventional applications.

CHAPTER III

III Research Methods

This chapter outlines the methods used to investigate the hypothesis that enhancing anatomical brain models with the addition of effects from space-occupying lesions will improve the predictive fidelity of biomechanical models of the brain for use in neurosurgical and interventional applications. In the scope of this thesis, three experiments were performed. While all of these specific investigations looked into different aspects of the same hypothesis, they all involved the usage of finite element modeling and optimization.

This chapter summarizes the methods and techniques used to investigate the aims of this thesis. A combination of animal and patient data was collected and used in these aims. Generally, Aim 1 used porcine data to study the use of enhanced modeling of the normal brain. Aim 2 developed and assessed the fidelity of tumor modeling with respect to classifying tumor recurrence and radiation-induced necrosis within a retrospective patient study. Aim 3 combined the model of a normal brain with a model of tumor growth to evaluate the influence of quantifying tumor growth for application in image-guided neurosurgery in a retrospective patient and simulation study.

Section III.1 outlines the experimental procedures used to collect the animal and patient data necessary to perform all of these investigations. Section III.2 presents the governing equations, derivations, and finite element modeling techniques used. As a means of fitting the finite element models (Section III.2) to the experimental data (Section III.1), different methods of optimization were used. The specific optimization techniques used depended on the nature of the data and the objective of each aim. These optimization methods will be detailed in Section III.3.

III.1 Experimental Procedures

III.1.1 Retrospective *in Vivo* Porcine Experiment of Enhanced Brain Modeling

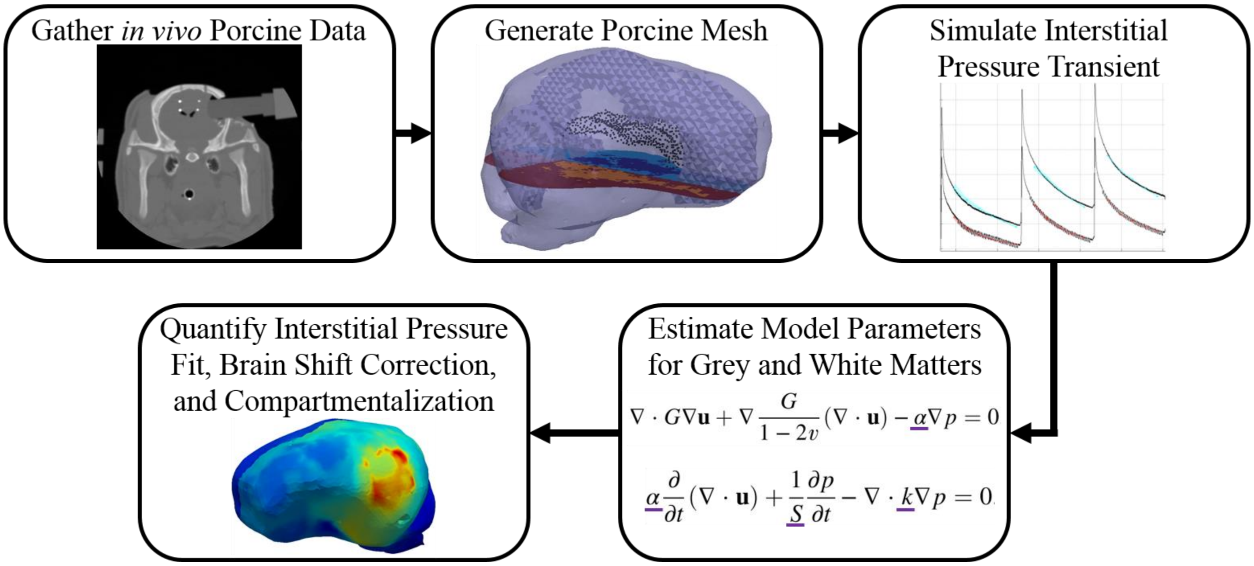

Figure III. 1: This is a flowchart illustrating the methods employed to investigate the impact of enhanced anatomical modeling of a normal brain undergoing mock surgical loads. In a porcine study, finite element methods combined with an inverse model were used to estimate *in vivo* interstitial pressure measurements.

The objective of this investigation was to study the impact of enhancing the modeling of a normal, healthy brain by accounting for anatomical constraints and reconstructing material properties of the brain. This was done in order to establish a model of brain biomechanics before incorporating disease. To investigate this, experiments were performed to test if the poroelastic biphasic model equations ((III.1.a) and (III.1.b)) with enhanced features could accurately capture *in vivo*, interstitial, porcine pressure gradients and compartmentalization. The finite element implementation of these equations is explained in Section III.2.2. The details of this procedure are expanded upon in Chapter IV and [91].

The porcine data was collected previously in [16]. In accordance with the Institutional Animal Care and Use Committee, a Yorkshire pig had a pressure transducer implanted in the left and right hemispheres of its brain along with a grid of stainless steel beads after being anesthetized. Before the implantation, a T_1-weighted magnetic resonance (MR) of the brain was collected. A temporal craniotomy was made on one side of the skull, and through this craniotomy, a mock surgical load was induced with a piston-like source (Figure III.2). This piston was moved in increments of 2 and 4 mm [16]. A baseline computed tomography (CT) scan of the porcine brain was obtained prior to this experiment. CT scans of the brain were subsequently obtained after each piston translation. The measured pressure data was gathered continuously via the implanted pressure transducers, and using the registered CT scans, brain shift was tracked by measuring the movement of the stainless steel beads [16]. The displacement and pressure measured at the 8 mm, 10 mm, and 12 mm piston translations were used.

The influence of three anatomical characteristics were investigated. These three features were the dural septa, the ventricle boundary condition, and the saturation parameters, which we hypothesized served as an approximation of the influence of the sulci and gyri [91]. In order to investigate the influence of the dural septa, using the preoperative MR, two custom finite element meshes of the porcine brain were generated (Figure III.1). The first mesh included the dural septa, and the second mesh did not [91]. In total there were four model descriptions. These were the full anatomical model description (FACD), which had the dural septa present, treated the ventricle boundary as the reference pressure, enabled the brain to be unsaturated, and had a total of 6 material properties being estimated from the governing equation ($k, \alpha, \frac{1}{S}$ for grey and white matters). The second model description, condition without dural septa description (CwoDSD), differed from FACD by not including the dural septa within the finite element mesh. The third model description, condition without ventricle boundary description (CwoVBD), differed from FACD by treating the brain stem as the reference pressure instead of the ventricles. The fourth model description, conventional fully saturated model (CFSM), used the conventional assumption that the brain is a fully saturated material ($\alpha = 1, \frac{1}{S} = 0$), which reduced the number of material properties being estimated to two [91].

Using an inverse model (Section III.3.2), the material properties ($k, \alpha, \frac{1}{S}$ for grey and white matters) of the biphasic model were estimated in order to best match the model estimated pressures at the transducer locations to the interstitial pressure values measured from the transducers (Figure III.1). This was done with all four of the model descriptions, for each piston translation, with 20 randomized initial starting property guesses, generating a total of 240 runs of the inverse model [91]. At the conclusion of the interstitial pressure simulations, estimates for the model parameters for the grey and white matters were generated for each of the model descriptions (Figure III.1). Using the best parameter estimations (based on pressure fits), pressure and displacement solutions using Equations (III.1.a) and (III.1.b) were generated. The solutions for the piston fits of the four model descriptions were then assessed based on how they fit the interstitial pressure gradients, predicted brain shift, and captured pressure compartmentalization. The results of this investigation are in Chapter IV.

III.1.2 Retrospective Tumor Modeling Experiment - Recurrence vs Necrosis

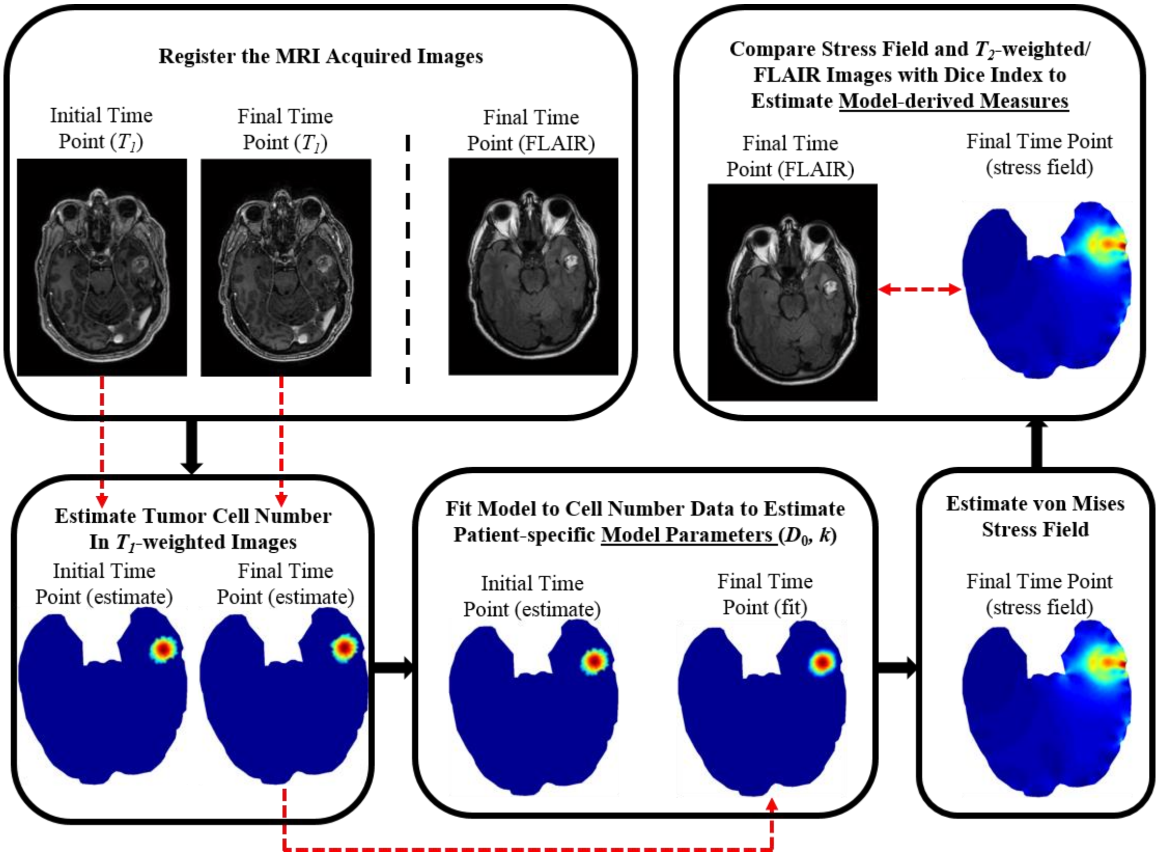

Figure III. 2: This is a flowchart of the methods used to investigate whether a mechanically coupled reaction-diffusion model of tumor growth could be used to noninvasively differentiate tumor recurrence from radiation-induced necrosis.

The purpose of this study was to develop and assess the fidelity of a model of tumor growth. In order to accomplish this, a mechanically coupled reaction-diffusion model (Equations (III.17.a), (III.17.b), and (III.17.c)) of intracranial tumors was used to noninvasively differentiate radiation-induced necrosis from tumor recurrence in patients who had previously undergone stereotactic radiosurgery (SRS). The hypothesis was that differences in the biophysics of the two etiologies would result in differences in the model parameters and model-derived measures. The specifics of this procedure are further detailed in Chapter V, [92], and [93].

Ten de-identified clinical data sets of serial MRI scans were obtained under the Vanderbilt University Institutional Review Board as a retrospective study [92]. All of these patients had a metastatic lesion which was treated with SRS, and two time points of the patient scans were evaluated. Five of these patients had been diagnosed with radiation-induced necrosis, while the other five had been diagnosed with tumor recurrence [92]. Two sets of MRI scans were obtained at two time points. One of these sets of MRI scans consisted of FLAIR or T_2-weighted and T_1-weighted collected prior to diagnosis. The other set of MRI scans were T_1-weighted scans collected prior to these. The timing between the two sets of scans varied among patients depending on the clinicians [92]. The scans for a given patient were registered to one another (Figure III.2), and the axial slice with the most volumetric change was selected for evaluation [93].

As a first-order approximation, a Gaussian distribution of tumor cell density was assumed, and the ‘observed tumor cellularity’ in the segmentations of the T_1-weighted scans were estimated (Figure III.2). The mechanically coupled tumor growth model’s (Equations (III.17.a), (III.17.b), and (III.17.c)) prediction of tumor cellularity was fit to the ‘observed tumor cellularity’ using a Levenberg-Marquardt parameter optimization (Section III.3.2). For details on the finite element implementation of the governing equations, refer to Section III.2.3. This provided estimates of the model parameters, diffusion (D_0) and proliferation (k) for each patient (Figure III.2). Using these estimates of the model parameters and the governing equations ((III.17.a), (III.17.b), and (III.17.c)), the von Mises stress field was calculated (Figure III.2). The regional similarity between this stress field at multiple contours and the segmented edematous region (T_2-weighted or FLAIR), was quantified using the Dice similarity index to estimate the model-derived measures (Figure III.2) [92]. Additionally, morphometric analysis methods, including the ratio of lesion size in two imaging types and changes in the segmented tumor volumes, were tested on the same set of patients as a clinical frame of reference. The estimated model parameters and model-derived measures were then used to classify the patients as either having tumor recurrence or radiation-induced necrosis. The results of this work are in Chapter V.

III.1.3 Retrospective Brain Shift Correction Experiment

This final investigation combined the enhanced description of brain anatomy and the influence of a space-occupying lesion. The purpose of this study was to evaluate the influence of quantifying tumor growth for brain shift correction in image-guided neurosurgery (IGNS). This was tested by evaluating the influence of predicting brain shifts due to debulking in IGNS. In this investigation, ‘debulking’ was defined as the process of brain shift specific to tumor cavity collapse due to tumor resection. The details of this experiment are expanded on in Chapter VI.

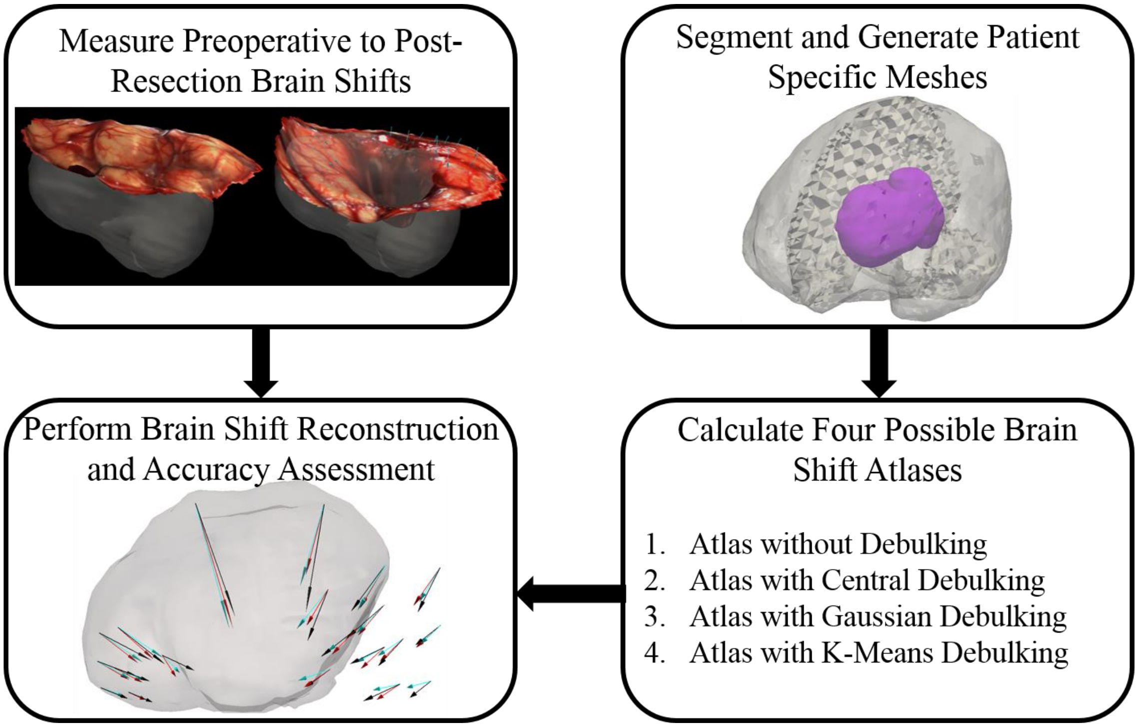

Figure III. 3: This is a flowchart of the methods used to investigate the influence of accounting for brain shifts due to debulking in image-guided neurosurgery.

The influence of debulking was tested in two simulation studies and retrospectively in six patients who had experienced debulking, based on metrics to quantify debulking proposed in the scope of this investigation. For all of the cases, preoperative to post-resection brain shifts were quantified (Figure III.3). The patient data was collected using laser range scans, intraoperative MR, and intraoperative ultrasound [15], [94], [95]. These collections were done in compliance with the Vanderbilt Institutional Review Board and the Brigham and Women’s Hospital Institutional Review Board. The simulated brain shifts were generated with forward runs of the finite element models in Sections III.2.2 and III.2.4. It was specified that the simulated brain shifts were not represented within the atlas solutions. All of the cases had patient specific finite element meshes generated (Figure III.3).

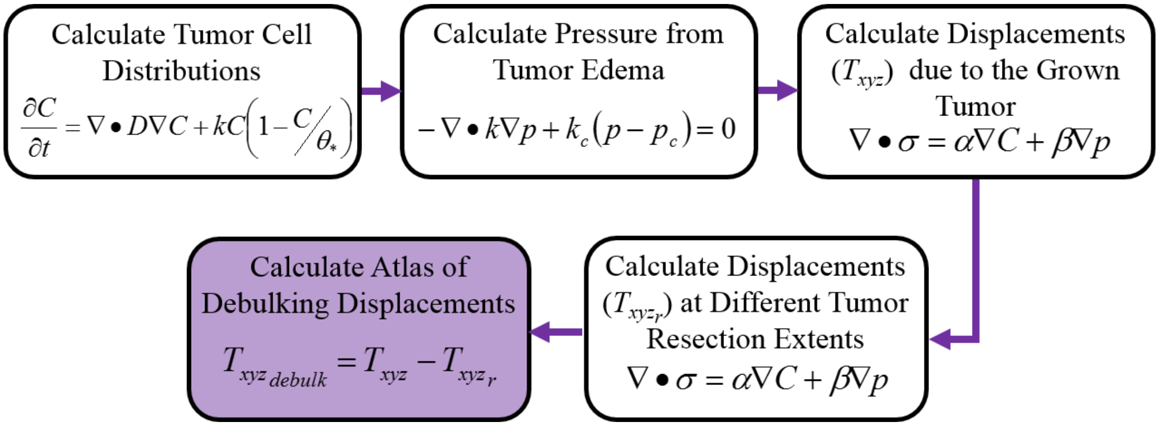

Figure III. 4: This is a flowchart of illustrating the physics of debulking, which was used to generate the debulking atlases.

Four possible brain shift atlases were investigated (Figure III.3). The baseline atlas (Atlas without Debulking) accounted for brain shifts from gravity, hyperosmotic drugs, and swelling. The other three atlases had shifts representing debulking incorporated in addition to the aforementioned causes of brain shift. The fundamental difference between the three debulking atlases (central debulking atlas, Gaussian debulking atlas, and k-means debulking atlas) was the method of calculation of the tumor cell distribution. The physics of debulking was shared between all three debulking atlases, and we will briefly summarize it here (Figure III.4) (Section III.2.4). First, the tumor cell distribution was calculated, either using a Gaussian distribution for the Gaussian atlas or the finite element representation of equation (III.38) for the other two debulking atlases. Optionally, the pressure distribution due to edema being present was calculated using the finite element representation of equations (III.48.a) and (III.48.b). The displacements with the full tumor present and when the tumor had been partially resected were calculated with equation (III.59). Finally, using these calculated displacements the atlas of debulking displacements is generated (Figure III.4).

The central debulking atlas consisted of a total of 108 solutions which captured three central tumor seed locations, three temporal evolutions, three possible craniotomies, and four resection extents. The Gaussian debulking atlas consisted of 36 displacement solutions representing three Gaussian cellular distributions, three craniotomies, and four resections. The k-means debulking atlas consisted of 72 solutions reflecting six possible tumor seed locations (determined with k-means clustering), three craniotomies, and four resection extents. Brain shift reconstruction was performed for each case with all four atlases (Figure III.5). Using a constrained least-squared minimization (Section III.3.3), the error between model predicted displacements and the measured brain shifts was minimized. The solved weighting coefficients were used to combine the deformation atlases in order to reconstruct the displacements of the full brain volume. The quality of the brain shift reconstructions were assessed and their accuracies assessed. The results of this investigation are in Chapter VI.

III.2 Finite Element Modeling

III.2.1 Finite Element Method Introduction

The finite element method (FEM) is a method to calculate an approximate solution to an unknown true solution. This is accomplished by sub-dividing a larger problem into finite subdomains or finite elements [96]. More specifically, the approximate solution to the problem is defined over the entire problem domain in terms of a set of finite basis functions. These mathematical basis functions have properties that are well defined. The approximation to the true solution obtained by using FEM is the summation of the product of a set of coefficients and these basis functions [96]. The coefficients are the unknowns being solved for in the FEM. Generally, a residual (difference between approximate solution and true solution) is defined using governing equations and a set of boundary conditions, which capture the problem. This residual is forced to be zero over the domain of finite elements [96]. The domain, or mesh, consists of elements and nodes. The finite elements used in this thesis are linear triangles in two-dimensional problems and linear tetrahedra in three-dimensional problems.

A governing partial differential equation, which captures the physics of the problem being solved, is identified. The unknown variable(s) can be approximated using a set of scalar functions of position (standard C° local Lagrange polynomial interpolants). This approximation can be used to define the residual of the problem [96]. The residual is multiplied by a selected weighting function. In order to obtain the exact solution, this product integrated over the finite element domain would equal zero. FEM can be treated as a method of weighted residuals [96]. The specific method of weighted residuals used within this thesis is the Galerkin Method of Weighted Residuals. In the Galerkin Method of Weighted Residuals, the basis and weighting functions are selected to be the same functional description [96]. The weighting function used for this work is the Lagrange interpolating function. Lagrange interpolating functions are characterized by being one at the expansion node and zero everywhere else.

FEM was used to investigate all of the aims within this thesis. Specific Aim 1, which studied enhanced modeling of a normal brain, used a poroelastic model of the brain tissue. Specific Aim 2 assessed the fidelity of tumor modeling with a mechanically coupled tumor growth model. The last aim, Specific Aim 3, evaluated the influence of predicting brain shifts from tumor cavity collapse (debulking). This aim involved the use of three distinct models. The governing equations and finite element analysis used are detailed below in Sections III.2.2, III.2.3, and III.2.4.

III.2.2 Poroelastic Model of Brain Tissue

The governing equations for the poroelastic model of brain tissue derived from Biot's description of consolidation theory are (III.1.a) and (III.1.b) [97]. In these equations p is the interstitial pressure and $\vec{u}$ is the displacement vector. G is the tissue shear modulus, t is time, ν is Poisson's ratio, and k is hydraulic conductivity. The ratio of fluid volume extracted to the volume change of tissue under compression is represented by α, and the void compressibility is represented by $\frac{1}{\mathrm{S}}$ [91]. Equation (III.1.a) relates mechanical equilibrium of the matrix and the interstitial pressure gradient [91]. Equation (III.1.b) relates volumetric strain and the conservation of fluid within a porous media [91].

$$\nabla\cdot G\nabla\vec{u}+\nabla\frac{G}{1-2\nu}(\nabla\cdot\vec{u})-\alpha\nabla p=0 \tag{III.1.a}$$

$$\alpha\frac{\partial}{\partial t}(\nabla\cdot\vec{u})+\frac{1}{\mathrm{S}}\frac{\partial p}{\partial \mathrm{t}}-\nabla\cdot k\nabla p=0 \tag{III.1.b}$$

Using the Galerkin Method of Weighted Residuals, equations (III.1.a) and (III.1.b) are multiplied with ϕ_i (a spatially-continuous weighting function) [96]. The $\langle * \rangle$ represents integration over the problem domain. Also, ϕ_i, is the i$^{\text{th}}$ member of the standard C° local Lagrange polynomial interpolants associated with finite elements [70].

$$\langle\nabla\cdot G\nabla\vec{u},\phi_i\rangle+\langle\nabla\frac{G}{1-2\nu}(\nabla\cdot\vec{u}),\phi_i\rangle-\langle\alpha\nabla p,\phi_i\rangle=0 \tag{III.2.a}$$

$$\langle\alpha\frac{\partial}{\partial t}(\nabla\cdot\vec{u}),\phi_i\rangle+\langle\frac{1}{\mathrm{S}}\frac{\partial p}{\partial \mathrm{t}},\phi_i\rangle-\langle\nabla\cdot k\nabla p,\phi_i\rangle=0 \tag{III.2.b}$$

The divergence and gradient integral identities are (III.3.a), (III.3.b), and (III.3.c).

$$\langle\nabla\cdot(G\nabla\vec{u}\phi_i)\rangle=\oint \mathrm{G}\hat{n}\cdot\nabla\vec{u}\phi_i ds=\langle\phi_i\nabla\cdot G\nabla\vec{u}\rangle+\langle G\nabla\vec{u}\cdot\nabla\phi_i\rangle \tag{III.3.a}$$

$$\langle\nabla\frac{G}{1-2\nu}(\nabla\cdot\vec{u})\phi_i\rangle=\oint\frac{G}{1-2\nu}\hat{n}(\nabla\cdot\vec{u})\phi_i ds=\langle\phi_i\nabla\left(\frac{G}{1-2\nu}\nabla\cdot\vec{u}\right)\rangle+\langle\frac{G}{1-2\nu}(\nabla\cdot\vec{u})\nabla\phi_i\rangle \tag{III.3.b}$$

$$\langle\nabla\cdot(k\nabla p\phi_i)\rangle=\oint \mathrm{k}\,\hat{n}\cdot\nabla p\phi_i ds=\langle\phi_i\nabla\cdot k\nabla p\rangle+\langle k\nabla p\cdot\nabla\phi_i\rangle \tag{III.3.c}$$

These equations lead to the weak form of (III.2.a) and (III.2.b). $\oint *$ represents the integration over the problem domain boundary, and $\hat{n}$ represents the outward-pointing normal to the boundary.

$$-\langle G\nabla\vec{u}\cdot\nabla\phi_i\rangle+\oint \mathrm{G}\hat{n}\cdot\nabla\vec{u}\phi_i ds+-\langle\frac{G}{1-2\nu}(\nabla\cdot\vec{u})\nabla\phi_i\rangle+\oint\frac{G}{1-2\nu}\hat{n}(\nabla\cdot\vec{u})\phi_i ds-\langle\alpha\nabla p,\phi_i\rangle=0 \tag{III.4.a}$$

$$\langle\alpha\frac{\partial}{\partial t}(\nabla\cdot\vec{u}),\phi_i\rangle+\langle\frac{1}{\mathrm{S}}\frac{\partial \mathrm{p}}{\partial \mathrm{t}},\phi_i\rangle-\oint k\,\hat{n}\cdot\nabla p\phi_i ds+\langle k\nabla p\cdot\nabla\phi_i\rangle=0 \tag{III.4.b}$$

Rewriting (III.4.a) and (III.4.b) creates (III.5.a) and (III.5.b).

$$\langle G\nabla\vec{u}\cdot\nabla\phi_i\rangle+\langle\frac{G}{1-2\nu}(\nabla\cdot\vec{u})\nabla\phi_i\rangle+\langle\alpha\nabla p,\phi_i\rangle=\oint \mathrm{G}\hat{n}\cdot\nabla\vec{u}\phi_i ds+\oint\frac{G}{1-2\nu}\hat{n}(\nabla\cdot\vec{u})\phi_i ds \tag{III.5.a}$$

$$\langle\alpha\frac{\partial}{\partial t}(\nabla\cdot\vec{u}),\phi_i\rangle+\langle\frac{1}{\mathrm{S}}\frac{\partial p}{\partial \mathrm{t}},\phi_i\rangle+\langle k\nabla p\cdot\nabla\phi_i\rangle=\oint k\,\hat{n}\cdot\nabla p\phi_i ds \tag{III.5.b}$$

Equations (III.5.a) and (III.5.b) are integrated in time with two-point weighting. With θ used as a weighting factor between the implicit (at t_{n+1}) and explicit at (t_n) solutions. In this expression $0\leq\theta\leq 1$ and $\Delta t=t_{n+1}-t_n$.

$$\int_{t_n}^{t_{n+1}} f(t)dt = \Delta t\,[\theta f(t_{n+1}) + (1-\theta)f(t_n)] \tag{III.6}$$

The system is treated as fully implicit, i.e. $\theta = 1$. Therefore (III.6) is simplified to (III.7).

$$\int_{t_n}^{t_{n+1}} f(t)dt = \Delta t\,[f(t_{n+1})] \tag{III.7}$$

The representation of (III.5.a) and (III.5.b) in the time domain is (III.8.a) and (III.8.b).

$$\begin{aligned}\Delta t\langle G\nabla\vec{u}\cdot\nabla\phi_i\rangle^{\mathrm{k+1}} + \Delta t\,\langle\tfrac{G}{1-2\nu}(\nabla\cdot\vec{u})\nabla\phi_i\rangle^{\mathrm{k+1}} + \Delta t\langle\alpha\nabla\mathrm{p}\phi_i\rangle^{\mathrm{k+1}} &=\\ \Delta t[\oint \mathrm{G}\hat{\mathrm{n}}\nabla\vec{u}\phi_i ds]^{\mathrm{k+1}} + \Delta t\left[\oint \tfrac{G}{1-2\nu}\hat{\mathrm{n}}(\nabla\cdot\vec{u})\phi_i ds\right]^{\mathrm{k+1}}&\end{aligned} \tag{III.8.a}$$

$$\langle\alpha(\nabla\cdot\vec{u})\phi_i\rangle^{k+1} + \langle\tfrac{1}{\mathrm{S}}p\phi_i\rangle^{\mathrm{k+1}} + \Delta t\langle k\nabla p\cdot\nabla\phi_i\rangle^{\mathrm{k+1}} = \langle\alpha(\nabla\cdot\vec{u})\phi_i\rangle^{k} + \langle\tfrac{1}{\mathrm{S}}p\phi_i\rangle^{\mathrm{k}} + \Delta t[\oint \mathrm{k}\,\hat{\mathrm{n}}\cdot\nabla p\phi_i ds]^{\mathrm{k+1}} \tag{III.8.b}$$

The spatial discretization of (III.8.a) and (III.8.b) is completed by expanding the unknown variables as the summation of unknown coefficients, which are functions of time, multiplied by known functions of position [96].

$$\vec{u}(x,y,z,t) \approx \sum_{j=1}^{N}\vec{u_j}(t)\,\phi_j(x,y,z) \tag{III.9.a}$$

$$p(x,y,z,t) \approx \sum_{j=1}^{N}p_j(t)\phi_j(x,y,z) \tag{III.9.b}$$

Substituting (III.9.a) and (III.9.b) into the weak form generates equations (III.10.a) and (III.10.b).

$$\begin{aligned}\Delta t\sum_{j=1}^{N}\vec{u_j}\,\langle G\nabla\phi_j\cdot\nabla\phi_i\rangle^{\mathrm{k+1}} + \Delta t\sum_{j=1}^{N}\vec{u_j}\,\langle\tfrac{G}{1-2\nu}\big(\nabla\cdot\phi_j\big)\nabla\phi_i\rangle^{\mathrm{k+1}} + \Delta t\sum_{j=1}^{N}p_j\,\langle\alpha\nabla\phi_j\phi_i\rangle^{\mathrm{k+1}} &=\\ \Delta t[\oint G\hat{n}\cdot\nabla\vec{u}\phi_i ds]^{\mathrm{k+1}} + \Delta t\left[\oint\tfrac{G}{1-2\nu}\hat{n}(\nabla\cdot\vec{u})\phi_i ds\right]^{\mathrm{k+1}}&\end{aligned} \tag{III.10.a}$$

$$\begin{aligned}\sum_{j=1}^{N}\vec{u_j}\,\langle\alpha\big(\nabla\cdot\phi_j\big)\phi_i\rangle^{k+1} + \sum_{j=1}^{N}p_j\,\langle\tfrac{1}{\mathrm{S}}\phi_j\phi_i\rangle^{\mathrm{k+1}} + \Delta t\sum_{j=1}^{N}p_j\,\langle k\nabla\phi_j\cdot\nabla\phi_i\rangle^{\mathrm{k+1}} &=\\ \sum_{j=1}^{N}\vec{u_j}\,\langle\alpha\big(\nabla\cdot\phi_j\big)\phi_i\rangle^{k} + \sum_{j=1}^{N}p_j\,\langle\tfrac{1}{\mathrm{S}}\phi_j\phi_i\rangle^{\mathrm{k}} + \Delta t[\oint k\,\hat{n}\cdot\nabla p\phi_i ds]^{\mathrm{k+1}}&\end{aligned} \tag{III.10.b}$$

The discrete system expressed in matrix formulation is (III.11).

$$A_{ij}U^{n+1} = B_{ij}U^{n} + C^{n+\theta} \tag{III.11}$$

The system is treated as fully implicit, i.e. $\theta = 1$. Substituting into (III.11) generates (III.12).

$$AU^{n+1} = BU^{n} + C^{n+1} \tag{III.12}$$

The submatricies which compose A and B are (III.13) and (III.14).

$$A_{ij} =$$

$$\left[\begin{matrix} G\,\langle\frac{2(1-v)}{1-2v}\frac{\partial\phi_j}{\partial x}\frac{\partial\phi_i}{\partial x} + \frac{\partial\phi_j}{\partial y}\frac{\partial\phi_i}{\partial y} + \frac{\partial\phi_j}{\partial z}\frac{\partial\phi_i}{\partial z}\rangle & G\,\langle\frac{2v}{1-2v}\frac{\partial\phi_j}{\partial y}\frac{\partial\phi_i}{\partial x} + \frac{\partial\phi_j}{\partial x}\frac{\partial\phi_i}{\partial y}\rangle & \dots\\ G\,\langle\frac{2v}{1-2v}\frac{\partial\phi_j}{\partial x}\frac{\partial\phi_i}{\partial y} + \frac{\partial\phi_j}{\partial y}\frac{\partial\phi_i}{\partial x}\rangle & G\,\langle\frac{2(1-v)}{1-2v}\frac{\partial\phi_j}{\partial y}\frac{\partial\phi_i}{\partial y} + \frac{\partial\phi_j}{\partial x}\frac{\partial\phi_i}{\partial x} + \frac{\partial\phi_j}{\partial z}\frac{\partial\phi_i}{\partial z}\rangle & \dots\\ G\,\langle\frac{2v}{1-2v}\frac{\partial\phi_j}{\partial x}\frac{\partial\phi_i}{\partial z} + \frac{\partial\phi_j}{\partial z}\frac{\partial\phi_i}{\partial x}\rangle & G\,\langle\frac{2v}{1-2v}\frac{\partial\phi_j}{\partial y}\frac{\partial\phi_i}{\partial z} + \frac{\partial\phi_j}{\partial z}\frac{\partial\phi_i}{\partial y}\rangle & \dots\\ \alpha\,\langle\frac{\partial\phi_j}{\partial x}\phi_i\rangle & \alpha\,\langle\frac{\partial\phi_j}{\partial y}\phi_i\rangle & \dots \end{matrix}\right.$$

$$\begin{matrix} \cdots & G\langle\frac{2v}{1-2v}\frac{\partial\phi_j}{\partial z}\frac{\partial\phi_i}{\partial x}+\frac{\partial\phi_j}{\partial x}\frac{\partial\phi_i}{\partial z}\rangle & \alpha\langle\frac{\partial\phi_j}{\partial x}\phi_i\rangle \\ \cdots & G\langle\frac{2v}{1-2v}\frac{\partial\phi_j}{\partial z}\frac{\partial\phi_i}{\partial y}+\frac{\partial\phi_j}{\partial y}\frac{\partial\phi_i}{\partial z}\rangle & \alpha\langle\frac{\partial\phi_j}{\partial y}\phi_i\rangle \\ \cdots & G\langle\frac{2(1-v)}{1-2v}\frac{\partial\phi_j}{\partial z}\frac{\partial\phi_i}{\partial z}+\frac{\partial\phi_j}{\partial x}\frac{\partial\phi_i}{\partial x}+\frac{\partial\phi_j}{\partial y}\frac{\partial\phi_i}{\partial y}\rangle & \alpha\langle\frac{\partial\phi_j}{\partial z}\phi_i\rangle \\ \cdots & \alpha\langle\frac{\partial\phi_j}{\partial z}\phi_i\rangle & \Delta tk\langle\frac{\partial\phi_j}{\partial x}\frac{\partial\phi_i}{\partial x}+\frac{\partial\phi_j}{\partial y}\frac{\partial\phi_i}{\partial y}+\frac{\partial\phi_j}{\partial z}\frac{\partial\phi_i}{\partial z}\rangle+\frac{1}{s}\langle\phi_j\phi_i\rangle \end{matrix}\Bigg] \tag{III.13}$$

$$B_{ij}=\begin{bmatrix} 0 & 0 & 0 & 0 \\ 0 & 0 & 0 & 0 \\ 0 & 0 & 0 & 0 \\ \alpha\langle\frac{\partial\phi_j}{\partial x}\phi_i\rangle & \alpha\langle\frac{\partial\phi_j}{\partial y}\phi_i\rangle & \alpha\langle\frac{\partial\phi_j}{\partial z}\phi_i\rangle & \frac{1}{s}\langle\phi_j\phi_i\rangle \end{bmatrix} \tag{III.14}$$

The subvectors which compose U and C are (III.15) and (III.16).

$$U_j^n=\begin{Bmatrix} u_{x_j}(t_n) \\ u_{y_j}(t_n) \\ u_{z_j}(t_n) \\ p_j(t_n) \end{Bmatrix} \tag{III.15}$$

$$C_i^{n+\theta}=\begin{Bmatrix} \hat{x}\cdot\oint\sigma_s(t_{n+\theta})\cdot\hat{n}\phi_i ds \\ \hat{y}\cdot\oint\sigma_s(t_{n+\theta})\cdot\hat{n}\phi_i ds \\ \hat{z}\cdot\oint\sigma_s(t_{n+\theta})\cdot\hat{n}\phi_i ds \\ \Delta t\oint k\nabla p(t_{n+\theta})\cdot\hat{n}\phi_i ds \end{Bmatrix} \tag{III.16}$$

III.2.3 Mechanically Coupled Tumor Growth Model

The governing equations (III.17.a-III.17.c) represent a coupled biophysical model of tumor growth. In these equations $\vec{u}$ is the displacement vector, and N is the cell number which varies spatially and temporally. D is the cellular diffusion coefficient of the tumor cells when mechanical stress is present, while D_0 is the cellular diffusion coefficient when there is no stress present [92]. k is the tumor cell proliferation rate, θ_* is the tumor cell carrying capacity, and σ_{VM} is the von Mises stress. The coupling coefficients are γ and λ. G is the tissue shear modulus, and ν is the Poisson's ratio [92]. Equation (III.17.a) defines the rate of tumor cell number change in time as the sum of logistic growth and cellular diffusion. Equation (III.17.b) couples tumor cell transport to a changing tissue stress state, effectively capturing the mechano-inhibition of cellular diffusion. Equation (III.17.c) represents mechanical equilibrium when an external expansive force, a tumor, is present [92].

$$\frac{\partial N(\bar{x},t)}{\partial t}=\nabla\cdot\left(D\nabla N(\bar{x},t)\right)+kN(\bar{x},t)\left(1-\frac{N(\bar{x},t)}{\theta_*}\right) \tag{III.17.a}$$

$$D=D_0e^{-\gamma\sigma_{VM}(\bar{x},t)} \tag{III.17.b}$$

$$\nabla\cdot G\nabla\vec{u}+\nabla\frac{G}{1-2v}(\nabla\cdot\vec{u})-\lambda\nabla\mathrm{N}(\bar{x},t)=0 \tag{III.17.c}$$

Reaction-Diffusion Equation (III.17.a)

To begin the analysis of this set of coupled equations, start with (III.17.a). Rewriting equation (III.17.a) generates (III.18).

$$\frac{\partial N}{\partial t} = \nabla \cdot (D\nabla N) + kN - \frac{kN^2}{\theta_*} \tag{III.18}$$

Once again, using the Galerkin Method of Weighted Residuals, equations (III.18) is multiplied with ϕ_i [96]. Also, the $\langle * \rangle$ represents integration over the problem domain; ϕ_i, is the i$^{\text{th}}$ member of the standard C° local Lagrange polynomial interpolants associated with finite elements [70].

$$\langle \frac{\partial N}{\partial t}, \phi_i \rangle = \langle \nabla \cdot (D\nabla N), \phi_i \rangle + \langle kN, \phi_i \rangle - \langle \frac{kN^2}{\theta_*}, \phi_i \rangle \tag{III.19}$$

The divergence and gradient integral identity for the second derivative term is (III.20).

$$\langle \nabla \cdot (D\nabla N), \phi_i \rangle = \oint D\hat{n} \cdot \nabla N \phi_i ds = \langle \phi_i \nabla \cdot D\nabla N \rangle + \langle D\nabla N \cdot \nabla \phi_i \rangle \tag{III.20}$$

This leads to the weak form of (III.19). Recall, $\oint *$ represents the integration over the problem domain boundary, and $\hat{n}$ represents the outward-pointing normal to the boundary.

$$\langle \frac{\partial N}{\partial t}, \phi_i \rangle = -\langle D\nabla N \cdot \nabla \phi_i \rangle + \oint D\hat{n} \cdot \nabla N \phi_i ds + \langle kN, \phi_i \rangle - \langle \frac{kN^2}{\theta_*}, \phi_i \rangle \tag{III.21}$$

Rewriting (III.21) generates (III.22).

$$\langle \frac{\partial N}{\partial t}, \phi_i \rangle + \langle D\nabla N \cdot \nabla \phi_i \rangle - \langle kN, \phi_i \rangle + \langle \frac{kN^2}{\theta_*}, \phi_i \rangle = \oint D\hat{n} \cdot \nabla N \phi_i ds \tag{III.22}$$

Equations (III.22) is integrated in time with two-point weighting. In this expression $0 \le \theta \le 1$ and $\Delta t = t_{n+1} - t_n$.

$$\int_{t_n}^{t_{n+1}} f(t)dt = \Delta t \, [\theta f(t_{n+1}) + (1-\theta) f(t_n)] \tag{III.6}$$

Unlike previously, here the system is treated as fully explicit, i.e. $\theta = 0$. Therefore (III.6) is simplified to (III.23).

$$\int_{t_n}^{t_{n+1}} f(t)dt = \Delta t \, [\, f(t_n)] \tag{III.23}$$

The fully explicit representation of (III.22) is (III.24).

$$\langle N\phi_i \rangle^{k+1} - \langle N\phi_i \rangle^{k} + \Delta t \langle D\nabla N \cdot \nabla \phi_i \rangle^{k} - \Delta t \langle kN\phi_i \rangle^{k} + \Delta t \, \langle \frac{kN^2}{\theta_*} \phi_i \rangle^{k} = \Delta t [\oint D\hat{n} \cdot \nabla N \phi_i ds]^{\mathrm{k}} \tag{III.24}$$

The spatial discretization of (III.24) is completed by expanding the unknown variable as the summation of unknown coefficients, which are time-varying, multiplied by known functions of position [96].

$$N(x,y,z,t) \approx \hat{N}(x,y,z,t) = \sum_{j=1}^{M} N_j(t) \phi_j(x,y,z) \tag{III.25.a}$$

$$\frac{\partial \hat{N}}{\partial x} = \sum_{j=1}^{N} N_j \frac{\partial \phi_j}{\partial x} \tag{III.25.b}$$

$$\frac{\partial \hat{N}}{\partial y} = \sum_{j=1}^{N} N_j \frac{\partial \phi_j}{\partial y} \tag{III.25.c}$$

$$\frac{\partial \hat{N}}{\partial z} = \sum_{j=1}^{N} N_j \frac{\partial \phi_j}{\partial z} \tag{III.25.d}$$

Plugging in these discretized representations into (III.24) generates (III.26).

$$\sum_{j=1}^{N} N_j \langle \phi_j \phi_i \rangle^{k+1} = \sum_{j=1}^{N} N_j \langle \phi_j \phi_i \rangle^{k} - \Delta t \sum_{j=1}^{N} N_j \langle D \nabla \phi_j \cdot \nabla \phi_i \rangle^{k} + \Delta t \sum_{j=1}^{N} N_j \langle k \phi_j \phi_i \rangle^{k} - \Delta t \sum_{j=1}^{N} N_j{}^2 \langle \frac{k}{\theta_*} \phi_j \phi_i \rangle^{k} + \Delta t [\oint D \hat{n} \cdot \nabla N \phi_i ds]^{k} \tag{III.26}$$

For simplification, these terms can be condensed in matrix notation. In order to do this, matrix terms are defined in (III.27.a) through (III.27.d).

$$M_{ij} = \langle \phi_j \phi_i \rangle \tag{III.27.a}$$

$$L_{ij} = \langle D \nabla \phi_j \cdot \nabla \phi_i \rangle - k M_{ij} \tag{III.27.b}$$

$$H_{ij} = \frac{k}{\theta_*} M_{ij} \tag{III.27.c}$$

$$\{r\} = right\ hand\ side\ term \tag{III.27.d}$$

Rewriting (III.26) with matrix terms yields (III.28).

$$[M]\{N^{k+1}\} = [M - \Delta t L]\{N^k\} - [\Delta t H]\{N^k\}^2 + \{r\} \tag{III.28}$$

This can be further regrouped and condensed to obtain (III.29).

$$[A_N]\{N^{k+1}\} = \{b_N^k\} \tag{III.29}$$

Mechanical Coupling Equation (III.17.c)

Next, analysis is started on the third governing equation. Using the Galerkin Method of Weighted Residuals, equation (III.17.c) is multiplied with ϕ_i [96].

$$\langle \nabla \cdot G \nabla \vec{u}, \phi_i \rangle + \langle \nabla \frac{G}{1-2\nu} (\nabla \cdot \vec{u}), \phi_i \rangle - \langle \lambda \nabla N, \phi_i \rangle = 0 \tag{III.30}$$

Using the divergence and gradient integral identities, (III.3.a) and (III.3.b), the weak form of (III.30) is (III.31).

$$\langle G \nabla \vec{u} \cdot \nabla \phi_i \rangle + \langle \frac{G}{1-2\nu} (\nabla \cdot \vec{u}) \nabla \phi_i \rangle + \langle \lambda \nabla N \phi_i \rangle = \oint \mathrm{G} \hat{n} \cdot \nabla \vec{u} \phi_i ds + \oint \frac{G}{1-2\nu} \hat{n} (\nabla \cdot \vec{u}) \phi_i ds \tag{III.31}$$

The spatial discretization of (III.32) is completed by expanding the unknown variables as the summation of unknown coefficients multiplied by known functions of position [96].

$$\vec{u}(x,y,z) \approx \sum_{j=1}^{N} \vec{u_j} \phi_j(x,y,z) \tag{III.32.a}$$

$$N(x,y,z) \approx \sum_{j=1}^{N} N_j \phi_j(x,y,z) \tag{III.32.b}$$

Plugging in (III.32.a) and (III.32.b) into (III.31) generates the discretized form, (III.33).

$$\sum_{j=1}^{N} \vec{u_j} \langle G \nabla \phi_j \cdot \nabla \phi_i \rangle + \sum_{j=1}^{N} \vec{u_j} \langle \frac{G}{1-2\nu} (\nabla \cdot \phi_j) \nabla \phi_i \rangle + \sum_{j=1}^{N} N_j \langle \lambda \nabla \phi_j \phi_i \rangle = \oint \frac{G}{1-2\nu} \hat{n} (\nabla \cdot \vec{u}) \phi_i ds + \oint \mathrm{G} \hat{n} \cdot \nabla \vec{u} \phi_i ds \tag{III.33}$$

Total Governing Equation Representation

Combining the cellular and linear elastic relationships generates the final representation of this finite element problem. The fully explicit forward Euler representation is (III.34) [98].

$$[A]\{\bar{x}\}^{t+\Delta t} = \{b(\bar{x})\}^{t} \tag{III.34}$$

The Coupled Solution Vector represented by $\bar{x}$ is (III.35) [98].

$$\{\bar{x}\} = \begin{Bmatrix} u \\ v \\ w \\ N \end{Bmatrix} \tag{III.35}$$

The local stiffness matrix, A, from (III.34) is (III.36).

$$A_{ij} = \left[\begin{array}{ccc} G\left\langle \frac{2(1-v)}{1-2v}\frac{\partial\phi_j}{\partial x}\frac{\partial\phi_i}{\partial x} + \frac{\partial\phi_j}{\partial y}\frac{\partial\phi_i}{\partial y} + \frac{\partial\phi_j}{\partial z}\frac{\partial\phi_i}{\partial z}\right\rangle & G\left\langle \frac{2v}{1-2v}\frac{\partial\phi_j}{\partial y}\frac{\partial\phi_i}{\partial x} + \frac{\partial\phi_j}{\partial x}\frac{\partial\phi_i}{\partial y}\right\rangle & \cdots \\ G\left\langle \frac{2v}{1-2v}\frac{\partial\phi_j}{\partial x}\frac{\partial\phi_i}{\partial y} + \frac{\partial\phi_j}{\partial y}\frac{\partial\phi_i}{\partial x}\right\rangle & G\left\langle \frac{2(1-v)}{1-2v}\frac{\partial\phi_j}{\partial y}\frac{\partial\phi_i}{\partial y} + \frac{\partial\phi_j}{\partial x}\frac{\partial\phi_i}{\partial x} + \frac{\partial\phi_j}{\partial z}\frac{\partial\phi_i}{\partial z}\right\rangle & \cdots \\ G\left\langle \frac{2v}{1-2v}\frac{\partial\phi_j}{\partial x}\frac{\partial\phi_i}{\partial z} + \frac{\partial\phi_j}{\partial z}\frac{\partial\phi_i}{\partial x}\right\rangle & G\left\langle \frac{2v}{1-2v}\frac{\partial\phi_j}{\partial y}\frac{\partial\phi_i}{\partial z} + \frac{\partial\phi_j}{\partial z}\frac{\partial\phi_i}{\partial y}\right\rangle & \cdots \\ 0 & 0 & \cdots \end{array}\right.$$

$$\left.\begin{array}{ccc} \cdots & G\left\langle \frac{2v}{1-2v}\frac{\partial\phi_j}{\partial z}\frac{\partial\phi_i}{\partial x} + \frac{\partial\phi_j}{\partial x}\frac{\partial\phi_i}{\partial z}\right\rangle & \lambda\left\langle \frac{\partial\phi_j}{\partial x}\phi_i\right\rangle \\ \cdots & G\left\langle \frac{2v}{1-2v}\frac{\partial\phi_j}{\partial z}\frac{\partial\phi_i}{\partial y} + \frac{\partial\phi_j}{\partial y}\frac{\partial\phi_i}{\partial z}\right\rangle & \lambda\left\langle \frac{\partial\phi_j}{\partial y}\phi_i\right\rangle \\ \cdots & G\left\langle \frac{2(1-v)}{1-2v}\frac{\partial\phi_j}{\partial z}\frac{\partial\phi_i}{\partial z} + \frac{\partial\phi_j}{\partial x}\frac{\partial\phi_i}{\partial x} + \frac{\partial\phi_j}{\partial y}\frac{\partial\phi_i}{\partial y}\right\rangle & \lambda\left\langle \frac{\partial\phi_j}{\partial z}\phi_i\right\rangle \\ \cdots & 0 & A_N \end{array}\right] \tag{III.36}$$

The subvector which composes b from (III.34) is (III.37).

$$b_i = \begin{Bmatrix} \hat{x}\cdot\oint\sigma(t+\Delta t)\cdot\hat{n}\phi_i ds \\ \hat{y}\cdot\oint\sigma(t+\Delta t)\cdot\hat{n}\phi_i ds \\ \hat{z}\cdot\oint\sigma(t+\Delta t)\cdot\hat{n}\phi_i ds \\ b_N + \Delta t\oint D\nabla N(t+\Delta t)\cdot\hat{n}\phi_i ds \end{Bmatrix} \tag{III.37}$$

III.2.4 Model of Tumor Cavity Collapse from Resection

The modeling of brain shift from cavity collapse caused by tumor resection (debulking) involves three distinct finite element models. The first of which is a reaction-diffusion model of tumor growth. The second is a model which enables the pressure associated with edema from the grown tumor to be calculated. This edema calculation is not necessary for cavity collapse to occur, but permits an additional aspect of tumor growth to be accounted for in this description of cavity collapse. Finally, the displacements associated with the full tumor present or with the tumor resected are calculated two separate times using the same finite element model. The first calculation is solving for the displacements of the brain parenchyma, treated like a linear elastic material, when the tumor is still present. The second calculation is solving for the displacements of the brain parenchyma after a portion of the tumor has been resected. The displacement profile associated with resection cavity collapse, referred to as debulking, is equal to the difference between the displacement solution calculated when the tumor is present and when the tumor has been resected.

Reaction-Diffusion Model of Tumor Growth

The governing equation, which describes tumor growth, is (III.38). In Equation (III.38), *C* is the tumor cell concentration, *t* is time, *k* is the tumor cell proliferation rate, *D* is the tumor cell diffusion rate, and θ_* is the cellular carrying capacity [98].

$$\frac{\partial C}{\partial t} = \nabla \cdot (D\nabla C) + kC\left(1 - \frac{C}{\theta_*}\right) \tag{III.38}$$

In a method analogous to the steps outlined in equations (III.18) through (III.22), Equation (III.38) can be rewritten, weighted, and transformed into its weak form shown below in equation (III.39).

$$\langle \frac{\partial C}{\partial t}, \phi_i \rangle + \langle D\nabla C \cdot \nabla\phi_i \rangle - \langle kC, \phi_i \rangle + \langle \frac{kC^2}{\theta_*}, \phi_i \rangle = \oint D\hat{n} \cdot \nabla C \phi_i ds \tag{III.39}$$

The spatial discretization of (III.39) is completed by expanding the unknown variable as the summation of unknown coefficients, which are time-varying, multiplied by known functions of position [96].

$$C(x, y, z, t) \approx \hat{C}(x, y, z, t) = \sum_{j=1}^{M} C_j(t)\phi_j(x, y, z) \tag{III.40}$$

Rewriting (III.39) results in (III.41) [96].

$$[M]\left\{\frac{\partial C}{\partial t}\right\} = [KL]\{C_j\} + [KN]\{C_j\}^2 + \{r\} \tag{III.41}$$

In (III.41), $[M]$, $[KL]$, and $[KN]$ are (III.42.a), (III.42.b), and (III.42.c) respectively.

$$M_{ij} = \langle \phi_j \phi_i \rangle \tag{III.42.a}$$

$$KL_{ij} = -\langle D\nabla\phi_j \cdot \nabla\phi_i \rangle + \langle k\phi_j\phi_i \rangle \tag{III.42.b}$$

$$KN_{ij} = \langle \frac{k}{\theta_*} \phi_j \phi_i \rangle \tag{III.42.c}$$

Integrating (III.41) in time with two point weighting, and treating it as fully explicit ($\theta = 0$), (III.43) is obtained.

$$[M]\{C^{k+1}\} = [M]\{C^k\} + \Delta t[KL]\{C_j^k\} - \Delta t[KN]\{C_j^k\}^2 + \{r\} \tag{III.43}$$

In (III.43), the local vector for r is (III.44).

$$r_i = [\oint D\hat{n} \cdot \nabla C \phi_i ds] \tag{III.44}$$

The local matrices for M_{ij}, KN_{ij},and KL_{ij} are (III.45), (III.46), and (III.47) respectively. M_{ij} is the expression of $\langle \phi_j \phi_i \rangle$, and the lumped treatment of the mass matrix is (III.45). KN_{ij} is the nonlinear term, $\langle \frac{k}{\theta_*} \phi_j \phi_i \rangle$. KL_{ij} is the linear term, $-\langle D\nabla\phi_j \cdot \nabla\phi_i \rangle + \langle k\phi_j\phi_i \rangle$.

$$M_{ij} = \begin{bmatrix} V/4 & 0 & 0 & 0 \\ 0 & V/4 & 0 & 0 \\ 0 & 0 & V/4 & 0 \\ 0 & 0 & 0 & V/4 \end{bmatrix} \tag{III.45}$$

$$KN_{ij} = \frac{k}{\theta_*}\begin{bmatrix} V/10 & V/20 & V/20 & V/20 \\ V/20 & V/10 & V/20 & V/20 \\ V/20 & V/20 & V/10 & V/20 \\ V/20 & V/20 & V/20 & V/10 \end{bmatrix} \tag{III.46}$$

$$KL_{ij} = \left[\begin{matrix} -D\left\langle \frac{\partial\phi_j}{\partial x}\frac{\partial\phi_i}{\partial x} + \frac{\partial\phi_j}{\partial y}\frac{\partial\phi_i}{\partial y} + \frac{\partial\phi_j}{\partial z}\frac{\partial\phi_i}{\partial z}\right\rangle + k\frac{V}{10} & -D\left\langle \frac{\partial\phi_j}{\partial x}\frac{\partial\phi_i}{\partial x} + \frac{\partial\phi_j}{\partial y}\frac{\partial\phi_i}{\partial y} + \frac{\partial\phi_j}{\partial z}\frac{\partial\phi_i}{\partial z}\right\rangle + k\frac{V}{20} & \cdots \\ -D\left\langle \frac{\partial\phi_j}{\partial x}\frac{\partial\phi_i}{\partial x} + \frac{\partial\phi_j}{\partial y}\frac{\partial\phi_i}{\partial y} + \frac{\partial\phi_j}{\partial z}\frac{\partial\phi_i}{\partial z}\right\rangle + k\frac{V}{20} & -D\left\langle \frac{\partial\phi_j}{\partial x}\frac{\partial\phi_i}{\partial x} + \frac{\partial\phi_j}{\partial y}\frac{\partial\phi_i}{\partial y} + \frac{\partial\phi_j}{\partial z}\frac{\partial\phi_i}{\partial z}\right\rangle + k\frac{V}{10} & \cdots \\ -D\left\langle \frac{\partial\phi_j}{\partial x}\frac{\partial\phi_i}{\partial x} + \frac{\partial\phi_j}{\partial y}\frac{\partial\phi_i}{\partial y} + \frac{\partial\phi_j}{\partial z}\frac{\partial\phi_i}{\partial z}\right\rangle + k\frac{V}{20} & -D\left\langle \frac{\partial\phi_j}{\partial x}\frac{\partial\phi_i}{\partial x} + \frac{\partial\phi_j}{\partial y}\frac{\partial\phi_i}{\partial y} + \frac{\partial\phi_j}{\partial z}\frac{\partial\phi_i}{\partial z}\right\rangle + k\frac{V}{20} & \cdots \\ -D\left\langle \frac{\partial\phi_j}{\partial x}\frac{\partial\phi_i}{\partial x} + \frac{\partial\phi_j}{\partial y}\frac{\partial\phi_i}{\partial y} + \frac{\partial\phi_j}{\partial z}\frac{\partial\phi_i}{\partial z}\right\rangle + k\frac{V}{20} & -D\left\langle \frac{\partial\phi_j}{\partial x}\frac{\partial\phi_i}{\partial x} + \frac{\partial\phi_j}{\partial y}\frac{\partial\phi_i}{\partial y} + \frac{\partial\phi_j}{\partial z}\frac{\partial\phi_i}{\partial z}\right\rangle + k\frac{V}{20} & \cdots \end{matrix}\right.$$

$$\left.\begin{matrix} \cdots & -D\left\langle \frac{\partial\phi_j}{\partial x}\frac{\partial\phi_i}{\partial x} + \frac{\partial\phi_j}{\partial y}\frac{\partial\phi_i}{\partial y} + \frac{\partial\phi_j}{\partial z}\frac{\partial\phi_i}{\partial z}\right\rangle + k\frac{V}{20} & -D\left\langle \frac{\partial\phi_j}{\partial x}\frac{\partial\phi_i}{\partial x} + \frac{\partial\phi_j}{\partial y}\frac{\partial\phi_i}{\partial y} + \frac{\partial\phi_j}{\partial z}\frac{\partial\phi_i}{\partial z}\right\rangle + k\frac{V}{20} \\ \cdots & -D\left\langle \frac{\partial\phi_j}{\partial x}\frac{\partial\phi_i}{\partial x} + \frac{\partial\phi_j}{\partial y}\frac{\partial\phi_i}{\partial y} + \frac{\partial\phi_j}{\partial z}\frac{\partial\phi_i}{\partial z}\right\rangle + k\frac{V}{20} & -D\left\langle \frac{\partial\phi_j}{\partial x}\frac{\partial\phi_i}{\partial x} + \frac{\partial\phi_j}{\partial y}\frac{\partial\phi_i}{\partial y} + \frac{\partial\phi_j}{\partial z}\frac{\partial\phi_i}{\partial z}\right\rangle + k\frac{V}{20} \\ \cdots & -D\left\langle \frac{\partial\phi_j}{\partial x}\frac{\partial\phi_i}{\partial x} + \frac{\partial\phi_j}{\partial y}\frac{\partial\phi_i}{\partial y} + \frac{\partial\phi_j}{\partial z}\frac{\partial\phi_i}{\partial z}\right\rangle + k\frac{V}{10} & -D\left\langle \frac{\partial\phi_j}{\partial x}\frac{\partial\phi_i}{\partial x} + \frac{\partial\phi_j}{\partial y}\frac{\partial\phi_i}{\partial y} + \frac{\partial\phi_j}{\partial z}\frac{\partial\phi_i}{\partial z}\right\rangle + k\frac{V}{20} \\ \cdots & -D\left\langle \frac{\partial\phi_j}{\partial x}\frac{\partial\phi_i}{\partial x} + \frac{\partial\phi_j}{\partial y}\frac{\partial\phi_i}{\partial y} + \frac{\partial\phi_j}{\partial z}\frac{\partial\phi_i}{\partial z}\right\rangle + k\frac{V}{20} & -D\left\langle \frac{\partial\phi_j}{\partial x}\frac{\partial\phi_i}{\partial x} + \frac{\partial\phi_j}{\partial y}\frac{\partial\phi_i}{\partial y} + \frac{\partial\phi_j}{\partial z}\frac{\partial\phi_i}{\partial z}\right\rangle + k\frac{V}{10} \end{matrix}\right] \tag{III.47}$$

Model of Pressure Based on the Tumor's Edema

This finite element model accounts for two scenarios: when there is edema present and when there is not edema present. Depending on the nature of the element in the mesh (edema or not), one of the two governing equations is used to characterize the specific element. This enables edema to be enforced locally, congruent with tumors having local areas of edema versus widespread edema. The governing equation used to model pressure when edema from the tumor is present is (III.48.a). In equations (III.48.a) and (III.48.b), p is pressure, k is hydraulic conductivity, k_c is capillary permeability, and p_c is intracapillary pressure [64].

$$-\nabla \cdot k\nabla p + k_c(p - p_c) = 0 \tag{III.48.a}$$

The governing equation when edema is not present is (III.48.b).

$$-\nabla \cdot k\nabla p = 0 \tag{III.48.b}$$

Again, using the Galerkin Method of Weighted Residuals, equations (III.48.a) and (III.48.b) are multiplied with ϕ_i [96]. Recall $\langle * \rangle$ represents integration over the problem domain. Also, ϕ_i is the ith member of the standard C° local Lagrange polynomial interpolants [70].

$$\langle -\nabla \cdot k\nabla p, \phi_i \rangle + \langle k_c(p - p_c), \phi_i \rangle = 0 \tag{III.49.a}$$

$$\langle -\nabla \cdot k\nabla p, \phi_i \rangle = 0 \tag{III.49.b}$$

The divergence and integral identity for the second derivative term is (III.50).

$$\langle \nabla \cdot (k\nabla p\phi_i) \rangle = \oint \mathrm{k}\,\hat{n} \cdot \nabla p\phi_i ds = \langle \phi_i \nabla \cdot k\nabla p \rangle + \langle k\nabla p \cdot \nabla\phi_i \rangle \tag{III.50}$$

This leads to the weak form of (III.49.a) and (III.49.b). Recall, $\oint *$ represents the integration over the problem domain boundary, and $\hat{n}$ represents the outward-pointing normal to the boundary. The weak form of (III.49.a) is (III.51.a).

$$\langle k\nabla p \cdot \nabla\phi_i\rangle + \langle k_c(p - p_c), \phi_i\rangle = \oint k\,\hat{n}\cdot\nabla p\phi_i ds \qquad \text{(III.51.a)}$$

The weak form of (III.49.b) is (III.51.b).

$$\langle k\nabla p \cdot \nabla\phi_i\rangle = \oint k\,\hat{n}\cdot\nabla p\phi_i ds \qquad \text{(III.51.b)}$$

The spatial discretization of (III.51.a) and (III.51.b) is completed by expanding the unknown variable as the summation of unknown coefficients multiplied by known functions of position [96].

$$p(x,y,z) \approx \textstyle\sum_{j=1}^{N} p_j\phi_j(x,y,z) \qquad \text{(III.52)}$$

Plugging (III.52) into (III.51.a) and (III.51.b) generates (III.53.a) and (III.53.b).

$$\textstyle\sum_{j=1}^{N} p_j\langle k\nabla\phi_j \cdot \nabla\phi_i\rangle + \sum_{j=1}^{N} p_j\langle k_c(\phi_j - p_c), \phi_i\rangle = \oint k\,\hat{n}\cdot\nabla p\phi_i ds \qquad \text{(III.53.a)}$$

$$\textstyle\sum_{j=1}^{N} p_j\langle k\nabla\phi_j \cdot \nabla\phi_i\rangle = \oint k\,\hat{n}\cdot\nabla p\phi_i ds \qquad \text{(III.53.b)}$$

For simplification in a matrix representation of this model, (III.54.a) through (III.54.d) represent the matrices and vectors associated with this problem.

$$A_{ij_a} = \langle k\nabla\phi_j \cdot \nabla\phi_i\rangle + \langle k_c\phi_j\phi_i\rangle \qquad \text{(III.54.a)}$$

$$A_{ij_b} = \langle k\nabla\phi_j \cdot \nabla\phi_i\rangle \qquad \text{(III.54.b)}$$

$$b_{i_a} = \langle k_c p_c\phi_i\rangle + \oint k\,\hat{n}\cdot\nabla p\phi_i ds \qquad \text{(III.54.c)}$$

$$b_{i_b} = \oint k\,\hat{n}\cdot\nabla p\phi_i ds \qquad \text{(III.54.d)}$$

Using this notation (III.53.a) and (III.53.b) can be rewritten in matrix notation as (III.55.a) and (III.55.b).

$$A_{ij_a}\{p_j\} = \{b_{i_a}\} \qquad \text{(III.55.a)}$$

$$A_{ij_b}\{p_j\} = \{b_{i_b}\} \qquad \text{(III.55.b)}$$

The local matrices for A_{ij_a} and A_{ij_b} are (III.56.a) and (III.56.b) respectively.

$$A_{ij_a} = \left[\begin{matrix}
k\left\langle\frac{\partial\phi_j}{\partial x}\frac{\partial\phi_i}{\partial x} + \frac{\partial\phi_j}{\partial y}\frac{\partial\phi_i}{\partial y} + \frac{\partial\phi_j}{\partial z}\frac{\partial\phi_i}{\partial z}\right\rangle + k_c\frac{V}{10} & k\left\langle\frac{\partial\phi_j}{\partial x}\frac{\partial\phi_i}{\partial x} + \frac{\partial\phi_j}{\partial y}\frac{\partial\phi_i}{\partial y} + \frac{\partial\phi_j}{\partial z}\frac{\partial\phi_i}{\partial z}\right\rangle + k_c\frac{V}{20} & \cdots \\
k\left\langle\frac{\partial\phi_j}{\partial x}\frac{\partial\phi_i}{\partial x} + \frac{\partial\phi_j}{\partial y}\frac{\partial\phi_i}{\partial y} + \frac{\partial\phi_j}{\partial z}\frac{\partial\phi_i}{\partial z}\right\rangle + k_c\frac{V}{20} & k\left\langle\frac{\partial\phi_j}{\partial x}\frac{\partial\phi_i}{\partial x} + \frac{\partial\phi_j}{\partial y}\frac{\partial\phi_i}{\partial y} + \frac{\partial\phi_j}{\partial z}\frac{\partial\phi_i}{\partial z}\right\rangle + k_c\frac{V}{10} & \cdots \\
k\left\langle\frac{\partial\phi_j}{\partial x}\frac{\partial\phi_i}{\partial x} + \frac{\partial\phi_j}{\partial y}\frac{\partial\phi_i}{\partial y} + \frac{\partial\phi_j}{\partial z}\frac{\partial\phi_i}{\partial z}\right\rangle + k_c\frac{V}{20} & k\left\langle\frac{\partial\phi_j}{\partial x}\frac{\partial\phi_i}{\partial x} + \frac{\partial\phi_j}{\partial y}\frac{\partial\phi_i}{\partial y} + \frac{\partial\phi_j}{\partial z}\frac{\partial\phi_i}{\partial z}\right\rangle + k_c\frac{V}{20} & \cdots \\
k\left\langle\frac{\partial\phi_j}{\partial x}\frac{\partial\phi_i}{\partial x} + \frac{\partial\phi_j}{\partial y}\frac{\partial\phi_i}{\partial y} + \frac{\partial\phi_j}{\partial z}\frac{\partial\phi_i}{\partial z}\right\rangle + k_c\frac{V}{20} & k\left\langle\frac{\partial\phi_j}{\partial x}\frac{\partial\phi_i}{\partial x} + \frac{\partial\phi_j}{\partial y}\frac{\partial\phi_i}{\partial y} + \frac{\partial\phi_j}{\partial z}\frac{\partial\phi_i}{\partial z}\right\rangle + k_c\frac{V}{20} & \cdots
\end{matrix}\right.$$

$$\left.\begin{matrix}
\cdots & k\left\langle\frac{\partial\phi_j}{\partial x}\frac{\partial\phi_i}{\partial x} + \frac{\partial\phi_j}{\partial y}\frac{\partial\phi_i}{\partial y} + \frac{\partial\phi_j}{\partial z}\frac{\partial\phi_i}{\partial z}\right\rangle + k_c\frac{V}{20} & k\left\langle\frac{\partial\phi_j}{\partial x}\frac{\partial\phi_i}{\partial x} + \frac{\partial\phi_j}{\partial y}\frac{\partial\phi_i}{\partial y} + \frac{\partial\phi_j}{\partial z}\frac{\partial\phi_i}{\partial z}\right\rangle + k_c\frac{V}{20} \\
\cdots & k\left\langle\frac{\partial\phi_j}{\partial x}\frac{\partial\phi_i}{\partial x} + \frac{\partial\phi_j}{\partial y}\frac{\partial\phi_i}{\partial y} + \frac{\partial\phi_j}{\partial z}\frac{\partial\phi_i}{\partial z}\right\rangle + k_c\frac{V}{20} & k\left\langle\frac{\partial\phi_j}{\partial x}\frac{\partial\phi_i}{\partial x} + \frac{\partial\phi_j}{\partial y}\frac{\partial\phi_i}{\partial y} + \frac{\partial\phi_j}{\partial z}\frac{\partial\phi_i}{\partial z}\right\rangle + k_c\frac{V}{20} \\
\cdots & k\left\langle\frac{\partial\phi_j}{\partial x}\frac{\partial\phi_i}{\partial x} + \frac{\partial\phi_j}{\partial y}\frac{\partial\phi_i}{\partial y} + \frac{\partial\phi_j}{\partial z}\frac{\partial\phi_i}{\partial z}\right\rangle + k_c\frac{V}{10} & k\left\langle\frac{\partial\phi_j}{\partial x}\frac{\partial\phi_i}{\partial x} + \frac{\partial\phi_j}{\partial y}\frac{\partial\phi_i}{\partial y} + \frac{\partial\phi_j}{\partial z}\frac{\partial\phi_i}{\partial z}\right\rangle + k_c\frac{V}{20} \\
\cdots & k\left\langle\frac{\partial\phi_j}{\partial x}\frac{\partial\phi_i}{\partial x} + \frac{\partial\phi_j}{\partial y}\frac{\partial\phi_i}{\partial y} + \frac{\partial\phi_j}{\partial z}\frac{\partial\phi_i}{\partial z}\right\rangle + k_c\frac{V}{20} & k\left\langle\frac{\partial\phi_j}{\partial x}\frac{\partial\phi_i}{\partial x} + \frac{\partial\phi_j}{\partial y}\frac{\partial\phi_i}{\partial y} + \frac{\partial\phi_j}{\partial z}\frac{\partial\phi_i}{\partial z}\right\rangle + k_c\frac{V}{10}
\end{matrix}\right] \qquad \text{(III.56.a)}$$

$$A_{ij_b} = \left[\begin{matrix} k\langle \frac{\partial \phi_j}{\partial x}\frac{\partial \phi_i}{\partial x} + \frac{\partial \phi_j}{\partial y}\frac{\partial \phi_i}{\partial y} + \frac{\partial \phi_j}{\partial z}\frac{\partial \phi_i}{\partial z}\rangle & k\langle \frac{\partial \phi_j}{\partial x}\frac{\partial \phi_i}{\partial x} + \frac{\partial \phi_j}{\partial y}\frac{\partial \phi_i}{\partial y} + \frac{\partial \phi_j}{\partial z}\frac{\partial \phi_i}{\partial z}\rangle & \ldots \\ k\langle \frac{\partial \phi_j}{\partial x}\frac{\partial \phi_i}{\partial x} + \frac{\partial \phi_j}{\partial y}\frac{\partial \phi_i}{\partial y} + \frac{\partial \phi_j}{\partial z}\frac{\partial \phi_i}{\partial z}\rangle & k\langle \frac{\partial \phi_j}{\partial x}\frac{\partial \phi_i}{\partial x} + \frac{\partial \phi_j}{\partial y}\frac{\partial \phi_i}{\partial y} + \frac{\partial \phi_j}{\partial z}\frac{\partial \phi_i}{\partial z}\rangle & \ldots \\ k\langle \frac{\partial \phi_j}{\partial x}\frac{\partial \phi_i}{\partial x} + \frac{\partial \phi_j}{\partial y}\frac{\partial \phi_i}{\partial y} + \frac{\partial \phi_j}{\partial z}\frac{\partial \phi_i}{\partial z}\rangle & k\langle \frac{\partial \phi_j}{\partial x}\frac{\partial \phi_i}{\partial x} + \frac{\partial \phi_j}{\partial y}\frac{\partial \phi_i}{\partial y} + \frac{\partial \phi_j}{\partial z}\frac{\partial \phi_i}{\partial z}\rangle & \ldots \\ k\langle \frac{\partial \phi_j}{\partial x}\frac{\partial \phi_i}{\partial x} + \frac{\partial \phi_j}{\partial y}\frac{\partial \phi_i}{\partial y} + \frac{\partial \phi_j}{\partial z}\frac{\partial \phi_i}{\partial z}\rangle & k\langle \frac{\partial \phi_j}{\partial x}\frac{\partial \phi_i}{\partial x} + \frac{\partial \phi_j}{\partial y}\frac{\partial \phi_i}{\partial y} + \frac{\partial \phi_j}{\partial z}\frac{\partial \phi_i}{\partial z}\rangle & \ldots \end{matrix}\right.$$

$$\left.\begin{matrix} \ldots & k\langle \frac{\partial \phi_j}{\partial x}\frac{\partial \phi_i}{\partial x} + \frac{\partial \phi_j}{\partial y}\frac{\partial \phi_i}{\partial y} + \frac{\partial \phi_j}{\partial z}\frac{\partial \phi_i}{\partial z}\rangle & k\langle \frac{\partial \phi_j}{\partial x}\frac{\partial \phi_i}{\partial x} + \frac{\partial \phi_j}{\partial y}\frac{\partial \phi_i}{\partial y} + \frac{\partial \phi_j}{\partial z}\frac{\partial \phi_i}{\partial z}\rangle \\ \ldots & k\langle \frac{\partial \phi_j}{\partial x}\frac{\partial \phi_i}{\partial x} + \frac{\partial \phi_j}{\partial y}\frac{\partial \phi_i}{\partial y} + \frac{\partial \phi_j}{\partial z}\frac{\partial \phi_i}{\partial z}\rangle & k\langle \frac{\partial \phi_j}{\partial x}\frac{\partial \phi_i}{\partial x} + \frac{\partial \phi_j}{\partial y}\frac{\partial \phi_i}{\partial y} + \frac{\partial \phi_j}{\partial z}\frac{\partial \phi_i}{\partial z}\rangle \\ \ldots & k\langle \frac{\partial \phi_j}{\partial x}\frac{\partial \phi_i}{\partial x} + \frac{\partial \phi_j}{\partial y}\frac{\partial \phi_i}{\partial y} + \frac{\partial \phi_j}{\partial z}\frac{\partial \phi_i}{\partial z}\rangle & k\langle \frac{\partial \phi_j}{\partial x}\frac{\partial \phi_i}{\partial x} + \frac{\partial \phi_j}{\partial y}\frac{\partial \phi_i}{\partial y} + \frac{\partial \phi_j}{\partial z}\frac{\partial \phi_i}{\partial z}\rangle \\ \ldots & k\langle \frac{\partial \phi_j}{\partial x}\frac{\partial \phi_i}{\partial x} + \frac{\partial \phi_j}{\partial y}\frac{\partial \phi_i}{\partial y} + \frac{\partial \phi_j}{\partial z}\frac{\partial \phi_i}{\partial z}\rangle & k\langle \frac{\partial \phi_j}{\partial x}\frac{\partial \phi_i}{\partial x} + \frac{\partial \phi_j}{\partial y}\frac{\partial \phi_i}{\partial y} + \frac{\partial \phi_j}{\partial z}\frac{\partial \phi_i}{\partial z}\rangle \end{matrix}\right] \tag{III.56.b}$$

The local vectors for b_{i_a} and b_{i_b} are (III.57.a) and (III.57.b) respectively.

$$b_{i_a} = \{\langle k_c p_c \phi_i\rangle + \oint k\,\hat{n}\cdot\nabla p \phi_i ds\} \tag{III.57.a}$$

$$b_{i_b} = \{\oint k\,\hat{n}\cdot\nabla p \phi_i ds\} \tag{III.57.b}$$

Displacements with and without the Tumor Present

The governing equation to calculate the parenchyma displacements when a tumor is or is not present is (III.58). An isotropic Hookean linear elastic constitutive model is assumed. The constant coefficients α and β are empirically derived constants which dictate the amount of influence the tumor cells and edema have respectively [91]. G is the tissue shear modulus, and ν is the Poisson's ratio [92].

$$\nabla\cdot\sigma = \alpha\nabla C + \beta\nabla p \tag{III.58}$$

Equation (III.58) can be rewritten as (III.59).

$$\nabla\cdot G\nabla\vec{u} + \nabla\frac{G}{1-2\nu}(\nabla\cdot\vec{u}) = \alpha\nabla C + \beta\nabla p \tag{III.59}$$

With the Galerkin Method of Weighted Residuals, equations (III.59) is multiplied with ϕ_i (a spatially-continuous weighting function) [96]. Recall $\langle * \rangle$ represents integration over the problem domain. Once again, ϕ_i is the ith member of the standard C° local Lagrange polynomial interpolants associated with finite elements [70].

$$\langle\nabla\cdot G\nabla\vec{u}, \phi_i\rangle + \langle\nabla\frac{G}{1-2\nu}(\nabla\cdot\vec{u}), \phi_i\rangle = \langle\alpha\nabla C, \phi_i\rangle + \langle\beta\nabla p, \phi_i\rangle \tag{III.60}$$

Use the divergence and gradient integral identities (III.3.a) and (III.3.b). The weak form of (III.60) is (III.61).

$$\langle G\nabla\vec{u}\cdot\nabla\phi_i\rangle + \langle\frac{G}{1-2\nu}(\nabla\cdot\vec{u})\nabla\phi_i\rangle = \oint\frac{G}{1-2\nu}\hat{n}(\nabla\cdot\vec{u})\phi_i ds + \oint G\hat{n}\cdot\nabla\vec{u}\phi_i ds - \langle\alpha\nabla C, \phi_i\rangle - \langle\beta\nabla p, \phi_i\rangle \tag{III.61}$$

The spatial discretization of (III.61) is completed by expanding the unknown variable as the summation of unknown coefficients multiplied by known functions of position [96].

$$\vec{u}(x,y,z) \approx \textstyle\sum_{j=1}^{N} \vec{u_j}\, \phi_j(x,y,z) \tag{III.62}$$

Plugging (III.62) into (III.61), generates (III.63).

$$\begin{aligned}\textstyle\sum_{j=1}^{N} \vec{u_j} \langle G\nabla\phi_j \cdot \nabla\phi_i \rangle + \textstyle\sum_{j=1}^{N} \vec{u_j} \langle \frac{G}{1-2v} \left(\nabla \cdot \phi_j\right) \nabla\phi_i \rangle = \\ \oint \frac{G}{1-2v} \hat{n}(\nabla \cdot \vec{u})\phi_i ds + \oint \mathrm{G}\hat{n} \cdot \nabla\vec{u}\phi_i ds - \langle \alpha\nabla C, \phi_i \rangle - \langle \beta\nabla p, \phi_i \rangle\end{aligned} \tag{III.63}$$

The matrix representation of this problem is (III.64).

$$A_{ij} U = b_i \tag{III.64}$$

The local submatrix that composes A_{ij} is (III.65).

$$A_{ij} = \left[\begin{matrix} G \langle \frac{2(1-v)}{1-2v} \frac{\partial\phi_j}{\partial x} \frac{\partial\phi_i}{\partial x} + \frac{\partial\phi_j}{\partial y} \frac{\partial\phi_i}{\partial y} + \frac{\partial\phi_j}{\partial z} \frac{\partial\phi_i}{\partial z} \rangle & G \langle \frac{2v}{1-2v} \frac{\partial\phi_j}{\partial y} \frac{\partial\phi_i}{\partial x} + \frac{\partial\phi_j}{\partial x} \frac{\partial\phi_i}{\partial y} \rangle & \ldots \\ G \langle \frac{2v}{1-2v} \frac{\partial\phi_j}{\partial x} \frac{\partial\phi_i}{\partial y} + \frac{\partial\phi_j}{\partial y} \frac{\partial\phi_i}{\partial x} \rangle & G \langle \frac{2(1-v)}{1-2v} \frac{\partial\phi_j}{\partial y} \frac{\partial\phi_i}{\partial y} + \frac{\partial\phi_j}{\partial x} \frac{\partial\phi_i}{\partial x} + \frac{\partial\phi_j}{\partial z} \frac{\partial\phi_i}{\partial z} \rangle & \ldots \\ G \langle \frac{2v}{1-2v} \frac{\partial\phi_j}{\partial x} \frac{\partial\phi_i}{\partial z} + \frac{\partial\phi_j}{\partial z} \frac{\partial\phi_i}{\partial x} \rangle & G \langle \frac{2v}{1-2v} \frac{\partial\phi_j}{\partial y} \frac{\partial\phi_i}{\partial z} + \frac{\partial\phi_j}{\partial z} \frac{\partial\phi_i}{\partial y} \rangle & \ldots \end{matrix}\right.$$

$$\left.\begin{matrix} \ldots & G \langle \frac{2v}{1-2v} \frac{\partial\phi_j}{\partial z} \frac{\partial\phi_i}{\partial x} + \frac{\partial\phi_j}{\partial x} \frac{\partial\phi_i}{\partial z} \rangle \\ \ldots & G \langle \frac{2v}{1-2v} \frac{\partial\phi_j}{\partial z} \frac{\partial\phi_i}{\partial y} + \frac{\partial\phi_j}{\partial y} \frac{\partial\phi_i}{\partial z} \rangle \\ \ldots & G \langle \frac{2(1-v)}{1-2v} \frac{\partial\phi_j}{\partial z} \frac{\partial\phi_i}{\partial z} + \frac{\partial\phi_j}{\partial x} \frac{\partial\phi_i}{\partial x} + \frac{\partial\phi_j}{\partial y} \frac{\partial\phi_i}{\partial y} \rangle \end{matrix}\right] \tag{III.65}$$

The local subvector that composes b_i is (III.66).

$$b_i = \begin{Bmatrix} \hat{x} \cdot \oint \sigma_s(t_{n+\theta}) \cdot \hat{n}\phi_i ds - \alpha\nabla C\langle\phi_i\rangle - \beta\nabla p\langle\phi_i\rangle \\ \hat{y} \cdot \oint \sigma_s(t_{n+\theta}) \cdot \hat{n}\phi_i ds - \alpha\nabla C\langle\phi_i\rangle - \beta\nabla p\langle\phi_i\rangle \\ \hat{z} \cdot \oint \sigma_s(t_{n+\theta}) \cdot \hat{n}\phi_i ds - \alpha\nabla C\langle\phi_i\rangle - \beta\nabla p\langle\phi_i\rangle \end{Bmatrix} \tag{III.66}$$

Cavity Collapse

The cavity collapse, or debulking phenomenon, is calculated by subtracting the displacement solution when the tumor is present (T_{xyz}) from the displacement solution when the tumor has been resected (T_{xyz_r}). Since there are nodes in the mesh that exist in the non-resected solution, which are decoupled from the mesh in the resection solution, those nodes are decoupled in the displacement debulking solution ($T_{xyz_{debulk}}$) as well.

$$T_{xyz_{debulk}} = T_{xyz} - T_{xyz_r} \tag{III.67}$$

III.3 Optimization Methods

III.3.1 Optimization Introduction

Optimization is defined as either the maximization of or minimization of a given function based on a defined problem [99]. This can be represented by equation (III.68). In (III.68), x is the vector of unknowns, g is the objective function being minimized, and a_i are the constraint functions that x must satisfy. ε is a set of indices for the equality constraints, and ξ is a set of indices for the inequality constraints [99].

$$\min_{x \in R^n} g(x) \quad subject\ to \quad \begin{array}{l} a_i(x) = 0, \quad i \in \varepsilon \\ a_i(x) \geq 0, \quad i \in \xi \end{array} \tag{III.68}$$

There are numerous types of optimization including Newton's method, the Golden section method, conjugate gradient method, and Nelder-Mead simplex method to name a few. Generally, the algorithm of optimization methods is as follows. An initial guess of the solution of the unknown variable (x) is used to start the iterative optimization method. The given optimization method iterates as it generates improved estimates of x. Based on the method selected and/or user defined criteria the iterative process should terminate at the best solution possible. Usually the outputs of the objective function at each iteration are used in some manner to determine the next estimate [99]. The selection of the method type is dependent on the nature of the problem being optimized. For all three aims of this thesis, optimization was employed as a part of the methodology.

Aims 1 and 2 used two related methods, the trust region and Levenberg-Marquardt methods. In Aim 1, the trust region method was used. The material properties of the poroelastic model of the brain (Equations (III.1.a) and (III.1.b)) were estimated to minimize the difference between measured interstitial pressure and the simulated pressure [91]. The objective function in Aim 1 was a relative sum-squared error metric between the experimentally measured pressure transients and the model calculated pressure transients [91]. In Aim 2, the Levenberg-Marquardt optimization method was used [92]. The tumor cell diffusion coefficient and tumor cell proliferation rate in Equations (III.17.a) and (III.17.b) were estimated to minimize the difference between the observed tumor cellularity and the model estimated tumor cellularity [92]. The objective function, which was minimized, was the sum-squared error between the observed and model calculated cellularity [92]. Both of these methods were selected because they combine the speed benefits of Newton-like methods, with the reliability benefits of steepest descent methods. This proved important given the *in vivo* and patient data used to drive both aims. These related methods are robust and converged without stagnation in both aims.

The optimization method used in Aim 3 was distinct; Aim 3 used a constrained least-squared minimization method. The purpose of optimization in this aim was to use the deformation atlas to generate a combinatory solution correcting for the measured brain shift [94]. The least-squared error between the measured brain shift and model estimated brain shift is minimized. The objective function of this problem is shown in Equation (III.69). In (III.69) a are the non-negative regression coefficients being solved for,

u_{sparse} are the measured brain shifts, and M is a matrix containing the model generated deformation atlas [94]. The inverse problem was constrained such that the a coefficients must be non-negative and their sum must be less than or equal to one. This was done to ensure the directionality of the calculated displacements are not inverted, which would change their physical meanings, and prevent extrapolation of a single solution [94]. Essentially, these constraints on the regression coefficients being solved for prevent unreasonable model-predicted deformations from being selected as the solution to the optimization problem.

$$min\left\|Ma - u_{sparse}\right\|^2 \exists a_i \geq 0 \; and \; \sum_{i=1}^{m} a_i \leq 1 \tag{III.69}$$

Overall, the optimization method selections were made based on the nature of the data and what was being solved for (property values or weighting coefficients) in each aim. Detailed specifics of the trust region and Levenberg-Marquardt optimization method and the constrained least-squared minimization are in sections (III.3.2) and (III.3.3) respectively.

III.3.2 Trust Region and Levenberg – Marquardt

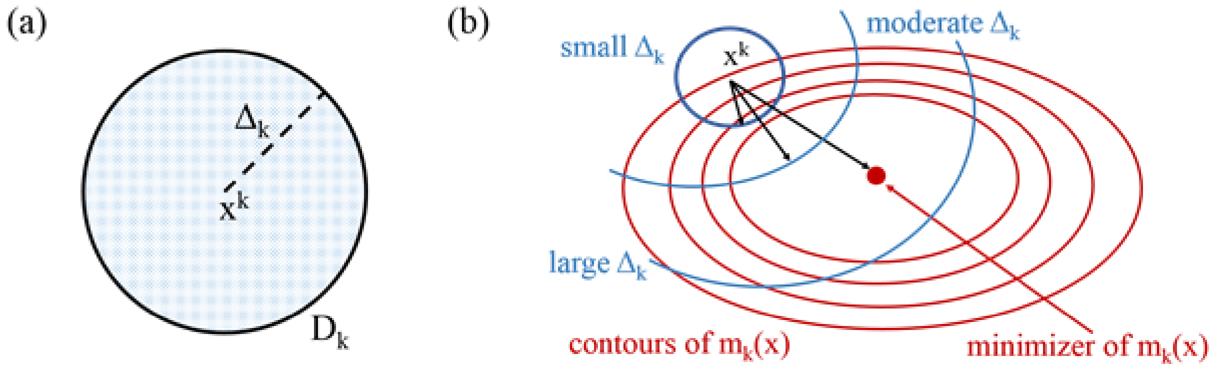

Figure III. 5: This reflects features of trust region methods. Panel (a) illustrates a trust region (D_k), with a trust radius of Δ_k in the neighborhood of x^k. Panel (b) demonstrates the possible trust radius selections (small, moderate, large) in order to find the minimizer of a function $m_k(x)$.

The trust region method is a combination of the Newton method and the steepest descent method [100]. When a region is not trustworthy, the algorithm behaves like a steepest descent method. On the other hand, when the region is trusted, the algorithm behaves like a Newton method. This behavior makes the method extremely robust. For a defined model, m_k, near a given point, x^k, there exists a trust region, D_k, with a trust radius of Δ_k (Figure III. 5 Panel (a)). Also let $p = x - x^k$. The trust region method is solving equation (III.70). One of three general step sizes can be taken (Figure III. 5 Panel (b)) during the iterative process to locate the minimizer of a given function. A small Δ_k is similar to a steepest descent direction, a large Δ_k is similar to a Newton step, and a moderate Δ_k is between these two step types [100]. For each step, the actual reduction in function value is computed using the previous and current estimate of the minimizer. This reduction is compared to the reduction predicted by the model. The size of the trust radius, Δ_k, is iteratively contracted or expanded based on how well the model (m_k) of the function predicted a decrease in function value [100].

$$\min\ m_k\left(x^k + p\right), \qquad \|p\| \leq \Delta_k \tag{III.70}$$

The Levenberg-Marquardt method is another perspective of the trust region method, as it operates on the same general principle [99]. In this algorithm, λ^* is called the Levenberg-Marquardt parameter or the Lagrange multiplier. Rather than operating on Δ_k, like in trust region, Levenberg-Marquardt operates on λ^*. These values are related. A small trust radius corresponds to a large Lagrange multiplier [99]. Both of these related nonlinear optimization techniques are robust.

III.3.3 Constrained Least-Squared Minimization

Constrained optimization techniques are used when a pre-existing limitation about the problem is known and must be enforced. Generally, least-squared minimization is the minimization of the residual between the measured values and the model predicted values [99]. In the specific optimization performed for Aim 3, this residual is the difference between predicted brain shifts, which are a linear combination of a precomputed atlas of deformations, and the measured brain shifts. The complexity arises from enforcing the constraint that the estimated coefficients must be non-negative and sum to less than or equal to one.

The fundamental principle of constrained optimization is that if there is a local minimizer (x^*) of a function (f) within a feasible set (S), which is defined by the constraints, as you move away from the local minimizer within the feasible set, the function value does not decrease [99]. Enforcing that some point (x) is a member of the feasible set, a cone of attainable directions for S at x can be defined [99]. The constraint type being enforced here is an inequality constraint, which specifies a minimum of a function that satisfies inequality (≥) constraints that define the feasible set, S.

The Karush-Kuhn-Tucker Conditions (KKTC) for inequality constraints are as follows. In order for x^* to be a local minimizer of a function, f, within the feasible set four conditions must be met. These tests can only be performed given that the function and any of the constraints enforced are continuous in their first derivative in the neighborhood being checked and the linear independence constraint qualification, or Kuhn-Tucker Constraint Qualification is met. The first condition is that x^* is member of the feasible set and there are real Lagrange multipliers ($\lambda_1^*, \ldots, \lambda_m^*$) which satisfy the second, third, and fourth KKTC. The second condition is that the gradient of the function at x^* is equal to the summation of the product of the Lagrange multipliers and the gradients of the constraints at x^*. The third condition is that the Lagrange multipliers must be greater than or equal to zero. The fourth condition is that the product of a given Lagrange multiplier and its associated inequality constraint at x^* must be equal to zero [99]. A simple example of this in practice is below.

Define function (Equation (III.71)) which is subject to the constraints specified. The problem is to find the minimum of this function subject to these constraints.

$$f(x) = (x_1 - 7)^2 + (x_2 - 3)^2 \qquad subject\ to\ x_1 + x_2 \leq 9 \tag{III.71}$$

The inequality can be expressed as $g_1(x) = 9 - x_1 - x_2 \geq 0$. First, check that the linear independence constraint qualification is met. Since $\nabla g_1(x) = (-1, -1)^T$ which is nonzero everywhere, the linear independence constraint qualification holds everywhere. In this problem, test the second condition of KKTC. This testing is visualized in equation (III.72).

$$\nabla f = \lambda_1 \nabla g_1 \colon \begin{bmatrix} 2(x_1 - 7) \\ 2(x_2 - 3) \end{bmatrix} = \lambda_1 \begin{bmatrix} -1 \\ -1 \end{bmatrix} \tag{III.72}$$

In order for the fourth condition of KKTC to hold true, either $\lambda_1 = 0$ or $g_1 = 0$. First testing $\lambda_1 = 0$ in (III.72), the solution for the point is $x_1 = 7$ and $x_2 = 3$. This point needs to be checked with the first condition, $g_i(x^*) \geq 0$. Substituting into $g_1(x) = 9 - x_1 - x_2 \geq 0$, it is evident that $g_i(x^*)$ is not greater than or equal to zero. Next, testing the $g_1 = 0$ condition, a system of equations can be generated, shown in (III.73).

$$2(x_1 - 7) + \lambda_1 = 0 \tag{III.73.a}$$

$$2(x_2 - 3) + \lambda_1 = 0 \tag{III.73.b}$$

$$x_1 + x_2 = 9 \tag{III.73.c}$$

Solving the system of equations gives $x_1 = \frac{13}{2}$, $x_2 = \frac{5}{2}$, and $\lambda_1 = 1$. Checking this solution versus the third KKTC, since $\lambda_1 \geq 0$, the condition is satisfied. Next, checking the solution versus the first KKTC, $g_1(x) = 9 - \frac{13}{2} - \frac{5}{2} \geq 0$, so it is satisfied. Therefore $\left(\frac{13}{2}, \frac{5}{2}\right)$ is the only candidate for the constrained local minimizer.

The problem being solved in Aim 3 is more complex than the example presented, but since it is a constrained optimization, the same principles apply. Specifically, a constraint is being enforced on a least-squared optimization method to ensure the quality of the solution within reason.

III.4 Method Conclusions

Overall the combined methods presented in this chapter reflect how the hypothesis of this thesis was investigated. As a whole, these clinically driven methodologies look into how enhanced anatomical brain models that account for tumors (primary and metastatic), improve the fidelity of biomechanical models of the brain. The data used was a combination of patient and animal cases, along with some simulation work. All of these individual aims shared the use of FEM and optimization techniques in order to evaluate the data in a patient and case specific manner.

CHAPTER IV

IV Enhanced Modeling of a Healthy Brain

IV.1 Summary and Contributions

The intent of this chapter was to enhance the modeling of normal brain biomechanics by incorporating realistic anatomical constraints and reconstructing material properties to more accurately represent compartmentalization within the brain. With interstitial pressure data from a porcine study, an inverse model was used to reconstruct material properties to capture *in vivo* brain tissue dynamics. The influence of three anatomical characteristics (the dural septa, the ventricles, and the treatment of the brain as a saturated media) of the brain were tested. To incrementally test these characteristics, four models were developed: the full anatomical condition description (FACD), the condition without dural septa description (CwoDSD), the condition without ventricle boundary description (CwoVBD), and the conventional fully saturated model description (CFSM).

The results of this investigation provided strong evidence for the ability of a biomechanical model with the proposed boundary conditions and material properties to accurately model *in vivo* interstitial pressures measured in a brain undergoing mock surgical loads. These results provided evidence that the poroelastic description of the parenchyma is uniquely appropriate for capturing the behavior of the brain under quasi-static surgical conditions. The work presented in Section IV.2 also represents a novel, systematic investigation of anatomical mesh specifications and boundary conditions required to capture the compartmentalization of intracranial pressure. Furthermore, material property values necessary to describe the poroelastic model of the brain were estimated using an inverse problem formulation. This was necessary, since these material property values are not established in the literature.

The work in Section IV.2 highlights the importance of incorporating features, such as tissue heterogeneity, the ventricles, and the dural septa in biomechanical models of the brain. It also challenges conventional assumptions regarding poroelastic theory applied to brain biomechanics. The evacuation of intra-sulci/intra-fissure fluid into subarachnoid spaces, though not explicitly modelled, may have been better captured in our model through the addition of fluid-compliance. Though this conclusion cannot be definitively drawn from this work, our results make it evident that their inclusion resulted in the accurate capturing of interstitial pressure magnitudes, transient behavior, and importantly the pressure spatial gradients which has not been accomplished previously. Overall, this study demonstrated the use of finite element modeling with patient-specific meshing, material properties, and boundary conditions as a method to capture intracranial pressure compartmentalization and gradients in response to space-occupying deformations. To the best of our knowledge the quality reconstructions accomplished in the full anatomical condition description have not been accomplished in other investigations of *in vivo* modeling of the brain.

IV.2 *In Vivo* Modeling of Interstitial Pressure in a Porcine Model: Approximation of Poroelastic Properties and Effects of Enhanced Anatomical Structure Modeling

The work in this section appears in:

Narasimhan, S., Weis, J. A., González, H. F. J., Thompson, R. C., Miga, M. I. (2018). "*In Vivo* modeling of interstitial pressure in a porcine model: approximation of poroelastic properties and effects of enhanced anatomical structure modeling", Journal of Medical Imaging, 5(4), 045002.

Abstract

The purpose of this investigation is to test whether a poroelastic model with enhanced structure could capture *in vivo* interstitial pressure dynamics in a brain undergoing mock surgical loads. Using interstitial pressure data from a porcine study, we use an inverse model to reconstruct material properties in an effort to capture these *in vivo* brain tissue dynamics. Four distinct models for the reconstruction of parameters are investigated (full anatomical condition description, condition without dural septa description, condition without ventricle boundary description, and the conventional fully saturated model). These models are systematic in their development to isolate the influence of three model characteristics: the dural septa, the treatment of the ventricles, and the treatment of the brain as a saturated media. This study demonstrates that to capture appropriate pressure compartmentalization, interstitial pressure gradients, pressure transient effects, and deformations within the brain, the proposed boundary conditions and structural enhancement coupled with a heterogeneous description invoking partial saturation was needed in a biphasic poroelastic model. These new findings suggest that with enhanced anatomical modeling and appropriate model assumptions, poroelastic models can be used to capture quite complex brain deformations and interstitial pressure dynamics.

IV.2.1 Introduction

Elevated intracranial pressure (ICP) can result from a variety of factors including cerebral edema, tumors, intracranial hemorrhages, accumulation of cerebrospinal fluid (CSF), and venous obstructions [55]. As a part of patient care in these disorders, ICP is sometimes monitored. Further, accurately monitoring elevated ICP is of real clinical relevance. In several studies of traumatic brain injury, it was indicated that patients who had their ICP monitored had a decrease in mortality [101]. There are multiple methods to monitor ICP including intraparenchymal and intraventricular techniques, which provide statistically similar measurements [102]. Experimental evidence suggests that ICP can vary spatially within the brain. This was suggested in a porcine study where an extradural temporal mass lesion was simulated with an epidural balloon [57]. A similar porcine experiment with an expanding frontal mass reported similar pressure gradient findings [58]. In a clinical study, four patients with unilateral mass lesions had bilateral subarachnoid pressure bolts inserted to measure ICP [103]. In all four cases, differential ICP's were found. The current standard of care is to measure ICP at one point in the brain and as a result of these findings the authors suggested modifying how ICP is monitored in this patient population [103]. Interhemispheric ICP gradients were also observed in a nonhuman primate study of reperfused hemispheric strokes [104]. It also was suggested that multiple ICP monitoring sites should be used in patients with midline shift and/or mass lesions larger than 25 ml to account for interhemispheric supratentorial ICP gradients [105]. With these pressure gradients in mind, the placement of ICP monitoring devices is important. However, multiple monitors can increase the risk of infection in patients. A noninvasive means of estimating pressure gradients could improve accurate measurement of ICP across the brain without increasing risk to the patient.

One method to noninvasively estimate pressure gradients would be through the development of patient specific computational models. There is an extensive history of using computational models in a patient specific manner [106], [63], [64]. Appropriate modeling of brain biomechanics for interventional applications has significant clinical implications, with the potential to provide noninvasive prediction of therapy delivery [79], reduce intraprocedural imaging requirements [14], and reduce unnecessary procedures [65, 93]. The brain's anatomy and mechanical behavior is complex, and in this paper we suggest that without careful modeling consideration, predictions can be confounded. Brain tissue exhibits mechanical heterogeneity and anisotropy. The Monro-Kellie doctrine has been a central working description of brain biomechanics which states that the cranial cavity is a fixed volume that is the sum of the volumes of brain tissue, intracranial blood, and CSF [54]. Treating the brain as only a solid tissue (often the case in models) negates the brain's biphasic nature. With respect to the exchange with interstitial fluid spaces within brain tissue, grey matter is not easily distorted and typically changes fluid content by approximately 1.5%, whereas, white matter has a more compliant structure and can increase as much as 10% [107]. Another important feature of the brain is that it is encapsulated by the dura [55]. The dura extends into folds of the brain forming the dural septa, consisting of the falx cerebri and the tentorium cerebelli. The dural septa serve the purpose of reducing displacements during motion [55]. The sulci are the groves in the brain, and the gyri are the plateaus formed by boundary ridges of sulci pairs [55]. Also, the ventricular cavities are filled with CSF and are connected to the central canal within the spinal cord and the space around the brain [55]. The brain tissue also consists of grey and white matters [55].

In order to accurately model brain biomechanics, quantifying the material properties of grey and white matters is necessary. There have been attempts to quantify the brain's material properties [108], [109], yet no consensus has been reached. One approach is to quantify these properties using magnetic resonance elastography [108]. Other approaches have been performed that correlated properties of grey and white matters in rectangular tissue samples undergoing shear testing under conditions of large strain [109]. These types of studies, which range from *in vitro* to *in vivo* testing, vary in protocols and in results [110]. The inconsistent property values obtained in these studies have led to variability within existing biomechanical modeling applications.

Moreover, despite extensive research done on biomechanical modeling of the brain, there is no consensus on what representation should be used [52], [65]. Model types include viscoelastic [67], poroelastic [69], elastic [71], and hyperelastic [73] models. From a physiological perspective, we suggest that the poroelastic description of the brain is most appropriate due to its ability to account for both solid and fluid components within the cranial cavity. In this work, we continue to investigate a poroelastic model which treats the brain as a material consisting of both an elastic solid matrix and a fluid component. We further suggest this biphasic representation is in better intuitive agreement with the Monro-Kellie Doctrine as well.

With respect to enhanced anatomical modeling of the brain, some work has already been accomplished [111]. One group used an inhomogeneous patient-specific model of the brain [111]. In another investigation, improved deformation behavior was found in seven clinical cases by accounting for the dural septa [14]. These investigations, among others, point towards the significance of accounting for brain geometry in modeling approaches. Ultimately, the predominant reason for variations in representation, both constitutive and geometric, arises from common investigational approaches that attempt to study soft-tissue in isolation rather than generating systems for *in vivo* observation. Unfortunately, this is a product of the extremely challenging nature of *in vivo* work and the deployment of instrumentation within that domain. In this study, we test whether a poroelastic biphasic model with enhanced anatomical features could can capture *in vivo* interstitial pressures under mock surgical loading.

We report on three important contributions in this investigation. First, we demonstrate the ability to accurately model *in vivo* interstitial pressures in a porcine experiment using a poroelastic model, including measured pressure gradients. While this does not validate the use of the poroelastic model for the brain under all loading conditions, it does provide meaningful evidence for its appropriateness in the biomechanical modeling of the brain under quasi-static surgical conditions. The second contribution is a systematic investigation of boundary conditions and anatomically-based mesh specifications, necessary to recapitulate the compartmentalization of intracranial pressure often seen with intracranial space occupying deformations. Finally, a set of approximate values describing brain tissue material properties in poroelastic biomechanical models is provided as an initial approach towards the generation of more accurate brain biomechanical models. As a whole, this work demonstrates the use of computational models as a means to investigate the complex interplay of boundary conditions, anatomical constraints, and material properties needed to capture ICP gradients and compartmentalization in the brain in response to acute space-occupying deformations.

IV.2.2 Materials and Methods

IV.2.2.1 In Vivo Porcine Data

The *in vivo* data used for this investigation was collected in a previous study [112]. The data reflects a porcine study, approved by the Institutional Animal Care and Use Committee, on a series of Yorkshire pigs (Parson's Farm, Hadley, M.A.) [112]. Once anesthetized, the porcine subject had pressure transducers (Johnson & Johnson Codman Microsensor ICP Transducer ~ Raynham, M.A., Part No. 82-6631) implanted in the midbrain/frontal region of both hemispheres [112]. One transducer was placed in the hemisphere ipsilateral to the mock surgical load, explained below, while the other transducer was placed in the contralateral hemisphere. These sensors measured interstitial pressures throughout the experiment. Before any procedure was performed, a T_1-weighted magnetic resonance (MR) image of the neuroanatomy was acquired [112]. After MR imaging stainless steel beads (1 mm diameter) were surgically implanted to monitor tissue movement [112]. A temporal craniotomy was performed, and a lateral compression was applied to create a mock surgical load against the intact dura using a piston-like source. This piston was attached to a stereotactic frame and translated in increments of 2 and 4 mm [112]. A baseline computed tomography (CT) scan of the head was obtained. A CT scan was performed after each piston translation, enabling the measurement of the bead displacements at the conclusion of each translation. The interstitial pressure was measured continuously in both hemispheres. A complete description of the protocols are in the original study [112]. For our investigation, the pressure and displacement data from three piston translations (8 mm, 10 mm, 12 mm) were used.

IV.2.2.2 Biphasic Poroelastic Model

With respect to our representation of brain biomechanics, we use a poroelastic model derived from Biot's description of consolidation theory [97] and adapted for use in surgical loading [113]. The governing equations are:

$$\nabla \cdot G\nabla \boldsymbol{u} + \nabla \frac{G}{1-2v}(\nabla \cdot \boldsymbol{u}) - \alpha \nabla p = 0 \qquad \text{(IV.1),}$$

$$\alpha \frac{\partial}{\partial t}(\nabla \cdot \boldsymbol{u}) + \frac{1}{S}\frac{\partial p}{\partial t} - \nabla \cdot k\nabla p = 0 \qquad \text{(IV.2).}$$

Table IV. 1: Equation Variables

Symbol	Meaning	Units
p	Interstitial pressure	Pa
$\boldsymbol{u}$	Displacement vector	m
G	Tissue shear modulus ($G = E/2(1+v)$)	Pa
E	Young's modulus	Pa
v	Poisson's ratio	(unitless quantity)
α	Ratio of fluid volume extracted to volume change of tissue under compression	(unitless quantity)
$\frac{1}{S}$	Void compressibility constant (amount of fluid capable of being forced into a tissue constant in volume)	Pa^{-1}
k	Hydraulic conductivity	$(\text{m}^3\text{s})/\text{kg}$

The variables in Equations (IV.1) and (IV.2) are identified in Table IV.1. Equation (IV.1) relates mechanical equilibrium to the interstitial pressure gradient. Equation (IV.2) relates volumetric strain to the conservation of fluid in a porous media.

The governing equations are solved using the Galerkin finite element method in 3-dimensions [96]. The finite element representation of Equations (IV.1) and (IV.2) have been previously described [70, 114]. A fully-implicit time stepping routine is used with a time step of 90 *seconds*. Both are based on a previous stability analysis of Equations (IV.1) and (IV.2) [114]. The total time varies based on the length of the experimental piston push. The first calculated pressure value from the solution occurs 90 *seconds* after our designated start time, which represents the peak pressure that occurs at each piston translation.

We generate two finite element meshes, representing the same porcine subject. The linear tetrahedral element meshes, visualized by the outer boundary of Fig. IV.1 are generated from manual segmentation of the MR volume [115]. The CT and MR spaces are coregistered using ANALYZE Version 7.5 – Biomedical Imaging Resource (Mayo Foundation, Rochester, M.N.) ensuring that the transducer and bead positions determined in measurement space (CT) are all located in computational model space (MR) [112]. To represent heterogeneity, the tetrahedral elements are classified according to the corresponding white and grey matters within an element from MR intensity [112],[116]. This is visualized in Fig. IV.1 in the axial slice. Ventricles were treated as a separate structure and serve as an internal boundary. The ventricular boundary surface is illustrated by the black points within Fig. IV.1.

Of the two meshes generated, one captures grey matter, white matter, and ventricles, but not the dural septa. The dural septa, visualized within Fig. IV.1, are incorporated using manual segmentation and a custom mesh splitting code which splits the mesh at specified planes. The second mesh generated contains this dural septa operation to study the dural septa's anatomical influence.

The values for both grey and white matters are designated with Young's modulus of 2,100 Pa and Poisson's ratio of 0.45. We elected to use values previously determined [117] with respect to a homogeneous model, reducing the degrees of freedom. Material properties of hydraulic conductivity (k) and the saturation constants ($\alpha, \frac{1}{S}$), are the subject of material property determination for both matters. These six material properties (k, α, and $\frac{1}{S}$ for both grey and white matters) are fit using an inverse problem approach.

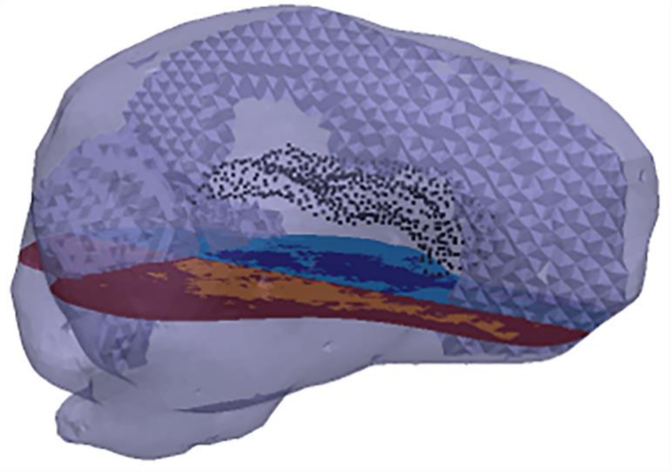

Figure IV. 1: Finite element mesh representation of the porcine brain. The dural septa splits are discernible within the mesh. The black points within the mesh visualize the nodes of the boundary between the brain parenchyma and the ventricles. The slice through the mesh visualizes the distinction between grey and white matters within the parenchyma. There is an additional distinction, which is not enforced in this study, between the tissues in either hemisphere.

Our geometric description of the mesh does not account for gyri and sulci. We hypothesize that the lack of resolution of these fine anatomical features leads to an effective source of bulk compliance, so we allowed for variability in the saturation constants to accommodate for this. These parameters have been historically prescribed as α=1 and $\frac{1}{S} = 0$ indicating a fully saturated media [14], [112]. Similar to what others have observed experimentally [57, 58], the propagation of pressure spatial distributions for this experiment, in response to a space occupying deformation at the macroscopic tissue scale level, seems to contradict this saturation assumption at the more coarse scale (meaning $\alpha \neq 1, \frac{1}{S} \neq 0$). This led to our approach suggesting that some of the finer fissure systems are acting as a source of compliance, much like the ventricular system does for space occupying lesions [118], [119].

IV.2.2.3 Model Sensitivity to Boundary Condition

The boundary conditions, meshes, and the material properties being estimated were systematically varied to isolate the influence of three features (dural septa, ventricle boundary condition, and saturation parameters) which reflect the creation of three model conditions that allowed for variations in the anatomical and saturation assumption: 1) the full anatomical model description, 2) the full anatomical description without dural septa, and 3) the full anatomical description without the ventricle boundary description. For completeness, we also included a more conventional model: 4) the full anatomical description with full saturation (α=1, $\frac{1}{S} = 0$). The boundary conditions of each model are explained in detail below, and a summary of these boundary conditions are in Table IV.2. In Table IV.2, each '*' indicates the boundary is active.

Table IV. 2: Summary of model conditions

	Dural Septa Present	Ventricle Treated as Reference Pressure	Unsaturated Effects Allowed ($\alpha \neq 1, \frac{1}{S} \neq 0$)	Number of Fit Material Properties
Full Anatomical Condition Description (FACD)	*	*	*	6
Condition without Dural Septa Description (CwoDSD)		*	*	6
Condition without Ventricle Boundary Description (CwoVBD)	*		*	6
Conventional Fully Saturated Model (CFSM)	*	*		2

IV.2.2.3.1 Full Anatomical Condition Description (FACD)

The FACD represents the model containing the full realization of the dural septa, ventricles, saturation constants, and heterogeneity. In FACD, the inverse model identifies the 6 model parameters associated with the material properties that best fit the measured interstitial pressure dynamics. These six properties are $k_{grey\,matter}$ (k_g), $k_{white\,matter}$ (k_w), $\alpha_{grey\,matter}$ (α_g), $\alpha_{white\,matter}$ (α_w), $1/S_{grey\,matter}$ ($1/S_g$), and $1/S_{white\,matter}$ ($1/S_w$). Hydraulic conductivity and saturation parameters are represented by k and α, $1/S$ respectively. Variable saturation parameters allow for compliance in the fluid component. The far-field cortical surfaces are fixed in displacement and experience no fluid drainage [112]. This decision is supported by the intact dura. The brain stem is stress-free and does not permit fluid drainage. Locations at the piston application are designated displacements associated with 8 mm, 10 mm, and 12 mm [112], and no drainage. The displacements of consecutive piston pushes do not rely on the previous loading as an initial condition. The region surrounding the piston area is stress-free and does not allow fluid drainage [112]. Consistent with the dural septa's role, the associated nodes are fixed in displacement and do not permit fluid drainage. Clinically, the ICP reference point is defined at the level of the foramen of Monro [56]. Additionally, the ventricular system is continuous with the central spinal canal [55]. We hypothesize that this permits the ventricles, when the dura is not compromised, to act as a reference pressure for the brain. As the ventricles represent a compliant internal boundary that can drain upon loading, they are allowed to deform, and the boundary pressure is zero, serving as a reference pressure. The solution of FACD incorporates the influence of the dural septa, ventricles, and sulci and gyri. To isolate the influence of these individual features, they are systematically removed within the 3 model conditions below.

IV.2.2.3.2 Condition without Dural Septa Description (CwoDSD)

To study dural septa influence, a model condition is created that eliminated the dural septa and its associated boundary condition from the FACD. Similar to FACD, this model fits the same six material properties.

IV.2.2.3.3 Condition without Ventricle Boundary Description (CwoVBD)

This model condition defines the influence of the ventricle boundary condition. The mesh includes the dural septa split and boundary conditions. However, the ventricles are considered non-draining surfaces. It is necessary to designate a reference pressure to be able to solve the system of equations. We use a previously used representation [112] whereby the brain stem surface is a constant reference pressure of zero. Similar to FACD and CwoDSD, the same six material properties are fit.

IV.2.2.3.4 Conventional Fully Saturated Model (CFSM)

The last model formulation is the traditional use of Biot's consolidation theory to represent the brain. More specifically, in this case, the brain is treated as a fully saturated media ($\frac{1}{S} = 0$ and $\alpha = 1$ for grey and white matters) [14], [112]. This reduces our parameterization to k_g and k_w. In the former conditions, we allow for unsaturated effects to accommodate missing structural compliance associated with sulci and gyri. In CFSM, we terminate that in favor of the more common assumptions.

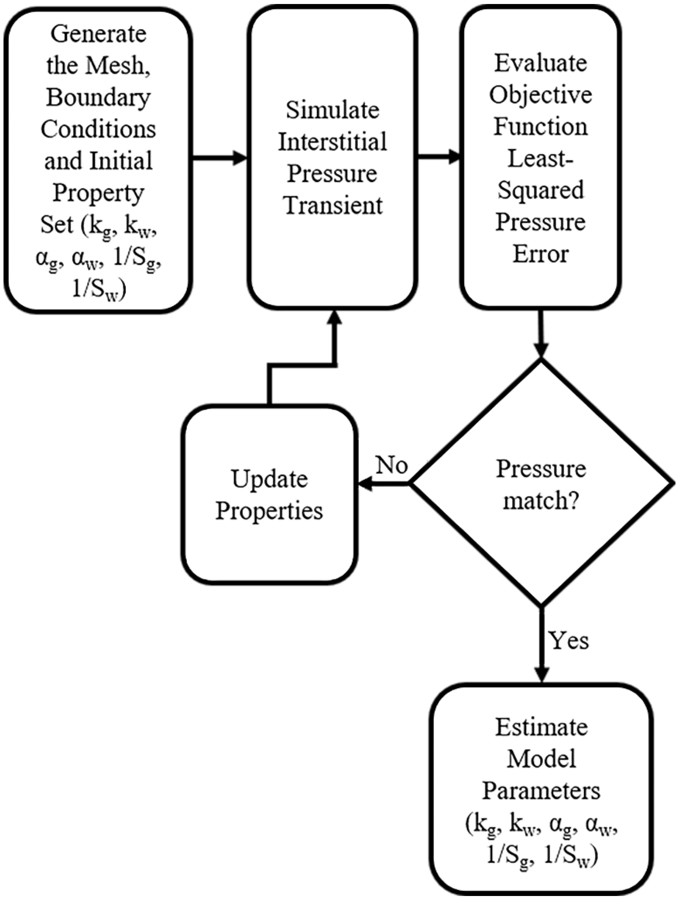

Figure IV. 2: Schematic illustrating the inverse model used to fit the model calculated intracranial pressure to the experimentally measured intracranial pressure while estimating the material properties.

IV.2.2.4 Inverse Model

The inverse model analysis in this work estimates the material properties to best fit measured interstitial pressure values from the transducers, given varying structural and material representations described above. This procedure is shown in Fig. IV.2. For all, except for the CFSM traditional framework, the parameters k_g, k_w, α_g, α_w, ${}^{1}/{}_{S_g}$, and ${}^{1}/{}_{S_w}$ are estimated with this approach. With respect to the CFSM, only the two hydraulic conductivity parameters are estimated. The material properties for each condition are independently estimated for each translation. To ensure repeatability, 20 randomized initial starting property guesses are performed for each piston translation for each inverse reconstruction. Therefore, there are 240 distinct executions of the inverse model (4 model conditions, 3 piston translations, 20 initial guesses each). The 20 initial guesses are generated by randomly perturbing each property value by +/- 25%. We should note, similar to many self-starting optimizations within the context of real experimental noise, our problem does require a good initial guess to avoid local minima and regularization to improve optimization behavior. To review, each inverse problem is driven by the objective function based on the acquired bilateral interstitial pressure data and to establish some sense of repeatability 20 initial guesses were used and allowed to converge to a minimum. We should note, prior to the 20 randomized initial guesses, the baseline initial guesses were determined empirically to ensure the values were reasonable for use in the inverse model; the +/- 25% noise was added subsequent to these guess determinations to ensure a more robust determination of properties.

These randomized initial guesses are input into the poroelastic, finite element model, with the appropriate boundary conditions, time step, and mesh. The interstitial pressure transient is simulated with the model based on a current guess at the material property distribution and an inverse problem approach is used to fit the material properties such that the difference between measured interstitial pressure at the two transducers and its simulated counterpart is minimized using a nonlinear least-squares constrained optimization in MATLAB (MathWorks Inc., Natick, M.A.). The objective function is a relative sum-squared error metric between experimentally measured pressure transients and its model-calculated counterpart and is calculated as:

$$SSE = \sum_{i=1}^{i=N} \left(\frac{(P_e - P_m)}{P_e}\right)_i^2 \qquad \text{(IV.3).}$$

P_e and P_m are the experimentally measured and model determined pressures respectively. i represents pressure value at the i^{th} time point in the transient.

With respect to Equation (IV.3), the experimental data consists of 200 data points (100 per transducer) evenly sampled along in time. Since the number of model calculated points is substantially less, due to the 90 *second* time step, the intra-time point values are linearly interpolated to fully utilize the experimental data. Using a customized trust region reflective optimization in MATLAB (MathWorks Inc., Natick M.A.), property values are iteratively estimated to minimize the SSE. The selection of the trust region method was based on its ability to combine the benefits of steepest descent and Newton-like methods. When tested, the trust region method was able to converge without stagnation, despite estimating parameters of very different orders of magnitude. This is important given the nature of the data and property values being fit. We use a custom convergence criteria based on the convergence of the SSE calculated at every iteration tested in work not shown. The SSE in Equation (IV.3) is used to measure quality of model fit.

Following parameter estimation of the 240 runs, we perform forward solves of the poroelastic model using the estimated parameters, generating pressure and displacement solutions. We designate two result types: 1) the ‘best fit’ is the parameter set that achieves the smallest SSE for a specific piston translation in a given model condition; 2) we denote the 'average pressure result' as an average given initial guess variability, as 20 parameter estimations for each piston translation and model condition are performed.

The inverse model is fit to the measured interstitial pressure, so the bead displacements serve as a source of validation. The percent shift correction is calculated using (IV.4).

$$\%Correction = 100\% * \left(1 - \frac{mean(\|\overrightarrow{d_e} - \overrightarrow{d_m}\|)}{mean(\|\overrightarrow{d_e}\|)}\right) \tag{IV.4}$$

$\overrightarrow{d_e}$ and $\overrightarrow{d_m}$ are the experimentally measured and model determined displacement vectors respectively.

IV.2.3 Results

IV.2.3.1 Optimization Performance

The convergence performance associated with our inverse problem model-fitting can be seen in Fig. IV.3 which reflects the percent SSE change relative to the median initial SSE in each set of 20 runs. We see a marked similarity with a substantive change in the objective function error with FACD and CwoDSD. With descriptions CwoVBD and CFSM, we see overall poor fit performance with very little reduction of the objective function.

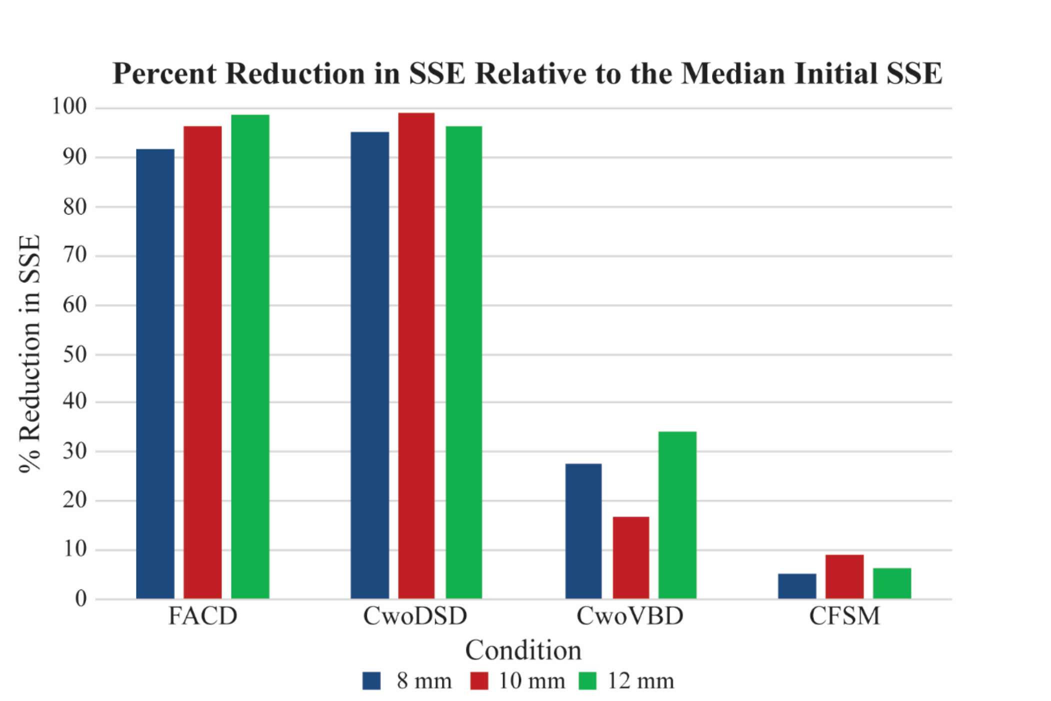

Figure IV. 3: Percent change in the median SSE at convergence relative to the median initial SSE over the set of 20 runs for each model representation of the brain. It shows a greater reduction in SSE and thus a better model fit for FACD and CwoDSD relative to CwoVBD and CFSM.

IV.2.3.2 Interstitial Pressure

We qualitatively and quantitatively assess the calculated interstitial pressures. In Fig. IV.4, observing the measured *in vivo* interstitial pressure, there is a sustained interhemispheric gradient and distinct transient behavior. The shaded regions represent the average model reconstructed pressure +/- two standard deviations with respect to the variable initial guesses. In all Fig. IV.4 panels, it is evident the methods provide repeatable fits within the initial guess range. The pressure fits shown in Fig. IV.4 are obtained from forward runs of the biphasic model using the optimized parameter values obtained during the 240 runs Fig. IV.4a representing FACD, shows that the enforced anatomical specificity captures the interhemispheric pressure amplitude and gradient, and transient. Fig. IV.4b represents CwoDSD and shows the quality of the

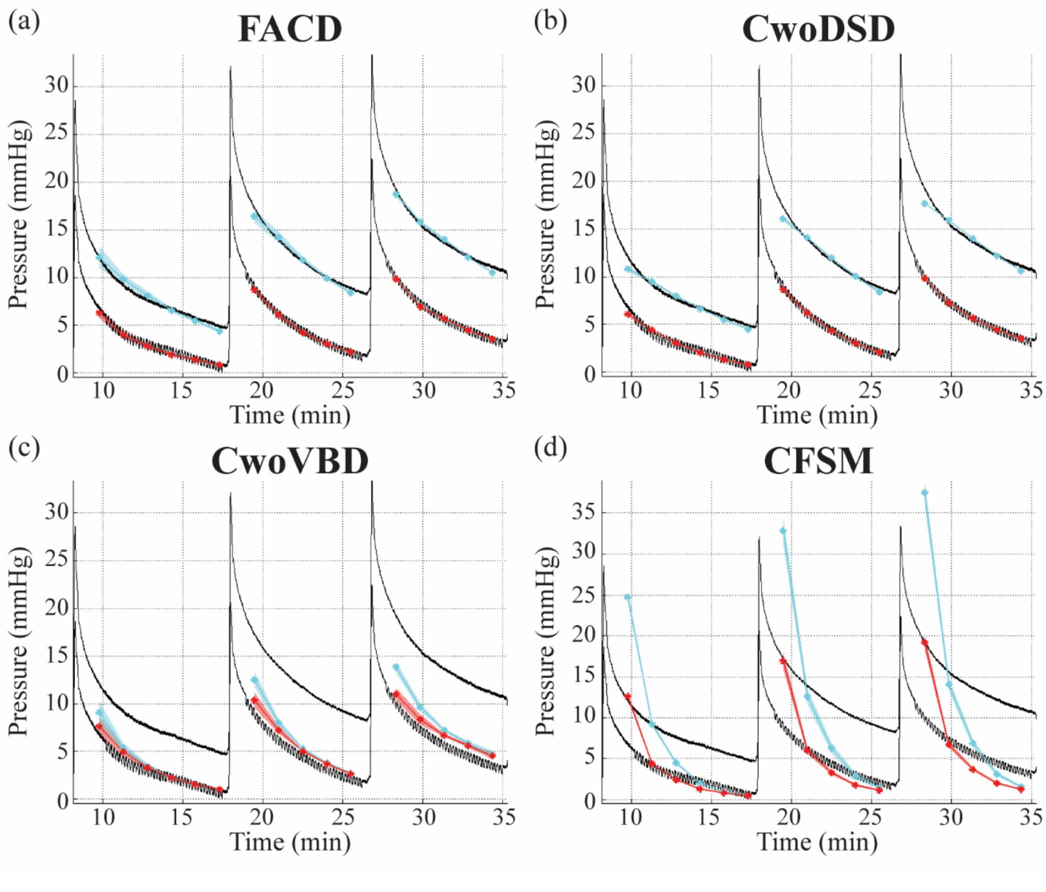

Figure IV. 4: Experimental and model-estimated pressure for each boundary condition. The solid black lines represent experimental pressure data measured with the transducers. The solid cyan and red lines are the average pressure results in the near hemisphere transducer and far hemisphere transducer, respectively. The translucent red and cyan areas are +/- two standard deviations of the average pressure result calculated at each time point. The pressure fits are the model estimated pressure obtained by the solution of the inverse problem for (a) the full anatomical condition (FACD), (b) the dural septa not included (CwoDSD), (c) the ventricle boundary condition not included (CwoVBD), and (d) the brain tissue treated as fully saturated (CFSM).

estimated trend of pressure obtained by the solution of the inverse problem is comparable to FACD's fits, which is illustrated in statistical testing below. Fig. IV.4c represents CwoVBD, and not only does it result in inaccurate pressure magnitudes, but it also does not maintain the sustained interhemispheric pressure gradient. Fig. IV.4d represents CFSM, and while initially there is a pressure gradient, it is not sustained over time. Additionally, the pressure is poorly estimated throughout the duration for CFSM.

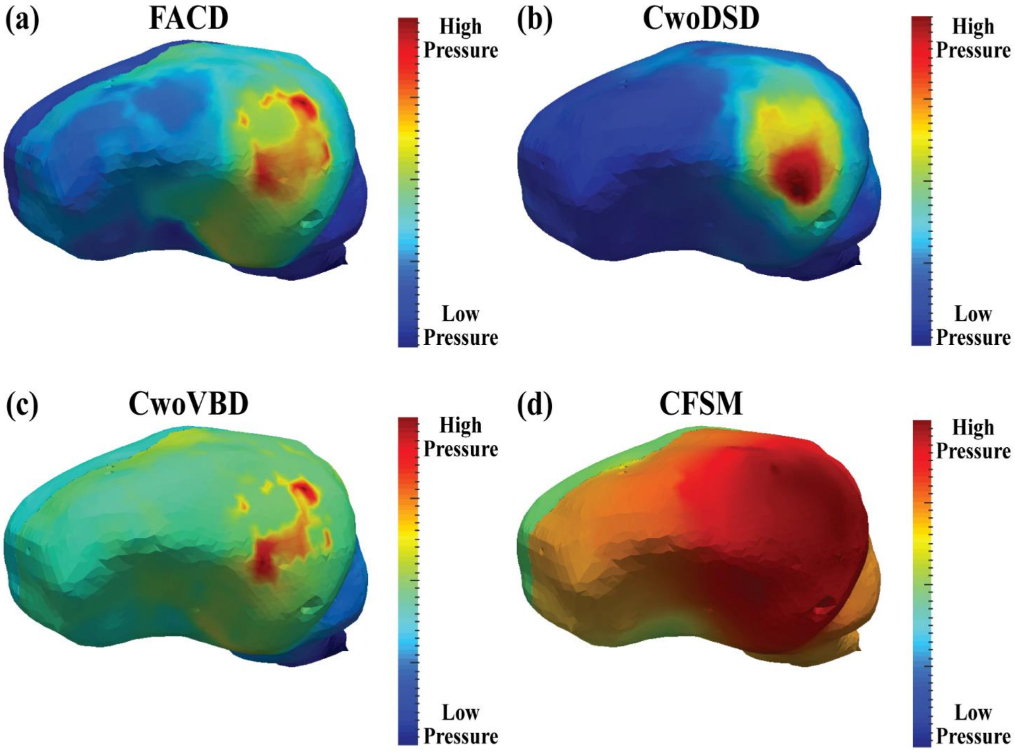

Figure IV. 5: Differences in pressure compartmentalization are seen based on the model conditions. For representation, the pressure values are scaled to the minimum and maximum of the specific solutions shown above. The solutions represent the best fits from each model condition from the first time step of the 10 mm piston translation for (a) all anatomical conditions (FACD) enforced, (b) the dural septa not included (CwoDSD), (c) the ventricle boundary condition not enforced (CwoVBD), and (d) the brain tissue treated as fully saturated (CFSM).

Using the Kruskal-Wallis test, we compare the SSE's of the final solution per model type to one another. The result of this indicated that the solutions, shown in Fig. IV.4, came from statistically different distributions. Based on test statistics from this group comparison, we also perform a pairwise comparison between the groups which indicated that the solutions of FACD and CwoDSD are not significantly different from each other, but are both significantly different than the other two conditions. Additionally, using the Wilcoxon rank sum test, we compare the SSE's of the final solution for each model type to one another to determine if statistically significant differences exist between model conditions. This shows that the pressure solutions of FACD, CwoDSD, CwoVBD, and CFSM are all statistically significantly different looking over all of the piston pushes. Based on the difference between measured and model estimated pressures, the best pressure fit is associated with CwoDSD, however, FACD is statistically comparable in the 12 mm piston translation using the Wilcoxon rank sum test. CwoVBD produces a dramatic decrease in the quality of fit, and CFSM results in the worst fit, with respect to average SSE.

Table IV. 3: Percent shift correction

PERCENT SHIFT CORRECTION		**Piston Translation**		
		8 mm	10 mm	12 mm
Condition	Full Anatomical Condition (FACD)	60.0	57.6	53.7
	Condition without Dural Septa Description (CwoDSD)	64.5	70.3	73.8
	Condition without Ventricle Boundary Description (CwoVBD)	58.1	60.2	64.8
	Conventional Fully Saturated Model (CFSM)	60.0	65.0	67.4

Qualitatively, the compartmentalization of the interstitial pressure can be visualized in Fig. IV.5. The images were individually scaled to capture the relative pressure distribution in each model condition. In Fig. IV.5a, which represents FACD, there are higher pressures in the hemisphere ipsilateral to the piston. There is also a distinction between the pressure within the ipsilateral hemisphere relative to the contralateral hemisphere and cerebellum. In CwoDSD, there was no interhemispheric compartmentalization, shown in Fig. IV.5b. In CwoVBD, compartmentalization between the hemispheres and the cerebrum and cerebellum is evident, shown Fig. IV.5c, however the extent of the interhemispheric difference is less distinct than in FACD. In Fig. IV.5d, which represents CFSM, there is a compartmentalization effect between the ipsilateral and contralateral hemispheres with the area of elevated pressure more pervasive. Additionally, there are higher pressures present in the cerebellum and brain stem regions.

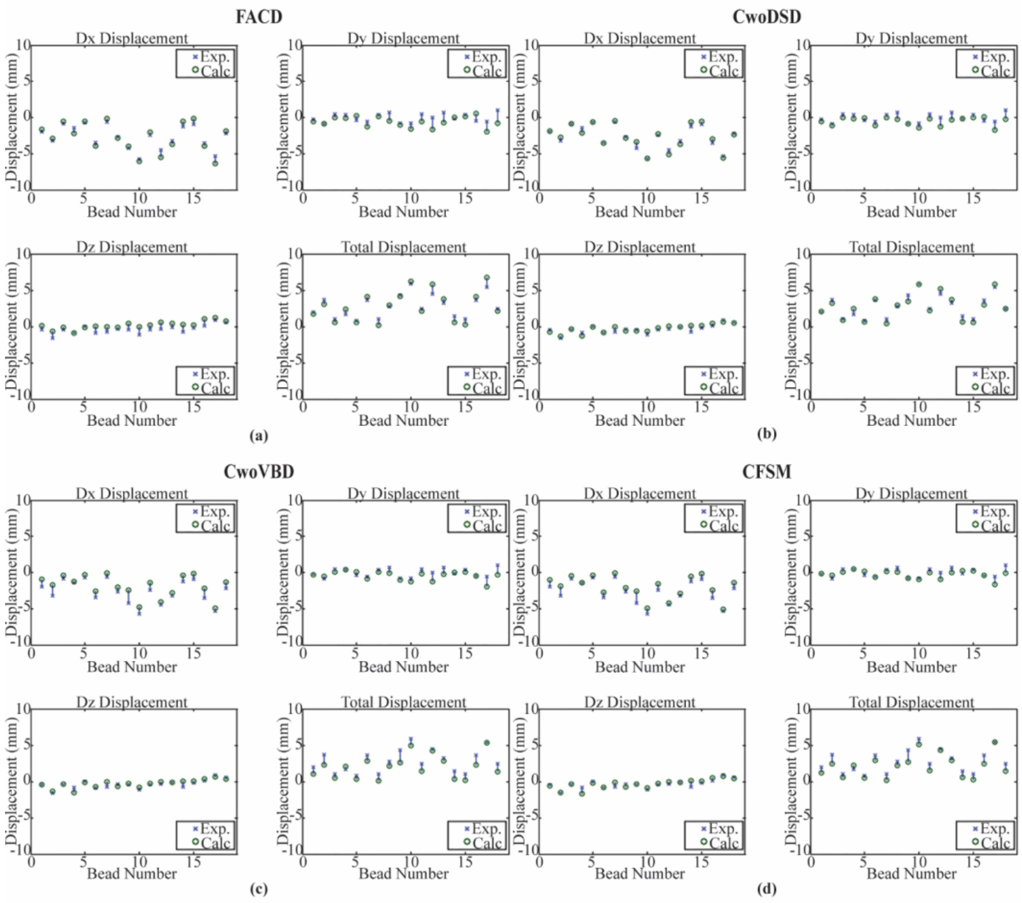

Figure IV. 6: Displacement calculations from the best fits runs from the 10 mm piston translation quantify the model calculated (Calc.) bead displacements at the conclusion of the simulated piston translation and compare them to the experimentally (Exp.) measured displacements. In each panel, the top left, top right, and bottom left subfigures represent the displacement calculations in the x, y, and z axis respectively, while the subfigure on the bottom right represents the total displacement.

IV.2.3.3 Shift Correction

Since the inverse model is fit to the experimental interstitial pressure, the bead displacements provide an internal source of validation. They also quantify the quality of the fits for the solid tissue component. To compare displacements, we calculated the percent shift correction using Equation (IV.4) at the conclusion of the piston translations per model condition performed (Table IV.3). The runs evaluated were the best fits for each of the piston translations and conditions respectively. Table IV.3 shows the best shift correction is consistently accomplished in CwoDSD.

Looking at individual bead displacements at the 10 mm piston translation, which reflects the general behavior, the same trend was observed (Fig. IV.6). Comparing all panels, it is evident that all model conditions were able to calculate shift corrections comparably.

Evaluating the same set of piston translations shown in Table IV.3, we use the Wilcoxon rank sum test to determine if the quality of displacement fits is statistically different between conditions. For each model condition type and piston translation, $\|\overrightarrow{d_e} - \overrightarrow{d_m}\|$ for the 18 beads is calculated for the run with the smallest SSE. Then the conditions are compared with respect to these sets of measurements (18 beads at every piston translation). Although some piston specific comparisons revealed statistical significance, these differences were not present in every comparison. Therefore, shift corrections between conditions were considered not statistically significantly different.

IV.2.3.4 Property Reconstruction

With respect to Fig. IV.3, it seems clear that the ventricular boundary and the fully compliant material parameter description are necessary for pressure distribution matching. This is more readily apparent in Fig. IV.4 which demonstrates that gradients are not captured by these descriptions. As a result, Table IV.4 shows the properties found in the best fits for FACD and CwoDSD. The property values estimated for grey and white matters are consistently different in all best fit properties across all piston translations and model conditions. This suggests heterogeneous material property descriptions are appropriate. Observing the changes in the best fits of k_g and k_w, there is a change in magnitude with translation changes with k_w consistently greater than k_g which is consistent with the literature. Although not always true, α_w trends closer to the historical value of 1 in contrast to α_g, which trends lower. The reconstructions of ${}^{1}\!/_{S_g}$ and ${}^{1}\!/_{S_w}$ were all non-zero indicating a need for compliance for appropriate matching.

Table IV. 4: Estimated properties summary (grey shaded columns represent monotonic behavior with piston translation)

Condition	Piston Translation	k_g Best Fit	k_w Best Fit	α_g Best Fit	α_w Best Fit	$1/S_g$ Best Fit	$1/S_w$ Best Fit
Full Anatomical Condition (FACD)	8 mm	2.7E-13	1.9E-11	4.3E-01	8.7E-01	3.3E-06	4.3E-05
	10 mm	3.2E-13	1.1E-11	4.5E-01	5.8E-01	2.6E-06	3.0E-05
	12 mm	1.8E-12	9.8E-12	4.8E-01	1.0E+00	2.3E-06	4.4E-05
AVERAGE		**8.0E-13**	**1.3E-11**	**4.5E-01**	**8.2E-01**	**2.7E-06**	**3.9E-05**
Condition without Dural Septa Description (CwoDSD)	8 mm	2.2E-14	8.0E-12	3.9E-03	8.8E-01	5.5E-10	2.2E-05
	10 mm	2.5E-14	2.8E-12	4.9E-03	4.2E-01	1.1E-13	9.1E-06
	12 mm	4.2E-14	9.0E-13	5.9E-03	1.8E-01	2.8E-11	4.7E-06
AVERAGE		**3.03-14**	**3.9E-12**	**4.9E-03**	**4.9E-01**	**1.9E-10**	**1.2E-05**

IV.2.4 Discussion

The error reduction results in Fig. IV.3 and pressure results shown in Fig. IV.4a and IV.4b reflect that interstitial pressure can be appropriately modeled using both FACD and CwoDSD conditions. The mismatch between the experimental pressure data and the model estimated pressure obtained by the solution of the inverse problem for CwoVBD and CFSM (Fig. IV.4c and IV.4d) is likely due to the necessary contributions of anatomic structure (i.e. inclusion of ventricular boundary) and compliance in material property description (i.e. relaxation of the saturation assumption). Despite the same optimization algorithm being used, in the CwoVBD and CFSM conditions, the parameters found with the solution of the inverse problem could not match the experimental pressure (Fig. IV.4). This is also indicated by the illustration of the inverse problem's convergence shown with SSE in Fig. IV.3. Incorrectly describing the anatomy of the brain in these model conditions likely caused these discrepancies. This is further evidence for our FACD being most appropriate for accurate estimation of ICP.

Comparing the pressure distributions of Fig. IV.5b, it is evident that the dural septa boundary defines the compartmentalization of pressure between hemispheres and between the cerebrum and cerebellum, however further investigation with multiple pressure transducers is needed to more fully capture the compartmentalization effect. The percent shift correction in CwoDSD is consistently better than other conditions (Table IV.3 and Fig. IV.6). To some degree, this was expected as all other material properties (namely, the elastic modulus and Poisson's ratio) were optimized under conditions that used a homogenous mesh without dural septa in previous work (quite similar to CwoDSD conditions which likely explains the monotonic increase in accuracy) [117]. With respect to FACD, with progressively larger deformations the displacement predicting fidelity behaves monotonically with displacement prediction performance decreasing with increased deformation. This performance difference is likely due to FACD being over constrained due to the enforcement of the dural septa boundary conditions. However, we should note that the model calculated shift corrections were not statistically significantly different from one another at every piston translation among these two models. To more appropriately address, a combined objective function (pressure and displacement) would be a viable direction to investigate more accurately capturing both displacement and pressure dynamics, however, in such an endeavor, more interstitial pressure measurements are likely needed as well as temporally-coupled measurements of bead displacements, a challenging experiment.

Excluding the ventricle boundary condition resulted in a substantially worse result, reflected by inaccurate interstitial pressures. The results of Fig. IV.4c and Fig. IV.5c indicate that the pressures in both hemispheres were similar in magnitude. This indicates that the appropriate treatment of the ventricle boundary has significant impact on brain models. Our decision to treat the boundary as a reference was motivated from clinical practice, which treats the level of the foramen of Monro as the ICP zero point [56].

Treating the brain as a fully saturated tissue (Fig. IV.4d) is the current convention in the literature when biphasic models are used [14], [112]. Our results indicate this may not be appropriate at the macroscopic surgical scale. The magnitudes of the experimental data were not matched, and the interhemispheric gradient was not sustained. The differences between Fig. IV.4a and IV.4d reflect that enabling the tissue to be unsaturated yields a substantial improvement in quality of fit. The results of the percent shift correction are also comparable to FACD (Table IV.3 and Fig. IV.6). In a previous study of volume regulation, the results led to a hypothesis that brain interstitial space could experience volume variations based on stresses present [107]. It is not definite what phenomena the saturation terms are capturing, but we hypothesize that the evacuation of fluid from fissures and sulci spaces into subarachnoid spaces during compression is the phenomenon that is introducing a net compliance in the macroscopic tissue descriptions.

The necessary goal of this work was to match the pressure gradients in the tissue and given the level of fit from Fig. IV.3, only FACD and CwoDSD are appropriate and, as such, reported in Table IV.4. The properties estimated in the two models are discernibly different which speaks to the variability depending on model sophistication. One interesting observation is that in many of the material parameters of Table IV.4, we see monotonicity with degree of piston translation (all grey columns of Table IV.4). This would indicate a need for a material nonlinearity to better capture the entire performance of the system over varying surgical loading.

We should note however, one shortcoming of this work is in regards to instrumentation. Our inverse model is driven by two transducers' pressure transients in only two locations within the brain taken over a finite length of time. While the reason for this was the natural experimental constraints of brain volume, this certainly limits fidelity of the property reconstructions.

However, our full anatomical condition in conjunction with the poroelastic model under modified saturation assumptions demonstrates an ability to capture *in vivo* interstitial pressures and tissue deformation. It also reflects the compartmentalization of interstitial pressure, agreeing with clinical observations [103, 120]. With respect to anatomical constraints, the presence of the dural septa is less critical than the ventricular structure with respect to cross-hemisphere pressure gradient development; however, there are modest differences in distribution amplitude with the septa. Based on the results of FACD, we infer that our incorporation of heterogeneity with grey and white matters is appropriate. Lastly, in Fig. IV.4 the relaxation of the saturation assumption leads to considerably better matching and sustaining of pressure gradients over the transient (i.e. Fig. IV.4d with CFSM shows early gradient but non-sustained, a noted limitation in the original study [112]).

IV.2.5 Conclusions

The purposes of this investigation are to accurately model *in vivo* interstitial pressures, determine the anatomical specificity necessary to capture interstitial pressures and their cross-parenchymal gradients accurately, and to estimate brain material property values. The results provide strong evidence for the utility of a poroelastic representation and the pivotal role that certain anatomical features play in accurately modeling pressure and deformation. To the best of our knowledge, the model reconstructions in the full anatomical condition description have not been accomplished in other studies of *in vivo* modeling. This work highlights the importance of incorporating features, such as tissue heterogeneity, the ventricles, and the dural septa in future biomechanical models. It also challenges conventional assumptions regarding poroelastic theory applied to brain biomechanics at the macroscopic level and postulates that sulci and gyri may be an apparent source of compliance in measurements. While we cannot conclusively say that adding fluid-compliance is explained by the evacuation of intra-sulci/intra-fissure fluid into subarachnoid spaces without further model development, it is evident that its incorporation results in better capturing of interstitial pressure magnitudes, transient behavior, and importantly the spatial gradient – effects that were very challenging and elusive to capture in past modeling efforts. While preliminary in nature, the work presented could have applications in modeling elevated ICP in order to predict potential *in vivo* pressure gradients which could be used to inform patient care or influence deployment of convection-enhanced delivery of therapeutics.

Acknowledgements

This work was supported by the NIH-National Institute of Neurological Disorders and Stroke R01NS049251, and the NIH Training Grant T32 EB021937. The authors would like to thank Professor of Surgery, P. Jack Hoopes, DVM, PhD from Geisel School of Medicine, Dartmouth College for his assistance in generating the original data from [16].

CHAPTER V

V Tumor Modeling Fidelity

V.1 Summary and Contributions

The intent of this chapter was to enhance brain modeling by developing tumor growth behaviors for the purpose of determining biomechanical effects. Patients with intracranial metastases often are treated with stereotactic radiosurgery (SRS). A side effect, which occurs in up to 20% of patients, is radiation-induced necrosis. Symptoms associated with radiation-induced necrosis can resolve independent of treatment, or the physician can treat it with corticosteroids. Radiation-induced necrosis and tumor recurrence both appear as indistinguishable radiographic changes in multiple MR imaging sequences. This poses a significant clinical challenge as current clinical practice definitively determines the etiology of these radiographic changes either by serial imaging observation resulting in delayed patient therapy or invasive intracranial lesion biopsy with histological diagnosis.

This investigation, detailed in Section V.2, used serial MR scans obtained during standard of care imaging. Five patients with tumor recurrence and five patients with radiation-induced necrosis were retrospectively processed using a patient-specific biomechanically coupled tumor growth model. This model was used to estimate model-derived measures and patient-specific model parameters to noninvasively differentiate the two etiologies. Using the estimated parameterized biophysics of lesion growth with this framework, this study was able to differentiate lesion etiology with up to 100% accuracy in the group of patients studied. Furthermore, when compared with conventional morphometric analysis methods the performance of the proposed framework was consistently superior to the morphometric analyses.

The work in Section V.2 generates a novel framework for noninvasively differentiating radiation-induced necrosis and tumor recurrence. The results of this study indicate that the image-data-driven biophysical model-based analysis framework for estimating model-derived measurements and patient-specific model parameters can noninvasively differentiate between tumor recurrence and radiation-induced necrosis. While this investigation was limited to patients with metastatic disease, it could easily be applied to patients with primary intracranial tumors who have undergone SRS. Radiation-induced necrosis is also observed in these patients. If the work presented here is equally accurate in a larger patient cohort, it has large implications for patients who have undergone SRS and experience radiographic changes after their treatment. A noninvasive diagnostic technique would be a significant improvement upon the current clinical gold-standards and would obviate the need for invasive intracranial biopsy.

V.2 Biophysical Model-Based Parameters to Classify Tumor Recurrence from Radiation-Induced Necrosis for Brain Metastases

The work in this section appears in:

Narasimhan, S., Johnson, H.B., Nickles, T.M., Miga, M. I., Rana, N., Attia, A., Weis, J. A. (2019). "Biophysical model-based parameters to classify tumor recurrence from radiation-induced necrosis for brain metastases", Journal of Medical Physics and Biology, 46(5), 2487-2496.

Abstract

Purpose: Stereotactic radiosurgery (SRS) is used for local control treatment of patients with intracranial metastases. As a result of SRS, some patients develop radiation-induced necrosis. Radiographically, radiation-induced necrosis can appear similar to tumor recurrence in magnetic resonance (MR) T_1-weighted contrast-enhanced imaging, T_2-weighted MR imaging, and Fluid-Attenuated Inversion Recovery (FLAIR) MR imaging. Radiographic ambiguities often necessitate invasive brain biopsies to determine lesion etiology or cause delayed subsequent therapy initiation. We use a biomechanically-coupled tumor growth model to estimate patient-specific model parameters and model-derived measures to noninvasively classify etiology of enhancing lesions in this patient population. Methods: In this initial, preliminary retrospective study, we evaluated five patients with tumor recurrence and five with radiation-induced necrosis. Longitudinal patient-specific MR imaging data was used in conjunction with the model to parameterize tumor cell proliferation rate and tumor cell diffusion coefficient, and Dice correlation coefficients were used to quantify degree of correlation between model estimated mechanical stress fields and edema visualized from MR imaging. Results: Results found four statistically relevant parameters which can differentiate tumor recurrence and radiation-induced necrosis. Conclusions: This preliminary investigation suggests potential of this framework to noninvasively determine the etiology of enhancing lesions in patients who previously underwent SRS for intracranial metastases.

V.2.1 Introduction

A common treatment option for intracranial metastases is stereotactic radiosurgery (SRS). SRS helps establish local control, but complications may arise; potential post-radiation treatment effects include pseudoprogression and radiation-induced necrosis [121, 122]. Pseudoprogression occurs within 3 months of SRS, versus radiation-induced necrosis which usually appears around 3 months and later [121, 122]. Radiation-induced necrosis is an adverse reaction to radiation treatment [9, 34]. Following SRS, up to 20% of patients exhibit radiation-induced necrosis [9, 35], which often appears as an enhancing lesion in MR T_1-weighted contrast-enhanced imaging with accompanying T_2-weighted and Fluid-Attenuated Inversion

Recovery (FLAIR) abnormalities [9, 36, 37]. Accurate diagnosis presents enormous clinical challenges as symptoms and radiographic findings for recurrence and radiation-induced necrosis are often indistinguishable.

Misidentification can have adverse clinical outcomes since treatment and prognosis of radiation-induced necrosis and tumor progression are different. Treatments for radiation-induced necrosis include observation and corticosteroids, with symptoms sometimes resolving independently [39]. These treatments could accelerate tumor progression. Repeat SRS can treat recurrence, but would exacerbate radiation-induced necrosis and expose patients to unnecessary radiation. Brain biopsies are the diagnostic gold standard, but introduce risk and are often not possible due to patient condition or lesion location. Indeterminate lesions are often followed with costly follow-up imaging that can cause deleterious outcomes for recurrent tumors with delayed subsequent therapy [9]. Serial examinations usually include conventional MR with T_1-weighted contrast-enhanced imaging and FLAIR imaging, but are diagnostically confounded. Patients that undergo SRS for intracranial metastases would benefit greatly from noninvasive diagnosis.

There is a history of studies attempting to employ quantitative imaging modalities to noninvasively distinguish the etiologies [123], with reproducible results proving challenging. Conventional MRI (magnetic resonance imaging) has been studied with mixed interpretations [36, 37]. There have been studies into mean fractional anisotropy [124, 125], perfusion imaging [9, 43], positron emission tomography [44], magnetic resonance spectroscopy [9, 46], and diffusion weighted imaging [125, 126]. As an overall observation, there remains a lack of consensus in quantitative imaging for diagnosis. Here, a novel framework is introduced that utilizes medical imaging data combined with biophysical models of tumor growth dynamics to noninvasively distinguish between tumor recurrence and radiation-induced necrosis in a binary classification of enhancing lesion etiology. Congruent with clinical practice, we will not sub-differentiate pseudoprogression and radiation-induced necrosis, referring to both as radiation-induced necrosis.

There is support for patient-specific tumor growth modeling in clinical settings [8, 127]. Development and use of tumor growth models within the brain have been investigated [7, 17, 128-130], with work often related to either accurate model development, or its use to assess a potential clinical aspect [129-131]. While these are concerned with tumor progression, other work focused on the surrounding environment and its influence. There have been studies investigating the influence of surrounding mechanical environment on tumor growth [88, 132] and using modeling to predict radiotherapy effect [7]. In related work by our group, a mechanically-coupled reaction-diffusion model was used to develop a predictive framework of breast cancer treated with neoadjuvant chemotherapy [98, 133, 134]. This demonstrated an ability to predict patients' responsiveness using early cycle treatment changes [98]. Building upon these, we use an image-data-driven biophysical model of tumor growth as a tool to classify space-occupying enhancing lesions in the brain following SRS.

In this investigation, we evaluate patient-specific model parameters by fitting a biomechanically-coupled tumor growth model to longitudinal lesion changes observed from MRI data following SRS for brain metastasis and calculate model-derived measures. We hypothesize the biophysics of the etiologies will result in differences in patient-specific model parameters and model-derived measures allowing for non-invasive classification.

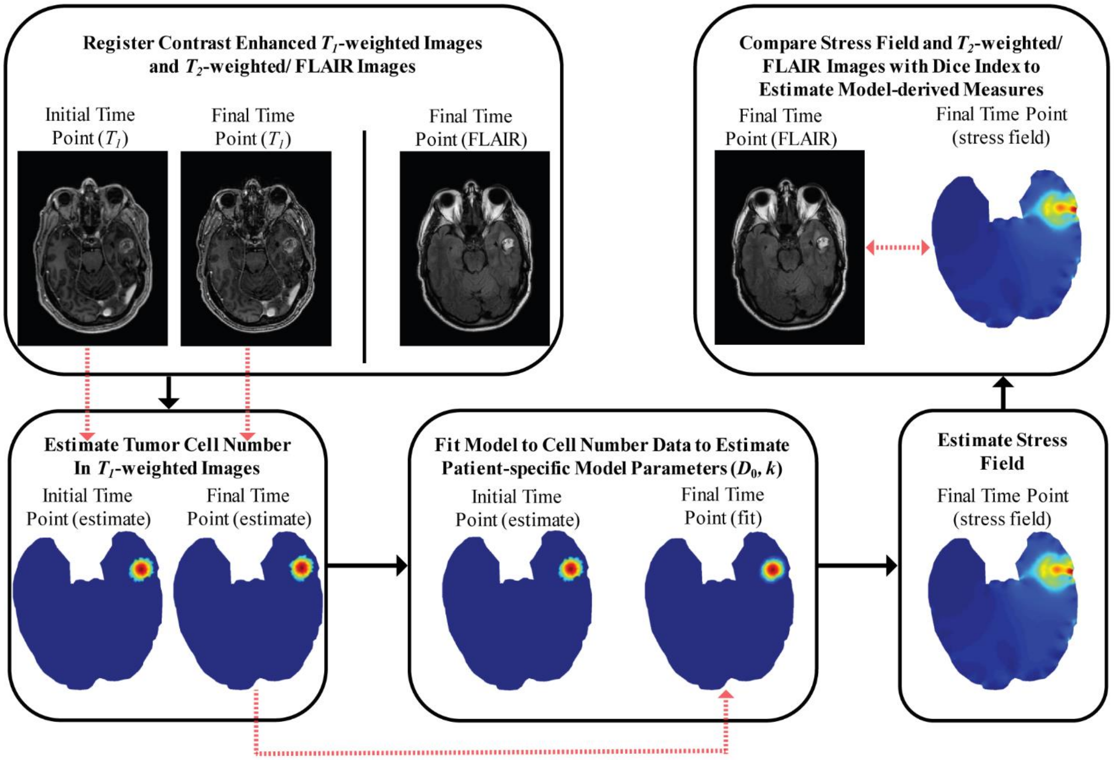

Figure V. 1: Framework to estimate different patient-specific model parameters and model-derived measures for differentiating tumor recurrence and radiation-induced necrosis.

V.2.2 Materials and Methods

V.2.2.1 Patient Data

Ten de-identified clinical data sets were obtained under the Vanderbilt University Institutional Review Board approved study to analyze retrospective MR imaging data. Data sets were collected after patients were treated with SRS, ensuring we are modeling effects of recurrent enhancing lesions following SRS. The datasets represent 5 patients with tumor recurrence and 5 with radiation-induced necrosis. Diagnoses were pathologically confirmed or retrospectively determined through long-term clinical follow-up, with incidence of all recurrence and 3 of 5 radiation-induced necrosis lesions biopsy confirmed. Data consists of serial MR imaging with standard-of-care T_1-weighted contrast-enhanced and FLAIR imaging sequences acquired following SRS, prior to diagnosis. To assess longitudinal changes, two time points of T_1-weighted MR scans obtained immediately prior to diagnosis are used (Figure V.1). Time between scans varied according to the clinician from under 1 month to approximately 9 months, with an average of 3.5 months. Use of sparse MR imaging data from two time points has three purposes: (1) demonstrates use of standard-of-care serial imaging data, (2) potentially shows a pathway to replace inconclusive serial imaging, and (3) if it allows earlier detection, it could reduce time between detected changes and clinical action. Note radiographic similarities in T_1-weighted MR images (Figure V.2a, Figure V.3a). T_2-weighted or FLAIR MR images obtained immediately prior to diagnosis were also used (Figure V.1). Due to this retrospective study, T_2-weighted and FLAIR MR images are used interchangeably to segment edema based on availability.

V.2.2.2 Biophysical Model of Tumor Growth

The realistic biomechanically-coupled biophysical tumor growth model was adapted from previous work from our group [98, 132-134]. A complete description is in previous publications [98, 133, 134]. The governing equations are:

$$\frac{\partial N(\bar{x},t)}{\partial t} = \nabla \cdot \left(D(\sigma_{VM}, \bar{x}, t)\nabla N(\bar{x},t)\right) + kN(\bar{x},t)\left(1 - \frac{N(\bar{x},t)}{\theta}\right) \qquad \text{(V.1)}$$

$$D(\sigma_{VM}, \bar{x}, t) = D_0 e^{-\gamma \sigma_{VM}(\bar{x},t)} \qquad \text{(V.2)}$$

$$\nabla \cdot G\nabla\vec{u} + \nabla\frac{G}{1-2v}(\nabla \cdot \vec{u}) - \lambda\nabla N(\bar{x},t) = 0 \qquad \text{(V.3)}$$

Equation (V.1) describes rate of tumor cell number change at a given time and location as the sum of random cell diffusion and logistic growth. Equation (V.2) represents mechano-inhibition of cellular diffusion coefficient, coupling tumor cell transport to evolving tissue stress state. As tissue distorts due to mass effects, tumor diffusive transport is inhibited. Equation (V.3) models linear elastic, isotropic mechanical equilibrium in the presence of an external expansive force [98, 133, 134]. In (V.1), (V.2), and (V.3) $\vec{u}$ is the displacement vector; N is the spatiotemporal varying cell number. D is the local cellular diffusion coefficient of tumor cells in the presence of mechanical stress; D_0 (mm^2/day) is the cellular diffusion coefficient without mechanical stress present. Tumor cell proliferation rate is represented by k (day^{-1}), which reflects how proliferative lesion cells are. Von Mises stress is represented by σ_{VM} (Pa). v (0.45) is Poisson's ratio; G (689.66 Pa) represents shear modulus. γ (0.0050) and λ (0.010) are empirically derived coupling coefficients. We solve Equations (V.1-V.3) using the Galerkin method of weighted

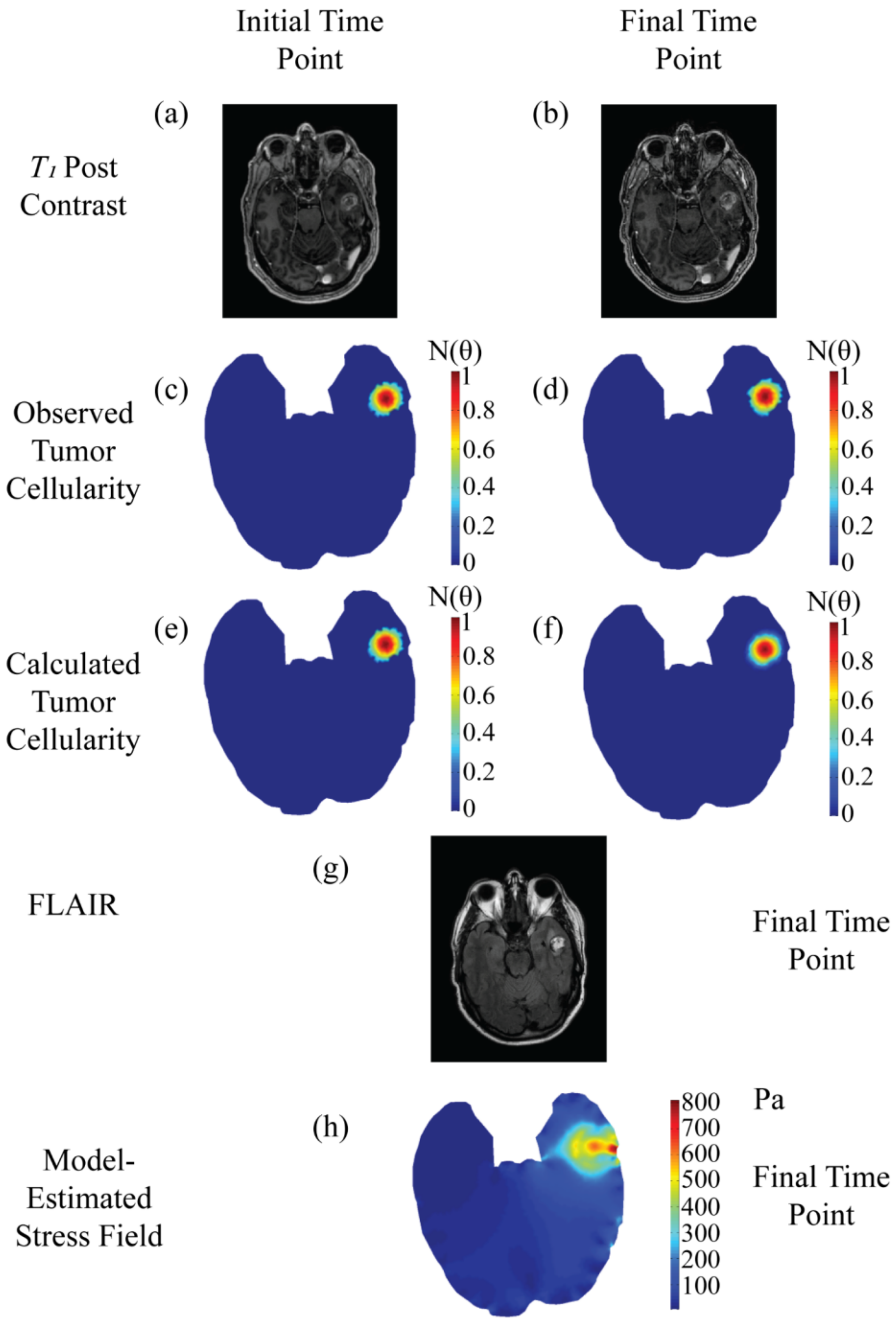

Figure V. 2: Patient diagnosed with tumor recurrence at starting time point (a,c,e), and final time point taken before diagnosis of lesion etiology (b,d,f,g). Post-contrast T_1-weighted MR images (a,b) are used to estimate observed tumor cellularity (c,d) and the model is fit to estimate tumor cellularity (e,f). FLAIR imaging at the time point prior to diagnosis (g) is compared to estimated mechanical stress field (h) at the final time point.

residuals on triangular finite elements described by standard linear Lagrange basis functions [135]. Temporal resolution employs a fully explicit forward Euler method. The time step is 1 day, and in work not shown here, stability analysis was performed. Representing the dural surface, the displacement boundary conditions on the mesh outer surface permits surface tangential displacement, but do not allow normal displacement. The cortical surface is treated with a boundary condition of no flux of tumor cells across the boundary. Meshes have a nominal element edge length of 2.5 mm, an average of 7182 elements, and an average of 3700 nodes. We treat the parenchyma as homogenous. The biophysical model is based on a central slice taken through the region-of-interest (ROI), and two-dimensional (2D) plane strain approximation is employed.

As a first-order approximation for tumor cellular density, we assume the enhancing lesion has a Gaussian distribution of tumor cell density. Maximal cellular carrying capacity, θ, occurs at the enhancing lesion's center. This density decreases outward to a minimum density of $0.25 * \theta$ at the lesion's maximal long axis dimension.

V.2.2.3 Patient-Specific Model Parameters

For each patient, two time points of T_1-weighted contrast-enhanced image volumes are selected (scan immediately prior to diagnosis and an earlier scan). Central axial slices with the most radiographic volumetric change with respect to the enhancing portion of the T_1-weighted MR image were selected. Image volumes are longitudinally rigidly co-registered to the most recent time point (Figure V.1) [136]. Enhancing lesions in both T_1-weighed images are manually segmented. Using the segmentations, the tumor cell number in both T_1-weighted images are estimated using the Gaussian description and denoted as 'observed tumor cellularity' (Figure V.2c-d, Figure V.3c-d). We fit our tumor growth model to the 'observed tumor cellularity', with the first distribution as the starting point and final distribution as the desired outcome using a custom Levenberg-Marquardt parameter optimization algorithm in MATLAB (MathWorks Inc., Natick, MA) to estimate designated patient-specific model parameters: tumor cell diffusion coefficient (D_0) and tumor cell proliferation rate (k). The objective function that was minimized is the sum-squared error between observed and model-estimated tumor cellularity. Convergence occurs if one of the following

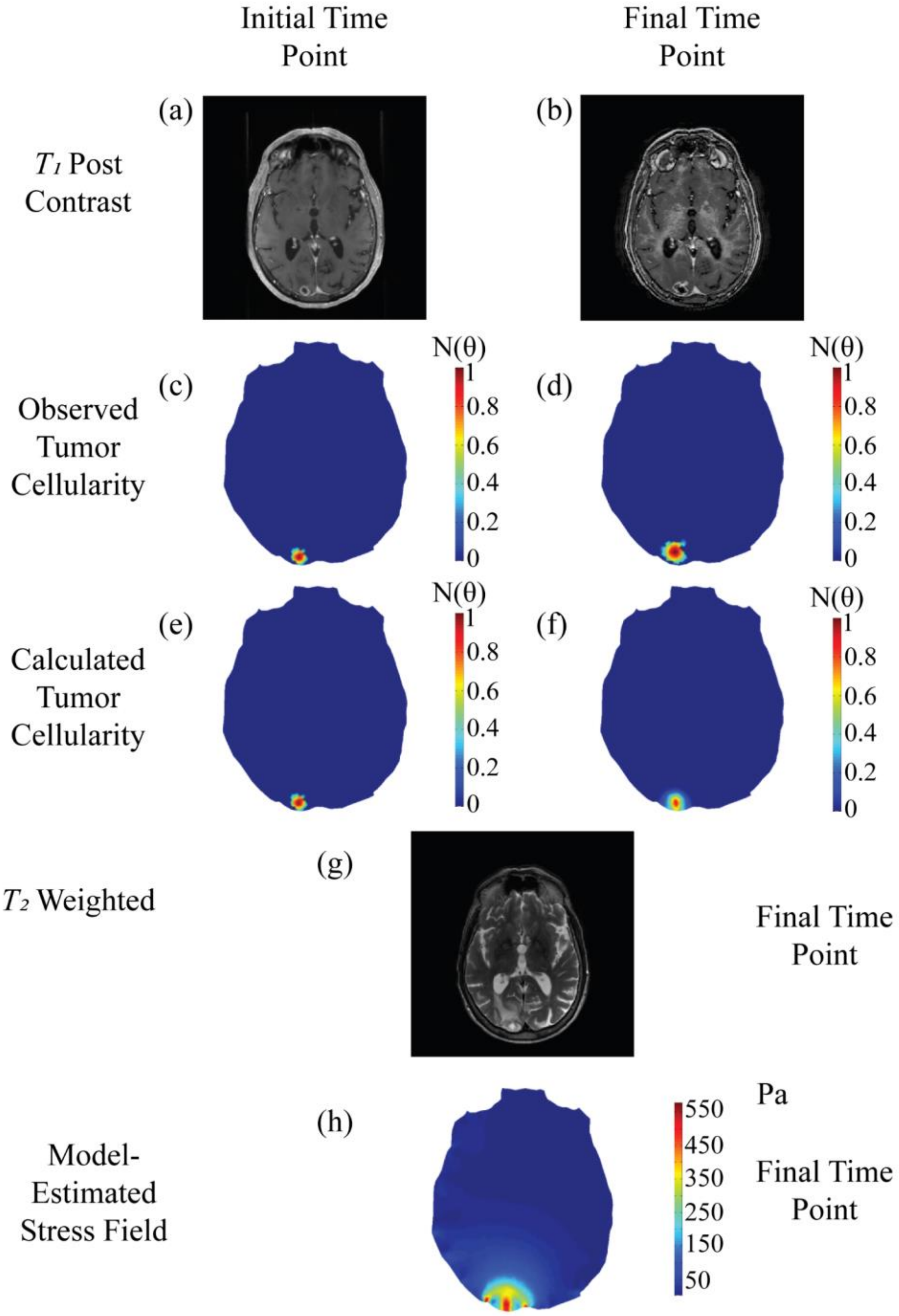

Figure V. 3: Patient diagnosed with radiation-induced necrosis at starting time point (a,c,e), and final time point taken before diagnosis of lesion etiology (b,d,f,g). Post-contrast T_1-weighted MR images (a,b) are used to estimate observed tumor cellularity (c,d) and the model is fit to estimate tumor cellularity (e,f). T_2-weighted imaging at the time point prior to diagnosis (g) is compared to estimated mechanical stress field (h) at the final time point.

criteria are met. These criteria include: (1) if the absolute objective function value is less than 1e-4, (2) the relative change in the objective function between iterations is less than 1e-4, (3) a maximum of 500 iterations occur, or (4) a maximum of 1000 function evaluations occur. In analysis not shown, these proved robust. These are appropriate since we treat all lesions as recurrent tumors (Equations (V.1-3)) with estimated parameter set differences guiding diagnosis. We assume model parameters are homogenous over the lesion.

V.2.2.4 Model-Derived Measures

Based on estimates of patient-specific model parameters, von Mises stress field due to tumor growth at the final time point is estimated by our mechanically-coupled reaction-diffusion model (Figure V.1). Model-derived measures were calculated to compare observed edema to model-estimated stress field. This originates from our previous work, coupling mechanical effects from the surrounding tissue extracellular matrix to tumor growth models [98]. Here, von Mises stress is used to describe tissue loading due to lesion growth [98]. We hypothesize tissue loading represents an edema-causative event due to restricted diffusivity in areas with higher stress similar to previous work [76]. We investigate the relationship between observed edema and model-calculated von Mises stress fields as a model-derived measurement. We quantify edema using T_2-weighted or FLAIR images (based on availability) from the last time point prior to diagnosis. The T_2-weighted or FLAIR scan is rigidly registered to T_1-weighted contrast-enhanced images. Then the enhancing region, associated with edema, is manually segmented. The choice to use manual segmentation in our methodology was based on the heterogeneous nature of clinically-acquired imaging data as well as the patient lesions and edema. Therefore, manual segmentation provided the most robust representation of the regions of interest. We quantify regional similarity between edema location and model-estimated stress field using the Dice similarity index. We designate five isocontours from low stress to high stress at 100, 200, 300, 400, and 500 Pa of the model-estimated stress field and calculated the Dice index of the segmented edematous region and each mechanical stress isocontour, denoted as Dice_{100}, Dice_{200}, Dice_{300}, Dice_{400}, and Dice_{500}, respectively.

V.2.2.5 Morphometric Analysis Methods

We evaluated other diagnostic radiologic metrics based on image morphometric analysis, including some used in clinical treatment, to compare our methodology to conventional radiologic assessments. We evaluated the ratio of lesion size in T_2 imaging to lesion size in T_1 imaging [137]. We performed this by taking the ratio of the edema area (T_2-weighted or FLAIR MR imaging) to the lesion area (T_1-weighted MR imaging). As proposed by the Response Assessment in Neuro-Oncology Brain Metastasis working group, we evaluated the change in the lesion's longest diameter [138]. We calculated longitudinal change in maximum lesion length from outlined lesions of T_1-weighted images at both time points as percent change from baseline. We performed morphometric analysis evaluating the segmented lesion area and lesion perimeter using the same central axial slice that was used to perform modeling analysis. Finally, we manually segmented the full three-dimensional (3D) lesion ROI in each image for full volume and surface area morphometric analysis. Full 3D morphometric analysis represents additional data not analyzed under our current 2D framework, extracting additional information from the images. While our work herein compares our analysis to conventional morphometric metrics, it is important to note that this is a limited comparison. These selected conventional analysis metrics represent a good initial evaluation comparison, but other geometric and texture-based metrics are certainly possible. More extensive comparisons to other types of analysis metrics are warranted in future studies with larger cohorts. Morphometric analysis was performed for both T_1-weighted and FLAIR images, with T_1-weighted lesions evaluated as the percent change between the two time points. These measurements are designated as T_1 Surface Area, T_1 Volume, FLAIR Surface Area, and FLAIR Volume.

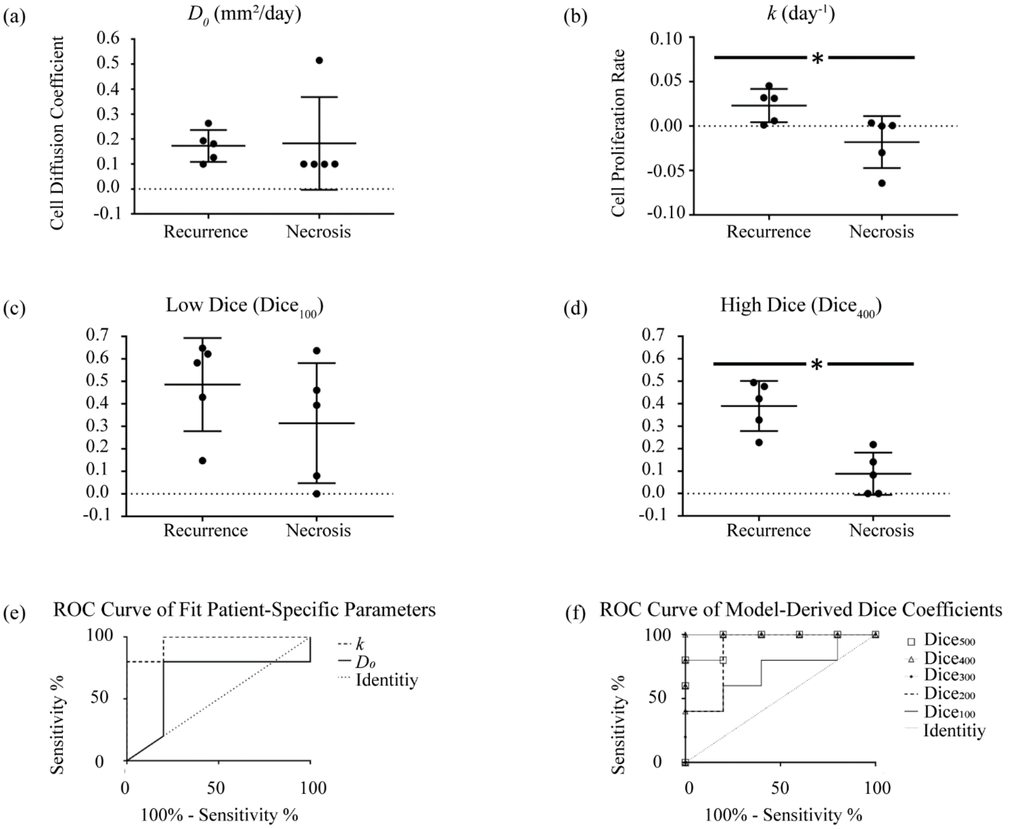

Figure V. 4: Distribution plots for (a) cell diffusion coefficient (D_0, mm^2/day), (b) cell proliferation rate (k, day^{-1}), (c) low stress isocontour Dice coefficient (Dice$_{100}$), and (d) high stress isocontour Dice coefficient (Dice$_{400}$) for patients with tumor recurrence and radiation-induced necrosis. The middle horizontal line in both represents the mean value; the outer two lines represent the standard deviations. The ROC curve for (e) cell diffusion coefficient (D_0) and cell proliferation rate (k) and (f) ROC curve for the Dice correlation coefficients. In both, the dotted line represents the line of identity.

V.2.3 Results

Patient-specific model parameters and model-derived measures are calculated using our biomechanically-coupled tumor growth model fit to serial patient-specific imaging data. D_0 and k are obtained by fitting the tumor growth model to the pairs of longitudinal T_1-weighted post contrast images. Dice_{100}, Dice_{200}, Dice_{300}, Dice_{400}, and Dice_{500} are the Dice indices between isocontours of model-estimated stress-field and the segmented edematous region. Examples of the framework execution are in Figure V.2 and Figure V.3.

Table V. 1: Statistical tests of patient-specific model parameters, model-derived measures, and morphometric analysis. (*) denotes statistical significance of $p<0.05$.

Metric	**Statistical Tests**	
	Mann – Whitney *U* Test P Values	**ROC Area Under Curve (AUC)**
D_0	0.4603	0.66
k	0.0159*	0.96
Dice_{100}	0.3095	0.72
Dice_{200}	0.0556	0.88
Dice_{300}	0.0079*	1.00
Dice_{400}	0.0079*	1.00
Dice_{500}	0.0159*	0.96
T_1 Area	0.3095	0.72
T_1 Perimeter	0.0952	0.84
T_1 Surface Area	0.6905	0.60
T_1 Volume	0.4206	0.68
FLAIR Area	0.2222	0.76
FLAIR Surface Area	0.8413	0.56
FLAIR Volume	0.8413	0.56
T_2/T_1 Ratio	0.4206	0.68
% Change Length	0.4206	0.68

Distribution of patient-specific model parameters are in Figure V.4a and Figure V.4b, reflecting an evident distinction in proliferation rate. Examples of low and high Dice values, in Figure V.4c and Figure

V.4d, respectively, indicate a distribution difference in the high Dice value. Using the Mann-Whitney *U* Test, we obtained the results in Table V.1. In agreement with Figure V.4a-d, k, Dice$_{300}$, Dice$_{400}$, and Dice$_{500}$ are statistically significantly different with P values of 0.0159, 0.0079, 0.0079, and 0.0159, respectively. We plotted a receiver operating characteristic curve (ROC curve) for model parameters in Figure V.4e and model-derived measures in Figure V.4f. From Figure V.4e-f, we see k and multiple high Dice indexes can classify etiologies. This is verified by observing areas under the ROC curves (Table V.1).

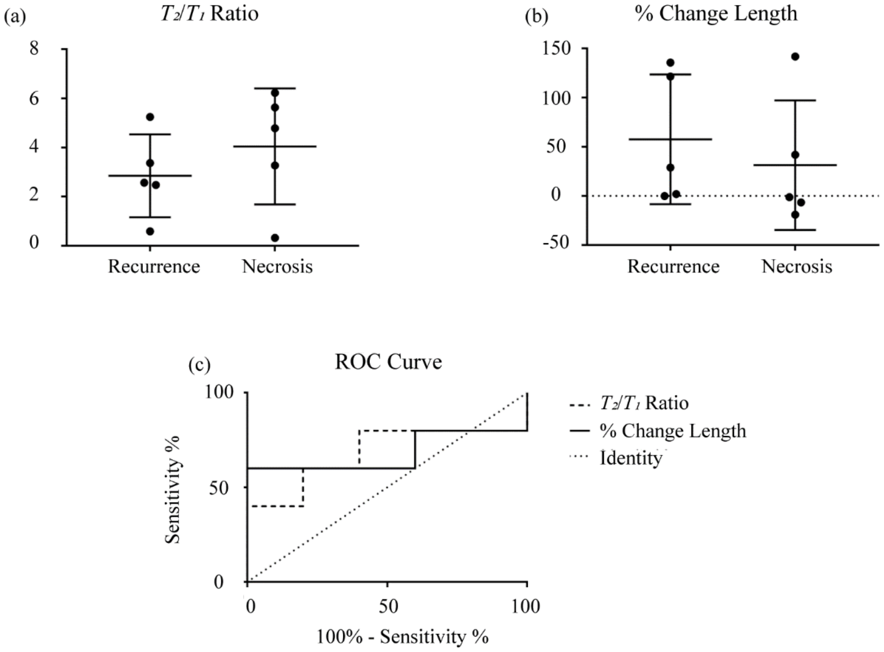

Figure V. 5: Conventional morphometric assessment methods for determining local control with estimated parameter value distributions for (a) T_2/T_1 ratio and (b) percent change in length. (c) ROC curve for the morphometric assessment methods. The dotted line represents the line of identity.

Conventional metrics of T_2/T_1 ratio and percent change in length are in Figure V.5a-c. We found a lack of diagnostic performance in differentiating etiologies using conventional morphometric analysis, with ROC AUC for T_2/T_1 ratio and percent change in length of 0.68 and 0.68, respectively, and no statistical significance between etiologies. Shown in Table V.1, we further assessed input imaging data by analyzing morphometric data in both 2D central slice analysis and 3D full volumetric analysis from segmented lesions. We assessed 2D change in lesion area and perimeter between T_1-weighted scans as well as the lesion area in FLAIR. We assessed 3D change in lesion volume and surface area between T_1-weighted scans as well as lesion volume and surface area in FLAIR. The poor performance of conventional image analysis metrics is highlighted by no statistically significant metrics being found.

V.2.4 Discussion

We present a framework to estimate patient-specific model parameters and model-derived measures based on non-invasive MRI data from patients with brain metastasis treated with SRS. Parameterizing the biophysics of lesion growth could accurately differentiate lesions based on differences in estimated parameters with up to 100% accuracy in our preliminary, initial patient cohort. We compared our modeling results to conventional analysis methods. Our methodology outperformed conventional methods using the same input data, or less input data in the case of 3D image morphometry. It is evident that k and Dice indexes associated with higher stress von Mises isocontours can differentiate etiologies (Table V.1). The Dice metrics (Figure V.4c-d) are not independent observations. When estimating D_0 and k, our model is fit to 'observed tumor cellularity'. Based on these fit parameters, the von Mises stress distribution was calculated and compared to observed edema. Therefore our Dice metrics represent linked discriminators permitting mechanistic statistical comparison to additional data. As the von Mises stress isocontour is changed, the statistical relationship with edema is changed, which is why a range of isocontours were compared. Our biophysical model enables proliferative differences to be compared in novel ways capable of accurately differentiating the etiologies.

Speaking to limitations, we used T_2-weighted and FLAIR imaging interchangeably to indicate edema. Visual confirmation in Figure V.2g and Figure V.3g, as well as the Dice indexes differentiating the etiologies, indicate our use of imaging data is reasonable. Next, the brain's heterogeneity has been incorporated into other tumor growth models [17]. We treated the brain as homogeneous isotropic tissue. In future studies, we intend to increase model specificity by incorporating heterogeneity and anisotropy. Mechanical heterogeneity will result in a spatially varying distribution of mechanical properties throughout tissue types (shear modulus and Poisson's ratio in Equation (V.3)). Anisotropy will increase the number of material parameters used to describe the mechanical constitutive behavior in Equation (V.3). Since biomechanical coupling enables the surrounding brain tissue to impact the tumor's growth, including heterogeneity and anisotropy will manifest in changes to diffusion via the von Mises stress term in Equation (V.2) [91]. We treated patient-specific model parameters as homogeneous within the lesion. Our current imaging data constrains us to a global estimate of lesion properties, restricting our classification as entirely tumor recurrence or radiation-induced necrosis. Biopsies can consist of both recurrence and necrosis [126]. We will address this with additional sources of quantitative imaging to increase specificity. Previously, in other related research we used diffusion weighted MRI (DW-MRI) to estimate tumor cell density [98, 133, 134]. In future work, we will acquire DW-MRI data that would provide improved estimates of tumor cell density from patient scans. Using DW-MRI, which is a studied surrogate used for estimating tumor cellularity, will result in more accurate estimates of cellular distribution within the patients' lesion. This will not change the mathematical expression (Equations V.1-3), but rather specifically change the spatial variation of $N(\bar{x}, t)$ defined at imaging times. This will result in the inverse problem being driven by more accurate estimations of 'observed tumor cellularity' measurements, but will not change the number of parameters being estimated. Despite this, the standard-of-care clinical treatment is a binary diagnosis: no tumor recurrence or partial recurrence. Our framework accomplishes a similar binary classification, making this clinically-relevant and amenable to current clinical diagnostic workflows. Given the heterogeneous nature of clinically-acquired scans, manual segmentation was used rather than automated segmentation to prevent inaccuracy due to non-uniform intensities across patients and scan time points. In work not shown here, a separate blinded observer performed the same experimental analysis methods on the same patient imaging data (Table V.2). Comparing the Mann Whitney P Values and ROC AUC values for the patient-specific model parameters and model-derived measures reflected the same trends obtained in this manuscript with average difference in ROC areas under the curve for all metrics of 5% and largest difference of 13% (Table V.2). This investigation was performed in 2D; moving forward we will investigate these biophysical model-based parameters in 3D to capture volumetric changes, similar to our previous work [98]. The transition from 2D to 3D is nontrivial but tractable. The results of this 2D investigation indicate a 3D formulation of this framework has the potential to further enhance the noninvasive differentiation between the two etiologies. Furthermore, this preliminary investigation involved a total of 10 patients. For validation, the framework will need to be tested in a larger patient cohort. Finally, the use of edema from T_2-weighted and FLAIR imaging was incorporated as an external model-derived feature comparison. It would be interesting to include this data by extending our biomechanical model to include biphasic components that explicitly model the generation of edema from elevated intracranial pressure during tumor expansion, similar to modeling of capillary exchange in other work [76].

We identified a biophysical model-based approach to differentiate between the etiologies, whereas traditional image morphometric assessment of the same data was not capable of accurate identification. Patient-specific geometries varied depending on lesion location (Figure V.2, Figure V.3). Despite this, our framework accurately predicted etiology. There is an intuitive aspect to the parameters which differentiate the etiologies. There was no statistical difference between diffusion coefficients, suggesting diffusion is conserved between etiologies. There is a statistical difference in tumor proliferation rates. This is consistent with radiation-induced necrosis not being expected to proliferate. Recurrent tumors have model-estimated mechanical stress fields with significant correlation with the measured edema. We hypothesize this is the result of mechanical stress having a causative edema generation effect associated with recurrent tumor. The success of using patient-specific image-data-driven biophysical modeling to differentiate between both etiologies in patients with brain metastasis treated with SRS shows substantial promise. This is a limited sample size analysis and a larger cohort study is required. The temporal sampling was chosen just prior to diagnosis, but studying the framework's performance at earlier time points is desirable.

V.2.5 Conclusions

Results of this study indicate our image-data-driven biophysical model-based analysis framework for estimating patient-specific model parameters and model-derived measures has potential to noninvasively differentiate between radiation-induced necrosis and tumor recurrence. We only used standard-of-care imaging scans from the patients' clinical care, furthering the work's impact. If confirmed, our framework could be used in current clinical workflows to improve diagnosis. It is important to note that results of this investigation are preliminary given the limited number of patients used in this initial investigation. Confirmation of this framework will be needed with a larger patient cohort and further patient statistics. Furthermore, we restricted analysis to metastatic disease, but radiation-induced necrosis is also found in patients with primary intracranial disease who have undergone SRS [41], making this methodology applicable in patients with primary brain tumors. Our investigation demonstrates the potential of noninvasive differentiation of lesions of unknown etiology in patients who have undergone SRS by means of image-data-driven biophysical modeling.

Funding

This work is supported by the National Institutes of Health-National Institute of Neurological Disorders and Stroke R01NS049251; the National Institutes of Health-National Cancer Institute K25CA204599, P30CA012197; National Science Foundation Research Experiences for Undergraduates 1559700; and the VISE Seed Grant Program.

V.2.6 Supplemental Material: Sensitivity to Manual Segmentation

Given the highly heterogeneous nature of the clinically-acquired scans, manual segmentation was utilized versus an automated segmentation method that may be biased by non-uniform intensities across patients and scan time points. To assess the influence of manual segmentation, another observer associated with this manuscript performed the same analysis, blinded to both the segmentations and results from the initial observer's analysis. This second observer was provided with the same set of patient imaging data and performed the analysis from start to finish, independently of the original observer on a separate computer. The table below contains the results of both observers. On the left-hand side of the table are the results corresponding with Table V.1 of the manuscript. On the right-hand side are the results of the second observer who performed the analysis independently. Although the values are not identical, they are within close range and reflect similar trends in data with average difference in ROC areas under the curve for all metrics of 5% and largest difference at 13% (0.96 vs 0.84 for *k*). This segmentation sensitivity test indicates that manual segmentation did not significantly alter the results.

Table V. 2: Sensitivity to Manual Segmentation

	Mann Whitney P Values (Observer 1)	**ROC Area Under Curve (AUC) (Observer 1)**	**Mann Whitney P Values (Observer 2)**	**ROC Area Under Curve (AUC) (Observer 2)**
D_0	0.4603	0.66	0.5476	0.64
k	0.0159	0.96	0.0952	0.84
Dice_{100}	0.3095	0.72	0.2222	0.76
Dice_{200}	0.0556	0.88	0.0556	0.88
Dice_{300}	0.0079	1	0.317	0.92
Dice_{400}	0.0079	1	0.0079	1
Dice_{500}	0.0159	0.96	0.0079	1

CHAPTER VI

VI Quantifying Influence of Tumor Growth

VI.1 Summary and Contributions

The intent of this chapter was to evaluate the influence of quantifying tumor growth for application in image-guided neurosurgery by predicting intra-operative brain shifts that have resulted from the cavity collapse during tumor resection. Image-Guided Neurosurgical Systems (IGNS) are used during neurosurgical procedures in order to aid in tumor localization. IGNS treat patients' preoperative imaging as a static image which does not evolve as the surgery occurs. An established phenomenon which occurs during neurosurgery is brain shift, which can cause IGNS to become inaccurate. Brain shift can occur due to gravity, hyperosmotic drugs, cerebrospinal fluid loss, craniotomy extent, edema, and the resection of the tumor itself. While there has been extensive research into the mechanisms behind most of these causes of brain shift, to the best of our knowledge, no groups have developed a finite element model of tumor cavity collapse during tumor resection.

Building upon the works in Section IV.2 and V.2, the work in Section VI.2 investigates the influence of accounting for a space-occupying lesion within a brain. More specifically, the influence of using the developed model of tumor cavity collapse during resection was assessed with respect to predicting intraoperative brain shift. Three debulking atlases (central debulking, Gaussian debulking, and k-means debulking) were used to test this effect in a multimodal study of six patients that underwent intracranial tumor resection and in two simulations of intracranial tumor resections. While these atlases differed from one another in how the cellular distribution of the tumor was calculated, the physics dictating brain shift from tumor cavity collapse was common to all of the atlases.

To the best of our knowledge, this is a novel study accounting for influence of cavity collapse during tumor resection in brain shift predictions. It is also a novel description of cavity collapse during tumor resection. The central debulking atlas captured the global mass-effects from the tumor and its associated edema. The other two debulking atlases also accomplished improved brain shift predictions as compared to standard brain shift models that do not account for debulking. Section VI.2 presents the developed mathematical representation of intraoperative tumor cavity collapse. Both the patient and simulation studies indicated that the proposed mathematical representation could estimate and correct for brain shift due to cavity collapse from resection. These displacements have been extremely challenging to capture in previous finite element studies for brain shift correction. Moreover, this mechanism was corrected with patient data collected at multiple sites with multiple modalities (laser range scanner, intraoperative MR, and intraoperative ultrasound), speaking to the robustness of the proposed method.

VI.2 Accounting for Intraoperative Brain Shift Ascribable to Cavity Collapse during Intracranial Tumor Resection

Abstract

For many patients with intracranial tumors accurate surgical resection is a mainstay of their treatment paradigm. During surgical resection, image-guidance is used to aid in localization and resection. Brain shift, which occurs intraoperatively, can invalidate these guidance systems. One cause of intraoperative brain shift is cavity collapse due to tumor resection, which will be referred to as debulking within this manuscript. In this study, we develop a finite element model of debulking and evaluate the influence of predicting brain shift due to debulking for application in image-guided neurosurgery. We hypothesized that accounting for tumor debulking in an atlas framework would improve brain shift predictions. This was tested in two simulated intracranial tumor resections and six patient intracranial tumor resection intraoperative data sets. Three distinct atlases (central debulking, Gaussian debulking, and k-means debulking atlas) of debulking were constructed and employed to test the hypothesis. These atlases were compared to each other in their ability to account for brain shift and compared using statistical measures. Though all three proposed models of debulking were able to predict some aspects of debulking displacements, the central debulking method best captured global mass-effects resulting from the resected tumor and typically was often statistically the most appropriate model. These findings suggest brain shift predictions for use in image-guided neurosurgery could be improved by incorporating a finite element model of debulking, such as those developed in this work.

VI.2.1 Introduction

Between 2011 and 2015, approximately 121,277 malignant brain and other central nervous system tumors were diagnosed in the United States with a five year survival rate of 35.0% [21]. Initial treatment of accessible intracranial tumors is surgical resection. In a meta-analysis studying the extent of resection with patient survival in glioblastoma, the authors' concluded gross total resection of the tumor engendered the reduction of one and two year mortality [48]. Others have found that greater than 98% of a glioma's volume must be resected to provide maximal increased life expectancy [139], [4]. Accurate resection is also tied closely to tumor recurrence; 80% of recurrent glioblastomas recur within 2 cm of the original resection[49]. In low-grade gliomas, extent of resection is also a predictor of improved overall patient survival [50]. Therefore, optimal resection of intracranial tumors, regardless of etiology, requires the accurate intraoperative localization of diseased brain tissue.

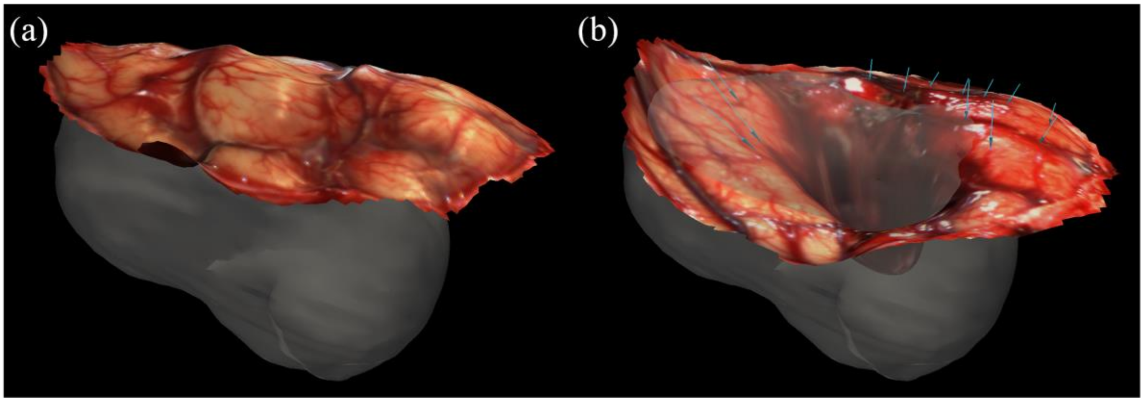

Figure VI. 1: This is an illustration of cavity collapse during tumor resection for Patient 1. The opaque shape in panels (a) and (b) is a visualization of the segmented tumor. In panel (a), the post-craniotomy, cranial surface can be visualized with the laser range scan obtained intra-operatively. The cranial surface was scanned again after the tumor was resected, and this laser range scan is shown in panel (b). The tissue movement was quantified using these scans, and the measured displacement vectors (pre- to intra–operative) are indicated by the blue arrows in panel (b).

Image-Guided Neurosurgical Systems (IGNS) are used during neurosurgery to aid in tumor localization and resection while minimally disturbing the surrounding healthy tissue [51], [52], [53]. Neuro-navigation involves registering preoperative imaging into intraoperative physical space to provide neurosurgeons guidance [53]. Unfortunately, IGNS is not always accurate. IGNS treat the patient's preoperative image as static and non-evolving with the events of surgery, which is not necessarily reflective of intraoperative changes to the neuroanatomy due to sources of error associated with brain shift [51], [52], [53].

Intraoperative brain shift can cause IGNS to inaccurately localize the patient's tumor by violating the assumed static relationship between image and physical space [52], [140]. When one considers that brain shifts up to 24 mm have been measured during tumor resection [141], the potential impact to the accuracy of IGNS is alarming. There are numerous causes of brain shift, including gravity, hyperosmotic drugs, loss of cerebrospinal fluid, removal of the tumor, edema, and extent of craniotomy [51], [52], [14], [13]. Multiple methods to compensate for brain shift intraoperatively have been researched including intraoperative magnetic resonance imaging (iMR), a finite element model (FEM) coupled with intraoperative measurements like laser range scanners (LRS) or stereo vision, and intraoperative ultrasound (iUS) [51], [139], [52], [142]. This manuscript focuses on brain shift correction using a FEM atlas based method that incorporates the effects of intraoperative cavity collapse [141], [76]. Extensive work has been done into modeling brain shift due to hyperosmotic drugs, swelling, gravity, retraction, and resection [64], [143], [144], [69]. However, to the best of our knowledge, no groups have developed a FEM of tumor cavity collapse during resection, despite evidence supporting its prominent impact on brain shift.

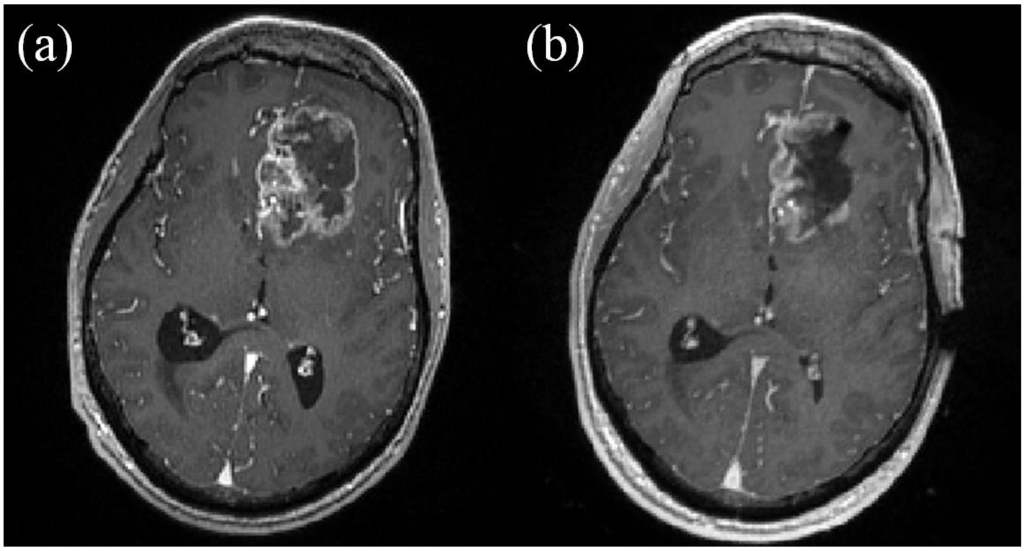

Figure VI. 2: This is an exemplar illustration of cavity collapse during tumor resection. The two T_1 weighted MRI scans were taken preoperatively (a) and intraoperatively (b). Both panels are an image of the same slice of the scan after the complete MRI volumes were registered. In panel (a) the total tumor can be visualized. In panel (b), the collapse in the tumor's original cavity can be perceived in this intraoperative, post-resection MRI.

Tumor cavity collapse has been observed and quantified by multiple groups [15], [77]. Intraoperative cavity collapsing was observed using iMR to quantify surface and subsurface brain shift that involved the resection cavity [145]. Comparing 41 patients' preoperative MRIs with their postoperative MRIs, the mean preoperative tumor volume was 14.23 cm^3 while the mean postoperative cavity volume was 8.53 cm^3 [146]. Another group compared preoperative and postoperative MRIs of 68 lesions and noted a decrease in postoperative cavity size related to the original tumor volume [147]. Additionally, several studies of intraoperative brain shift compensation using FEM have noted that measured displacements did have vector components toward the center of the tumor cavity, i.e. cavity collapse. Current methodologies are considerably limited in accommodating for this confounding factor in brain shift correction [14], [94], [11].

For the purposes of this manuscript, we will define 'debulking' as the process of brain shift specific to tumor cavity collapse due to the resection of the diseased tissue. The debulking mechanism can be seen in Figure VI.1 using LRS and Figure VI.2 using iMR. In Figure VI.1, the opaque region is the meshed patient tumor. The LRS surface immediately after the dura was opened is shown in Panel (a), and the LRS surface taken post resection is shown in Panel (b). The blue arrows are the displacement vectors measured using corresponding features in the LRS scans, and they demonstrate tumor cavity collapse. In Figure VI.2, the preoperative patient MR and iMR were registered to one another, and Panels (a) and (b) are corresponding slices. The boundary of the tumor can be visualized in Figure VI.2 Panel (a), and it qualitatively decreases in size during tumor resection, illustrating debulking, as shown in Figure VI.2 Panel (b).

Overall, extensive evidence supporting improved patient survival with improved extent of tumor resection [148] highlights the clinical need for accurate resection which could be improved by advanced models of brain shift. Compensating for brain shift would improve the fidelity of IGNS and effectively improve patient outcomes. In this investigation, we evaluate the influence of predicting brain shifts due to debulking for application in IGNS. We hypothesize that accounting for tumor debulking in an atlas framework will improve the brain shift predictions.

VI.2.2 Materials and Methods

VI.2.2.1 Retrospective Patient Selection

There were a total of 18 possible tumor resection cases in 18 distinct patients with intraoperative data considered in this study. All tumors were manually segmented and the measured intraoperative displacement vectors were registered into the same space. The methods of data collection will be elaborated on in the *Methods–Data Collection* section. Expanding upon prior work [141], [14], we proposed metrics to determine if debulking was present within the measured shift data. Additionally, in effort to reduce bias incurred by choice of selection criteria, four separate metrics were investigated.

For all cases at every intraoperative data measurement the 'debulk vector' was calculated. The 'debulk vector' is the unit vector between the start of the displacement measurement and the tumor centroid. The centroid was calculated by taking the average of the three-dimensional (3D) coordinates prescribing the outer contour of the segmented tumor per patient. The 'debulk vector' estimates the vector of pure tumor-centroid-cavity collapse. Method one (Equation (VI.1)) quantifies the amount of debulking by taking the mean of the normalized dot product of the measured displacement vector for each measurement (*n*) and the 'debulk vector' at each measurement (*n*). Method two (Equation (VI.2)) quantifies the amount of debulking by taking the mean of the dot product of the measured displacement vector for each measurement (*n*) and the ‘debulk vector’ at each measurement (*n*). Both methods one and two weight all measured points equally.

Methods three and four weight debulking motion closer to the tumor larger than measurements taken further away. Therefore, we generated a weighting scheme from 0.1 (to prevent measurement exclusion) to 1, where 0.1 was assigned to the largest distance to the centroid and 1 was assigned to the smallest distance to the centroid for a given patient. The weights of the remaining measurements points were calculated by normalizing the weights from 0.1 to 1 based on a given patient. Using this weighting schema, each measurement (*n*) had an associated weight based on its proximity to the tumor. Methods three (Equation (VI.3)) and four (Equation (VI.4)) are the weighted versions of methods one and two respectively. For each method type, a threshold was empirically selected to determine if the measured displacements per patient could be classified as debulking or not. This selection was based on the distribution of the values obtained within the sample population.

$$Method\ One\ = mean\left(\frac{\overrightarrow{measured\ displacement_n}\cdot debul\widehat{k\ ve}ctor_n}{\left\|\overrightarrow{measured\ displacement_n}\right\|}\right) \tag{VI.1}$$

$$Method\ Two = mean(\overrightarrow{measured\ displacement_n}\cdot debul\widehat{k\ ve}ctor_n) \tag{VI.2}$$

$$Method\ Three\ = mean\left(\left(\frac{\overrightarrow{measured\ displacement_n}\cdot debul\widehat{k\ ve}ctor_n}{\left\|\overrightarrow{measured\ displacement_n}\right\|}\right)(weight_n)\right) \tag{VI.3}$$

$$Method\ Four = mean\left(\left(\overrightarrow{measured\ displacement_n}\cdot debul\widehat{k\ ve}ctor_n\right)(weight_n)\right) \tag{VI.4}$$

VI.2.2.2 Simulation Study

Two possible instances of brain shift during neurosurgery were simulated and evaluated in the same manner as the patient data. The simulated cases were generated to account for brain shift resulting from gravity, hyperosmotic drugs, and debulking mechanisms. The two simulated cases were constructed such that the shifts in these simulated cases were not included within the atlases of brain shift used to reconstruct the brain shifts. The differences from the calculated atlases, elaborated on below, include the size of the craniotomy, the direction of gravity, the size of the tumor, the cellular distribution of the tumor, the initialization of tumor growth, resection cavity size, and cerebrospinal fluid level. Furthermore, the percent of brain shift due to gravity, hyperosmotic drugs, and debulking construction for both of these simulations were distinct from one another. The measured brain shifts from both simulations represented a mixture of craniotomy surface and subsurface measurements near the boundary of the tumor.

VI.2.2.3 Patient Data Collection

Using the debulking quantification methods described above, six patients were selected for this investigation. This will be elaborated on within *Results-Retrospective Patient Selection*. For the remainder of this manuscript, the cases will be referred to as Patients 1 through 6. The method of intraoperative data collection for the patients varied and included the use of LRS (Patients 1-3), iMR (Patient 4), and iUS (Patients 5-6). Preoperatively, the surgeons provided us with an estimate of the patients' head orientation during surgery and the approximate size and location of the craniotomy they would perform intraoperatively.

For Patients 1-3, intraoperative data was acquired using LRS. The patients were enrolled in a study at Vanderbilt University Medical Center and were consented in accordance with the Vanderbilt Institutional Review Board [15]. The preoperative MRI scans were collected as a part of standard clinical care [15]. Tracking of measurement instruments was accomplished intraoperatively using an optical tracking system (Polaris Spectra, Northern Digital Inc., Waterloo, ON, Canada) [15]. Intraoperatively, an optical tracking rigid body (Medtronic, Minneapolis, MN, USA), attached to the patient was used to obtain all of the collected data in the same coordinate frame [15]. An optically tracked LRS (Pathfinder Therapeutic Inc., Nashville, TN, USA) was used to obtain scans of the region of interest at two intraoperative time points: (i) after the initial opening of the dura (e.g. Figure VI.1 Panel a) and (ii) after resection of the tumor (e.g. Figure VI.1 Panel b) [15]. The measured brain shift was calculated by tracking homologous points in the pre- and post- resection LRS collected data.

Patient 4 had their preoperative MR data collected using an Ax T_1 MPRAGE sequence [94]. Patient 4 was consented for imaging in accordance with the Brigham and Women's Hospital Institutional Review Board [94]. The intraoperative iMR scanner was a 3T, wide bore MRI scanner (Siemens Magnetom Verio, Erlangen, Germany) [94]. The preoperative MR and iMR scans were rigidly registered to one another. Using Analyze 9.0 (AnalyzeDirect, Overland Park, Kansas) and 3D-Slicer [149], homologous surface and subsurface points were collected in both scans to quantify the brain shift [94].

Patients 5 and 6 had intraoperative data acquired using 3D iUS. The data was collected under the Institutional Review Board protocol at Brigham and Women's Hospital's Advanced Multimodality Imaged Guided Operating (AMIGO) suite [150]. Preoperatively, patient MRs were obtained in accordance with standard clinical care. Intraoperatively, iUS was collected using a 2D BK5000 cranial probe through the patients' craniotomy [95]. To construct the 3D iUS, the collected sequences of 2D ultrasound images were registered and combined as described in [150]. The 3D iUS data used in this investigation was collected at two time points: (i) after the dura was opened and (ii) after a maximal portion of the tumor had been resected [150]. Features were matched in pairs of iUS images manually and using a matched feature extraction method detailed in [151]. The brain shift was quantified using both the automatic and manual iUS data, pre- and post- resection automatic and manual iUS data.

VI.2.2.4 Segmentation and FEM Mesh Construction

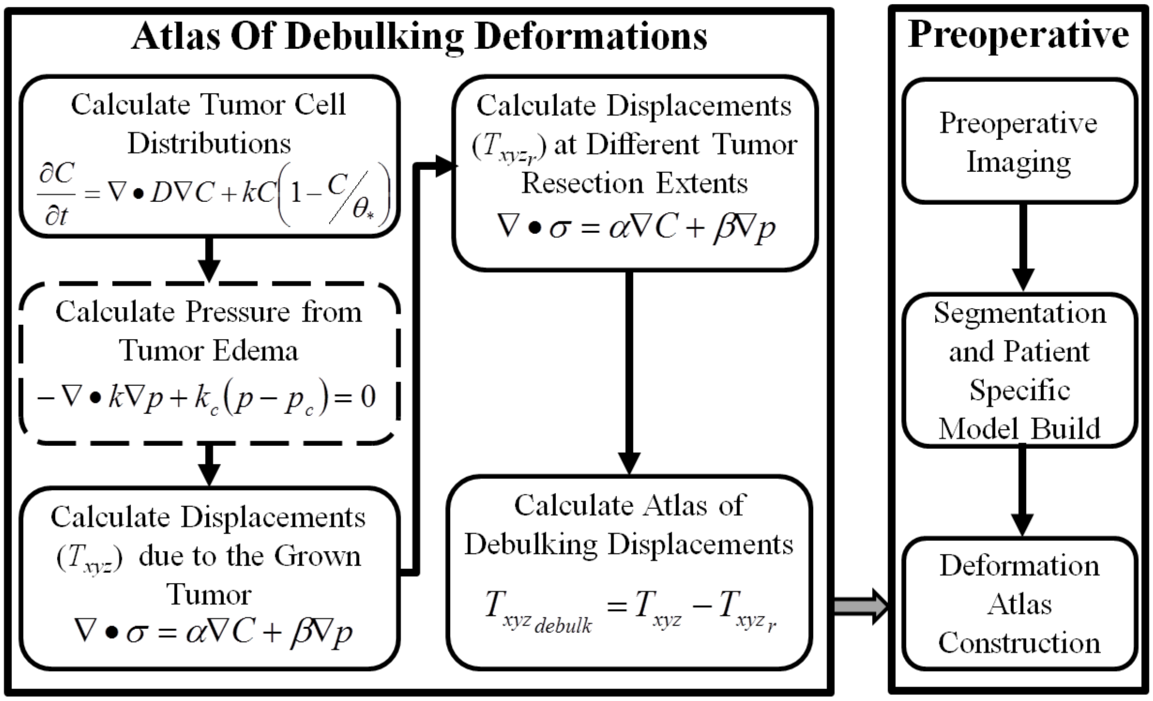

Figure VI. 3: This flow chart illustrates the general debulking brain shift prediction methods. The right hand side illustrates where the atlas of debulking deformations is introduced into the brain shift correction method. The left hand side is the flow chart of the physics of debulking as described in this manuscript. The dashed line around calculating pressure from the tumor edema illustrates that it is an optional step in calculating the physics of debulking.

All six patients were analyzed in the same manner. The brains and tumors were expertly segmented from the preoperative T_1 weighted MRI scans using ITK-Snap (www.itksnap.org). For the simulation cases, the brains were based on the segmentation of a patient case, while the tumors were specified to be spherical in shape. The segmentations for the simulations and patients were registered to an atlas image set using the adaptive bases algorithm and the normalized mutual information algorithm [136], [152]. A marching cubes algorithm was then used, followed by a custom mesh generator to create a 3D tetrahedral mesh [115]. The average number of nodes in the six patient meshes was 26,764, and the average number of elements was 134,393. This generated 6 patient-specific finite element meshes describing the six patients and their tumors, in addition to the simulation meshes.

VI.2.2.5 Brain Shift Atlas without Debulking

Atlases describing sources of brain shift other than debulking have been developed [64], [143]. In this work, we assume measured brain shift consists of debulking plus these previously studied factors. We tested our debulking mechanism retrospectively using a framework called model-updated image-guided neurosurgery (MUIGNS) [153]. MUIGNS uses sparse measurements of intraoperative brain shift in an inverse problem framework using patient-specific FEM solutions. These FEM solutions are calculated preoperatively and represent the possible intraoperative brain deformations [15]. The solution of the inverse problem is then used to deform the preoperative scans to correct for intraoperative brain shift.

In order to assess the influence of our proposed debulking atlas, we first performed brain shift corrections with a baseline brain shift FEM atlas, that has been extensively studied, that did not include debulking [64], [94]. This atlas accounts for gravity-induced, hyperosmotic drug-induced, and swelling-induced brain shift. Controlling variables were perturbed to generate a distribution of possible motion due to each category [94]. A poroelastic biomechanical FEM description of brain tissue is used which was based on Biot's theory of consolidation [97]. A detailed description of this biomechanical model can be found in [76] ,[64], [91]. A total of 378 possible deformations due to gravity, 378 possible deformations due to hyperosmotic drugs, and 9 possible deformations due to swelling of the brain comprise the 765 total possible deformation solutions in the brain shift atlas without debulking [94]. Next, we performed brain shift corrections with an FEM atlas that included debulking FEM solutions in the same patients and simulations.

VI.2.2.6 Physics of Debulking

In this investigation, we created three distinct atlases of debulking and hypothesized that our description of debulking could capture intraoperative cavity collapse elements of brain shift not captured in previous atlases. The principle difference among the three debulking atlases (central debulking atlas, Gaussian debulking atlas, and k-means debulking atlas) developed lies in the calculation of tumor cell distribution. The general physics used to calculate debulking is shared between the three atlas descriptions. The flowchart of our proposed physics is in Figure VI.3. For all patients and atlas reconstructions, the same patient-specific finite element meshes were used. To estimate debulking, the tumor cell distributions for the tumor is calculated. The seeding of the tumors can be visualized in Figure VI.4. In the central debulking atlas and k-means debulking atlas, this was computed using a custom finite element model of Equation (VI.5). In Equation (VI.5), C is the tumor cell concentration, t is time, k (0.08 day^{-1}) is the tumor cell proliferation rate, D (8×10^{-9} m^2/day) is the tumor cell diffusion rate, and θ_* (1.7678×10^{8}) is the cellular carrying capacity [98]. The Galerkin Method of Weighted Residuals is used to spatially integrate Equation (VI.5) in the 3D domain of tetrahedral elements [96] and temporal evolution is performed using a forward Euler explicit formulation.

$$\frac{\partial C}{\partial t} = \nabla \cdot D \nabla C + kC(1 - \frac{C}{\theta_*}) \qquad \text{(VI.5)}$$

The next step is calculating pressure based on an approximation of the tumor edema (Figure VI.3). This step is optional given the focus of our description of debulking centers around the mass-effect of the tumor. The edema step was only included in the central debulking atlas which sought to capture the entirety of the tumor's influence. Based on the distribution of tumor cells calculated, the elements associated with edema are defined. Since tumors often have leaky vasculature along their outer contours, we assumed that edema was present where the cellular concentration is between the contour lines of $0.15 \times \theta_*$ and $0.05 \times \theta_*$. The values of pressure were solved using Equation (VI.6). The Galerkin Method of Weighted Residuals was once again used in a custom built FEM model of Equation (VI.6) [96]. In Equation (VI.6), p is pressure, k (1×10^{-10} m^{3}s/kg) is hydraulic conductivity, k_c (1.15×10^{-8} m^{3}s/kg) is capillary permeability, and p_c (3633 Pa) is intracapillary pressure [64].

$$-\nabla \cdot k \nabla p + k_c(p - p_c) = 0 \qquad \text{(VI.6)}$$

Building upon a steady-state formulation of the poroelastic model and a biomechanically coupled model of tumor growth, Equation (VI.7) was used to account for the tumor and its edema (Figure VI.3) mechanical effects [154], [92]. An isotropic Hookean linear elastic constitutive model was assumed. The constant coefficients α (1×10^{-4}) and β (8.2×10^{-1} or 0) are empirically derived constants which dictate the amount of influence the tumor cells and edema have respectively [91]. Poisson's ratio is set to 0.45, and the Young's modulus is 2100 Pa based on previous work [91]. The Galerkin Method of Weighted Residuals was used to spatially integrate Equation (VI.7) [96], and a custom FEM model was generated to solve the equation. The displacements of the brain when the fully grown tumor was present were calculated with Equation (VI.7). Then, the displacements of the brain after the tumor was resected at variable extents is calculated (Figure VI.3). The resection of the tumor was accomplished by removing the model equation contributions associated with the resected tissue elements from the finite element matrix system [69].

$$\nabla \cdot \sigma = \alpha \nabla C + \beta \nabla p \qquad \text{(VI.7)}$$

The atlas of debulking solutions is calculated with Equation (VI.8) (Figure VI.3). In Equation (VI.8), $T_{xyz_{debulk}}$ is the brain shift displacement associated with debulking. T_{xyz} is the displacement when the entire tumor is present (preoperative state). T_{xyz_r} is the displacement when the tumor has been resected at different extents (intraoperative and postoperative states).

$$T_{xyz_{debulk}} = T_{xyz} - T_{xyz_r} \qquad \text{(VI.8)}$$

This description of debulking physics was applied to all three debulking atlases developed within this investigation. The debulking solutions were then incorporated into the atlas without debulking to account for this form of brain shift (Figure VI.3).

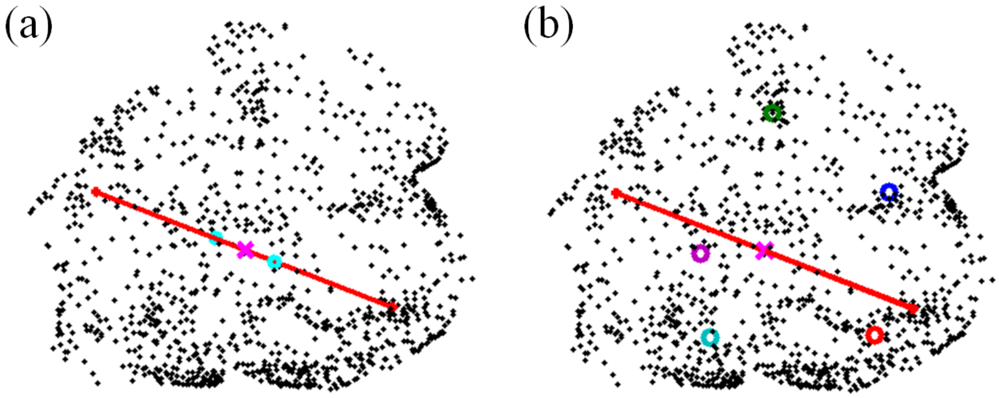

Figure VI. 4: This illustrates the differences in the center of the tumor seeds used for Patient 4. The black dots in both panels correspond with the segmented tumor boundary. The red line represents the longest axis in the tumor which passes closest to the centroid. The magenta ‘x’ in both panels marks the center of the longest axis. Panel (a) marks the relative positions of the three centers of the seeds for tumor growth for the central debulking and Gaussian debulking atlases with the magenta 'x' and the two cyan circles. Panel (b) marks the five centers of the seeds for tumor growth determined using k-means clustering with the five circles. Those five centers in addition to the magenta cross mark the six centers of tumor seeding used in the k-means debulking atlas.

VI.2.2.7 Brain Shift Atlas with Central Debulking

The central debulking atlas generates a total of 108 deformation solutions. The tumor is grown from three possible spatial locations (Figure VI.4 Panel (a)) and three temporal variations. The longest axis in the tumor that passes closest to the mathematical centroid of the tumor is calculated. The three spatial seed locations are: at the center of the longest axis, and +/- 10% of the longest axis from the center (Figure VI.4 Panel (a)). This was done to reflect radiographic practice of measuring the tumor along its longest axis [92]. The length of time the tumor grew was unknown, since no serial MRI was available. To calculate the unknown time final, while Equation (VI.5) was being solved, every five time steps the distance between the closest-point from the $0.05 \times \theta_*$ isocontour of the growing tumor to the segmented tumor contour was compared and stored. $TimeFinal$ was the time when the closest point distance is minimized. Once $TimeFinal$ was determined, three variants of this growing time were used to populate the temporal component of the atlas ($1.00 \times TimeFinal$, $0.85 \times TimeFinal$, $0.70 \times TimeFinal$). A total of nine tumor cell distributions were grown (3 different seeds grown to 3 different endpoints). With respect to boundary conditions for these models, the boundary condition was no flux across the dural septa and skull. Based on the cellular contours, the pressure from the edema was calculated for each of the nine tumors. Pressure values at the skull nodes were set to a fixed reference pressure of zero Pa.

With respect to the above tumor growth variants, each was considered with respect to three different craniotomy sizes, where one size corresponds with the surgeon's preoperative plan and the other two are smaller and larger than the planned size to accommodate variability in intraoperative execution. Of note, nodes associated with the craniotomies were considered stress free while the remainder of the skull nodes were fixed in displacement. In addition to the above variants, four possible resection extents were allowed when estimating the atlas of debulking. This was performed by allowing for elements within four possible isocontours ($0.05 \times$ max (cell count in solution), $0.2875 \times$ max (cell count in solution), $0.5250 \times$ max (cell count in solution), $0.7625 \times$ max (cell count in solution)) of the grown tumors being treated as resected tissue. Finally, the preoperative and postoperative displacements were subtracted from one another generating debulking atlas solutions. In summary, for the central debulking atlas a total of 108 solutions would entail the debulking atlas (3 different seeds x 3 different temporal evolutions x 3 different craniotomy spans x 4 different resection extents).

VI.2.2.8 Brain Shift Atlas with Gaussian Debulking

The Gaussian debulking atlas generates a total of 36 debulking solutions. It differs from the central debulking atlas in several significant ways. A Gaussian cellular distribution in the tumor is assumed. Using three seeds, three spatial Gaussian distributions of tumor cells are calculated. The seeds are on the longest axis in the tumor that passes closest to the centroid of the tumor. The locations are at the center of the axis and +/- 15% from the center (Figure VI.4 Panel (a)). It was specified that the tumor cell density decreases outwardly from the designated center with a minimum tumor cell density of $0.05 \times \theta_*$ at the maximal long dimension [93]. Since the focus of the debulking atlas is the mass effect, no pressure due to edema is calculated. The three possible displacements in presence of the three preoperative tumors were calculated with the same boundary conditions as the central debulking atlas (assumed 3 different craniotomy spans). In addition, similar to the previous atlas, 4 different resection extents are considered. As a result, a total of 36 solutions would entail the Gaussian debulking atlas (3 different Gaussian based distributions for tumor cell concentration x 3 different craniotomy spans x 4 different resection extents).

VI.2.2.9 Brain Shift with K-Means Debulking

The k-means debulking atlas generates a total of 72 debulking solutions. The tumor is grown from six spatial locations (Figure VI.4 Panel (b)). As in the first two debulking atlases, the first seed was centered at the center of the longest axis in the tumor that passes closest to the centroid of the tumor. This was done to account for highly asymmetric tumors. The five other seed centers (Figure VI.4 Panel (b)) were determined using a k-means clustering algorithm in MATLAB which identified 5 regional clusters within each of the segmented tumors (MathWorks Inc., Natick, Massachusetts). This was proposed to capture the asymmetries of patient tumors. Six unknown time finals were calculated for each of the six tumor seed centers using the same method previously described. Six possible tumors were grown with the same boundary conditions used in the central debulking atlas. The pressure due to edema was not included to prioritize the tumor mass effects. Six displacement distributions were calculated with boundary conditions similar to the above (nodes on the skull to be fixed, with stress free boundary conditions assumed within three different craniotomy spans). Again, four possible resection extents were calculated. As a result, a total of 72 solutions would entail k-means form of the debulking atlas (6 different distributions for tumor cell concentration based on k-means x 3 different craniotomy spans x 4 different resection extents).

VI.2.2.10 Brain Shift Reconstruction and Quantification

The displacements describing the movement between the preoperative and intraoperative features were used to drive the inverse problem for brain shift reconstruction. The reconstruction was performed for each patient and simulation using each of the four atlases (one without debulking and baseline with three debulking atlases). The optimization problem is a constrained minimization of a least-squared error between the model predicted displacements and the measured experimental displacements [14], [155]. The objective function is Equation (VI.9).

$$min\left\| Ma - u_{sparse} \right\|^2 \exists a_i \geq 0 \; and \; \sum_{i=1}^{m} a_i \leq 1 \qquad \text{(VI.9)}$$

In Equation (VI.9), a are the non-negative regression coefficients being solved. The inverse problem is constrained such that the a coefficients must be non-negative and their sum is less than or equal to one. M is a matrix containing the deformation atlas that is the dimensions of the number of measured displacements by the number of solutions within the given atlas [94]. In Equation (VI.9), u_{sparse} are the sparse measured displacements collected. Once the weighting coefficients are solved for they are used to combine the deformations of the atlas to reconstruct the displacements of the full patient brain. This brain shift reconstruction procedure was applied to all of the experiments performed.

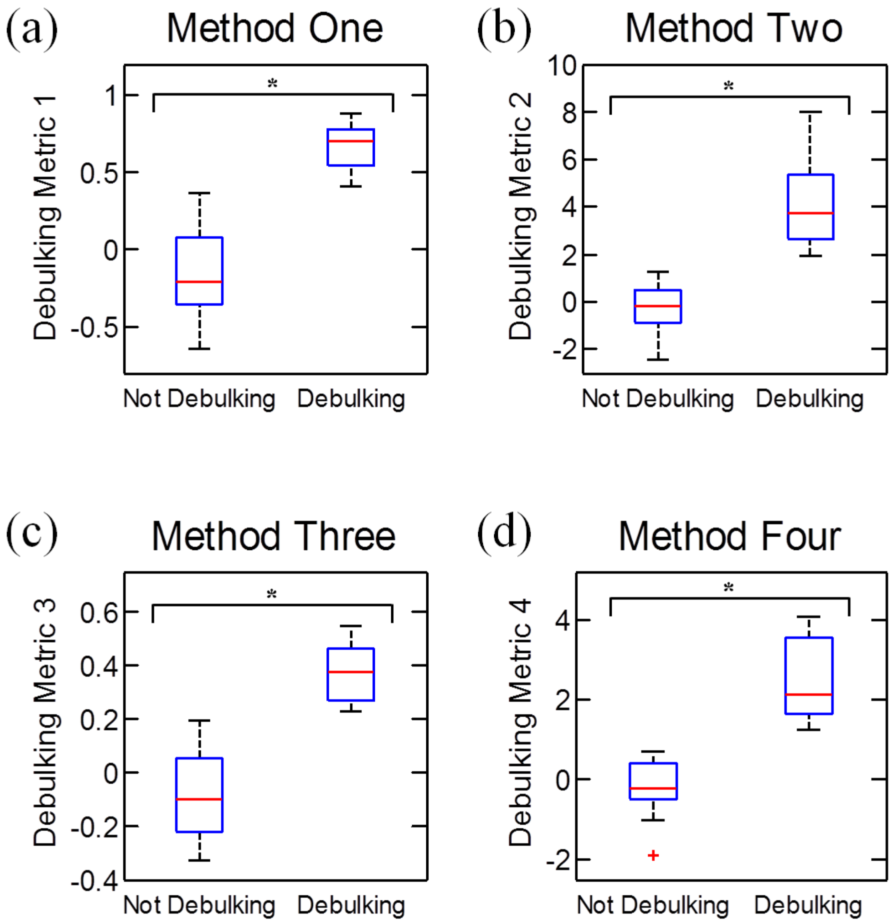

Figure VI. 5: These are the box plots representing sorting the patients into debulking or not debulking cases using the four methods described in *Materials and Methods-Retrospective Patient Selection*. In all of the panels the y-axis is the value obtained using each method. The box on the left hand side of each panel is the distribution of values below or equal to the threshold of the method (not debulking), and the right hand side is the distribution of values above the threshold (debulking). In all plots, the central red mark designates the median, and the bottom and top of the boxes are the 25th and 75th percentile respectively. Panels (a), (b), (c), and (d) are the results of methods one, two, three, and four respectively. (* indicates p<0.001)

The percent brain shift correction was calculated using Equation (VI.10) where $\overrightarrow{d_m}$ and $\overrightarrow{d_e}$ are the model estimated and experimentally measured displacements respectively [91]. For statistical testing, Equation (VI.11) was calculated on the ten largest measured displacements for each patient to assess the changes correction using the debulking atlases [91]. Since we could not assume normality of the values obtained from Equation (VI.11), we used a nonparametric test. Additionally, since the samples were not guaranteed to be independent, we used a two-sided Wilcoxon signed rank test to test statistical significance. It is important to note a difference in the calculation of percent correction and statistical significance between the simulation studies and patient analysis. For the simulation studies the data used to drive the inverse problem and the data used for validation were different. Since the shift was simulated, knowledge of the entire brain volume was available. For the patient studies, however, the data used to drive the inverse problem and the data for validation were the same. This was due to the limited intraoperative data available.

$$Percent\ Correction = 100\% \times \left[1 - \frac{mean(\|\overrightarrow{d_e} - \overrightarrow{d_m}\|)}{mean(\|\overrightarrow{d_e}\|)}\right] \tag{VI.10}$$

$$Correction\ per\ Measured\ Displacement = \left\|\overrightarrow{d_e} - \overrightarrow{d_m}\right\| \tag{VI.11}$$

Type of Atlas Correction	Average Error Mag. (mm)	Standard Deviation Error Mag. (mm)	Maximum Error Mag. (mm)	Percent Shift Correction (%)	AIC
SIMULATION 1					
No Correction	6.6725	4.0516	14.9767	N/A	N/A
Correction without Debulking	3.7738	3.1873	10.2869	32.2825	33.9275
Correction with Central Debulking	2.7893	2.6637	8.1972	51.4103	20.6757
Correction with Gaussian Debulking	2.5545	3.0030	10.3376	43.0032	32.7151
Correction with K-Means Debulking	2.9501	2.8270	9.4272	47.2144	24.0010
SIMULATION 2					
No Correction	2.1413	0.8011	4.0594	N/A	N/A
Correction without Debulking	0.6575	0.5736	2.1196	54.3190	-41.4662
Correction with Central Debulking	0.3055	0.2876	1.3354	73.7529	-62.6820
Correction with Gaussian Debulking	0.5175	0.5611	2.6081	61.1339	-41.6530
Correction with K-Means Debulking	0.4902	0.4813	1.5867	65.1286	-51.8254

Table VI. 1: This contains a summary of the shift correction of the measured points in the two simulations in the four types of atlas corrections performed. Magnitude is abbreviated with mag..

Since the number of coefficients and observed displacements varied between each patient and atlas type, another statistical test was used to test the quality of the results. This test is the Akaike Information Criteria (AIC) which reflects the balance between how well a model fits the data and number of coefficients being fit [156]. The equation used to calculate AIC is (VI.12). In this equation, *RSS* is the residual sum of squares, n is the number of measured displacements, and k is the number of parameters which is the number of solutions in a given atlas [156].

$$AIC_c = 2k + nln\left(\frac{RSS}{n}\right) + \frac{2k(k+1)}{n-k-1} \tag{VI.12}$$

VI.2.3 Results

VI.2.3.1 Retrospective Patient Selection

All four methods to quantify debulking were applied successfully to the 18 patients. The results are summarized in Figure VI.5. Cases larger than the selected threshold were considered to be debulking cases. Qualitatively, Figure VI.5 reflects that the four methods resulted in the classification of patient cases. The values in the two groups generated (debulking and not debulking) were compared to one another using a two-sided Wilcoxon rank sum test. All four of the tests indicated that the groups created were different from one another (p<0.001, two-sided Wilcoxon rank sum). Furthermore, the same six patients were identified as debulking cases using all four sorting methods. The six identified patients were used in this investigation to test our proposed physics of debulking.

Type of Atlas Correction	Gravity Atlas Solutions (%)	Hyperosmotic Drug Atlas Solutions (%)	Swelling Atlas Solutions (%)	Debulking Atlas Solutions (%)
SIMULATION 1				
Correction without Debulking	26.9061	51.5351	21.5597	0.0000
Correction with Central Debulking	0.0000	14.3942	0.0000	85.6079
Correction with Gaussian Debulking	0.0000	32.5795	0.0000	67.4220
Correction with K-Means Debulking	0.0000	15.4552	0.0000	84.5475
SIMULATION 2				
Correction without Debulking	89.7593	4.8914	5.1422	0.0000
Correction with Central Debulking	72.0720	3.3902	13.1517	11.3862
Correction with Gaussian Debulking	73.1607	2.9135	2.5871	21.3387
Correction with K-Means Debulking	33.6301	4.8188	31.6673	29.8839

Table VI. 2: This contains a summary of the brain shift categories used to reconstruct the two simulation measured displacements based on atlas type.

VI.2.3.2 Brain Shift Atlas with Central Debulking

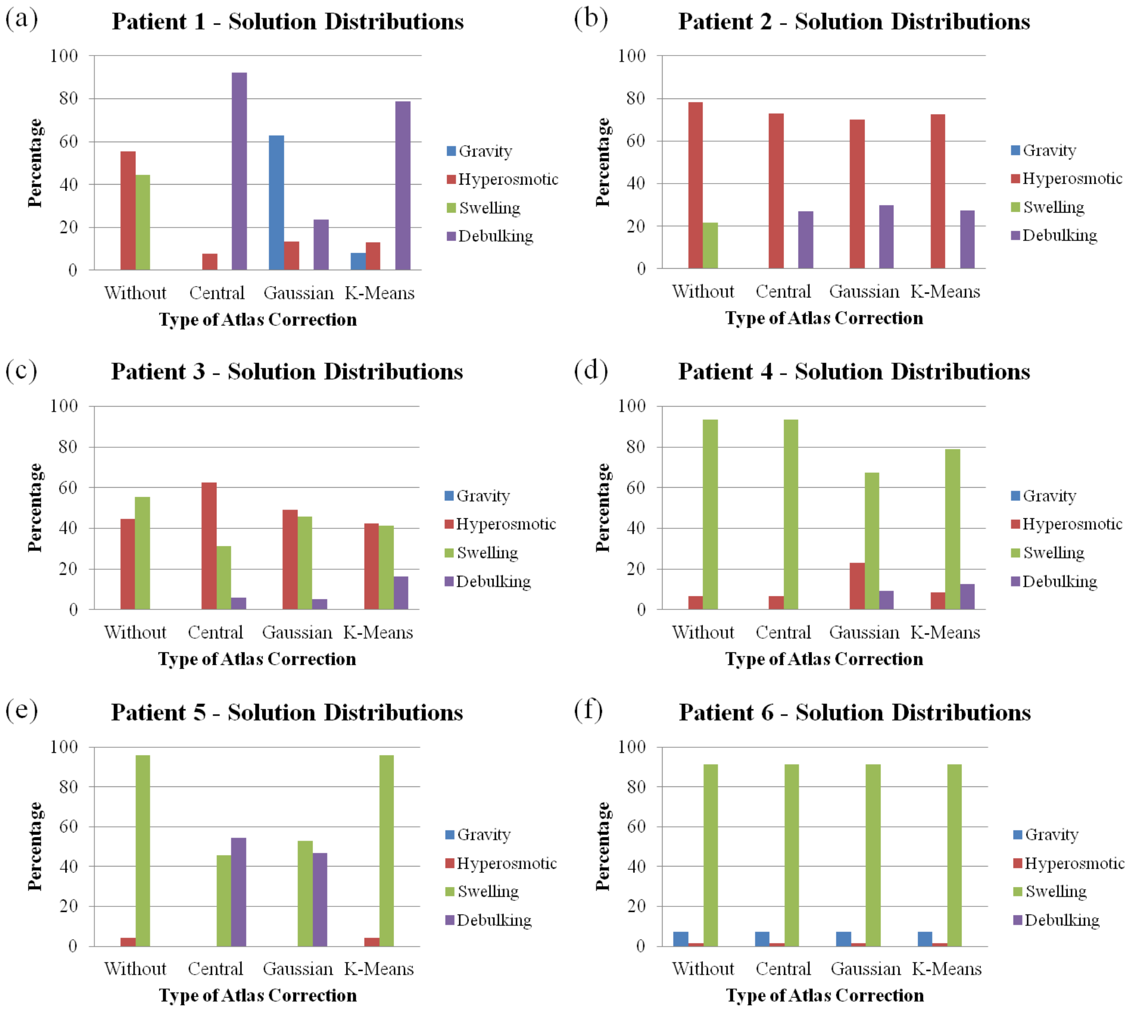

Figure VI. 6: This illustrates the brain shift categories used to reconstruct the patients' measured displacements based on atlas type. The four general shift categories are gravity, hyperosmotic, swelling, and debulking. In all six panels, 'without' refers to the atlas without debulking solutions present. 'Central' refers to the atlas with the central debulking solutions present. 'Gaussian' refers to the atlas with the Gaussian debulking solutions present, and 'K-Means' refers to the atlas with the k-means debulking solutions present. It is enforced that the sum of the weighting coefficients of the solutions is equal to 1, so the percent of the four categories in every reconstruction sums to 100%. Panels (a)-(f) contain the distributions of Patients 1-6 respectively.

The results of the central debulking atlas are in Figure VI.6 and Tables VI.1 through VI.3. Figure VI.6 visualizes the types of brain shift solutions used in order to reconstruct the six patients' measurements using the four atlases. The types of brain shifts included were shifts from gravity, hyperosmotic drugs, swelling, and debulking. Qualitatively, from Figure VI.6, we can see that the central debulking atlas was used in four of the six patients. In these four patients (Patients 1, 2, 3, and 5), the inclusion of the central debulking atlas

Type of Atlas Correction	Average Error Mag. (mm)	Standard Deviation Error Mag. (mm)	Maximum Error Mag. (mm)	Percent Shift Correction (%)	AIC
PATIENT 1					
No Correction	4.8224	4.5190	14.0973	N/A	N/A
Correction without Debulking	3.1000	2.4309	8.4744	21.5949	11.9961
Correction with Central Debulking	2.9706	2.3720	8.1758	24.9839	10.6059
Correction with Gaussian Debulking	2.9793	2.3393	8.3450	24.2852	11.3085
Correction with K-Means Debulking	2.4699	1.7428	6.5798	31.0743	7.8390
PATIENT 2					
No Correction	19.9444	4.6933	28.5180	N/A	N/A
Correction without Debulking	0.6942	0.5150	1.7243	88.8478	-3.8821
Correction with Central Debulking	0.5404	0.4755	1.5240	89.2693	-4.6655
Correction with Gaussian Debulking	0.4893	0.4272	1.4694	89.5963	-5.7156
Correction with K-Means Debulking	0.4570	0.4152	1.3963	89.5447	-5.4570
PATIENT 3					
No Correction	7.6969	4.8462	22.8068	N/A	N/A
Correction without Debulking	1.0839	1.2951	5.2778	71.3358	-3.9421
Correction with Central Debulking	0.9230	0.8880	3.4921	74.5653	-10.9028
Correction with Gaussian Debulking	0.9790	1.1361	4.6194	72.9721	-7.4554
Correction with K-Means Debulking	1.2793	0.9651	4.0994	71.5920	-5.4953
PATIENT 4					
No Correction	3.7315	1.2455	6.7744	N/A	N/A
Correction without Debulking	1.2321	0.8990	3.8120	46.1244	-12.9672
Correction with Central Debulking	1.2321	0.8990	3.8120	46.1244	-12.7250
Correction with Gaussian Debulking	1.2114	0.8368	3.6961	47.0835	-13.6142
Correction with K-Means Debulking	1.2330	0.8973	3.7870	46.2296	-12.8321
PATIENT 5					
No Correction	8.4734	3.8903	15.7143	N/A	N/A
Correction without Debulking	6.1961	3.6876	13.5151	16.3892	31.6143
Correction with Central Debulking	5.1377	3.6994	12.9074	28.3421	28.8014
Correction with Gaussian Debulking	5.0334	3.9198	13.0338	27.9897	29.2652
Correction with K-Means Debulking	6.1961	3.6876	13.5151	16.3892	31.6632
PATIENT 6					
No Correction	3.0291	1.0201	5.1239	N/A	N/A
Correction without Debulking	1.1672	0.9569	3.2302	37.3371	-14.0157
Correction with Central Debulking	1.1672	0.9569	3.2302	37.3371	-13.8266
Correction with Gaussian Debulking	1.1672	0.9569	3.2302	37.3371	-13.9468
Correction with K-Means Debulking	1.1672	0.9569	3.2302	37.3371	-13.8840

Table VI. 3: This contains a summary of the shift correction of the measured points in all six patients in the four types of atlas corrections performed. Magnitude is abbreviated with mag..

changed the distribution of the other three shift categories relative to the reconstructions without debulking atlas. This behavior is also seen in Table VI.2, which summarizes the distributions for the two simulations, where the central debulking atlas was used in both simulations. When observing the percent shift correction for the simulations (Table VI.1), there was a marked improvement relative to when the solutions were not included. There was also a decrease in the average error magnitude, standard deviation of error, and maximum error magnitude. Table VI.3 shows an improvement in the percent shift correction relative to when these solutions are not included along with a decrease in the average error magnitude and the magnitude of the maximum error in the four patients.

The Wilcoxon signed rank test revealed statistically significant differences between the correction per measured displacement (Equation (VI.11)) in the reconstruction without debulking and the reconstruction with the central debulking atlas in Patients 2, 3 and 5 ($p<0.05$, two-sided Wilcoxon signed rank test. The AIC values in these instances for the reconstructions with the central debulking atlas were also lower (Table VI.3). This difference in reconstruction without debulking and reconstruction with the central debulking atlas was also present in Simulation 1 and 2 ($p<0.05$, two-sided Wilcoxon signed rank test). The AIC values were also lower in the reconstructions with the central debulking atlas (Table VI.1). There were differences between the reconstruction with the central debulking atlas and the k-means debulking atlas in Patients 3 and 5 ($p<0.05$, Wilcoxon signed rank test). The AIC values in the reconstructions with the central debulking atlas in these cases were lower compared to the reconstructions with the k-means debulking atlas (Table VI.3). In Patient 3 there were also differences between the reconstructions using the central debulking atlas and the Gaussian debulking atlas ($p<0.05$, Wilcoxon signed rank test). Once again the AIC value for the central debulking atlas reconstruction in this case was less than the Gaussian debulking atlas reconstruction in Patient 3. These differences in debulking reconstruction can also be visualized in Figure VI.7 which illustrates the results of Patient 3.

VI.2.3.3 Brain Shift Atlas with Gaussian Debulking

The results of the Gaussian debulking atlas are in Figure VI.6 and Tables VI.1 through VI.3. We can see that the Gaussian debulking atlas contributed to the brain shift solution in five of the six patients (Figure VI.6) and both of the simulated cases (Table VI.1). Once again, in these five patients (Patients 1, 2, 3, 4, 5) the inclusion of the Gaussian debulking atlas changed the distribution of weighting coefficients in the other shift categories relative to the reconstruction without debulking solutions, suggesting that the Gaussian debulking atlas was more representative of brain shift in these cases. This behavior was also observed in both of the simulation cases (Table VI.2). Table VI.3 reflects an increase in the percent shift correction, and a decrease in the average error and maximum error relative to when the debulking solutions were included for the patient cases. With respect to the two simulation cases, the inclusion of the Gaussian debulking solutions resulted in an increase in the percent shift correction, a decrease in the average error magnitude, and a decrease in the standard deviation of the error magnitude. In Patients 2 and 3, there were differences between reconstructions without debulking and reconstructions with the Gaussian debulking atlas ($p<0.05$, Wilcoxon signed rank test). The AIC values in this comparison were lower for the reconstructions performed with the Gaussian debulking atlas (Table VI.3). In Simulation 2, there were differences between the reconstructions with the central debulking method and the Gaussian debulking method ($p<0.01$, Wilcoxon signed rank test). However, the AIC value for the reconstruction with the central debulking method was lower (Table VI.1).

VI.2.3.4 Brain Shift Atlas with K-Means Debulking

The results of the k-means debulking atlas are in Figure VI.6 and Tables VI.1 through VI.3. The k-means debulking atlas was used in four of the six patients (Patients 1, 2, 3, 4) and both of the simulations. Once again, its inclusion altered the distribution of types of shift solutions used to reconstruct the measured brain shifts relative to the reconstructions without the debulking atlas in the patients (Figure VI.6) and the simulations (Table VI.2). It is also worth noting that the distribution of solutions pulled from in each patient varied between all of four of the atlas reconstructions (Figure VI.6) and the simulations (Table VI.2). For the four patients improved, the percent shift correction increased, and the standard deviation of error and maximum error decreased (Table VI.3). For the two simulations, the percent shift correction increased, the average error magnitude, the standard deviation of error, and the maximum error magnitude decreased. There were differences between the correction per measured displacement (Equation (VI.11)) in the reconstruction without debulking and the reconstruction with the k-means debulking atlas in Patient 2 ($p<0.05$, Wilcoxon signed rank test). The AIC value of the k-means debulking atlas reconstruction was lower than the reconstruction without debulking (Table VI.3). This difference was also observed in both of the simulations ($p<0.05$, Wilcoxon signed rank test). Once again, the AIC values of the k-means debulking atlas reconstructions were lower than when the reconstructions were performed without debulking (Table VI.1). There was a difference between the reconstruction using the Gaussian debulking atlas and the k-means debulking atlas in Patient 1 ($p<0.05$, Wilcoxon signed rank test). The AIC value was lower in this case in the reconstruction with the k-means debulking atlas (Table VI.3). Also, there was a difference between the reconstruction using the central debulking atlas and the k-means debulking atlas in Simulation 2 ($p<0.01$, Wilcoxon signed rank test). However, the AIC value of the reconstruction with the k-means debulking atlas was higher relative to the reconstruction with the central debulking method (Table VI.1).

VI.2.4 Discussion

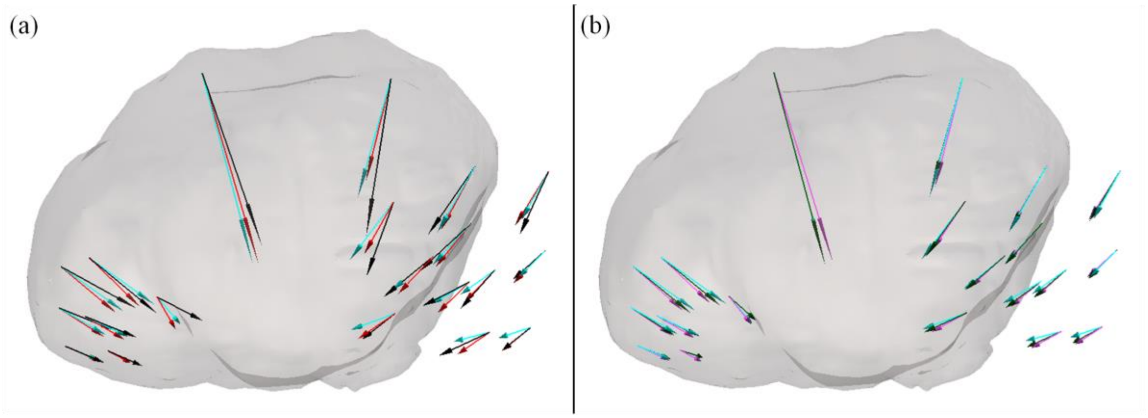

Figure VI. 7: Both panels demonstrate the results of Patient 3. The opaque area in both panels is the tumor in Patient 3. In Panel (a) the black arrows are the measured deformations, the red arrows are the estimated deformations when no debulking was included in the atlas, and the cyan arrows are the estimated deformations when the central debulking solutions are included in the atlas of solutions for reconstruction. In Panel (b), the cyan arrows once again are the estimated deformations when the central debulking solutions are included. The green arrows are the estimated deformations when the Gaussian debulking solutions are included. The magenta arrows are the estimated deformations when the k-means debulking solutions are included.

We present a mathematical representation of intraoperative tumor cavity collapse, that we propose captures physics of brain shift not captured in previous models. By modifying the calculated cellular distribution, we generated three distinct atlases that capture brain shift due to debulking. We were able to improve the percent brain shift correction in multiple cases with debulking. Our methodology changed the distribution of brain shift types included as well as improved the quality of results relative to when debulking solutions were not a part of the reconstruction.

Despite the common debulking physics, the three atlases captured different directions of tumor cavity collapse. Figure VI.7 Panel (a) illustrates the differences in the measured vectors, the vectors from the reconstruction without debulking, and the vectors from the reconstruction with debulking. Panel (b) illustrates the differences in the vectors from the reconstructions with the three debulking atlases. Despite all three debulking atlases sharing common physics, the differences in tumor cell distribution altered, sometimes significantly, the vectors reconstructed. Figure VI.6 and Table VI.2 also demonstrate this when observing differences in weighting coefficients within a given patient and subject.

The strength of the central debulking atlas is its ability to capture global mass effect as well as accurately calculate cellular distributions. Also, when statistical differences were found between reconstructions, this method consistently had lower AIC values, indicating a better balance between the number of coefficients being fit and the quality of the fit relative to its counterparts. However, as illustrated in Patient 4 (Figure VI.4) accurately fitting the grown tumors to the patients' original asymmetric tumors proved challenging. This may explain why the atlas was unable improve the percent shift correction in this case. A potential solution to this challenge for future work would be the use of a more sophisticated model of tumor growth, the incorporation of tissue heterogeneity, and mechanical coupling [93], [82]. The Gaussian debulking atlas improved the percent shift correction in five of the six patients. The success of this atlas highlights the importance of accurately capturing the global tumor geometry in our debulking method. The k-means debulking atlas improved four of the six cases. The atlas solutions captured localized debulking and more tumor specific geometry. In Patient 1, however, the reconstruction using the k-means atlas caused the finite element mesh to fold incorrectly. With the limited patient and observation size, it is unclear if this is due to the nature of the atlas solutions generated or the distribution of the measured data collected. It is also worth noting that the LRS scan of the post-resection surface (Figure VI.1 Panel (b)) captured a very dramatic tumor cavity collapse. Regardless, while this method did enable the more distinct geometries of the tumors to be captured, it did not capture the global mass effect as well as the other two atlases.

None of the debulking atlases were able to achieve shift correction improvements in Patient 6, despite all proposed debulking metrics indicating cavity collapse in Patient 6 (Figure VI.5). When comparing tumor volumes, it became evident that Patient 6 had a substantially smaller tumor relative to the other patients. Figure VI.8 highlights this by visualizing the largest tumor studied (Patient 3) and the smallest tumor (Patient 6). Another study into resection cavity dynamics noted that the pre-resection tumor volume was a predictor of postoperative cavity volume change [147]. While we cannot conclusively state it, we believe the tumor’s small volume caused the discrepancy in correction.

Two of the simplifications made in this work are areas of improvement for future work. The first is the assumption that edema is present within a set contour around the tumor. This was made due to a lack of access to T_2 weighted MRI scans. Segmenting the edema from this scan type would provide patient-specific edema distributions. Also, we only used the preoperative scan taken immediately prior to surgical resection, meaning we had no knowledge of how long the tumor grew. This would influence how diffuse the tumor was. In future studies, incorporation of serial imaging and biopsy specimen pathology may lead to more accurate calculated tumor cell distributions and higher fidelity brain shift corrections.

A limitation of this investigation is the number of patients studied, the variability of intraoperative modalities, and the variability in tumors. Therefore, while the results of this study are encouraging, further investigation is necessary to determine the fidelity of the proposed physics of debulking and the corresponding atlases. The shift correction being assessed with points outside of those used to drive the inverse problem in Simulation 1 and Simulation 2, provide evidence that our patient reconstructions may be accurate elsewhere within the patient brain volumes. However, this could not be verified without further patient studies. Despite these challenges, our ability to identify and correct for the debulking mechanism with patient data collected at multiple sites with multiple modalities (LRS, iMR, and iUS). This suggests not only the significant impact of accounting for cavity collapse when correcting for brain shift, but also indicates the robustness of our method.

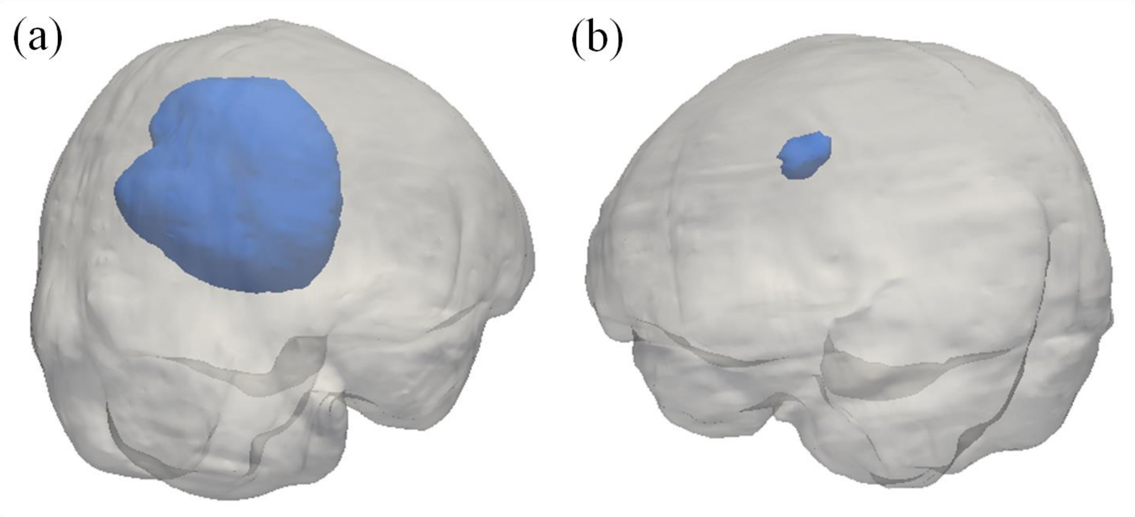

Figure VI. 8: In Panel (a), the brain mesh of Patient 3 can be seen in grey, and the tumor can be seen in blue. Patient 3 had the largest tumor by volume. In Panel (b), the brain mesh of Patient 6 can be seen in grey, and the tumor can be seen in blue. Patient 6 had the smallest tumor by volume.

Overall, based on the results of this investigation, the central debulking atlas, captured global mass-effects from the tumor and the influence of tumor edema. In Simulation 1 and Simulation 2, its inclusion resulted in the greatest increase in percent shift correction (Table VI.1). It provided statistically significantly different results relative to the baseline atlas in Patients 2, 3, and 5, and Simulations 1 and 2 ($p<0.05$ Wilcoxon signed rank test) with lower AIC values. It also provided results different than the other atlases in Patients 3 and 5 and Simulation 2 ($p<0.05$ Wilcoxon signed rank test). Its inability to improve shift correction in Patient 4 is most likely due to the geometry of the tumor. While it did not necessarily provide the most improvement in every patient, it is less susceptible to be biased by sparse intraoperative data collection. For example, the k-means atlas could provide less accurate results if the measurements made are collected in a relatively small area and used to drive the inverse problem. The central debulking atlas is less susceptible to such biases in collection, making it more robust.

Accurate resection of tumors is critical for patient survival [139], [4]. Knowledge of how the tumor cavity is evolving intraoperatively from debulking has the potential to improve the fidelity of tumor resections and inform tumor margin planning. While we have focused on applications in IGNS, there are a variety of other possible applications for our model of debulking. One of these applications is the prediction of the boundaries of the tumor cavity postoperatively to aid in planning stereotactic radiosurgery treatments [147]. Knowledge of how the cavity moves could help with patient treatment planning. Despite the noted limitations of this investigation, our multimodal study of debulking atlases demonstrates an ability to improve brain shift correction relative to a model-based atlas that does not account for debulking.

VI.2.5 Conclusions

The purpose of this investigation was to develop a method of predicting intraoperative brain shifts due to tumor debulking. The patient and simulation results indicate that debulking can be estimated and corrected for. Furthermore, the correction gained with debulking atlases is related to the calculated cellular distribution. To the best of our knowledge, this is the first model of cavity collapse during tumor resection (debulking). While, we cannot conclusively say that our method is ready for clinical implementation without further investigation, the results of this study are encouraging. Consistent improvements were obtained in the simulation studies, and limitations in the clinical results could be the result of noise within the data collection itself. Furthermore, we were able to predict debulking displacements which have been very challenging to capture in past FEM studies. The central debulking method captured global mass-effects from the tumor and can be refined with additional imaging studies. Furthermore, when statistical differences were identified, this method had the best balance between the number of degrees of freedom in the atlas and the quality of the brain shift correction. While preliminary in nature, the work presented could improve patient outcomes through applications in actively updating IGNS navigation as well as treatment planning in stereotactic radiosurgery.

Acknowledgements

This work was supported by the NIH—National Institute of Neurological Disorders and Stroke R01NS049251. It was also supported by the National Center for Image Guided Therapy grant P41-EB015898-09, and the National Cancer Institute grant K25CA204599. The NIH grants R01EB027134-01 and R01NS049251 also partially funded this work.

CHAPTER VII

VII Future Directions and Conclusions

VII.1 Evacuation of Other Intracranial Lesions

VII.1.1 Summary and Future Work

This thesis centers on the evacuation of solid space occupying intracranial lesions, namely tumors. While tumors are lesions within the brain, there are a variety of other possible intracranial lesions with varying mechanical properties. One such type of lesion is an intracerebral hemorrhage. Intracerebral hemorrhages are the result of ruptured blood vessels within the brain, and correspondingly have very different mechanical properties and interactions with the surrounding brain tissue. Based on the studies into tumor mechanics as they relate to intracranial tissue within the scope of this thesis, it is evident that the interactions between pathological and healthy tissue play a significant role in both their development and extraction. As a future study based on this work, the relationship between the parenchyma and intracerebral hemorrhages can be investigated for surgical planning. This would expand this research into another patient population. In an initial, preliminary investigation into the feasibility of this idea, a two-dimensional representation of intracerebral hemorrhage evacuation was performed. The results of this study are further evidence that studying the evacuation of non-solid space occupying lesions, namely intracerebral hemorrhages, warrants future studies.

The work in this section appears in:
Narasimhan, S., Weis, J. A., Webster, R., Miga, M. I. (2018). “Development of a Mechanics-Based Model of Brain Deformations during Intracerebral Hemorrhage Evacuation”, Medical Imaging 2017: Image-Guided Procedures, Robotic Interventions, and Modeling, Vol. 10135, 101350F, 2017.

VII.1.2 Abstract

Intracerebral hemorrhages (ICHs) occur in 24 out of 100,000 people annually and have high morbidity and mortality rates. The standard treatment is conservative. We hypothesize that a patient-specific, mechanical model coupled with a robotic steerable needle, used to aspirate a hematoma, would result in a minimally invasive approach to ICH management that will improve outcomes. As a preliminary study, three realizations of a tissue aspiration framework are explored within the context of a biphasic finite element

model based on Biot's consolidation theory. Short-term transient effects were neglected in favor of steady state formulation. The Galerkin Method of Weighted Residuals was used to solve coupled partial differential equations using linear basis functions, and assumptions of plane strain and homogeneous isotropic properties. All aspiration models began with the application of aspiration pressure sink(s), calculated pressures and displacements, and the use of von Mises stresses within a tissue failure criterion. With respect to aspiration strategies, one model employs an element-deletion strategy followed by aspiration redeployment on the remaining grid, while the other approaches use principles of superposition on a fixed grid. While the element-deletion approach had some intuitive appeal, without incorporating a dynamic grid strategy, it evolved into a less realistic result. The superposition strategy overcame this, but would require empirical investigations to determine the optimum distribution of aspiration sinks to match material removal. While each modeling framework demonstrated some promise, the superposition method's ease of computation, ability to incorporate the surgical plan, and better similarity to existing empirical observational data, makes it favorable.

VII.1.3 Introduction

Intracerebral hemorrhages (ICH) are the result of blood vessels within the brain rupturing. The incidence of ICH is approximately 24 out of 100,000 people a year. The median one-month mortality rate is 40%, and there is also a high incidence of morbidity [157]. ICHs make up approximately 10 to 15% of all strokes. Some primary causes of ICHs include hypertension, cerebral amyloid angiopathy, sympathomimetic drugs of abuse, and coagulopathy [158]. Uncontrolled hypertension is one of the most significant risk factors for reoccurring ICHs [159]. Treatment options include blood pressure management, coagulation management, and surgery [158]. In the INTERACT2 trial, the mortality and morbidity outcomes of patients with an ICH, less than 6 hours old, were similar between patients who underwent traditional management techniques and new intensive blood pressure lowering techniques [160]. Surgical approaches for ICH intervention have been attempted, but there has not been conclusive data showing that surgical intervention improves patient outcomes [158], [161]. Studies have also investigated treating ICHs with decompressive craniectomies. These studies revealed improved outcomes, but were limited by a small patient population [162]. Despite continuing innovations in the field, satisfactory ICH management remains a significant unsolved medical challenge.

There are investigational studies into less invasive techniques that seek to more effectively treat ICHs, but these techniques are not accepted as a standard method of treatment [163], [164], [165]. One proposed minimally invasive technique, which will be the focus of the model presented, is a needle-based robotic system for image-guided evacuation of ICHs [165]. The ICH robotic system consists of a sterilizable robotic actuation unit, an active cannula driven by the actuation unit, a trajectory guide, which enables the hemorrhage to be targeted using image guidance, an aspirator to evacuate the ICH, and a passive articulated arm. The cannula consists of a precurved and superelastic inner tube, and an outer tube which is straight and stiff [165], [166]. The proposed surgical workflow of this device is as follows. Preoperative computed tomography (CT) images of the patient would be obtained. Using an intraoperative scan of the patient's face, the preoperative CT will be registered into the patient space. Upon completion of the registration, the active cannula is then aligned [165]. A burr hole will be made in the skull, then the dura is opened, and the trajectory guide will be attached to the skull. Following this, the trajectory stem would then be attached to the base, and the alignment probe would then be inserted into the trajectory stem, while using the image guidance system for alignment [165]. A locking ring would then be tightened, fixing the trajectory stem into place, and once this is complete, the alignment probe would be removed [165]. The robot is then brought into the surgical field and attached to the trajectory stem. Finally, the active cannula is then passed into the brain through the trajectory stem and navigated through the ICH, based on a preplanned path. As the inner cannula is deployed, the ICH is evacuated in a systematic manner [165]. In order to limit the number of intraoperative CT scans that would need to be obtained, a mechanics based model of the evacuation of the ICH is necessary to ensure safety of the procedure.

A previous study analyzed ICH shapes using a two-dimensional (2D), finite element model, representing the ICH as six vectors radiating outwards. This study concluded that computational models could improve the clinical understanding of ICH patients [167]. Other computational models have been used to represent intraoperative events, including retraction and resection [69]. Developing a model that captures the deformations and dynamics of the surgical interaction involved with the evacuation of an ICH may be an important complement for creating minimally invasive techniques for this patient population. The combined development of a biomechanical patient-specific model and robotic platform could be an innovative guidance solution for patients suffering from an ICH. In this study, it is hypothesized that a patient specific, biomechanical model could augment an active cannula designed to access the intracerebral hemorrhage through a minimal path, and be used to guide ICH aspiration process and likely complement intraoperative imaging. The purpose of the work presented in this paper is to develop a preliminary, computational, finite element model (FEM) to represent ICH aspiration. To the best of our knowledge, this study creates the first, preliminary, computational, biomechanical model of ICH evacuation. If this work is fully realized it can ultimately be utilized with the ICH robot system described previously and reduce the number of intraoperative CT scans to which the patient would be exposed thus significantly reducing ionizing radiation exposure. In addition, if possible, reduction of intraoperative CT scans would improve clinical procedural work-flow. This work may also be extended by providing additional guidance for other minimally invasive ICH evacuation techniques in development.

VII.1.4 Methods

Table VII. 1: Equation Definitions

$\boldsymbol{G}$	Shear modulus	*(Pa)*
$\vec{\boldsymbol{u}}$	Displacement vector	*(m)*
$\boldsymbol{v}$	Poisson's ratio	
$\boldsymbol{\alpha}$	Ratio of fluid volume extracted to volume change of tissue when compressed	
$\boldsymbol{p}$	Pore fluid pressure	*(Pa)*
$\boldsymbol{1/S}$	Amount of fluid that can be forced into the tissue under a constant volume	*(1/Pa)*
$\boldsymbol{k}$	Hydraulic conductivity	*(m^3s/kg).*

VII.1.4.1 Continuum, Finite Element Model of Brain Deformations

The model treats brain tissue as a fluid saturated poro-elastic medium [64], [70] represented by biphasic consolidation theory. The associated partial differential equations were used to calculate pressure, displacements, and von Mises stress distributions [64], [70], [97]. The equations for consolidation in soft-tissue can be written as [64], [70], [97]:

$$\nabla \cdot G\nabla\vec{u} + \nabla\frac{G}{1-2v}(\nabla\cdot\vec{u}) - \alpha\nabla p = 0 \tag{VII.1.a}$$

$$\alpha\frac{\partial}{\partial t}(\nabla\cdot\vec{u}) + \frac{1}{S}\frac{\partial p}{\partial t} - \nabla\cdot k\nabla p = 0 \tag{VII.1.b}$$

where Equation (VII.1.a) relates the mechanical equilibrium to the pressure gradient, which is treated as a body force on the control volume. Equation (VII.1.b) relates volumetric strain to the conservation of fluid in a porous media [64], [70], [97]. The brain is treated as a fully saturated medium, $\alpha=1$ and $1/S=0$. In this study, the equations (VII.1.a and VII.1.b) were simplified into their steady state forms and linear elastic mechanical behavior was employed. With these assumptions and simplifications, the governing equations of this model can be written as:

$$\nabla \cdot G\nabla\vec{u} + \nabla\frac{G}{1-2v}(\nabla\cdot\vec{u}) - \nabla p = 0 \tag{VII.2.a}$$

$$-\nabla\cdot k\nabla p = 0 \tag{VII.2.b}$$

Using the Galerkin Method of Weighted Residuals, the governing equations (VII.2.a and VII.2.b) are treated using the standard weighted residual method [16].

$$\langle G\nabla\vec{u}\cdot\nabla\phi_i\rangle + \left\langle\frac{G}{1-2v}(\nabla\cdot\vec{u})\nabla\phi_i\right\rangle + \langle\phi_i\nabla p\rangle = \oint G\hat{n}\cdot\nabla\vec{u}\phi_i\,ds + \oint\frac{G}{1-2v}\hat{n}(\nabla\cdot\vec{u})\phi_i\,ds \tag{VII.3.a}$$

$$\langle k\nabla p\cdot\nabla\phi_i\rangle = \oint k\hat{n}\cdot\nabla p\phi_i\,ds \tag{VII.3.b}$$

In these expressions, $\langle * \rangle$ represents integration over the domain of the problem. Also, ϕ_i, is the i^{th} member of the standard C° local Lagrange polynomial interpolants associated with finite elements [70]. $\oint *$ represents integration over the contained boundary and $\hat{n}$ is the outward-pointing normal to the enclosed boundary. The spatial discretization of (VII.3.a) and (VII.3.b) is concluded using the Galerkin method in order to expand the unknown fluid pressure, p, and the unknown displacement vector, $\vec{u}$. These are represented as the summation of unknown coefficients, which vary spatially, that are multiplied by known functions of position [70], [96].

$$\vec{u}(\vec{x}) = \sum_j \vec{u}_j \phi_j(\vec{x}) \tag{VII.4.a}$$

$$p(\vec{x}) = \sum_j p_j \phi_j(\vec{x}) \tag{VII.4.b}$$

The spatially discretized, set of ordinary differential equations are:

$$\sum_j \vec{u}_j \langle G\nabla\phi_j \cdot \nabla\phi_i\rangle + \sum_j \vec{u}_j \cdot \left\langle \nabla\phi_j \frac{G}{1-2v} \nabla\phi_i \right\rangle + \sum_j p_j \langle \nabla\phi_j \phi_i\rangle = \oint G\hat{n}\cdot\nabla\vec{u}\phi_i\, ds + \oint \frac{G}{1-2v}\hat{n}(\nabla\cdot\vec{u})\phi_i\, ds \tag{VII.5.a}$$

$$\sum_j p_j \langle k\nabla\phi_j \cdot \nabla\phi_i\rangle = \oint k\hat{n}\cdot\nabla p\phi_i\, ds \tag{VII.5.b}$$

In Cartesian coordinates, equations (VII.5.a) and (VII.5.b) can be represented in matrix form.

$$[A]\{U\} = \{B\} \tag{VII.6}$$

In this matrix expression, (VII.6), *[A]* consists of submatrices built from element integrations, $\{U\}$ represents the unknown values of displacements and pressure, and $\{B\}$ consists of known systems forcing and boundary conditions. The two-dimensional (2D) representation of the local element contribution to the global matrix representation is seen below. *[A]* is determined for each weighted residual equation and concerned coefficient as seen in (VII.7.a), and $\{U\}$ and $\{B\}$ are the *j^th^* set of coefficients and known forcing conditions as defined by (VII.7.b) and (VII.7.c) respectively.

$$[A]_{ij} = \begin{bmatrix} G\left\langle \frac{2(1-v)}{1-2v}\frac{d\phi_j}{dx}\frac{d\phi_i}{dx} + \frac{d\phi_j}{dy}\frac{d\phi_i}{dy}\right\rangle & G\left\langle \frac{2v}{1-2v}\frac{d\phi_j}{dy}\frac{d\phi_i}{dx} + \frac{d\phi_j}{dx}\frac{d\phi_i}{dy}\right\rangle & \left\langle \frac{d\phi_j}{dx}\phi_i\right\rangle \\ G\left\langle \frac{2v}{1-2v}\frac{d\phi_j}{dx}\frac{d\phi_i}{dy} + \frac{d\phi_j}{dy}\frac{d\phi_i}{dx}\right\rangle & G\left\langle \frac{2(1-v)}{1-2v}\frac{d\phi_j}{dy}\frac{d\phi_i}{dy} + \frac{d\phi_j}{dx}\frac{d\phi_i}{dx}\right\rangle & \left\langle \frac{d\phi_j}{dy}\phi_i\right\rangle \\ \langle 0\rangle & \langle 0\rangle & k\left\langle \frac{d\phi_j}{dx}\frac{d\phi_i}{dx} + \frac{d\phi_j}{dy}\frac{d\phi_i}{dy}\right\rangle \end{bmatrix} \tag{VII.7.a}$$

$$\{U\}_j = \begin{Bmatrix} u_{x_j}(t_n) \\ u_{y_j}(t_n) \\ p_j(t_n) \end{Bmatrix} \tag{VII.7.b}$$

$$\{B\}_j = \begin{Bmatrix} \hat{x}\cdot\oint \sigma_s(t_n)\cdot\hat{n}\phi_i\, ds \\ \hat{y}\cdot\oint \sigma_s(t_n)\cdot\hat{n}\phi_i\, ds \\ \oint k\,\nabla p(t_n)\cdot\hat{n}\phi_i\, ds \end{Bmatrix} \tag{VII.7.c}$$

We should note that the expressions shown in Equation (VII.7.a-c) readily extend to three dimensions using basis functions associated with tetrahedral elements [96]. These discretized matrix representations were used for all ICH evacuation models, namely, the element-deletion model, and superposition approach (described in Sections VII.1.4 and VII.1.5, respectively).

VII.1.4.2 Analytical Validation of Two and Three Dimensional Models

To validate the accuracy of the biphasic, poro-elastic model in this work, a 2D and 3D mesh were generated and their solutions were compared to a one-dimensional (1D) analytical solution of an equivalent domain, with the same boundary conditions (BCs). The dimensions are shown in Figure VII.1.

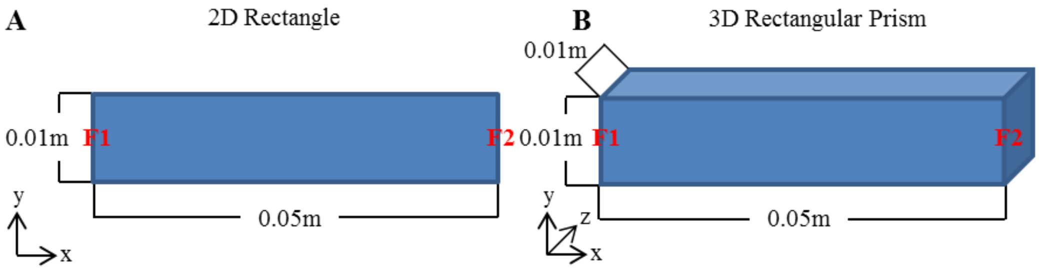

Figure VII. 1: For the validation of the model, two meshes were generated. Panel A represents the dimensions of the 2D mesh used to validate the 2D FEM solution. Panel B represents the dimensions of the 3D, rectangular prism mesh to validate the 3D FEM solution. F1 and F2 indicate face 1 and face 2 respectively. The arrows indicate the axes for x, y, and z in Cartesian coordinates. The origin is in the bottom left corner for both meshes.

With respect to the simulation, the BC on the left side assumes that pressure and displacement is equal to zero. On the right hand side (x=0.05 m), it is assumed that the pressure is equal to 1333 Pascals (Pa), and the BC associated with solid matrix is stress free. The equations associated with (VII.2.a) and (VII.2.b) can be reduced to equations (VII.8.a) and (VII.8.b) in 1D. Using the BCs provided above, an analytical solution for pressure and displacement comparisons can be determined for comparison and is shown in equations (VII.9.a) and (VII.9.b), respectively. In these equations *E* is elastic modulus, and P_o is the value of pressure applied (1333 Pa).

$$E\frac{\partial^2 \vec{u}}{\partial x^2} - \frac{\partial p}{\partial x} = 0 \quad \text{(VII.8.a)}$$

$$\frac{\partial^2 p}{\partial x^2} = 0 \quad \text{(VII.8.b)}$$

$$p(x) = \left(\frac{P_o}{0.05}\right)x \quad \text{(VII.9.a)}$$

$$\vec{u}(x) = \left(\frac{P_o}{2E(0.05)}\right)x^2 + \frac{-P_o}{E}x \quad \text{(VII.9.b)}$$

For the 2D FEM comparison, the rectangular mesh, illustrated in Figure VII.1.a, was governed by the equations (VII.5.a) and (VII.5.b). Using Dirichlet BCs, at face 1 (F1), pressures and displacements were set to zero. At face 2 (F2), using Dirichlet BCs, the pressure values were set equal to 1333 Pa, while conditions on the elastic matrix were stress free. BCs associated with top and bottom of the domain are allowed to slide along the wall in the *x*-axis direction, but are prohibited from displacing in the y-axis direction. BCs similar to the 2D framework were used in the 3D simulation. The elastic modulus (*E*) is 2100 Pa for both the 2D and 3D comparisons. In order to make the 2D and 3D approximations similar to the 1D analytical solution, the Poisson's ratio value is 0. For validation, the displacement and pressure values at a distance from the origin are compared.

VII.1.4.3 Common Model Properties for the ICH Evacuation Representations

There are three representations of ICH evacuation presented in this work. They differ in how evacuation is represented with respect to applied boundary conditions, but their core structure is common. For the sake of discussion, these are referred to as the central evacuation representation (Section VII.2.4 below) and the superposition evacuation representations (1) and (2) (Section VII.2.5 below). They were evaluated in 2D. All models were constructed on a FEM, fixed grid, and governed by Equations (VII.2.a) and (VII.2.b). The matrices associated with Equations (VII.6), (VII.7.a), (VII.7.b), and (VII.7.c) were constructed based on a predefined brain mesh, which is illustrated in Figure 2. The elastic modulus of the brain parenchyma, ventricles, and ICH are 2100 Pa, 1Pa, and 1050 Pa respectively. The Poisson's ratio (v) is 0.45. The hydraulic conductivity constant for the brain parenchyma /ICH and ventricles are $1x10^{-7}$ m^3s/kg and $1x10^{-3}$ m^3s/kg respectively. Along the skull boundary, which is the outermost limit of the mesh, Dirichlet BCs were used to set the pressure and displacements equal to zero. This represents the skull constraints on the brain and defining the pressure at the skull as zero relative to the applied evacuation pressure. The sole difference between the representations of ICH evacuation is how the evacuation is applied computationally, which is illustrated in Figure VII.2.a and VII.2.b. These will be outlined in Sections VII.4 and VII.5.

VII.1.4.4 Two-Dimensional, Central Evacuation Representation

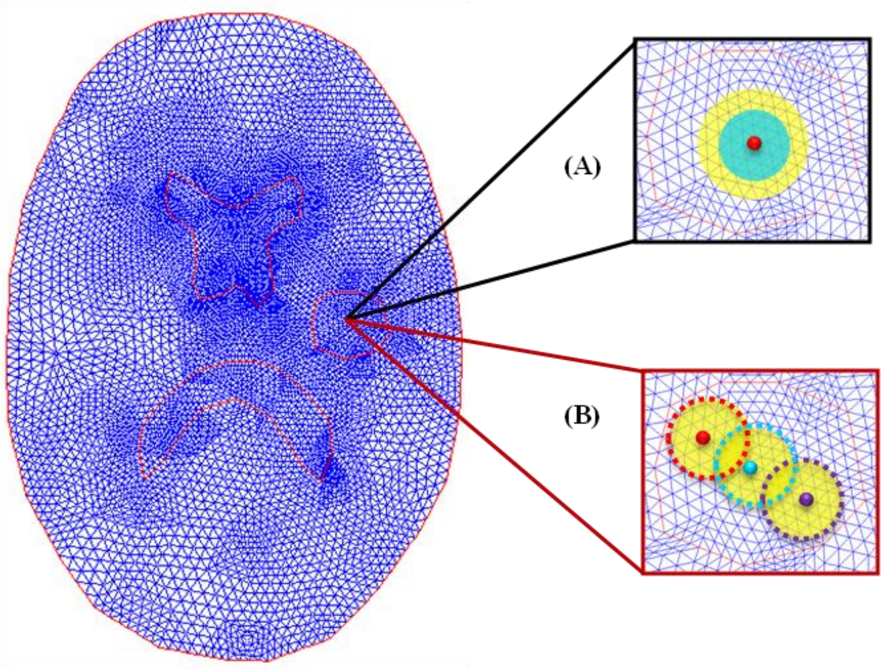

Figure VII. 2: This figure displays the three models being tested on a brain mesh. (A) represents the deployment of pressure in the central evacuation representation of ICH evacuation. (B) represents the deployment of pressure in both superposition evacuation representations of ICH evacuation. The outermost boundary of the mesh represents the skull. The two asymmetric, internal boundaries represent the brain's ventricles. The circular portion of the mesh, which is also displayed in the details, represents the ICH.

The behavior of the central ICH evacuation is visualized in Figure VII.2.a. Generally, in this representation, the net aspiration of the cannula is treated as a source originated from the center of the ICH, which produces an increasingly larger cavity as material is removed. At the completion of consecutive iterations, the final evacuated cavity can be estimated. In the central evacuation representation, the pressure of the cannula is treated as a Dirichlet BC with magnitude equaling the applied pressure. In this simulation, the magnitude of the pressure was selected to be -1333 Pa. A total of three iterations were completed in this simulation, where each iteration represents one complete application of the cannula. During the first iteration, the application of the cannula is represented by a single, Dirichlet BC at a single node (red dot in Figure VII.2.a). After this, the pressure, displacement, and von Mises stress distribution are calculated. The von Mises stress distribution, calculated per element, was used as the failure criterion in order to determine if an element, which represents a section of tissue, was flagged for deletion. Due to the lack of experimental data, the yield criterions for the three materials are determined empirically during the first iteration of this procedure. The yield criterion for the ICH was set to be 0.95 times the maximum von Mises stress calculated in the ICH during this first iteration. The yield criterion for the brain and ventricles are set as 10 times the maximum von Mises stress of the brain and ventricles respectively calculated during the first iteration. This is representative of the ICH being evacuated more readily than the other tissue types. These yield criterion were selected to effectively demonstrate the behavior of this evacuation representation. In order to accurately select a yield criterion, an empirical investigation would be needed; but as the purpose of this simulation study is to just understand performance differences under similar conditions, it is not needed here. If the elements were flagged for deletion (stress higher than criterion), they were removed from the solver by not including them in the next construction of the matrices, while leaving the un-evacuated mesh intact. Moving into the next iteration, during the matrix assembly, elements which were evacuated during the previous iteration were not built, effectively removing their influence from the solution of the iteration. The new boundary of the evacuated cavity, represented by the blue circle in Figure VII.2.a is where the applied pressure is now redeployed during the second iteration. This represents the remaining tissue migrating towards the cannula during the second iteration, and the pressure applied from the cannula now deployed over a greater area. This is enforced using Dirichlet boundary conditions. Upon completion of the second iteration, the displacement, pressure, and von Mises stress distributions are once again calculated, and a new list of deleted elements, representing evacuated tissue, is generated using the previously calculated yield criterions. Entering the final iteration, the same process is repeated. The elements which were flagged for deletion are not included in the matrix assembly, and the pressure applied by the cannula is now deployed over the outer boundary of the new evacuated cavity, as seen by the yellow circle in Figure VII.2.a. This method requires the recalculation of the *[A]* matrix (Equation VII.6) every iteration due to the elimination of element contributions and the redeployment of Dirichlet boundary conditions in new regions of the mesh. In this simulation, only three iterations were conducted, but this general process can be performed as many times as necessary, capturing the entire evacuation process.

VII.1.4.5 Two-Dimensional, Superposition Evacuation Representation

The behavior of the superposition evacuation of an ICH is visualized in Figure VII.2.b. The motivation of this representation is that during the evacuation procedure, the cannula is moving along a preplanned path. Rather than capturing the net evacuation, as done with the central evacuation representation, this method follows the cannula along its preplanned path. Each location within its trajectory is treated as one complete application of the cannula, and at the completion of one application, the model moves to the next location as dictated by the surgical plan. At the completion of the path, the total evacuated cavity can be estimated by superimposing the separate evacuation solutions. In this presented simulation, a total of three cannula applications are performed at three different cannula locations. Unlike the central evacuation, each suction is treated as a volumetric sink with an empirically determined magnitude to engender pressures in the mesh equivalent to -1333 Pa. This representation was approached two ways, superposition representation (1) and superposition representation (2).

In superposition representation (1), during the first iteration, represented by the red dot in Figure VII.2.b, the cannula is deployed on a node as a volumetric sink. Using this, the model was solved for the first iteration and pressure, displacement, and von Mises stress distributions were calculated and stored. Using von Mises stress as the failure criterion, elements, representative of tissue, are flagged for deletion. Similar to the central evacuation representation, the von Mises yield criterion is empirically determined based on the stress distribution calculated during the first iteration. In a similar manner to the central evacuation method, in order to illustrate the behavior of this evacuation method, the yield criterion for the ICH was selected as 0.75 times the maximum von Mises stress of the ICH. The yield criterion of the brain and ventricles are selected as 10 times the maximum von Mises stress in both materials respectively. These values are stored and used as the yield criterion for all three material types during the simulation. The list of elements that were deleted after the first cannula deployment are stored, and the evacuated cavity of this suction can be visualized by the dashed red line in Figure VII.2.b. Moving onto the second iteration, the cannula location is moved to its second position, and the same volumetric sink is applied on this node. This is visualized in Figure VII.2.b as the light blue dot. Then the model is solved to estimate pressures, displacements, and von Mises stresses, and these solutions are stored. The tissue evacuated as the result of the second iteration is stored, and this evacuation is visualized by the light blue dashed circle in Figure VII.2.b. Moving onto the final iteration, the same process is repeated. The cannula is moved to its third location and is visualized as the purple dot on Figure VII.2.b. The elements deleted due to this iteration are shown by the purple dashed line in Figure VII.2.b. This process can be repeated indefinitely, as required to appropriately represent the path of the cannula during the ICH evacuation. The final estimated evacuated cavity is formed by determining the outer contours resulting from the superposition of the elements flagged for deletion during all three iterations performed. This is done by adding the three results together. This is illustrated by the yellow shape in Figure VII.2.b. This method only requires the *[A]* matrix (Equation VII.6) to be factored once, since each iteration is independent of each other and representations of aspiration are based on right-hand-side equation adjustments only.

In superposition representation (2), rather than solving three iterations of the model for pressure, displacement, and von Mises stresses, only one iteration is performed. This further simplification of the superposition representation requires the formation and factorization of the *[A]* matrix once. Then, using a series of volumetric sinks, the $\{B\}$vector (Equation VII.6) is populated with three conditions representing the same three deployments of the cannula. This reflects a path the cannula would travel in the surgical procedure. The deployment of these sinks is visualized as the red, blue, and purple dots in Figure 2B. Using this, the model was solved for the first iteration and pressure, displacement, and von Mises stress distributions were calculated and stored. The yield criterion for the ICH was selected as 0.75 times the maximum von Mises stress of the ICH material during this single iteration. The yield criterion of the brain and ventricles are selected as 10 times the maximum von Mises stress in both materials respectively. The deleted cavity is solved in a single iteration and is visualized by the yellow shape in Figure VII.2.b. Superposition representation (2) can be modified by altering the number of and location of the volumetric sinks enforced, thereby representing different cannula trajectories within the surgical plan.

VII.1.4.6 Three-Dimensional, Continuum, Finite Element Model of Brain Deformations

As a preliminary study into applying the evacuation methods in 3D, an example mesh of a human brain with an artificial ICH was made using a custom-built mesh generator and consisted of 21076 nodes and 113183 linear tetrahedral elements. The material properties selected for this mesh were 2100 Pa for the elastic modulus of the brain, 1050 Pa for the elastic modulus of the ICH, and 0.45 for the Poisson's ratio of both materials. Also, the hydraulic conductivity was set uniformly as 1 m^3s/kg for the entire mesh, which is appropriate given the nature of the equations. The shear modulus (G) value is defined such that $G = E/\left(2 * (1 + v)\right)$. The governing equations were the same as the 2D case, Equations (VII.2.a) and (VII.2.b). The boundary conditions used to solve this 3D representation take into consideration the outermost boundary of the brain mesh, which represents the boundary of the brain with the skull. The first condition is that there is no displacement at the skull. This is enforced using Dirichlet boundary conditions, setting displacements in the normal and tangential directions to be equal to zero. The second condition, is that the pressure at this boundary is 0 Pa, and is applied as Dirichlet boundary conditions. To represent the applied suction, the magnitude of pressure, -1333 Pa, was applied on the four nodes of one tetrahedral element contained within the artificial ICH. This entire simulation is representative of applying a single suction to the ICH. At the completion of this simulation, displacements and pressures were estimated for each node.

VII.1.5 Results

VII.1.5.1 Analytical Validation Results

The continuum, finite element model of brain deformations were solved in 2D and 3D and compared to the analytical 1D solution. They were simulated using the same material properties, dimensions, and constraints. The results of the 2D solution are shown in Figure VII.3. Figure VII.3.a shows the overlay of the model solution and the analytical solution for displacement, and reflects that the solutions are in agreement. The relative average displacement error is less than 1% over the entire domain. Figure VII.3.b overlays the analytical solution and the model solution for pressure, and reflects that the relative pressure error is less than 1%.

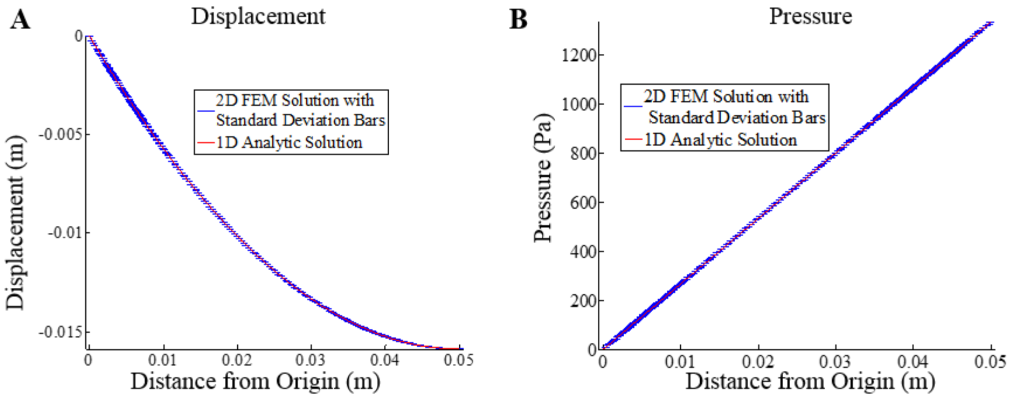

Figure VII. 3: Comparison of the 2D finite element model solution in a rectangular mesh to a 1D analytical solution. Panel A represents the displacement along the primary axis, and panel B represents the pressure at the corresponding locations. The error bars represent the standard deviation at each point. The relative average displacement and relative pressure error are both less than 1%.

The results of the 3D validation are shown in Figure VII.4. In Figure VII.4.a, the 3D displacement FEM solution is overlaid with the 1D analytical solution of displacement, with relative average displacement error less than 1%. In Figure VII.4.b, the 3D FEM solution for pressure is overlaid with the 1D analytical solution, and the relative pressure error is less than 1%.

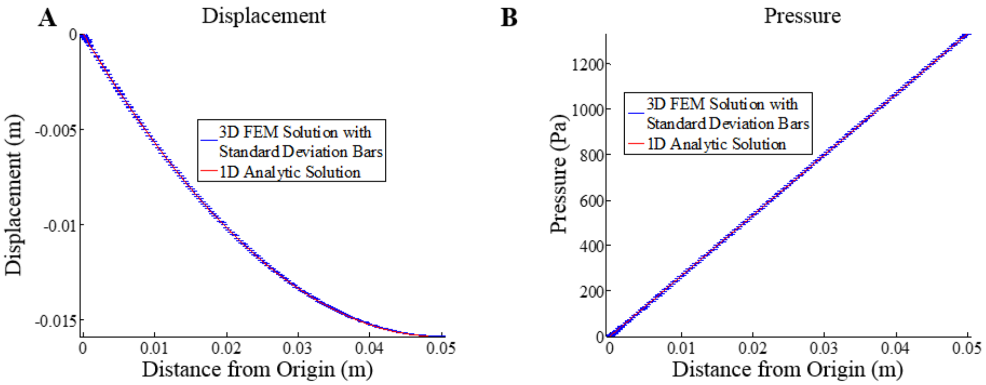

Figure VII. 4: Comparison of the 3D finite element model solution in a rectangular prism to a 1D analytical solution. Panel A represents the displacement in the primary axis, and panel B represents the pressure at the corresponding locations. The error bars represent the standard deviation at each point. The relative average displacement and relative pressure error are both less than 1%.

VII.1.5.2 Comparison of Evacuation Methods

A table summarizing the results from the model solutions is below.

Table VII. 2: Comparison of the three 2D representations of ICH evacuation in the same finite element mesh. This is a summary of how all three representations compare in reference to the percent of ICH evacuated, percent of brain parenchyma evacuated, the computational burden associated with the LU factorization, and the computational burden associated with the back substitution for the solution. *B* is bandwidth, and *N* is the number of unknowns.

Model	Percent ICH Evacuation	Percent Brain Evacuation	Computational Burden - LU Factorization	Back Substitution for Solution	Total Cost
Central Evacuation	100.00%	0.51%	$\sim 3 * O(B^2 \cdot N)$	$3 * N^2$	$\sim 3B^2 \cdot N + 3N^2$
Superposition Evacuation (1)	14.50%	0.00%	$O(B^2 \cdot N)$	$3 * N^2$	$\sim B^2 \cdot N + 3N^2$
Superposition Evacuation (2)	18.90%	0.00%	$O(B^2 \cdot N)$	N^2	$B^2 \cdot N + N^2$

As described in Sections VII.2.4 and VII.2.5, the difference between the central evacuation representation, superposition evacuation representation (1), and superposition evacuation representation (2) of ICH aspiration is how the volumetric sinks create the aspiration condition resulting from the cannula within the model. In the simulations of the central evacuation (Figure VII,5, Panels a-c), the superposition evacuation (1) (Figure VII.5, Panels d-f), and the superposition evacuation (2) (Figure VII.5, Panels g-i) represented in Figure VII.5, three volumetric sinks representing three cannula applications, were applied in all three scenarios. All panels are representative of the evacuation after the deployment of three sets of pressure boundary conditions, and from a qualitative observation, they exhibit dissimilar behavior. After three iterations, the percent of the ICH evacuated in the central evacuation method is 100%, and the percent of brain parenchyma evacuated is 0.51% (Table VII.1). After three iterations, in the superposition evacuation method (1), the percent of the ICH evacuated is 14.5%, and no brain parenchyma was evacuated (Table VII.1). After the single deployment of three pressures in the superposition evacuation method (2), the percent of the ICH evacuated is 18.90%, and no brain parenchyma was evacuated (Table VII.1). All three methods were able to identify the removal of ICH tissue, calculate pressure (Figure VII.5, Panels a, d, and g) and displacements at every node, and estimate the von Mises stress per element (Figure VII.5, Panels b, e, and h). Additionally, they capture the bulk deformation of the surrounding tissue towards the area of evacuation (Figure VII.5, Panels c, f, and i).

A significant difference between the evacuation methods is the computational burden involved with their executions (Table VII.1). All three models presented involve approximately the same memory allocation. They differ significantly in matrix assembly and the number of operations required. For memory efficiency, lower upper (LU) decomposition can be used. The factoring of matrix *[A]* (Equation VII.6) is the most computational expensive step in calculating the solution of the models [96]. The computational burden involved in factorization is $O(B^2 \cdot N)$, where B is the bandwidth of the *[A]* matrix, and N is the number of unknowns being solved for [96]. Both B and N are the same in the three models. The central evacuation representation, however, redefines the *[A]* matrix every iteration. This means that the computational burden in factorization is approximately $3 * O(B^2 \cdot N)$. On the other hand, both superposition representations only requires the construction of one *[A]* matrix used for all iterations. Therefore the total computational burden of factorization is only $O(B^2 \cdot N)$. The 3 fold increase in computational burden for the central evacuation coupled with the need to rebuild the *[A]* matrix is a significant limitation versus the other methods. Even in the case where only local regions where evacuations are occurring and only small changes to the global *[A]* matrix were needed, it would still require storing an addition *[A]* matrix to accommodate this process. Ultimately, Table VII.1 indicates some strong advantages for superposition methods.

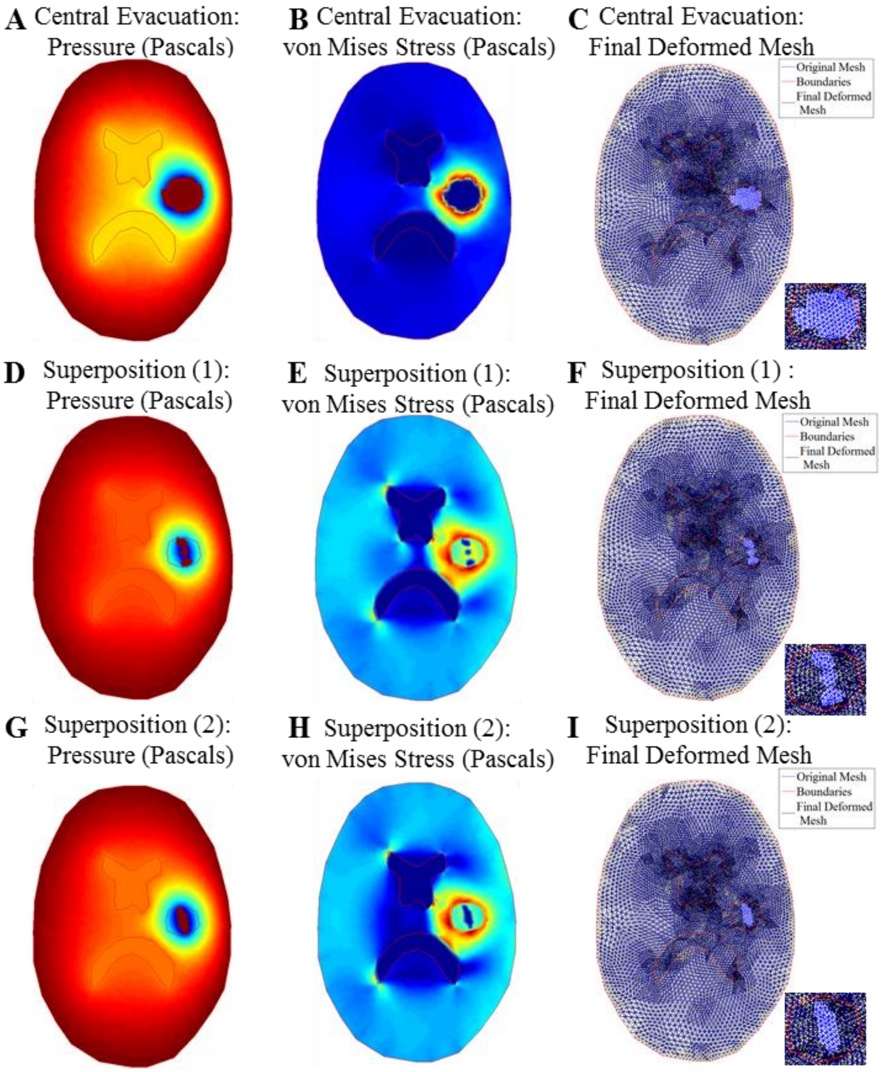

Figure VII. 5: Comparison of the three representations ICH evacuation in the same finite element mesh. The top row (A-C) is the central evacuation model solution after the completion of three iterations. The middle row (D-F) is the superposition model (1) solution after adding the solutions of the three iterations together. The bottom row (G-I) is the superposition model (2) solution after a single iteration containing three applied pressure sources. A, D, and G represent the pressure distribution throughout the mesh, where cooler colors indicate larger negative pressures, warmer colors indicate less negative pressures, and maroon indicates deleted elements. B. E, and H represent the von Mises stress distribution, where warmer colors indicate higher positive von Mises stresses, cooler colors indicate smaller von Mises stresses, and dark blue indicates zero stresses and evacuated elements. C, F, and I show the change in mesh structure from its initial configuration point (blue) to its final deformed state (black). On the bottom right of C, F, and I is an enlarged view of the ICH.

VII.1.5.3 Preliminary Three-Dimensional Model

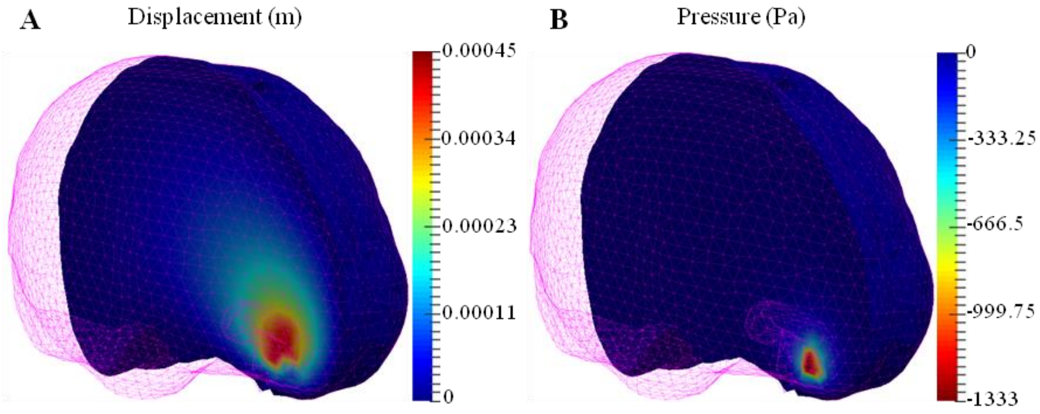

Figure VII. 6: For these simulations, a pressure of -1333 Pa was placed within the ICH. Panel A is a slice through the 3D brain mesh, representing the displacement solution. Panel B is a slice through the 3D brain mesh, representing the pressure solution.

The results of the 3D FEM model solution are shown in Figure VII.6. In both panels, the magenta lines visualize the brain mesh and artificial ICH used in this simulation. The cannula's pressure was deployed within the ICH, and solutions for displacement and pressure were estimated at all nodes within the mesh in this 3D simulation. A slice through the brain, near the location of the cannula deployment is shown in Figure VII.6. In Figure VII.6.a, it is evident that the bulk of the motion occurs closest to the location of pressure deployment. Similarly, in Figure VII.6.b, the highest pressures are at the location of the cannula. This is qualitatively the same behavior seen in the 2D model, and is indicative of the 3D model being viable for ICH evacuation solutions.

VII.1.6 Discussion

The overall goal of this study was to develop a model to estimate the aspiration of an ICH using a needle-based robotic system for image-guided evacuation of ICHs. Interpreting the results of the 2D and 3D simulations performed, the relative average errors between the analytical solution and the FEM solution were less than 1%. These errors are acceptable, indicating the acceptability of the steady-state model used to solve for ICH evacuation in 2D. Minor discrepancies between the model solutions and the analytical solutions, seen in Figures VII.3 and VII.4, may be the result of the numerical error due to resolution of the mesh used in the solution. The accuracy of the model solutions, both in 2D and 3D, support its use as a means to capture steady-state brain deformation and pressure in a model of ICH evacuation. An additional improvement could be obtained through the incorporation of the temporal aspect of the equations for consolidation in soft-tissue, shown in Equations (VII.1.a) and (VII.1.b).

Comparing the 2D models used to estimate the deformations, there are several evident trends. There are substantial differences in the representation of the cannula between the central evacuation representation and both of the superposition evacuation representations. The amount of ICH removed after three pressure deployments was significantly different; however all models were able to capture the removal of an ICH, indicate if brain parenchyma was evacuated, and estimate the distribution of pressure and displacements. The advantage of the central evacuation representation is that it only relies on knowing the applied evacuation and the node approximately in the center of the ICH. However, while intuitive with respect to application, it would require special care with respect to failure criterion to maintain stability. More specifically, as elements that violate the von Mises criterion are eliminated, simply just reapplying the pressure leads to increasing forces due to increased area exposure. To prevent this, the use of a dynamic grid and an alternative failure criterion is likely needed. The superposition evacuation representation, both (1) and (2), do not have this problem as they are calculated on a fixed grid. In addition, they enable incorporating knowledge of the cannula's path during ICH aspiration. They are also likely more adaptable to other ICH evacuation methods that may have different approaches. Even more importantly, the computational burden of superposition evacuation (1) and superposition evacuation (2) is significantly less than the central evacuation representation which may be a considerable advantage when translating to the intraoperative setting. A limitation of the superposition representation is its inability to accommodate the impact of continual removal during the aspiration process. Additionally, all three methods are limited by the use of the von Mises stress as a failure criterion for material evacuation. The method performance is dependent on the definition and number of successive cannula applications. This would undoubtedly require tuning to match biological conditions, and the extrapolation to novel brains may not be straight forward. This concept of empirical tuning of one of these basic biophysical models acting as a type of biophysical filter for ICH aspiration is intriguing and an area for future development.

The three-dimensional model solution is a first step towards implementing the approximations of ICH evacuation in a patient specific manner. By generating meshes from patient-specific, preoperative scans, ICH evacuation can be simulated using knowledge of the patient's physiology and the surgeon's therapeutic plan for evacuation. Moving forward, the second superposition representation of evacuation should be favored, due to its ability to more realistically reflect the surgical procedure and its decreased computational burden. In order to more fully validate the accuracy of the superposition evacuation representation (2), phantom studies will be needed. Generally, the results of our simulations indicate the feasibility of modeling ICH evacuation using finite element modeling, but further work into its development is needed.

VII.1.7 Conclusions

While the methods presented in this paper show aspects of promise, more work is needed in order to capture the complexity of ICH aspiration and its associated material failure criterion. The novelty of the work presented in this preliminary study is that to the best of our knowledge, it is the first computational model of ICH evacuation. Three methods of representing ICH evacuation were investigated, but the second superposition representation better accounts for the surgical environment behavior and is more readily incorporated into an intra-operative environment. Moving forward, following realization and validation of the 3D patient-specific model this framework research can be applied to the ICH robot system. It would enable the reduction of intra-operative CT scans used to ensure healthy tissue would not be aspirated. This work can also be applied to other minimally invasive techniques used in the brain for other aspiration based mechanisms.

Acknowledgements

This work is supported by the NIH-National Institute of Neurological Disorders and Stroke R01NS049251 and R21NS087796. This work was also supported by the Vanderbilt Institute in Surgery and Engineering Seed Grant program.

VII.2 Modeling of Fissures

VII.2.1 Background

The brain is a highly complex organ, with a variety of physical structures. The brain is heterogeneous, consisting of grey and white matters. It also contains many structures, including the ventricular cavities, dural septa, fissures, and sulci and gyri [5], [168]. Fissures divide the brain into lobes; sulci are the groves in the brain, and the gyri are the plateaus formed by the boundary ridges of the sulci pairs [5], [168]. In the scope of this thesis, the influence of ventricular cavities and dural septa were investigated in depth using *in vivo* data. The influence the fissures, sulci, and gyri were not investigated as thoroughly. A preliminary investigation into modeling their influenced, indicate their potential importance in accurately capturing pressure and displacement distributions accurately.

VII.2.2 Treatment of Fissures

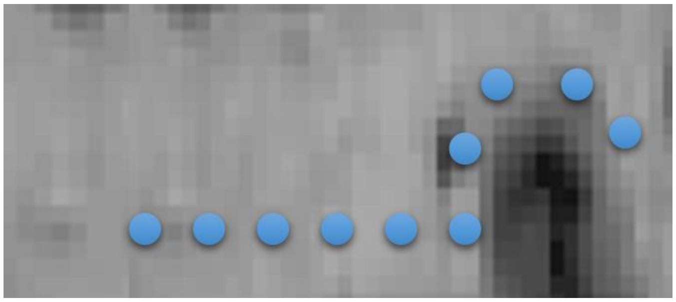

Figure VII. 7: This is an MRI of a block of brain tissue, where the Sylvian fissure is apparent (dark pixels). The blue points represent the theorized movement of the fluid within the tissue. It is around the fissure, rather than through it.

As an initial approximation of the behavior of the fissure, we theorized that while the tissue on either side of a fissure can move together, the fluid present in the brain has to move around them (Figure VII.7). We hypothesized that at fissure boundaries, strain can communicate across (coupled mechanically), but pressure is unable to communicate across. In a preliminary implementation of this methodology, a custom, 3D, finite element steady state poroelastic model of the brain was generated governed by the following equations.

$$\nabla \cdot G\vec{u} + \nabla \frac{G}{1-2v}(\nabla \cdot \vec{u}) - \nabla p = 0 \qquad \text{(VII.10)}$$

$$-\nabla \cdot k\nabla p = 0 \qquad \text{(VII.11)}$$

All simulations were constructed on a tetrahedral finite element mesh. Fissure boundaries were generated using a custom mesh splitting code. For all nodes, not designated as a fissure boundary or another boundary condition, the governing equations are enforced as shown above. At fissure boundary nodes, however, while strain is permitted to communicate across the split in the mesh, a no flux boundary is enforced, with respect to pressure. Essentially, the tissue can move together at fissures, but fluid cannot flow across the fissure. The influence of the fissure boundary was investigated in soil column investigations as well as simulated pressure infusion within a brain.

VII.2.3 Soil Column Investigations

VII.2.3.1 Unsplit

Pressure (Pa) - 0 to 100 Pa

Displacements (mm) - 0 to 17.70 mm

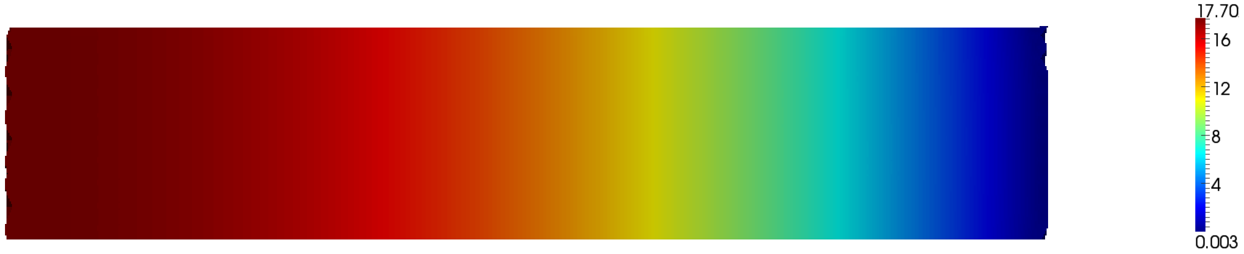

Figure VII. 8: These are the pressure and displacement solutions when 100 Pa was applied to the left hand side of the column, and it was specified that the pressure and displacement on the right hand side of the column is 0. This rectangular mesh was unsplit. Warm colors represent higher pressure and displacement values, while cooler colors represent lower pressure and displacement values.

To investigate the influence of the developed fissure boundary condition, initial soil column investigations were performed. A 3D, tetrahedral, finite element mesh in the shape of a rectangular prism was generated to represent a column of soil. Like the brain, soil is poroelastic. As a baseline, the rectangular column remained intact (Figure VII.8). On the left hand side of the column, 100 Pa of pressure was applied. On the right hand side of the column, the pressure and displacement was fixed at 0. In this unsplit mesh, the gradient in pressure and displacement was communicated across the entire rectangle (Figure VII.8).

Pressure (Pa) - 0 to 100 Pa

Displacements (mm) - 0 to 25.24 mm

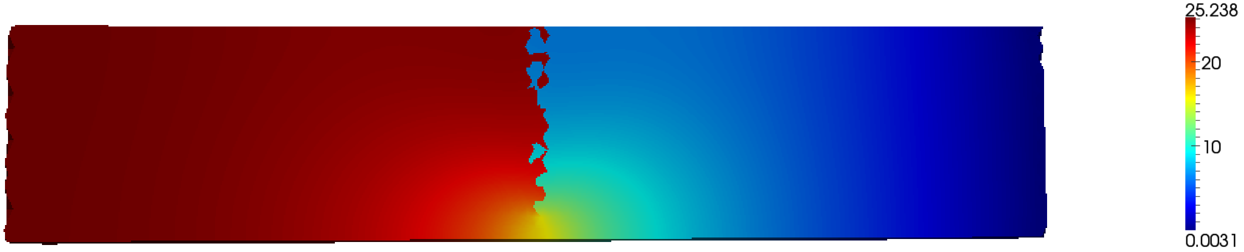

Figure VII. 9: These are the pressure and displacement solutions when 100 Pa was applied to the left hand side of the column, and it was specified that the pressure and displacement on the right hand side of the column is 0. This rectangular mesh was split, with no boundary conditions enforced at the split within the mesh. Warm colors represent higher pressure and displacement values, while cooler colors represent lower pressure and displacement values.

VII.2.3.2 Split

To understand the impact of simply splitting the same rectangular mesh partially, the same boundary conditions applied to the unsplit mesh are applied to a partially split mesh (Figure VII.9). In this mesh, no boundary conditions are enforced at the split within the mesh. The pressure solution differs from the unsplit mesh, and compartmentalization was evident. Due to the partial split of the mesh, some pressure was still moved from the left hand side of the rectangle to the right hand side. Looking at the deformed solution, it was evident that the left hand side of the rectangle folded into the right hand side of the rectangle (Figure VII.9). This solution does not make physical sense, which led us to the conclusion that simply splitting the mesh was not sufficient to represent a fissure boundary.

VII.2.3.3 Fixed Split (dural septa)

In the next iteration of this soil column experiment, the same pressure and displacement boundary conditions as the unsplit mesh were applied to the split mesh. However, the split boundary condition was fixed in displacement. This is similar to how the dura of the brain is treated in the majority of this thesis. The solutions in displacement were more reasonable, since the mesh did not fold in on itself (Figure VII.10). However, the boundary condition on the split led to a highly restricted displacement, limiting the majority of the deformations to the left hand side of the rectangular mesh.

Pressure (Pa) - 0 to 100 Pa

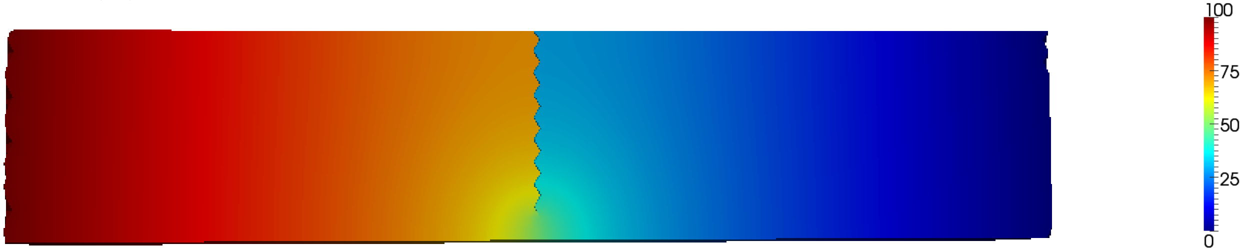

Displacements (mm) - 0 to 3.15 mm

Figure VII. 10: These are the pressure and displacement solutions when 100 Pa is applied to the left hand side of the column, and it was specified that the pressure and displacement on the right hand side of the column is 0. This rectangular mesh was split, and the split is fixed in displacement. Warm colors represent higher pressure and displacement values, while cooler colors represent lower pressure and displacement values.

VII.2.3.4 Fissure

To understand the influence of the developed fissure boundary condition, the same split mesh had 100 Pa applied to the left hand side, and the right hand side of the rectangle was prescribed as 0 Pa and fixed in displacement. The split was treated with the fissure boundary condition (Figure VII.11). The nodes on either side of the split are coupled mechanically, however fluid is not permitted to flow through it. The pressure distribution appears similar in nature to the pressure distributions when the split is unconstrained (Figure VII.9) or fixed (Figure VII.10). The displacement solution, when the fissure is treated as a fissure boundary condition, how permits displacement to communicate across the divide (Figure VII.11). This behavior was in line with our hypothesis that fissures within the brain allow strain to communicate, but fluid cannot flow through them. Also, the mesh did not fold over itself, indicating the physical validity of the solution.

Pressure (Pa) - 0 to 100 Pa

Displacements (mm) - 0 to 12.23 mm

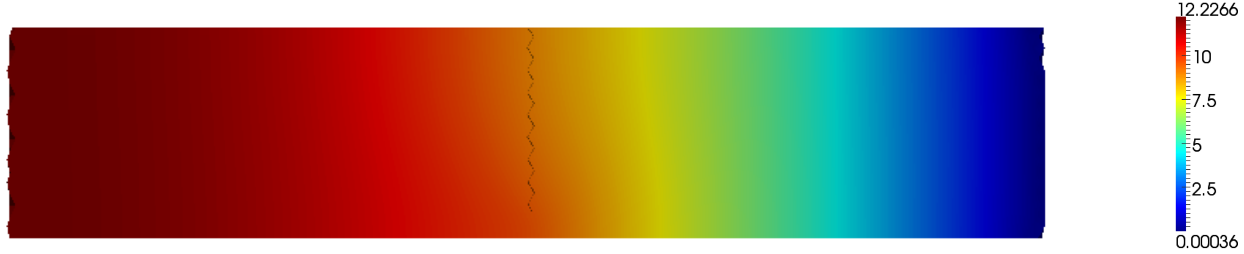

Figure VII. 11: These are the pressure and displacement solutions when 100 Pa is applied to the left hand side of the column, and it is specified that the pressure and displacement on the right hand side of the column is 0. This rectangular mesh is split, and the split is treated as a fissure. Strain can communicate across the split, but fluid cannot flow through it. Warm colors represent higher pressure and displacement values, while cooler colors represent lower pressure and displacement values.

VII.2.4 Brain Pressure Infusion Simulations

VII.2.4.1 Methods

Due to the lack of clinical or animal data, several simulation studies of pressure infusion within a brain were simulated to understand the impact of including fissure boundary conditions within a model of the brain. Once again, all of the simulations were constructed on a tetrahedral finite element mesh. The two governing equations were Equations (VII.10) and (VII.11). Three simulations were performed. They all represented interstitial fluid flow from a pressure infusion source. The boundary conditions applied to all three was a slip condition on the outer surface of all three meshes (Figure VII.12), representing the outer dura of the brain. The pressure at the outer surface of all three meshes (Figure VII.12) were prescribed to be 0 Pa with a Dirichlet boundary condition. The pressure infusion source, simulating a catheter, visualized by the red sphere in all three details of Figure VII.12, was treated as a Dirichlet boundary condition with a

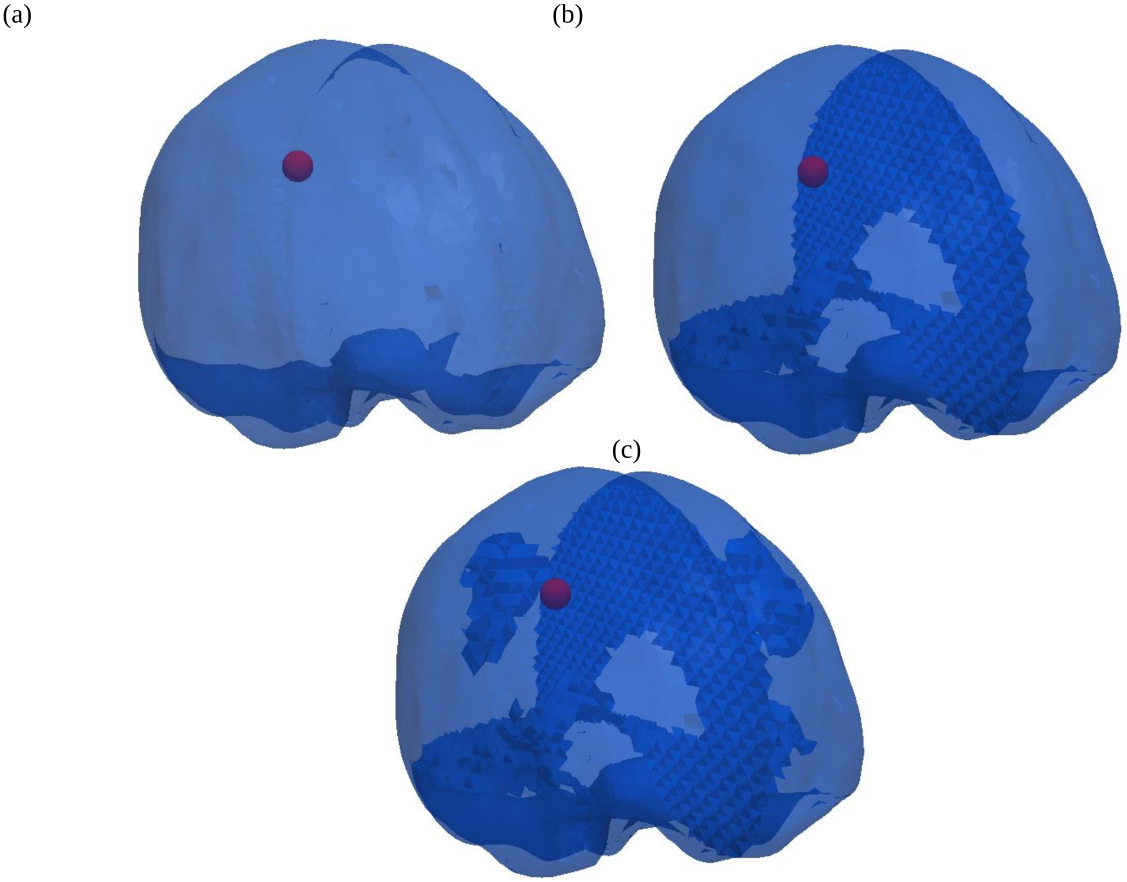

Figure VII. 12: The mesh in Detail (a) shows the brain treated as a homogenous material. The mesh in Detail (b) illustrates the brain as homogenous tissue with the dural septa. The mesh in Detail (c) represents the brain as homogenous tissue with the dural septa, Sylvian fissure, and central sulcus.

hydraulic pressure of 1333 Pa. The elastic modulus of the brain was 2100 Pa, and the Poisson ratio value was 0.45 for all three simulations.

The three simulations differed in what brain anatomy was included. In simulation one, the brain was treated as a homogeneous material with no anatomical features (Figure VII.12.a). The second simulation of interstitial fluid flow from a catheter, incorporated the dural septa into the mesh (Figure VII.12.b). The dural septa consists of the falx, and the left and right tentorium. They were incorporated into the original mesh using a custom splitting code, which splits the mesh along the membrane. The dural septa is a rigid structure within the brain. In order to capture this within the model, the dural septa nodes were rigidly fixed using Dirichlet boundary conditions, prescribing 0 displacement. These nodes also had Neumann boundary conditions prescribing no flux in pressure. The third simulation of the interstitial fluid flow from the pressure infusion source introduced more structural specificity with the central sulcus and Sylvian fissure in addition to the dural septa. This mesh can be visualized in Figure VII.12.c. The boundary conditions used to describe the dural septa were kept the same as in the second simulation. The central sulcus and the

Sylvian fissure were incorporated using the splitting code. The fissure and sulcus are physical divisions between the lobes of the brain, but the tissue on either side of the features are in physical contact with each other. Fluid, however, cannot flow across the fissure because it is a void space. In the model, at the fissure and sulcus, it was prescribed that strain could communicate across, but fluid could not flow across the fissure and sulcus.

VII.2.4.2 Results

All three of the simulations were solved, providing displacement and pressure solutions. In simulation one, deformations occurred in both hemispheres (Figure VII.13.a), and the pressure gradient radiated symmetrically from the catheter (Figure VII.14.a). In simulation two, the deformations were limited to the right hemisphere (Figure VII.13.b). There was also an alteration in the pressure solution distribution (Figure VII.14.b) due to the presence of the dural septa. In simulation three, the additional presence of the fissure/ sulcus, modifies the deformation pattern (Figure VII.13.c), and the movement of the fluid is additionally constrained as evident from the pressure solution (Figure VII.14.c). The symmetric pressure gradient is no longer present.

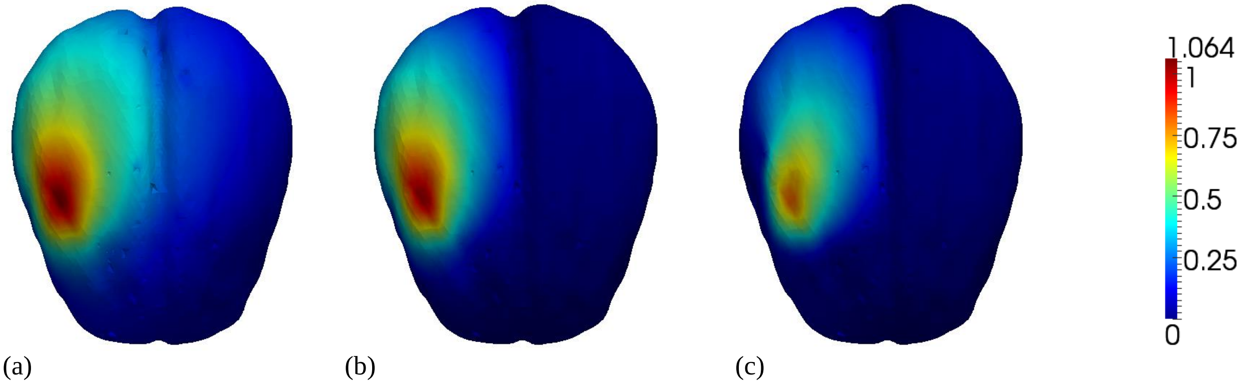

Figure VII. 13: This is an image of the displacement solution (mm) on the surface of the meshes. Detail (a) is the results of the mesh, which treats the brain as a completely homogenous material. Detail (b) is the result of the mesh with the dural septa incorporated. Detail (c) is the result of the mesh with the dural septa, Sylvian fissure, and central sulcus incorporated.

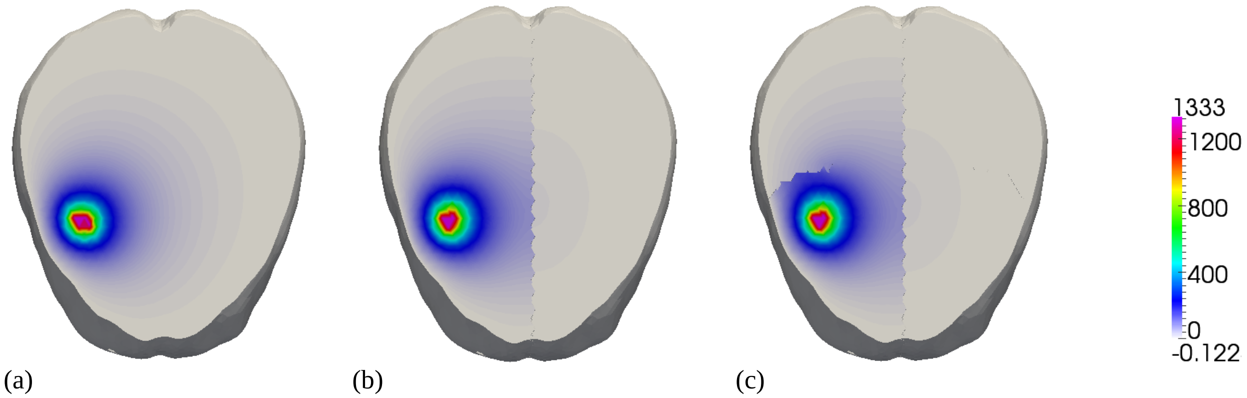

Figure VII. 14: This is an image of the pressure solution (Pa) at the same cross section. Detail (a) is the results of the mesh, which treats the brain as a completely homogenous material. Detail (b) is the result of the mesh with the dural septa incorporated. Detail (c) is the result of the mesh with the dural septa, Sylvian fissure, and central sulcus incorporated.

As an additional assessment of the influence the fissure boundary played in influencing the results, the pressure gradients were calculated in the area around the simulated catheter. Figure VII.15, visualizes these calculations. While simulation one and two did not contain the fissure boundary condition, the closest fissure boundary was visualized in all three details of Figure VII.15 in order to provide a spatial frame of reference and better interpret the change in pressure gradient, based on the boundary conditions. When the simulated brain had no features, the pressure moved away from the source in all directions approximately evenly; also, the pressure gradients moved through the spatial location of the fissure without any interference (Figure VII.15.a). The addition of the dural septa into the mesh changed the pressure gradients, relative to the simulation with no features, however there were still gradients through the fissure boundary (Figure VII.15.b). Accounting for the fissure boundary condition dramatically changed the pressure gradient behavior (Figure VII.15.c). Rather than moving through this feature, there was a clear movement of fluid around the fissure, which is in agreement with Figure VII.14.

While preliminary in nature, both the soil column studies and brain simulation studies provide evidence that our hypothesized treatment of fissure boundary conditions result in changes in poroelastic solutions. This fissure boundary treatment allows the tissue, divided by a split, to move together, while preventing fluid motion through the divide.

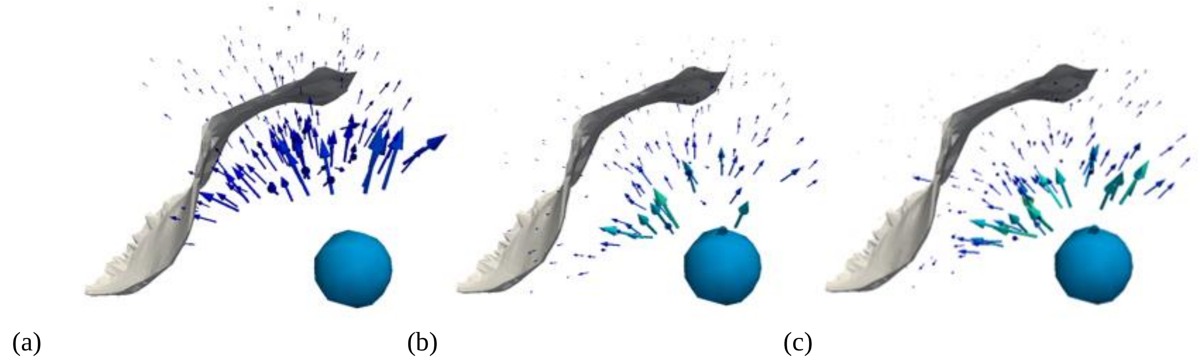
(a) (b) (c)

Figure VII. 15: This is visualization of the gradients in pressure calculated from the pressure solution (Pa). In all three details, the blue sphere represents the pressure infusion source. The white plane is one of the fissure boundaries. Detail (a) is the results of the mesh, which treats the brain as a completely homogenous material. Detail (b) is the result of the mesh with the dural septa incorporated. Detail (c) is the result of the mesh with the dural septa, Sylvian fissure, and central sulcus incorporated.

VII.2.5 Clinical Applications

Elevated intracranial pressure (ICP) is a relatively common complication arising from central nervous system disorders, stroke, hydrocephalus, space occupying lesions, cerebral edema, and traumatic brain injuries [56]. ICP is governed by the Monroe-Kellie Doctrine, which states that the cranial cavity is of a fixed volume, consisting of blood, cerebrospinal fluid (CSF), and brain tissue. Therefore an increase in volume of one of the three components is compensated for by a decrease in volume of another [54]. When tumors grow to a point where CSF and blood can no longer be displaced, ICP elevates. The anatomical features in the brain separates it into sections, and some features can serve as a barrier to interstitial fluid flow. Incorporating more detailed neuroanatomy, including fissures, within biotransport simulations is important for predicting biomechanical reactions to ICP-altering disorders. This can help develop diagnostic tools in a wide range of medical situations associated with elevated ICP.

One such situation includes determining if a patient is at risk for brain herniation [59]. Herniation is the movement of a portion of the brain into another part of the brain, and is dependent on the location of the disturbance in pressure [59]. The most common herniation is the uncal herniation, where a portion of the temporal lobe gets dislodged [59]. This illustrates the significance of compartmentalization within the brain. More accurately representing the behavior of the brain by modeling fissured could aid in treatment planning for patients at risk for brain herniation and a wide range of other disorders associated with elevated ICP. Another potential direction for this work drug delivery, specifically convection-enhanced drug delivery. The blood brain barrier prohibits the motion of chemotherapeutic agents to tumors. As a means to circumvent this, a catheter can be placed within the brain, and convection is used to transport the chemotherapeutic agents within the brain [169]. This technique is not widely accepted due to how difficult it is to direct the chemotherapeutic agent to the desired target. Therefore using computational models to plan drug delivery is an area of significant clinical impact.

VII.2.6 Future Studies to Investigation Fissure Representation

The results of the simulation studies into the hypothesized modeling of fissures indicates that their presence alters both the solid and fluid movement of poroelastic materials, specifically the brain. This is encouraging, however, without either animal or human studies, it was not possible within the scope of this thesis to investigate this concept beyond simulation studies. Based on the work within this thesis, it is clear that anatomical features, both normal and diseased, play significant roles in brain tissue behavior. The ability to account for additional features with greater accuracy could increase the use of computational modeling in neurosurgical applications.

In order to test the validity of this description of fissures, an animal study is necessary An *in vivo* porcine study where a traceable agent is infused into the brain, in a method similar to convection-enhanced drug delivery would be ideal. Before the infusion, obtaining a high resolution T_1 weighted MRI scan of the animal subject would enable the fissures and other structures to be digitized after the experiment for meshing. Serial scans, selected based on the nature of the infused agent, would be needed in short time intervals at the time of and for the time following the infusion of the agent. During these times, it will be necessary to note the exact time of scan, for temporal information, and ensure the porcine skull can be digitized in every image of the agent's transport. Having the skull within frame would permit the scans to be rigidly registered to one another, ensuring the data is useable. After the animal experiment is concluded, a mesh should be generated based on the anatomical porcine scan. In a follow-up simulation study, similar to the one described in the preliminary investigation, the agent transportation should be simulated when no features are accounted for, features not including the fissures are accounted for, and when everything, including the fissures are included. The results of the simulated agent transport can be directly compared to the *in vivo* imaging of the agent transport obtained during the physical experiment. Based on the results, the description of the fissure boundary condition can be refined further. If this experiment is successful, additional animal studies and retrospective human studies can be used to assess the importance and validity of modeling fissures within the brain.

Overall, the preliminary results obtained indicate that incorporating these boundaries change both the behavior of poroelastic materials. Based on the conclusions drawn from this thesis as a whole, incorporating enhanced anatomical features can improve the fidelity of computational models of the brain. Investigating the role of fissures, specifically, can potentially lead to interesting breakthroughs related to elevated ICP and drug transport.

VII.3 Thesis Conclusions

An estimated 296,851 new cases of brain and nervous system cancer were diagnosed globally in 2018 with 241,037 of these cases resulting in the patient’s death [1]. Between 2011 and 2015, the five year survival rate of malignant brain and other central nervous system tumors diagnosed in the United States was approximately 35.0% [21]. Two clinical challenges that directly influence this survival rate are accurate diagnosis and complete resection of the tumor. This research hypothesizes that enhancing anatomical models of intracranial biomechanics with the addition of effects from space-occupying lesions will improve the predictive fidelity of biomechanical models for use in neurosurgical and interventional applications. Modeling of normal brain structures was enhanced using novel anatomical constraints and material property reconstructions, resulting in the accurate capturing of intracranial pressure compartmentalization. Investigating the effects of space-occupying lesions, a biophysical model-based framework for intracranial tumors was developed to estimate biophysical tumor growth properties using standard-of-care imaging and was capable of noninvasive discrimination of tumor recurrence from radiation-induced necrosis. Accounting for both normal brain structure and the influence of a growing tumor, a model-based atlas of tumor cavity collapse was conceived that predicted intra-operative brain shifts from tumor resection. Accounting for both patient-specific structure and disease, the models in this work improve the fidelity of biomechanical modeling for neurosurgical and interventional applications.

APPENDIX

A Analytic Solutions for Section III.1.4

A.1 Summary and Contributions

The finite element models used to model tumor resection and cavity collapse (section III.1.4) were custom built using C++. The reaction-diffusion model of tumor growth was validated by comparing the results of the model, at different points in time, versus the solutions generated of the same test problem in COMSOL. As a means of validating the model of pressure based on the tumor's edema and the model of displacement with a tumor present, analytic solutions of test problems were generated and compared to the finite element model solutions. The finite element models were analytically verified. The analytical solutions which they were compared to are contained within this appendix.

A.2 Analytical Solution - Model of Pressure Based on the Tumor's Edema

A.2.1 Geometry

The 3D solution generated by the finite element model was compared to an analogous 1D solution in Cartesian coordinates. The geometry of the 3D mesh was a rectangular prism. The geometry of the 1D problem is a rectangle (Figure A.1), where the movement in pressure was restricted to be along the x-axis.

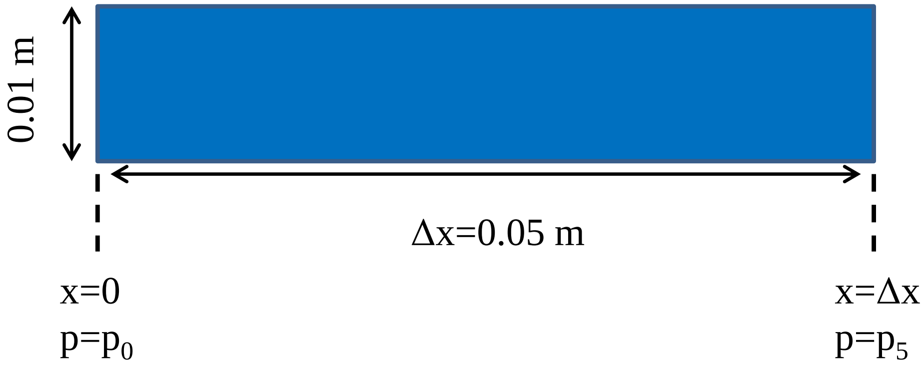

Figure A. 1: This is a visualization of the geometry used to generate the analytical solution. On the left-hand side of the rectangle, a pressure of p_0 is enforced. On the right-hand side of the rectangle, a pressure of p_5 is enforced.

A.2.2 Test Problem 1 – No Edema Everywhere

The governing equation is (III.49.a). In Equation (III.49.a), p is pressure, k is hydraulic conductivity, k_c is capillary permeability, and p_c is intracapillary pressure.

$$-\nabla \cdot k\nabla p + k_c(p - p_c) = 0 \qquad \text{(III.49.a)}$$

In test problem 1, no edema is present, so the governing equation becomes (III.49.b):

$$-\nabla \cdot k\nabla p = 0 \qquad \text{(III.49.b)}$$

Rewriting (III.49.b) in 1-dimension (1D), it becomes (A.1).

$$-k\frac{\partial^2 p}{\partial x^2} = 0 \qquad \text{(A.1)}$$

The analytic form of the solution to (A.1) is (A.2).

$$p(x) = c_2 x + c_1 \qquad \text{(A.2)}$$

The boundary condition on left hand side of the rectangle (Figure A.1) is a fixed pressure of p_0 ($x = 0$, $p = p_0$). Enforcing the boundary condition in (A.3.a), the constant, c_1, can be solved.

$$p(0) = c_2(0) + c_1 = p_0 \qquad \text{(A.3.a)}$$

$$c_1 = p_0 \qquad \text{(A.3.b)}$$

The boundary condition on right hand side of the rectangle (Figure A.1) is a fixed pressure of p_5 ($x = \Delta x$, $p = p_5$). Enforcing the boundary condition in (A.3.a), c_2 can be solved.

$$p(\Delta x) = c_2(\Delta x) + c_1 = p_5 \qquad \text{(A.4.a)}$$

$$p(\Delta x) = c_2(\Delta x) + p_0 = p_5 \qquad \text{(A.4.b)}$$

$$c_2 = \frac{p_5 - p_0}{\Delta x} \qquad \text{(A.4.c)}$$

Substituting (A.3.b) and (A.4.c) into the analytic form, (A.2), the analytic solution to test problem 1 is (A.5).

$$p(x) = c_2 x + c_1 \qquad \text{(A.2)}$$

$$p(x) = \left(\frac{p_5 - p_0}{\Delta x}\right) x + p_0 \qquad \text{(A.5)}$$

A.2.3 Test Problem 2 – Edema Everywhere

The governing equation is (III.49.a).

$$-\nabla \cdot k\nabla p + k_c(p - p_c) = 0 \qquad \text{(III.49.a)}$$

This equation can be rewritten.

$$-\nabla \cdot k\nabla p + k_c p = k_c p_c \qquad \text{(III.49.a)}$$

Rewriting (III.49.a) in 1D, (A.6) is obtained.

$$-k\frac{\partial^2 p}{\partial x^2} + k_c p = k_c p_c \qquad \text{(A.6)}$$

The analytic form of the solution to (A.6) is (A.7).

$$p(x) = c_1 e^{\left(\sqrt{\frac{k_c}{k}}x\right)} + c_2 e^{-\left(\sqrt{\frac{k_c}{k}}x\right)} + p_c \tag{A.7}$$

The boundary condition on left hand side of the rectangle (Figure A.1) is a fixed pressure of p_0 ($x = 0, p = p_0$). Enforcing the boundary condition in (A.7), a representation of c_1 can obtained.

$$p(0) = c_1 e^{\left(\sqrt{\frac{k_c}{k}}0\right)} + c_2 e^{-\left(\sqrt{\frac{k_c}{k}}0\right)} + p_c = p_0 \tag{A.8.a}$$

$$p(0) = c_1 e^{(0)} + c_2 e^{-(0)} + p_c = p_0 \tag{A.8.b}$$

$$c_1 = p_0 - p_c - c_2 \tag{A.8.c}$$

The boundary condition on right hand side of the rectangle (Figure A.1) is a fixed pressure of p_5 ($x = \Delta x$, $p = p_5$).

$$p(\Delta x) = c_1 e^{\left(\sqrt{\frac{k_c}{k}}\Delta x\right)} + c_2 e^{-\left(\sqrt{\frac{k_c}{k}}\Delta x\right)} + p_c = p_5 \tag{A.9.a}$$

Substituting (A.8.c) into (A.9.a), c_2 can be solved.

$$p(\Delta x) = (p_0 - p_c - c_2) e^{\left(\sqrt{\frac{k_c}{k}}\Delta x\right)} + c_2 e^{-\left(\sqrt{\frac{k_c}{k}}\Delta x\right)} + p_c = p_5 \tag{A.9.b}$$

$$(p_0 - p_c) e^{\left(\sqrt{\frac{k_c}{k}}\Delta x\right)} - c_2 e^{\left(\sqrt{\frac{k_c}{k}}\Delta x\right)} + c_2 e^{-\left(\sqrt{\frac{k_c}{k}}\Delta x\right)} = p_5 - p_c \tag{A.9.c}$$

$$c_2 \left(e^{-\left(\sqrt{\frac{k_c}{k}}\Delta x\right)} - e^{\left(\sqrt{\frac{k_c}{k}}\Delta x\right)} \right) = p_5 - p_c - (p_0 - p_c) e^{\left(\sqrt{\frac{k_c}{k}}\Delta x\right)} \tag{A.9.d}$$

$$c_2 = \frac{p_5 - p_c - (p_0 - p_c) e^{\left(\sqrt{\frac{k_c}{k}}\Delta x\right)}}{e^{-\left(\sqrt{\frac{k_c}{k}}\Delta x\right)} - e^{\left(\sqrt{\frac{k_c}{k}}\Delta x\right)}} \tag{A.9.e}$$

Substituting (A.8.c) and (A.9.e) into the analytic form, (A.7), the analytic solution to test problem 2 is (A.10).

$$p(x) = c_1 e^{\left(\sqrt{\frac{k_c}{k}}x\right)} + c_2 e^{-\left(\sqrt{\frac{k_c}{k}}x\right)} + p_c \tag{A.7}$$

$$p(x) = \left(p_0 - p_c - \frac{p_5 - p_c - (p_0 - p_c) e^{\left(\sqrt{\frac{k_c}{k}}\Delta x\right)}}{e^{-\left(\sqrt{\frac{k_c}{k}}\Delta x\right)} - e^{\left(\sqrt{\frac{k_c}{k}}\Delta x\right)}} \right) e^{\left(\sqrt{\frac{k_c}{k}}x\right)} + \left(\frac{p_5 - p_c - (p_0 - p_c) e^{\left(\sqrt{\frac{k_c}{k}}\Delta x\right)}}{e^{-\left(\sqrt{\frac{k_c}{k}}\Delta x\right)} - e^{\left(\sqrt{\frac{k_c}{k}}\Delta x\right)}} \right) e^{-\left(\sqrt{\frac{k_c}{k}}x\right)} + p_c \tag{A.10}$$

A.3 Analytical Solution – Displacements with the Tumor Present

A.3.1 Geometry

The 3D solution generated by the finite element model was compared to an analogous 1D solution in spherical coordinates. The geometry of the 3D mesh was a concentric sphere. The geometry of the 1D problem is a concentric circle (Figure A.2), where the displacement was restricted to be along the radial direction.

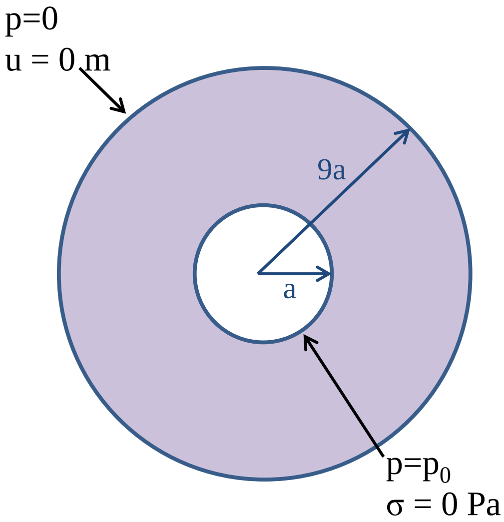

Figure A. 2: This is a visualization of the geometry used to generate the analytical solution. There is a 9 to 1 ratio between the outer and inner radii of the concentric circle. On the outer boundary of the circle, the displacement is fixed and pressure is set to 0. On the inner boundary of the circle, it is stress free and a pressure of p_0 is prescribed.

A.3.2 Analytic Solution of the Pressure Gradient

The governing equation is (III.58). In this equation, an isotropic Hookean linear elastic constitutive model is assumed. The constant coefficients, α and β, are empirically derived constants which dictate the amount of influence the tumor cells and edema have respectively. The analytical solution for this equation is found in Sections (A.3.2) and (A.3.3).

$$\nabla \cdot \sigma = \alpha \nabla C + \beta \nabla p \tag{III.58}$$

In the test problem, only edema is present, so (III.58) can be rewritten as (A.11).

$$\nabla \cdot \sigma = \beta \nabla p \tag{A.11}$$

First, the functional form of the gradient of pressure in spherical coordinates needs to be obtained. For the purposes of this test problem, it is assumed that pressure only moves in the radial direction. The governing equation for pressure, (III.49.b), can be written in spherical coordinates, (A.12.d).

$$-\nabla \cdot k \nabla p = 0 \tag{III.49.b}$$

$$-k \frac{\partial^2 p}{\partial r^2} = 0 \tag{A.12.a}$$

$$\frac{\partial^2 p}{\partial r^2} = 0 \tag{A.12.b}$$

$$\frac{\partial^2 p}{\partial r^2} = \frac{1}{r^2}\frac{\partial}{\partial r}\left(r^2\frac{\partial p}{\partial r}\right) = \frac{1}{r^2}\left(r^2\frac{\partial^2 p}{\partial r^2} + \frac{\partial p}{\partial r}2r\right) = 0 \tag{A.12.c}$$

$$\frac{\partial^2 p}{\partial r^2} + \frac{2}{r}\frac{\partial p}{\partial r} = 0 \tag{A.12.d}$$

For simplification, substitute in $y = \frac{\partial p}{\partial r}$ and $y' = \frac{\partial^2 p}{\partial r^2}$ into (A.12.d) to get (A.13.a). An analytical form of the solution to (A.13.a) can be written as (A.13.e).

$$y' + \frac{2}{r}y = 0 \tag{A.13.a}$$

$$y' = -\frac{2}{r}y \tag{A.13.b}$$

$$\int \frac{\partial y/\partial r}{y}\partial r = \int -\frac{2}{r}\partial r \tag{A.13.c}$$

$$\ln\big(y(r)\big) = -2\ln(r) + c_1 \tag{A.13.d}$$

$$y(r) = \frac{c_1}{r^2} \tag{A.13.e}$$

Substitute back in the expressions for $y(r)$ in (A.13.e), (A.13.f) is obtained. This can be solved to find the analytic form (A.13.h) which is the solution to (A.12.d).

$$\frac{\partial p}{\partial r} = \frac{c_1}{r^2} \tag{A.13.f}$$

$$\int \partial p = \int \frac{c_1}{r^2}\partial r \tag{A.13.g}$$

$$p = -\frac{c_1}{r} + c_2 \tag{A.13.h}$$

The first boundary condition is no pressure on the outer radius (Figure A.2) ($p(9a) = 0$). Plugging in the boundary condition information into (A.13.h), c_2 can be solved for.

$$p(9a) = 0 = -\frac{c_1}{9a} + c_2 \tag{A.14.a}$$

$$c_2 = \frac{c_1}{9a} \tag{A.14.b}$$

The second boundary condition is a constant pressure of $p_0$on the inner radius (Figure A.2) ($p(a) = p_0$). Plugging in the boundary condition into (A.13.h), c_1 can be solved for.

$$p(a) = p_0 = -\frac{c_1}{a} + c_2 = -\frac{c_1}{a} + \frac{c_1}{9a} = \left(\frac{-8}{9a}\right)c_1 \tag{A.15.a}$$

$$c_1 = \frac{-9ap_0}{8} \tag{A.15.b}$$

Substitute (A.14.b) and (A.15.b) back into (A.13.h) to obtain the analytic solution of (A.13.h). This solution is (A.16).

$$p = -\frac{c_1}{r} + c_2 \tag{A.13.h}$$

$$p(r) = \frac{1}{r}\left(\frac{9ap_0}{8}\right) - \frac{p_o}{8} \tag{A.16}$$

Taking the first derivative of (A.16), the analytic form of the gradient is (A.17).

$$\frac{\partial p}{\partial r} = \left(\frac{-9ap_0}{8}\right)\frac{1}{r^2} \tag{A.17}$$

A.3.3 Analytic Solution of Displacement

Once again, the governing equation is (A.11).

$$\nabla \cdot \sigma = \beta \nabla p \tag{A.11}$$

Substitute in the analytic solution of the gradient, (A.17), into (A.11), (A.18.a) is obtained. From (A.18.a) an expression of radial displacement ($u(r)$) due to a pressure gradient in spherical coordinates can be obtained. This is equation (A.18.g).

$$\nabla \cdot \sigma = \beta\left(\frac{-9ap_0}{8}\right)\frac{1}{r^2} \tag{A.18.a}$$

$$(2\mathrm{G}+\lambda)\frac{\partial}{\partial \mathrm{r}}\left(\frac{1}{r^2}\frac{\partial}{\partial \mathrm{r}}(r^2 u)\right) = -\beta\left(\frac{9ap_0}{8}\right)\frac{1}{r^2} \tag{A.18.b}$$

$$\frac{\partial}{\partial \mathrm{r}}\left(\frac{1}{r^2}\frac{\partial}{\partial \mathrm{r}}(r^2 u)\right) = -\frac{\beta}{(2\mathrm{G}+\lambda)}\left(\frac{9ap_0}{8}\right)\frac{1}{r^2} \tag{A.18.c}$$

$$\frac{\partial}{\partial \mathrm{r}}\left(\frac{1}{r^2}\left(\mathrm{r}^2\frac{\partial u}{\partial r} + u2r\right)\right) = -\frac{\beta}{(2\mathrm{G}+\lambda)}\left(\frac{9ap_0}{8}\right)\frac{1}{r^2} \tag{A.18.d}$$

$$\frac{\partial}{\partial \mathrm{r}}\left(\frac{\partial u}{\partial r} + \frac{1}{r}2u\right) = -\frac{\beta}{(2\mathrm{G}+\lambda)}\left(\frac{9ap_0}{8}\right)\frac{1}{r^2} \tag{A.18.e}$$

$$\frac{\partial^2 u}{\partial r^2} + \frac{2}{r}\frac{\partial u}{\partial r} - \frac{2u}{r^2} = -\frac{\beta}{(2\mathrm{G}+\lambda)}\left(\frac{9ap_0}{8}\right)\frac{1}{r^2} \tag{A.18.f}$$

$$r^2\frac{\partial^2 u}{\partial r^2} + 2r\frac{\partial u}{\partial r} - 2u = -\frac{\beta}{(2\mathrm{G}+\lambda)}\left(\frac{9ap_0}{8}\right) \tag{A.18.g}$$

Integrating (A.18.g) twice with respect to r, the analytic form of $u(r)$ and its derivative are (A.19) and (A.20) respectively.

$$u(r) = \frac{c_2}{r^2} + c_1 r + \frac{1}{2}\left(\frac{\beta}{2G+\lambda}\right)\left(\frac{9ap_0}{8}\right) \tag{A.19}$$

The derivative of $u(r)$ is (A.20).

$$\frac{\partial u}{\partial r} = -2\frac{c_2}{r^3} + c_1 \tag{A.20}$$

The first boundary condition is that the displacement at the outer radius (Figure A.2) is fixed to 0 ($u(9a) = 0$). Enforcing this boundary condition in (A.19), c_1 can be solved.

$$u(9a) = \frac{c_2}{(9a)^2} + c_1 9a + \frac{1}{2}\left(\frac{\beta}{2G+\lambda}\right)\left(\frac{9ap_0}{8}\right) = 0 \tag{A.21.a}$$

$$c_1 = -\frac{c_2}{729a^3} - \frac{\beta p_0}{16(2G+\lambda)} \tag{A.21.b}$$

The second boundary condition, represented in (A.22.a) is that the inner radius, a, is stress free.

$$\sigma(a) = 0 \tag{A.22.a}$$

In spherical coordinates $\sigma = (2G + \lambda)\frac{du}{dr} + \frac{2\lambda}{r}u$. Substituting this expression into (A.22.a), (A.22.b) is generated.

$$(2G + \lambda)\frac{du}{dr} + \frac{2\lambda}{a}u = 0 \tag{A.22.b}$$

Plugging in the expressions for $\frac{\partial u}{\partial r}$ (A.20) and u (A.19) into (A.22.b), (A.22.c) is generated.

$$(2G + \lambda)\left(-2\frac{c_2}{a^3} + c_1\right) + \frac{2\lambda}{a}\left(\frac{c_2}{a^2} + c_1 a + \frac{1}{2}\left(\frac{\beta}{2G+\lambda}\right)\left(\frac{9ap_0}{8}\right)\right) = 0 \tag{A.22.c}$$

$$(2G + \lambda)\left(-2\frac{c_2}{a^3} + c_1\right) + \frac{2\lambda}{a}\left(\frac{c_2}{a^2} + \left(-\frac{c_2}{729a^3} - \frac{\beta p_0}{16(2G+\lambda)}\right)a + \frac{1}{2}\left(\frac{\beta}{2G+\lambda}\right)\left(\frac{9ap_0}{8}\right)\right) = 0 \tag{A.22.d}$$

Simplifying (A.22.d), c_2 can be solved for.

$$c_2 = \left(\frac{729a^3}{-3\lambda-2918G}\right)\left(\frac{\beta p_0(2G-15\lambda)}{16(2G+\lambda)}\right) \tag{A.22.e}$$

Substituting the expressions for the constants, (A.21.b) and (A.22.e), into the analytic form, (A.19), the analytic solution (A.20) for radial displacements with a tumor present can be obtained.

$$u(r) = \frac{c_2}{r^2} + c_1 r + \frac{1}{2}\left(\frac{\beta}{2G+\lambda}\right)\left(\frac{9ap_0}{8}\right) \tag{A.19}$$

$$u(r) = \left[\left(\frac{729a^3}{-3\lambda-2918G}\right)\left(\frac{\beta p_0(2G-15\lambda)}{16(2G+\lambda)}\right)\right]\frac{1}{r^2} + \left[-\frac{1}{729a^3}\left(\frac{729a^3}{-3\lambda-2918G}\right)\left(\frac{\beta p_0(2G-15\lambda)}{16(2G+\lambda)}\right) - \frac{\beta p_0}{16(2G+\lambda)}\right]r + \frac{1}{2}\left(\frac{\beta}{2G+\lambda}\right)\left(\frac{9ap_0}{8}\right) \tag{A.20}$$

REFERENCES

[1] F. Bray, J. Ferlay, I. Soerjomataram, R. L. Siegel, L. A. Torre, and A. Jemal, "Global Cancer Statistics 2018: Globocan Estimates of Incidence and Mortality Worldwide for 36 Cancers in 185 Countries," *CA: a cancer journal for clinicians,* vol. 68, no. 6, pp. 394-424, 2018.

[2] Q. T. Ostrom *et al.*, "Cbtrus Statistical Report: Primary Brain and Central Nervous System Tumors Diagnosed in the United States in 2008-2012," *Neuro Oncol,* vol. 17 Suppl 4, pp. iv1-iv62, Oct 2015.

[3] B. A. Kohler *et al.*, "Annual Report to the Nation on the Status of Cancer, 1975-2007, Featuring Tumors of the Brain and Other Nervous System," *J Natl Cancer Inst,* vol. 103, no. 9, pp. 714-36, May 04 2011.

[4] M. Lacroix *et al.*, "A Multivariate Analysis of 416 Patients with Glioblastoma Multiforme: Prognosis, Extent of Resection, and Survival," *Journal of Neurosurgery,* vol. 95, no. 2, pp. 190-198, 2001.

[5] S. K. Kyriacou, A. Mohamed, K. Miller, and S. Neff, "Brain Mechanics for Neurosurgery: Modeling Issues," *Biomech Model Mechanobiol,* vol. 1, no. 2, pp. 151-164, Oct. 2002.

[6] H. L. P. Harpold, E. C. J. Alvord, and K. R. Swanson, "The Evolution of Mathematical Modeling of Glioma Proliferation and Invasion," *J Neuropathol Exp Neurol,* vol. 66, no. 1, pp. 1-9, 2007.

[7] R. Rockne *et al.*, "Predicting the Efficacy of Radiotherapy in Individual Glioblastoma Patients in Vivo: A Mathematical Modeling Approach," *Phys Med Biol,* vol. 55, no. 12, pp. 3271-85, Jun 21 2010.

[8] C. H. Wang *et al.*, "Prognostic Significance of Growth Kinetics in Newly Diagnosed Glioblastomas Revealed by Combining Serial Imaging with a Novel Biomathematical Model," *Cancer Res,* vol. 69, no. 23, pp. 9133-40, Dec 01 2009.

[9] N. Verma, M. C. Cowperthwaite, M. G. Burnett, and M. K. Markey, "Differentiating Tumor Recurrence from Treatment Necrosis: A Review of Neuro-Oncologic Imaging Strategies," *Neuro Oncol,* vol. 15, no. 5, pp. 515-34, May 2013.

[10] N. Rana *et al.*, "Image-Based Mathematical Modeling to Differentiate Radiation-Induced Necrosis from Tumor Recurrence Following Stereotactic Radiosurgery for Intracranial Metastasis," *International Journal of Radiation Oncology Biology Physics*, vol. 96, no. 2, 2016.

[11] A. M. Coffey , M. I. Miga , I. Chen , and R. C. Thompson, "Toward a Preoperative Planning Tool for Brain Tumor Resection Therapies," *Int J Comput Assist Radiol Surg,* vol. 8, no. 1, pp. 87–97, Jan. 2013.

[12] A. N. Kumar, M. I. Miga, T. S. Pheiffer, L. B. Chambless, R. C. Thompson, and B. M. Dawant, "Automatic Tracking of Intraoperative Brain Surface Displacements in Brain Tumor Surgery," presented at the Annual International Conference of the IEEE Engineering in Medicine and Biology Society, 2014.

[13] M. I. Miga *et al.*, "Clinical Evaluation of a Model-Updated Image-Guidance Approach to Brain Shift Compensation: Experience in 16 Cases," *Int J Comput Assist Radiol Surg,* vol. 11, no. 8, pp. 1467-1474, Aug. 2016.

[14] I. Chen *et al.*, "Intraoperative Brain Shift Compensation: Accounting for Dural Septa," *IEEE Trans Biomed Eng,* vol. 58, no. 3, pp. 499-508, Mar. 2011.

[15] A. L. Simpson *et al.*, "Evaluation of Conoscopic Holography for Estimating Tumor Resection Cavities in Model-Based Image-Guided Neurosurgery," *IEEE Trans Biomed Eng,* vol. 61, no. 6, pp. 1833-43, Jun 2014.

[16] M. I. Miga , K. D. Paulsen, P. J. Hoopes, F. E. Kennedy, A. Hartrov, and D. W. Roberts, "In Vivo Modeling of Interstitial Pressure in the Brain under Surgical Load Using Finite Elements," *Transactions of the ASME,* vol. 122, pp. 354-363, 2000.

[17] D. A. Hormuth, 2nd *et al.*, "A Mechanically Coupled Reaction-Diffusion Model That Incorporates Intra-Tumoural Heterogeneity to Predict in Vivo Glioma Growth," *J R Soc Interface,* vol. 14, no. 128, pp. 1-12, Mar 2017.

[18] I. T. Gavrilovic and J. B. Posner, "Brain Metastases: Epidemiology and Pathophysiology," *Journal of neuro-oncology,* vol. 75, no. 1, pp. 5-14, 2005.

[19] A. Sahgal *et al.*, "Phase 3 Trials of Stereotactic Radiosurgery with or without Whole-Brain Radiation Therapy for 1 to 4 Brain Metastases: Individual Patient Data Meta-Analysis," *International Journal of Radiation Oncology* Biology* Physics,* vol. 91, no. 4, pp. 710-717, 2015.

[20] Q. T. Ostrom *et al.*, "Cbtrus Statistical Report: Primary Brain and Other Central Nervous System Tumors Diagnosed in the United States in 2010-2014," *Neuro Oncol,* vol. 19, no. suppl_5, pp. v1-v88, Nov 6 2017.

[21] Q. T. Ostrom, H. Gittleman, G. Truitt, A. Boscia, C. Kruchko, and J. S. Barnholtz-Sloan, "Cbtrus Statistical Report: Primary Brain and Other Central Nervous System Tumors Diagnosed in the United States in 2011–2015," *Neuro-oncology,* vol. 20, no. suppl_4, pp. iv1-iv86, 2018.

[22] G. D'Andrea, L. Palombi, G. Minniti, A. Pesce, and P. Marchetti, "Brain Metastases: Surgical Treatment and Overall Survival," *World neurosurgery,* vol. 97, pp. 169-177, 2017.

[23] L. M. DeAngelis, "Brain Tumors," *New England Journal of Medicine,* vol. 344, no. 2, pp. 114-123, 2001.

[24] P. Y. Wen and S. Kesari, "Malignant Gliomas in Adults," *New England Journal of Medicine,* vol. 359, no. 5, pp. 492-507, 2008.

[25] M. Essig *et al.*, "Mr Imaging of Neoplastic Central Nervous System Lesions: Review and Recommendations for Current Practice," *American Journal of Neuroradiology,* vol. 33, no. 5, pp. 803-817, 2012.

[26] J. H. Suh, "Stereotactic Radiosurgery for the Management of Brain Metastases," *New England Journal of Medicine,* vol. 362, no. 12, pp. 1119-1127, 2010.

[27] W. Hollingworth *et al.*, "A Systematic Literature Review of Magnetic Resonance Spectroscopy for the Characterization of Brain Tumors," *American Journal of Neuroradiology,* vol. 27, no. 7, pp. 1404-1411, 2006.

[28] R. A. Patchell *et al.*, "Postoperative Radiotherapy in the Treatment of Single Metastases to the Brain: A Randomized Trial," *Jama,* vol. 280, no. 17, pp. 1485-1489, 1998.

[29] M. Kocher *et al.*, "Adjuvant Whole-Brain Radiotherapy Versus Observation after Radiosurgery or Surgical Resection of One to Three Cerebral Metastases: Results of the Eortc 22952-26001 Study," *Journal of Clinical Oncology,* vol. 29, no. 2, p. 134, 2011.

[30] A. Mahajan *et al.*, "Post-Operative Stereotactic Radiosurgery Versus Observation for Completely Resected Brain Metastases: A Single-Centre, Randomised, Controlled, Phase 3 Trial," *The Lancet Oncology,* vol. 18, no. 8, pp. 1040-1048, 2017.

[31] M. E. Linskey *et al.*, "The Role of Stereotactic Radiosurgery in the Management of Patients with Newly Diagnosed Brain Metastases: A Systematic Review and Evidence-Based Clinical Practice Guideline," *J Neurooncol,* vol. 96, no. 1, pp. 45-68, Jan 2010.

[32] M. E. Linskey *et al.*, "The Role of Stereotactic Radiosurgery in the Management of Patients with Newly Diagnosed Brain Metastases: A Systematic Review and Evidence-Based Clinical Practice Guideline," *Journal of neuro-oncology,* vol. 96, no. 1, pp. 45-68, 2010.

[33] D. E. Citrin, "Recent Developments in Radiotherapy," *New England Journal of Medicine,* vol. 377, no. 11, pp. 1065-1075, 2017.

[34] N. Lyubimova and J. W. Hopewell, "Experimental Evidence to Support the Hypothesis That Damage to Vascular Endothelium Plays the Primary Role in the Development of Late Radiation-Induced Cns Injury," *Br J Radiol,* vol. 77, no. 918, pp. 488-92, Jun 2004.

[35] D. Brandsma, L. Stalpers, W. Taal, P. Sminia, and M. J. van den Bent, "Clinical Features, Mechanisms, and Management of Pseudoprogression in Malignant Gliomas," *Lancet Oncol,* vol. 9, no. 5, pp. 453-61, 2008.

[36] A. J. Kumar *et al.*, "Malignant Gliomas: Mr Imaging Spectrum of Radiation Therapy- and Chemotherapy-Induced Necrosis of the Brain after Treatment," *Radiology,* vol. 217, no. 2, pp. 377-84, 2000.

[37] M. E. Mullins, G. D. Barest, P. W. Schaefer, F. H. Hochberg, R. G. Gonzalez, and M. H. Lev, "Radiation Necrosis Versus Glioma Recurrence: Conventional Mr Imaging Clues to Diagnosis," *AJNR Am J Neuroradiol,* vol. 26, no. 8, pp. 1967-72, 2005.

[38] G. Minniti *et al.*, "Stereotactic Radiosurgery for Brain Metastases: Analysis of Outcome and Risk of Brain Radionecrosis," *Radiation oncology,* vol. 6, no. 1, p. 48, 2011.

[39] M. C. Chamberlain, M. J. Glantz, L. Chalmers, A. Van Horn, and A. E. Sloan, "Early Necrosis Following Concurrent Temodar and Radiotherapy in Patients with Glioblastoma," *J Neurooncol,* vol. 82, no. 1, pp. 81-3, Mar 2007.

[40] R. F. J. Barajas *et al.*, "Differentiation of Recurrent Glioblastoma Multiforme from Radiation Necrosis after External Beam Radiation Therapy with Dynamic Susceptibility-Weighted Contrast-Enhanced Perfusion Mr Imaging," *Radiology,* vol. 253, no. 2, pp. 486-96, 2009.

[41] S. Bisdas *et al.*, "Distinguishing Recurrent High-Grade Gliomas from Radiation Injury: A Pilot Study Using Dynamic Contrast-Enhanced Mr Imaging," *Acad Radiol,* vol. 18, no. 5, pp. 575-83, May 2011.

[42] S. K. Ellika *et al.*, "Role of Perfusion Ct in Glioma Grading and Comparison with Conventional Mr Imaging Features," *AJNR Am J Neuroradiol,* vol. 28, no. 10, pp. 1981-7, Nov-Dec 2007.

[43] Y. H. Kim *et al.*, "Differentiating Radiation Necrosis from Tumor Recurrence in High-Grade Gliomas: Assessing the Efficacy of 18f-Fdg Pet, 11c-Methionine Pet and Perfusion Mri," *Clin Neurol Neurosurg,* vol. 112, no. 9, pp. 758-65, Nov 2010.

[44] Y. Terakawa *et al.*, "Diagnostic Accuracy of 11c-Methionine Pet for Differentiation of Recurrent Brain Tumors from Radiation Necrosis after Radiotherapy," *J Nucl Med,* vol. 49, no. 5, pp. 694-9, May 2008.

[45] C. Dowling *et al.*, "Preoperative Proton Mr Spectroscopic Imaging of Brain Tumors: Correlation with Histopathologic Analysis of Resection Specimens," *AJNR Am J Neuroradiol,* vol. 22, no. 4, pp. 604-12, 2001.

[46] E. A. Smith, R. C. Carlos, L. R. Junck, C. I. Tsien, A. Elias, and P. C. Sundgren, "Developing a Clinical Decision Model: Mr Spectroscopy to Differentiate between Recurrent Tumor and Radiation Change in Patients with New Contrast-Enhancing Lesions," *AJR Am J Roentgenol,* vol. 192, no. 2, pp. W45-52, Feb 2009.

[47] P. Weybright *et al.*, "Differentiation between Brain Tumor Recurrence and Radiation Injury Using Mr Spectroscopy," *AJR Am J Roentgenol,* vol. 185, no. 6, pp. 1471-6, Dec 2005.

[48] T. J. Brown *et al.*, "Association of the Extent of Resection with Survival in Glioblastoma: A Systematic Review and Meta-Analysis," *JAMA oncology,* vol. 2, no. 11, pp. 1460-1469, 2016.

[49] S. Eljamel *et al.*, "Comparison of Intraoperative Fluorescence and Mri Image Guided Neuronavigation in Malignant Brain Tumours, a Prospective Controlled Study," *Photodiagnosis and photodynamic therapy,* vol. 10, no. 4, pp. 356-361, 2013.

[50] T. Ius *et al.*, "Low-Grade Glioma Surgery in Eloquent Areas: Volumetric Analysis of Extent of Resection and Its Impact on Overall Survival. A Single-Institution Experience in 190 Patients," *Journal of Neurosurgery,* vol. 117, no. 6, pp. 1039-1052, 2012.

[51] S. Bayer, A. Maier, M. Ostermeier, and R. Fahrig, "Intraoperative Imaging Modalities and Compensation for Brain Shift in Tumor Resection Surgery," *International journal of biomedical imaging,* vol. 2017, 2017.

[52] I. J. Gerard, M. Kersten-Oertel, K. Petrecca, D. Sirhan, J. A. Hall, and D. L. Collins, "Brain Shift in Neuronavigation of Brain Tumors: A Review," *Med Image Anal,* vol. 35, pp. 403-420, Jan. 2017.

[53] C. Schulz, S. Waldeck, and U. M. Mauer, "Intraoperative Image Guidance in Neurosurgery: Development, Current Indications, and Future Trends," *Radiol Res Pract*, vol. 2012, p. 197364, 2012.

[54] A. Monro, *Observations on the Structure and Functions of the Nervous System* 1783.

[55] A. Siegel and H. N. Sapru, *Essential Neuroscience*, 3rd ed. Baltimore, MD: Lippincott Williams & Wilkins, 2015.

[56] W. D. Freeman, "Management of Intracranial Pressure," *Continuum (Minneap Minn),* vol. 21, no. 5 Neurocritical Care, pp. 1299–1323, Oct. 2015.

[57] C. E. Wolfla, T. G. Luerssen, and R. M. Bowman, "Regional Brain Tissue Pressure Gradients Created by Expanding Extradural Temporal Mass Lesion," *J Neurosurg,* vol. 86, no. 3, pp. 505–510, Mar. 1997.

[58] C. E. Wolfla, T. G. Luerssen, R. M. Bowman, and T. K. Putty, "Brain Tissue Pressure Gradients Created by Expanding Frontal Epidural Mass Lesion," *J Neurosurg,* vol. 84, no. 4, pp. 642-647, Apr. 1996.

[59] Y. Esquenazi, V. P. Lo, and K. Lee, "Critical Care Management of Cerebral Edema in Brain Tumors," *J Intensive Care Med,* vol. 32, no. 1, pp. 15-24, Jan 2017.

[60] M. Osgood, R. Compton, R. Carandang, W. Hall, G. Kershaw, and S. Muehlschlegel, "Rapid Unexpected Brain Herniation in Association with Renal Replacement Therapy in Acute Brain Injury: Caution in the Neurocritical Care Unit," *Neurocrit Care,* vol. 22, no. 2, pp. 176-183, Apr 2015.

[61] A. P. Fishman, "Brain Edema," *The New England Journal of Medicine,* vol. 293, pp. 706-711, 1975.

[62] O. Clatz *et al.*, "Robust Nonrigid Registration to Capture Brain Shift from Intraoperative Mri," *IEEE Trans Med Imaging,* vol. 24, no. 11, pp. 1417-1427, Nov. 2005.

[63] A. Mostayed *et al.*, "Biomechanical Model as a Registration Tool for Image-Guided Neurosurgery: Evaluation against Bspline Registration," *Ann Biomed Eng,* vol. 41, no. 11, pp. 2409-2425, Nov. 2013.

[64] K. Sun, T. S. Pheiffer, A. L. Simpson, J. A. Weis, R. C. Thompson, and M. I. Miga, "Near Real-Time Computer Assisted Surgery for Brain Shift Correction Using Biomechanical Models," *IEEE J Transl Eng Health Med,* vol. 2, p. 2500113, 2014.

[65] M. I. Miga, "Computational Modeling for Enhancing Soft Tissue Image Guided Surgery: An Application in Neurosurgery," *Ann Biomed Eng,* vol. 44, no. 1, pp. 128-138, Jan. 2016.

[66] A. Wittek, T. Hawkins, and K. Miller, "On the Unimportance of Constitutive Models in Computing Brain Deformation for Image-Guided Surgery," *Biomech Model Mechanobiol*, vol. 8, no. 1, pp. 77-84, Feb. 2009.

[67] A. Hagemann, K. Rohr, and H. S. Stiehl, "Coupling of Fluid and Elastic Models for Biomechanical Simulations of Brain Deformations Using Fem," *Medical Image Analysis*, vol. 6, no. 4, pp. 375–388, Dec. 2002.

[68] K. Miller, "Constitutive Model of Brain Tissue Suitable for Finite Element Analysis of Surgical Procedures," *J Biomech*, vol. 32, no. 5, pp. 531-537, May 1999.

[69] M. I. Miga *et al.*, "Modeling of Retraction and Resection for Intraoperative Updating of Images," *Neurosurgery*, vol. 49, no. 1, pp. 75-85, 2001.

[70] K. D. Paulsen, M. I. Miga, F. E. Kennedy, P. J. Hoopes, A. Hartov, and D. W. Roberts, "A Computational Model for Tracking Subsurface Tissue Deformation During Stereotactic Neurosurgery," *IEEE Trans Biomed Eng*, vol. 46, no. 2, pp. 213-225, Feb. 1999.

[71] C. DeLorenzo, X. Papademetris, L. H. Staib, K. P. Vives, D. D. Spencer, and J. S. Duncan, "Volumetric Intraoperative Brain Deformation Compensation: Model Development and Phantom Validation," *IEEE Trans Med Imaging*, vol. 31, no. 8, pp. 1607-1619, Aug. 2012.

[72] M. Ferrant *et al.*, "Serial Registration of Intraoperative Mr Images of the Brain," *Med Image Anal*, vol. 6, no. 4, pp. 337–359, Dec. 2002.

[73] G. Karami, N. Grundman, N. Abolfathi, A. Naik, and M. Ziejewski, "A Micromechanical Hyperelastic Modeling of Brain White Matter under Large Deformation," *J Mech Behav Biomed Mater,* vol. 2, no. 3, pp. 243-254, Jul. 2009.

[74] M. Ferrant, S. K. Warfield, A. Nabavi, F. A. Jolesz, and R. Kikinis, "Registration of 3d Intraoperative Mr Images of the Brain Using a Finite Element Biomechanical Model," in *International Conference on Medical Image Computing and Computer-Assisted Intervention*, 2000, pp. 19-28: Springer.

[75] B. Wirth and I. Sobey, "An Axisymmetric and Fully 3d Poroelastic Model for the Evolution of Hydrocephalus," *Math Med Biol*, vol. 23, no. 4, pp. 363-88, Dec 2006.

[76] P. Dumpuri, R. C. Thompson, B. M. Dawant, A. Cao, and M. I. Miga, "An Atlas-Based Method to Compensate for Brain Shift: Preliminary Results," *Med Image Anal*, vol. 11, no. 2, pp. 128-45, Apr 2007.

[77] M. M. Grabowski *et al.*, "Residual Tumor Volume Versus Extent of Resection: Predictors of Survival after Surgery for Glioblastoma," *Journal of Neurosurgery*, vol. 121, no. 5, pp. 1115-1123, 2014.

[78] K. Laksari, M. Shafieian, and K. Darvish, "Constitutive Model for Brain Tissue under Finite Compression," *Journal of Biomechanics*, vol. 45, no. 4, pp. 642-646, 2012.

[79] W. Dai, G. W. Astary, A. K. Kasinadhuni, P. R. Carney, T. H. Mareci, and M. Sarntinoranont, "Voxelized Model of Brain Infusion That Accounts for Small Feature Fissures: Comparison with Magnetic Resonance Tracer Studies," *J Biomech Eng*, vol. 138, no. 5, p. 051007, May 2016.

[80] K. R. Swanson, C. Bridge, J. D. Murray, and E. C. J. Alvord, "Virtual and Real Brain Tumors: Using Mathematical Modeling to Quantify Glioma Growth and Invasion," *J Neurol Sci*, vol. 216, no. 1, pp. 1-10, 2003.

[81] P. K. Burgess, P. M. Kulesa, J. D. Murray, and E. C. J. Alvord, "The Interaction of Growth Rates and Diffusion Coefficients in a Three-Dimensional Mathematical Model of Gliomas," *J Neuropathol Exp Neurol*, vol. 56, no. 6, pp. 704-713, 1997.

[82] K. R. Swanson, E. C. J. Alvord, and J. D. Murray, "A Quantitative Model for Differential Motility of Gliomas in Grey and White Matter," *Cell Prolif,* vol. 33, no. 5, pp. 317-329, 2000.

[83] S. Jbabdi *et al.*, "Simulation of Anisotropic Growth of Low-Grade Gliomas Using Diffusion Tensor Imaging," *Magn Reson Med,* vol. 54, no. 3, pp. 616-24, Sep 2005.

[84] P. Tracqui, G. C. Cruywagen, D. E. Woodward, G. T. Bartoo, J. D. Murray, and E. C. J. Alvord, "A Mathematical Model of Glioma Growth: The Effect of Chemotherapy on Spatio-Temporal Growth," *Cell Prolif,* vol. 28, no. 1, pp. 17-31, 1995.

[85] D. E. Woodward, J. Cook, P. Tracqui, G. C. Cruywagen, J. D. Murray, and E. C. J. Alvord, "A Mathematical Model of Glioma Growth: The Effect of Extent of Surgical Resection," *Cell Prolif,* vol. 29, no. 6, pp. 269-288, 1996.

[86] K. R. Swanson, E. C. J. Alvord, and J. D. Murray, "Virtual Resection of Gliomas: Effect of Extent of Resection on Recurrence," *Math Comput Model,* vol. 37, no. 11, pp. 1177-1190, 2003.

[87] D. A. Hormuth, 2nd *et al.*, "Predicting in Vivo Glioma Growth with the Reaction Diffusion Equation Constrained by Quantitative Magnetic Resonance Imaging Data," *Phys Biol,* vol. 12, no. 4, p. 046006, Jun 04 2015.

[88] G. Helmlinger, P. A. Netti, H. C. Lichtenbeld, R. J. Melder, and R. K. Jain, "Solid Stress Inhibits the Growth of Multicellular Tumor Spheroids," *Nat Biotechnol,* vol. 15, no. 8, pp. 778-83, Aug 1997.

[89] A. W. El-Kareh and T. W. Secomb, "A Mathematical Model for Comparison of Bolus Injection, Continuous Infusion, and Liposomal Delivery of Doxorubicin to Tumor Cells," *Neoplasia,* vol. 2, no. 4, pp. 325-338, 2000.

[90] M. A. Chaplain, "Mathematical Modelling of Angiogenesis," *J Neurooncol,* vol. 50, pp. 37-51, 2000.

[91] S. Narasimhan, J. A. Weis, H. F. J. Gonzalez, R. C. Thompson, and M. I. Miga, "In Vivo Modeling of Interstitial Pressure in a Porcine Model: Approximation of Poroelastic Properties and Effects of Enhanced Anatomical Structure Modeling," *J. Med. Imag.,* vol. 5, no. 4, p. 045002, 2018.

[92] S. Narasimhan *et al.*, "Biophysical Model-Based Parameters to Classify Tumor Recurrence from Radiation-Induced Necrosis for Brain Metastases," *Med Phys,* vol. 46, no. 5, pp. 2487-2496, May 2019.

[93] S. Narasimhan, M. I. Miga , N. Rana, H. B. Johnson, A. Attia, and J. A. Weis, "Differentiating Tumor Recurrence from Radiation-Induced Necrosis: An Image-Based Mathematical Modeling Framework," presented at the IEEE International Symposium on Biomedical Imaging (ISBI), Washington D.C., 2018.

[94] M. Luo *et al.*, "Retrospective Study Comparing Model-Based Deformation Correction to Intraoperative Magnetic Resonance Imaging for Image-Guided Neurosurgery," *J Med Imaging (Bellingham),* vol. 4, no. 3, p. 035003, Jul 2017.

[95] "Bk Medical, Analogic Corporation," ed. Peabody, USA.

[96] D. R. Lynch, *Numerical Partial Differential Equations for Environmental Scientists and Engineers: A First Practical Course*. New York, NY: Springer Science & Business Media 2005.

[97] M. A. Biot, "General Theory of Three-Dimensional Consolidation," *Journal of Applied Physics,* vol. 12, no. 2, pp. 155-164, 1941.

[98] J. A. Weis, M. I. Miga, and T. E. Yankeelov, "Three-Dimensional Image-Based Mechanical Modeling for Predicting the Response of Breast Cancer to Neoadjuvant Therapy," *Comput Methods Appl Mech Eng,* vol. 314, pp. 494-512, Feb 01 2017.

[99] J. Nocedal and S. Wright, *Numerical Optimization*. Springer Science & Business Media, 2006.

[100] A. R. Conn, N. I. Gould, and P. L. Toint, *Trust Region Methods*. Siam, 2000.

[101] Q. Yuan *et al.*, "Impact of Intracranial Pressure Monitoring on Mortality in Patients with Traumatic Brain Injury: A Systematic Review and Meta-Analysis," *J Neurosurg,* vol. 122, no. 3, pp. 574-587, Mar 2015.

[102] J. Vender, J. Waller, K. Dhandapani, and D. McDonnell, "An Evaluation and Comparison of Intraventricular, Intraparenchymal, and Fluid-Coupled Techniques for Intracranial Pressure Monitoring in Patients with Severe Traumatic Brain Injury," *J Clin Monit Comput,* vol. 25, no. 4, pp. 231-236, Aug 2011.

[103] D. D. Weaver, H. R. Winn, and J. A. Jane, "Differential Intracranial Pressure in Patients with Unilateral Mass Lesions," *J Neurosurg,* vol. 56, no. 5, pp. 660-665, 1982.

[104] A. L. D'Ambrosio *et al.*, "Interhemispheric Intracranial Pressure Gradients in Nonhuman Primate Stroke," *Surg Neurol,* vol. 58, no. 5, pp. 295-301, 2002.

[105] J. Sahuquillo, M. A. Poca, M. Arribas, A. Garnacho, and E. Rubio, "Interhemispheric Supratentorial Intracranial Pressure Gradients in Head-Injured Patients: Are They Clinically Important?," *J Neurosurg,* vol. 90, no. 1, pp. 16-26, 1999.

[106] K. Miller and K. Chinzei, "Constitutive Modelling of Brain Tissue: Experiment and Theory," *J Biomech,* vol. 30, no. 11-12, pp. 1115-1121, 1997.

[107] T. Doczi, "Volume Regulation of the Brain Tissue-a Survey*," *Acta Neurochir (Wien),* vol. 121, no. 1-2, pp. 1-8, 1993.

[108] M. A. Green, L. E. Bilston, and R. Sinkus, "In Vivo Brain Viscoelastic Properties Measured by Magnetic Resonance Elastography," *NMR Biomed,* vol. 21, no. 7, pp. 755-764, Aug. 2008.

[109] M. T. Prange and S. S. Margulies, "Regional, Directional, and Age-Dependent Properties of the Brain Undergoing Large Deformation," *J Biomech Eng,* vol. 124, no. 2, pp. 244-252, Apr. 2002.

[110] S. Chatelin, A. Constantinesco, and R. Willinger, "Fifty Years of Brain Tissue Mechanical Testing: From in Vitro to in Vivo Investigations," *Biorheology,* vol. 47, no. 5-6, pp. 255-276, 2010.

[111] J. Hu *et al.*, "Intraoperative Brain Shift Prediction Using a 3d Inhomogeneous Patient-Specific Finite Element Model," *J Neurosurg,* vol. 106, no. 1, pp. 164–169, Jan. 2007.

[112] M. I. Miga, K. D. Paulsen, P. J. Hoopes, F. E. Kennedy, A. Hartov, and D. W. Roberts, "In Vivo Modeling of Interstitial Pressure in the Brain under Surgical Load Using Finite Elements," *J Biomech Eng,* vol. 122, no. 4, pp. 354-363, Aug. 2000.

[113] M. I. Miga "Development and Quantification of a 3d Brain Deformation Model for Model-Updated Image-Guided Stereotactic Neurosurgery," Ph.D. thesis, Engineering, Dartmouth College, Hanover, 1998.

[114] M. I. Miga, K. D. Paulsen, and F. E. Kennedy, "Von Neumann Stability Analysis of Biot's General Two-Dimensional Theory of Consolidation," *International Journal For Numerical Methods In Engineering,* vol. 43, pp. 955–974, 1998.

[115] J. M. J. Sullivan, G. Charron, and K. D. Paulsen, "A Three-Dimensional Mesh Generator for Arbitrary Multiple Material Domains," *Finite Elem Anal Design,* vol. 25, no. 3-4, pp. 219-241, 1997.

[116] M. I. Miga, K. D. Paulsen, F. E. Kennedy, P. J. Hoopes, A. Hartov, and D. W. Roberts, "In Vivo Analysis of Heterogeneous Brain Deformation Computations for Model-Updated Image Guidance," *Comput Methods Biomech Biomed Engin,* vol. 3, no. 2, pp. 129-146, 2000.

[117] M. I. Miga , K. D. Paulsen, F. E. Kennedy, P. J. Hoopes, A. Hartov, and D. W. Roberts, "Modeling Surgical Loads to Account for Subsurface Tissue Deformation During Stereotactic Neurosurgery," presented at the IEEE SPIE Proceedings of Laser-Tissue Interaction IX, Part B: Soft-tissue Modeling, 1998.

[118] B. M. Dawant, S. L. Hartmann, S. Pan, and S. Gadamsetty, "Brain Atlas Deformation in the Presence of Small and Large Space-Occupying Tumors," *Comput Aided Surg,* vol. 7, no. 1, pp. 1-10, 2002.

[119] S. E. Maier, Y. Sun, and R. V. Mulkern, "Diffusion Imaging of Brain Tumors," *NMR Biomed,* vol. 23, no. 7, pp. 849-864, Aug. 2010.

[120] J. R. Carhuapoma, A. I. Qureshi, A. Bhardwaj, and M. A. Williams, "Interhemispheric Intracranial Pressure Gradients in Massive Cerebral Infarction," *J Neurosurg Anesthesiol,* vol. 14, no. 4, pp. 299-303, 2002.

[121] B. M. Ellingson, C. Chung, W. B. Pope, J. L. Boxerman, and T. J. Kaufmann, "Pseudoprogression, Radionecrosis, Inflammation or True Tumor Progression? Challenges Associated with Glioblastoma Response Assessment in an Evolving Therapeutic Landscape," *J Neurooncol,* vol. 134, no. 3, pp. 495-504, Sep 2017.

[122] K. Parvez, A. Parvez, and G. Zadeh, "The Diagnosis and Treatment of Pseudoprogression, Radiation Necrosis and Brain Tumor Recurrence," *Int J Mol Sci,* vol. 15, no. 7, pp. 11832-46, Jul 3 2014.

[123] R. Shah *et al.*, "Radiation Necrosis in the Brain: Imaging Features and Differentiation from Tumor Recurrence," *Radiographics,* vol. 32, no. 5, pp. 1343-59, 2012.

[124] J. L. Xu *et al.*, "Distinction between Postoperative Recurrent Glioma and Radiation Injury Using Mr Diffusion Tensor Imaging," *Neuroradiology,* vol. 52, no. 12, pp. 1193-9, Dec 2010.

[125] P. C. Sundgren *et al.*, "Differentiation of Recurrent Brain Tumor Versus Radiation Injury Using Diffusion Tensor Imaging in Patients with New Contrast-Enhancing Lesions," *Magn Reson Imaging,* vol. 24, no. 9, pp. 1131-42, Nov 2006.

[126] J. P. Rock *et al.*, "Associations among Magnetic Resonance Spectroscopy, Apparent Diffusion Coefficients, and Image-Guided Histopathology with Special Attention to Radiation Necrosis," *Neurosurgery,* vol. 54, no. 5, pp. 1111-7, 2004.

[127] T. E. Yankeelov *et al.*, "Clinically Relevant Modeling of Tumor Growth and Treatment Response," *Sci Transl Med,* vol. 5, no. 187, p. 187ps9, 2013.

[128] N. C. Atuegwu, D. C. Colvin, M. E. Loveless, L. Xu, J. C. Gore, and T. E. Yankeelov, "Incorporation of Diffusion-Weighted Magnetic Resonance Imaging Data into a Simple Mathematical Model of Tumor Growth," *Phys Med Biol,* vol. 57, no. 1, pp. 225-40, Jan 07 2012.

[129] O. Clatz *et al.*, "Realistic Simulation of the 3-D Growth of Brain Tumors in Mr Images Coupling Diffusion with Biomechanical Deformation," *IEEE Trans Med Imaging,* vol. 24, no. 10, pp. 1334-46, Oct 2005.

[130] C. Hogea, C. Davatzikos, and G. Biros, "An Image-Driven Parameter Estimation Problem for a Reaction-Diffusion Glioma Growth Model with Mass Effects," *J Math Biol,* vol. 56, no. 6, pp. 793-825, Jun 2008.

[131] A. Mohamed and C. Davatzikos, "Finite Element Modeling of Brain Tumor Mass-Effect from 3d Medical Images," *Med Image Comput Comput Assist Interv,* vol. 8, no. Pt 1, pp. 400-8, 2005.

[132] I. Garg and M. I. Miga, "Preliminary Investigation of the Inhibitory Effects of Mechanical Stress in Tumor Growth," in *Proc. SPIE*, vol. 6918, p. 69182L, 2008.

[133] J. A. Weis *et al.*, "A Mechanically Coupled Reaction-Diffusion Model for Predicting the Response of Breast Tumors to Neoadjuvant Chemotherapy," *Phys Med Biol,* vol. 58, no. 17, pp. 5851-66, Sep 07 2013.

[134] J. A. Weis *et al.*, "Predicting the Response of Breast Cancer to Neoadjuvant Therapy Using a Mechanically Coupled Reaction-Diffusion Model," *Cancer Res,* vol. 75, no. 22, pp. 4697-707, Nov 15 2015.

[135] D. R. Lynch, *Numerical Partial Differential Equations for Environmental Scientists and Engineers*. New York, NY: Springer Science+Business Media, Inc. , 2005.

[136] F. Maes, A. Collignon, D. Vandermeulen, G. Marchal, and P. Suetens, "Multimodality Image Registration by Maximization of Mutual Information," *IEEE Trans Med Imaging,* vol. 16, no. 2, pp. 187-98, 1997.

[137] I. M. Dequesada, R. G. Quisling, A. Yachnis, and W. A. Friedman, "Can Standard Magnetic Resonance Imaging Reliably Distinguish Recurrent Tumor from Radiation Necrosis after Radiosurgery for Brain Metastases? A Radiographic-Pathological Study.," *Neurosurgery,* vol. 63, no. 5, pp. 898-903, Nov 2008.

[138] N. U. Lin *et al.*, "Response Assessment Criteria for Brain Metastases: Proposal from the Rano Group," *Lancet Oncol,* vol. 16, no. 6, pp. e270-8, 2015.

[139] I. Y. Eyüpoglu, M. Buchfelder, and N. E. Savaskan, "Surgical Resection of Malignant Gliomas—Role in Optimizing Patient Outcome," *Nature reviews Neurology,* vol. 9, no. 3, p. 141, 2013.

[140] D. A. Orringer, A. Golby, and F. Jolesz, "Neuronavigation in the Surgical Management of Brain Tumors: Current and Future Trends," *Expert review of medical devices,* vol. 9, no. 5, pp. 491-500, 2012.

[141] C. Nimsky, O. Ganslandt, S. Cerny, P. Hastreiter, G. Greiner, and R. Fahlbusch, "Quantification of, Visualization of, and Compensation for Brain Shift Using Intraoperative Magnetic Resonance Imaging," *Neurosurgery,* vol. 47, no. 5, pp. 1070-1080, 2000.

[142] C. Nimsky, O. Ganslandt, B. von Keller, J. Romstöck, and R. Fahlbusch, "Intraoperative High-Field-Strength Mr Imaging: Implementation and Experience in 200 Patients," *Radiology,* vol. 233, no. 1, pp. 67-78, 2004.

[143] P. Dumpuri *et al.*, "A Fast and Efficient Method to Compensate for Brain Shift for Tumor Resection Therapies Measured between Preoperative and Postoperative Tomograms," *IEEE Transactions On Biomedical Engineering,* vol. 57, no. 6, pp. 1285-1296, 2010.

[144] X. Fan, S. Ji, K. Fontaine, A. Hartov, D. Roberts, and K. Paulsen, "Simulation of Brain Tumor Resection in Image-Guided Neurosurgery," in *Medical Imaging 2011: Visualization, Image-Guided Procedures, and Modeling,* 2011, vol. 7964, p. 79640U: International Society for Optics and Photonics.

[145] A. Nabavi *et al.*, "Serial Intraoperative Magnetic Resonance Imaging of Brain Shift," *Neurosurgery,* vol. 48, no. 4, pp. 787-798, 2001.

[146] L. A. Jarvis *et al.*, "Tumor Bed Dynamics after Surgical Resection of Brain Metastases: Implications for Postoperative Radiosurgery," *International Journal of Radiation Oncology* Biology* Physics,* vol. 84, no. 4, pp. 943-948, 2012.

[147] B. Atalar *et al.*, "Cavity Volume Dynamics after Resection of Brain Metastases and Timing of Postresection Cavity Stereotactic Radiosurgery," *Neurosurgery,* vol. 72, no. 2, pp. 180-185, 2012.

[148] Y. M. Li, D. Suki, K. Hess, and R. Sawaya, "The Influence of Maximum Safe Resection of Glioblastoma on Survival in 1229 Patients: Can We Do Better Than Gross-Total Resection?," *Journal of Neurosurgery,* vol. 124, no. 4, pp. 977-988, 2016.

[149] A. Fedorov *et al.*, "3d Slicer as an Image Computing Platform for the Quantitative Imaging Network," *Magnetic resonance imaging,* vol. 30, no. 9, pp. 1323-1341, 2012.

[150] S. Frisken *et al.*, "Preliminary Results Comparing Thin-Plate Splines with Finite Element Methods for Modeling Brain Deformation During Neurosurgery Using Intraoperative Ultrasound," in *Medical Imaging*

2019: Image-Guided Procedures, Robotic Interventions, and Modeling, 2019, vol. 10951, p. 1095120: International Society for Optics and Photonics.

[151] I. Machado *et al.*, "Non-Rigid Registration of 3d Ultrasound for Neurosurgery Using Automatic Feature Detection and Matching," *Int J Comput Assist Radiol Surg,* vol. 13, no. 10, pp. 1525-1538, Oct 2018.

[152] G. K. Rohde, A. Aldroubi, and B. M. Dawant, "The Adaptive Bases Algorithm for Intensity-Based Nonrigid Image Registration," *IEEE transactions on medical imaging,* vol. 22, no. 11, pp. 1470-1479, 2003.

[153] D. W. Roberts *et al.*, "Intraoperatively Updated Neuroimaging Using Brain Modeling and Sparse Data," *Neurosurgery,* vol. 45, no. 5, pp. 1199-1207, 1999.

[154] S. Narasimhan, J. A. Weis, I. S. Godage, R. J. Webster, K. Weaver, and M. I. Miga, "Development of a Mechanics-Based Model of Brain Deformations During Intracerebral Hemorrhage Evacuation," presented at the Medical Imaging 2017: Image-Guided Procedures, Robotic Interventions, and Modeling, 2017.

[155] P. Dumpuri and M. I. Miga, "Model-Updated Image Guidance: A Statistical Approach to Gravity-Induced Brain Shift," *Med Image Comput Comput Assist Interv,* vol. 2878, pp. 375-382, Nov 2003.

[156] X. Li *et al.*, "Statistical Comparison of Dynamic Contrast- Enhanced Mri Pharmacokinetic Models in Human Breast Cancer," *Magnetic resonance in medicine,* vol. 68, no. 1, pp. 261-271, 2012.

[157] C. J. J. van Asch, M. J. A. Luitse, G. J. E. Rinkel, I. van der Tweel, A. Algra, and C. J. M. Klijn, "Incidence, Case Fatality, and Functional Outcome of Intracerebral Haemorrhage over Time, According to Age, Sex, and Ethnic Origin: A Systematic Review and Meta-Analysis," *The Lancet Neurology,* vol. 9, no. 2, pp. 167-176, 2010.

[158] L. Elijovich, P. V. Patel, and J. C. Hemphill, 3rd, "Intracerebral Hemorrhage," *Semin Neurol,* vol. 28, no. 5, pp. 657-667, Nov 2008.

[159] S. P. Johnsen *et al.*, "Nonaspirin Nonsteroidal Anti-Inflammatory Drugs and Risk of Hospitalization for Intracerebral Hemorrhage," *Stroke,* vol. 34, no. 2, pp. 387-391, 2003.

[160] C. S. Anderson *et al.*, "Rapid Blood-Pressure Lowering in Patients with Acute Intracerebral Hemorrhage," *N Engl J Med,* vol. 368, no. 25, pp. 2355-2365, Jun 20 2013.

[161] J. Broderick, T. Brott, J. Duldner, T. Tomsick, and G. Huster, "Volume of Intracerebral Hemorrhage a Powerful and Easy-to-Use Predictor of 30-Day Mortality," *Stroke,* vol. 24, no. 7, pp. 987-993, 1993.

[162] J. M. K. Murthy, G. V. S. Chowdary, T. V. R. K. Murthy, P. Syed Ameer Bhasha, and T. Jaishree Naryana, "Decompressive Craniectomy with Clot Evacuation in Large Hemispheric Intracerebral Hemorrhage," *Neurocrit Care,* vol. 2, pp. 258-262, 2005.

[163] D. W. Newell *et al.*, "Minimally Invasive Evacuation of Spontaneous Intracerebral Hemorrhage Using Sonothrombolysis," *J Neurosurg,* vol. 115, no. 3, pp. 592-601, Sep 2011.

[164] D. Staykov *et al.*, "Natural Course of Perihemorrhagic Edema after Intracerebral Hemorrhage," *Stroke,* vol. 42, no. 9, pp. 2625-2629, Sep 2011.

[165] J. Burgner, P. J. Swaney, R. A. Lathrop, K. D. Weaver, and R. J. Webster, "Debulking from Within: A Robotic Steerable Cannula for Intracerebral Hemorrhage Evacuation," *IEEE Trans Biomed Eng,* vol. 60, no. 9, pp. 2567-2575, Sep 2013.

[166] P. E. Dupont, J. Lock, B. Itkowitz, and E. Butler, "Design and Control of Concentric-Tube Robots," *IEEE Trans Robot,* vol. 26, no. 2, pp. 209-225, Apr 1 2010.

[167] H. Takizawa, K. Sugiura, M. Baba, and J. D. Miller, "Analysis of Intracerebral Hematoma Shapes by Numerical Computer Simulation Using the Finite Element Method," *Neurol Med Chir (Tokyo)*, vol. 34, pp. 65-69, 1994.

[168] C. Nicholson, "Diffusion and Related Transport Mechanisms in Brain Tissue," *Reports On Progress In Physics*, vol. 64, pp. 815–884, 2001.

[169] D. S. Bidros, J. K. Liu, and M. A. Vogelbaum, "Future of Convection-Enhanced Delivery in the Tretment of Brain Tumors," *Future Oncology*, vol. 6, no. 1, pp. 117-125, 2010.